STUDY OF INSTABILITIES AND SHOCK PROPAGATION IN LASER IRRADIATED TARGETS

By

Steven Edward Coe

Imperial College

London

A thesis submitted for the degree of Doctor of Philosophy of the University of London and for the Diploma of Membership of Imperial College

Blackett Laboratory

Imperial College of Science,

Technology and Medicine

August 1989

ABSTRACT

This thesis describes experimental work in two areas of importance to proposed laser fusion schemes. Firstly, results are presented on the propagation of laser induced shocks in solid targets. In particular, the first direct experimental observation of the coalescence of two shocks generated by a temporally shaped laser pulse has been made. Optical streak photography of the rear surface of aluminium multiple step targets was used to study the breakout of these shocks and observe their behaviour. The experimental results are compared with simulations by a one−dimensional Lagrangian hydrodynamic code.

Secondly, results are presented on the interaction of a high power laser beam with a large underdense plasma. Measurements were made of the filamentation, Stimulated Raman Scattering and Stimulated Brillouin Scattering instabilities occurring during this interaction. In particular, time resolved measurements of the interaction beam after it has propagated through the preformed aluminium plasma show evidence of the break up the beam due to filamentation. This process was found to have a threshold near 10^{14} Wcm^{-2}, which is in agreement with theoretical predictions. For bismuth and high density aluminium plasmas whole beam self−focusing was observed. Measurements were also made of the effectiveness of a random phase plate or an induced spatial incoherence system to reduce the levels of these three instabilities by smoothing of the interaction beam profile. Both techniques were found to give significant reductions in the levels of the Raman and Brillouin instabilities. Measurements of the transmitted interaction beam appear to indicate some suppression of the filamentation instability by these techniques. Finally, optical probing measurements used to determine the uniformity of the large underdense plasmas are reported on. It was found that the presence of a formvar substrate to support the target can play a significant role in the expansion of the plasma produced.

ACKNOWLEDGEMENTS

Firstly, I would like to thank my supervisor Dr. O. Willi for his enthusiastic guidance and encouragement throughout the course of this work. The experimental work described in this thesis was carried out at the Central Laser Facility of the Rutherford Appleton Laboratory and would not have been possible without the valuable help of the staff employed there. In particular I would like to thank the Vulcan laser operations group led by C.N. Danson and the target preparation group led by Dr. P.T. Rumsby. Thanks are also due to the following people:

D. Bassett – for passing on so much of his experimental knowledge to me.

T. Afshar–rad – for supplying the S.R.S. and S.B.S. spectra presented in chapters 5 and 6.

J. Edwards – for supplying the modified form of the 2–D code POLLUX used in chapter 7 and for useful discussions on the simulations performed with the code.

A.K.L. Dymoke–Bradshaw – for his assistance in the construction of the optical framing camera, used in the experiments of chapters 5 and 6.

Finally, I would like to thank my colleagues in the plasma physics group at Imperial College for many illuminating discussions (helpful or otherwise) over the last 3 years.

CONTENTS

	page
Title page	1
Abstract	2
Acknowledgements	3
Contents	4
List of figures	7
List of frequently used symbols	10
Chapter 1 Introduction	12
1.1 Introduction	12
1.2 Absorption of laser energy	12
1.3 Thermal transport	17
1.4 Ablative compression	18
1.5 Instabilities	18
1.5.1 Parametric instabilities	19
1.5.2 Filamentation	19
1.5.3 Rayleigh-Taylor instability	19
1.6 Contents of thesis	22
1.7 Laser facility	23
1.8 Role of the author	23
Chapter 2 Study of Shock Coalescence in Laser Irradiated Targets	25
2.1 Introduction	25
2.2 Theory of shock propagation	26
2.2.1 Single shock in planar geometry	27
2.2.2 Shock sequences in planar geometry	31
2.2.3 Shock propagation in spherical geometry	35
2.3 Experimental arrangement	35
2.3.1 Experimental set-up	35
2.3.2 Experimental design	39
2.4 Computer Simulations	42
2.5 Experimental results for an unshaped laser pulse	43
2.5.1 Single shocks in foil and slab targets	43

2.5.2 Single shocks in aluminium step targets 47
2.6 Experimental results for a shaped laser pulse 53
2.7 Conclusion 61
2.8 Possible future work 61

Chapter 3 Theory of Coronal Plasma Instabilities 63

3.1 Parametric Instabilities 63
3.1.1 Stimulated Brillouin Scattering 64
3.1.2 Growth rates and thresholds for S.B.S. 67
3.1.3 Stimulated Raman Scattering 70
3.1.4 Growth rates and thresholds for S.R.S. 72
3.2 Filamentation 74
3.2.1 Growth rates for filamentation 75
3.2.2 Time scales for filamentation 77

Chapter 4 Experimental Arrangement for Study of Instabilities in a Large Underdense Plasma 78

4.1 Introduction 78
4.2 Experimental arrangement 79
4.3 Target design 81
4.4 Diagnostics 83
4.4.1 Measurements of the transmitted interaction beam 86
4.4.2 Optical framing camera 87
4.4.3 Measurements of S.R.S. and S.B.S. backscatter 92
4.4.4 Equivalent plane monitor 94

Chapter 5 Observations of Instabilities in a Long Scalelength Plasma 97

5.1 Introduction 97
5.2 Spectroscopic observations of S.R.S. and S.B.S. 97
5.3 Observations of the filamentary break up of the interaction beam 101
5.4 Observations of whole beam self-focusing 112
5.5 Conclusions 120

Chapter 6 Suppression of instabilities in a large underdense plasma 121

6.1 Introduction 121
6.2 Laser beam smoothing techniques 122
6.2.1 Random phase plate 122
6.2.2 Induced Spatial Incoherence 124
6.3 Suppression of S.R.S. and S.B.S. in a large underdense plasma 126
6.4 Suppression of filamentation in a large underdense plasma 140
6.4.1 Suppression of filamentation by a R.P.P. 140
6.4.2 Suppression of filamentation by I.S.I. 145
6.5 I.S.I. and R.P.P. hybrid system 145
6.6 Discussion and conclusions 150
6.6.1 Reproducibility of plasma conditions and results 150
6.6.2 General discussion 151

Chapter 7 Generation of Preformed Plasmas by Irradiation of Thin Foil Stripe Targets 154

7.1 Introduction 154
7.2 Plasma production by long pulse heating beams 155
7.2.1 Experimental results 155
7.2.2 Two dimensional simulations 155
7.3 Optical probing measurements of plasma expansion and uniformity 159
7.3.1 Details of the optical probing system 159
7.3.2 Experimental results 163
7.3.3 Uniformity of the plasma produced 168
7.4 Discussion and Conclusions 170

Chapter 8 Summary of Main Conclusions 172

8.1 Coalescing shock experiment 172
8.2 Study of instabilities in a large underdense plasma 172

Appendix A Ray Tracing Program 174

References 176

LIST OF FIGURES

		page
(1.1)	The mechanism of resonance absorption	15
(1.2)	Scenario for the Rayleigh-Taylor instability	21
(2.1)	Density profile of a shock front	27
(2.2)	Shock front in its own frame of reference	28
(2.3)	Shock Hugoniot	29
(2.4)	Predicted variation of shock velocity with pressure	32
(2.5)	Compression achieved with a sequence of shocks	33
(2.6)	Variation of effective adiabatic index with compression ratio	34
(2.7)	Experimental arrangement	36
(2.8)	Expected streak record for an unshaped laser pulse	38
(2.9)	Expected streak record for a shaped laser pulse	38
(2.10)	Typical pinhole camera image	44
(2.11)	Target rear side emission for a 25 μm aluminium foil	44
(2.12)	Target rear side emission for a 40 μm plastic slab	46
(2.13)	Shock breakout with a large 550 μm diameter focal spot	48
(2.14)	Shock breakout from an aluminium step target for an unshaped laser pulse	48
(2.15)	Variation of shock front position with time for an unshaped laser pulse	49
(2.16)	Experimentally measured laser temporal profile	50
(2.17)	Variation of shock velocity with laser irradiance	52
(2.18)	Shock breakout from an aluminium step target for a shaped laser pulse	54
(2.19)	Variation of shock front position with time for a shaped laser pulse (ΔT=1200 ps)	55
(2.20)	Variation of shock front position with time for a shaped laser pulse (ΔT=1000 ps)	56
(2.21)	Shock breakout observed from a 25 μm thick aluminium foil for a shaped laser pulse	58
(2.22)	MEDUSA simulation of the streak of fig. 2.21 (a)	59
(2.23)	MEDUSA simulation of the streak of fig. 2.21 (b)	60
(3.1)	Locations of instabilities in an underdense plasma	65
(3.2)	Matching conditions for S.B.S.	66

(3.3) Feedback loop for S.B.S. 67
(3.4) Matching conditions for S.R.S. 71
(3.5) Variation of S.R.S. shift with plasma conditions 73
(3.6) Schematic of ponderomotive filamentation 75

(4.1) Simulation of a large coronal plasma 78
(4.2) Principle of line focus generation 80
(4.3) Arrangement for generating a large underdense plasma 80
(4.4) Target design 82
(4.5) Prediction of variation of density with time 84
(4.6) Prediction of variation of temperature with time 84
(4.7) Overall experimental arrangement 85
(4.8) Mechanical design of the optical framing camera 88
(4.9) Electrical connections to the optical framing camera 89
(4.10) Voltage output of the pulse driver 91
(4.11) Pulse forming speed up module 91
(4.12) Voltage output of the speed up module 91
(4.13) Energy detector used to measure S.R.S. and S.B.S. levels 94
(4.14) Equivalent plane monitor 95

(5.1) Variation of the S.B.S. shift with plasma conditions 98
(5.2) Typical S.B.S. spectrum for a coherent beam 100
(5.3) Typical S.R.S. spectrum for a coherent beam 100
(5.4) Framing camera images of the transmitted interaction beam 102
(5.5) Streak of the transmitted interaction beam 104
(5.6) Framing camera image of the interaction beam (no plasma) 104
(5.7) Streak of the interaction beam (no plasma) 105
(5.8) Framing camera images of a short pulse interaction beam 106
(5.9) E.P.M. image of the interaction beam profile 108
(5.10) Predicted growth rates for filamentation 109
(5.11) Framing camera image of the transmitted interaction beam at a low irradiance 109
(5.12) Variation of minimum perturbation wavelength unstable to filamentation with irradiance 111
(5.13) Streak of whole beam self-focusing 113
(5.14) Framing camera image of whole beam self-focusing 115
(5.15) Probable beam path due to self-focusing 118
(5.16) Predicted beam path due to self-focusing 119

(6.1) Random phase plate 123
(6.2) Calculation of focal spot profile generated by the R.P.P. 123
(6.3) The induced spatial incoherence system 125
(6.4) Images of the far field focal spot distributions 128
(6.5) Variation of the S.B.S. level with laser irradiance 129
(6.6) Variation of the S.R.S. level with laser irradiance 131
(6.7) Typical S.R.S. spectra observed with a R.P.P. 134
(6.8) Typical S.R.S. spectra observed with I.S.I. 135
(6.9) Typical S.B.S. spectra observed with a R.P.P. 135
(6.10) Variation of S.R.S. level with laser irradiance for f/2.5 optics 137
(6.11) Beam profile 400 μm before focus for I.S.I. and f/2.5 focusing optics 138
(6.12) Variation of S.B.S. level with laser irradiance for f/2.5 optics 139
(6.13) Images of the transmitted interaction beam with a R.P.P. present 141
(6.14) Predicted growth rates for filamentation 143
(6.15) Transmitted interaction beam profiles with a R.P.P. present 144
(6.16) Images of the transmitted interaction beam with I.S.I. 146
(6.17) Far field beam profile for I.S.I./R.P.P. combination 148
(6.18) Near field beam profile for I.S.I./R.P.P. combination 149

(7.1) Comparison of target design 157
(7.2) POLLUX prediction of the density profile at interaction 157
(7.3) Generation of the optical probing pulse 161
(7.4) Layout of the four frame optical probing system 161
(7.5) The principle of Schlieren photography 162
(7.6) Optical probing images for a 350 nm thick H-target 164
(7.7) Optical probing images for a 300 nm thick stripe 165
(7.8) Optical probing images for a 175 nm thick H-target 167
(7.9) Results of ray tracing calculations for density profiles predicted by POLLUX 169

LIST OF FREQUENTLY USED SYMBOLS

c - Velocity of light in a vacuum

K - Boltzmanns constant

ϵ_0 - Permittivity of free space

e - Elementary charge

m_e - Electron mass

m_i - Ion mass

n_e - Electron density

n_i - Ion density

T_e - Electron temperature

T_i - Ion temperature

Z - Ion charge

ω_{pe} - Plasma frequency

ω_{pi} - Ion plasma frequency

λ_D - Debye length

v_{os} - Electron oscillation (or quiver) velocity

v_{th} - Electron thermal velocity

C_s - Ion sound speed

I - Laser irradiance

λ - Laser wavelength

To My Parents and Sara

CHAPTER 1

INTRODUCTION

(1.1) Introduction

The use of high power lasers to produce plasmas has allowed the study of hot matter over a wide range of conditions which are not otherwise accessible in laboratory conditions. In particular it has been suggested [1] that high power lasers could be used to compress matter to the conditions required for controlled thermonuclear fusion. It is envisaged that initially a potential reactor would be based on the reaction between deuterium and tritium nuclei.

$$D + T \rightarrow He^4 + n + 17.6\ Mev \qquad (1.1)$$

As well as requiring high temperatures (approximately 5 keV) for the ignition of this reaction in a thermal plasma, it is necessary that the Lawson criterion is satisfied for the plasma confinement. For inertial confinement fusion (I.C.F.) this condition, for energy breakeven, is typically taken as $n_i\tau > 10^{15}$ (where n_i is the ion density in cm^{-3} and τ the confinement time in s) [2,3]. The typical parameters envisaged for I.C.F. are $n_i \approx 10^{25}\ cm^{-3}$ and $\tau \approx 10^{-10}$ s. In this thesis experimental work on two areas of relevance to the feasibilty of successfully achieving I.C.F. will be reported on. As an introduction to this work some of the key processes occurring during the interaction of a high power laser beam with a plasma will be described in this chapter. Comprehensive accounts on laser plasma interactions and I.C.F. are given in several sources [3−9], consequently only a brief summary of the most important aspects of these subjects are discussed here.

(1.2) Absorption of laser energy

When a high power laser beam is incident on a solid target a plasma is rapidly produced, for example by processes such as multiphoton absorption. Due to the extremely short timescales over which the plasma is produced it becomes only necessary to consider the interaction and absorption of the laser beam with the plasma itself. The propagation of a light wave in a plasma satisfies the following dispersion relationship [10]

$$\omega^2 = \omega_{pe}^2 + k^2c^2 \qquad (1.2)$$

Where ω (k) is the frequency (wavenumber) of the incident laser beam and ω_{pe} is the plasma frequency, which for a plasma of electron density n_e is given by

$$\omega_{pe} = \left[\frac{n_e e^2}{m_e \epsilon_0}\right]^{\frac{1}{2}} \tag{1.3}$$

The main result that follows from eqs (1.2) and (1.3) is that the laser light can only propagate up to a certain critical density (n_{ec}) in the plasma which is solely a function of the laser wavelength.

$$n_{ec} = \frac{1.1 \times 10^{21}\ \text{cm}^{-3}}{(\lambda(\mu\text{m}))^2} \tag{1.4}$$

For densities less than, and up to critical, the laser light can be absorbed by several processes. One of the major causes of absorption of laser energy is due to inverse bremsstrahlung [9,10]. In this process electrons oscillating in the electric field of the laser undergo collisions with the ions present. This results in the transfer of energy from the coherent laser beam to random thermal energy of the plasma. If a Maxwellian distribution is assumed for the electron energies then the linear absorption coefficient, a_w, for this process is given by

$$a_w = \left[\frac{1}{2\pi}\right]^{\frac{1}{2}} \left[\frac{n_e n_i Z^2 e^6}{6\pi\epsilon_0{}^3 \omega^2 c (1-n_e/n_{ec})^{\frac{1}{2}}}\right] \left[\frac{1}{m_e K T_e}\right]^{3/2} \frac{\pi}{3^{\frac{1}{2}}}\, g_c \tag{1.5}$$

Where n_i (Z) is the ion density (charge), T_e the electron temperature and g_c is the gaunt factor [10]. It follows from this expression that the absorption increases with density, and hence the strongest absorption will occur at the maximum density to which the laser can propagate (i.e. near n_{ec}). Since from eq(1.4) $n_{ec} \propto 1/\lambda^2$ it follows that higher laser energy absorption will be achieved with shorter wavelength lasers. For this reason it is envisaged that short wavelength lasers will be used to drive laser fusion implosions, i.e. frequency tripled neodymium glass lasers ($\lambda = 0.35$ μm) or KrF lasers ($\lambda = 0.25$ μm). It also follows from eq(1.5) that absorption will be higher in low temperature, high Z plasmas.

The inverse bremsstrahlung absorption coefficient can be reduced by two non-linear effects for high laser irradiances. The first occurs when the oscillation velocity (v_{os}) of the electrons in the electric field of the laser beam becomes comparable or larger than the typical electron thermal velocity (v_{th}). The

electron−ion collision frequency is then determined by v_{os} rather than v_{th}. Since the electron−ion collision frequency scales with electron velocity as $\nu_{ei} \propto v^{-3}$ it follows that this will lead to a reduction in the collision frequency, and hence also in the inverse bremsstrahlung absorption. This effect becomes important for

$$\frac{v_{os}}{v_{th}} = \frac{\left[\frac{eE_\ell}{m_e\omega}\right]}{\left[\frac{KT_e}{m_e}\right]^{\frac{1}{2}}} > 1 \qquad (1.6)$$

Where E_ℓ is the magnitude of the electric field of the laser beam. The second effect occurs when the electrons gain energy at a rate faster than they can dissipate it, and still form a Maxwellian energy distribution. This tends to reduce the fraction of electrons with lower energies. Since it is the lower energy electrons which are primarily responsible for the laser absorption (since $\nu_{ei} \propto v^{-3}$) it follows that this will also lead to a reduction in the degree of inverse bremsstrahlung compared with the Maxwellian distribution case. For this effect to become important it is required that

$$Z\left[\frac{v_{os}}{v_{th}}\right]^2 > 1 \qquad (1.7)$$

This effect has been discussed in detail by Langdon [11].

Since absorption by inverse bremsstrahlung is primarily via electrons with lower velocities it is a favourable mechanism for absorption in laser fusion targets. This is because it will tend not to produce high energy electrons which will preheat the target core and reduce compression.

Laser energy can also be significantly absorbed at the critical density surface in a plasma due to a process called resonance absorption [9,10]. The basic principle of this process is illustrated in fig(1.1). For light incident on a plasma density gradient at a angle θ to the normal, the classical turning point for the wave will be at a density $n_e(\theta) = n_{ec}\cos^2\theta$, see fig(1.1). If the light wave is p−polarized (ie. in the plane formed by $\underline{k}$ and $\underline{\nabla}n_e$), then at the turning point the electric field of the light wave will point in the direction of $\underline{\nabla}n_e$. This electric field can then partially tunnel through to the critical density surface region of the plasma, where it can resonantly drive electron plasma oscillations. If these electrostatic plasma oscillations are then damped, either by collisional or collisionless

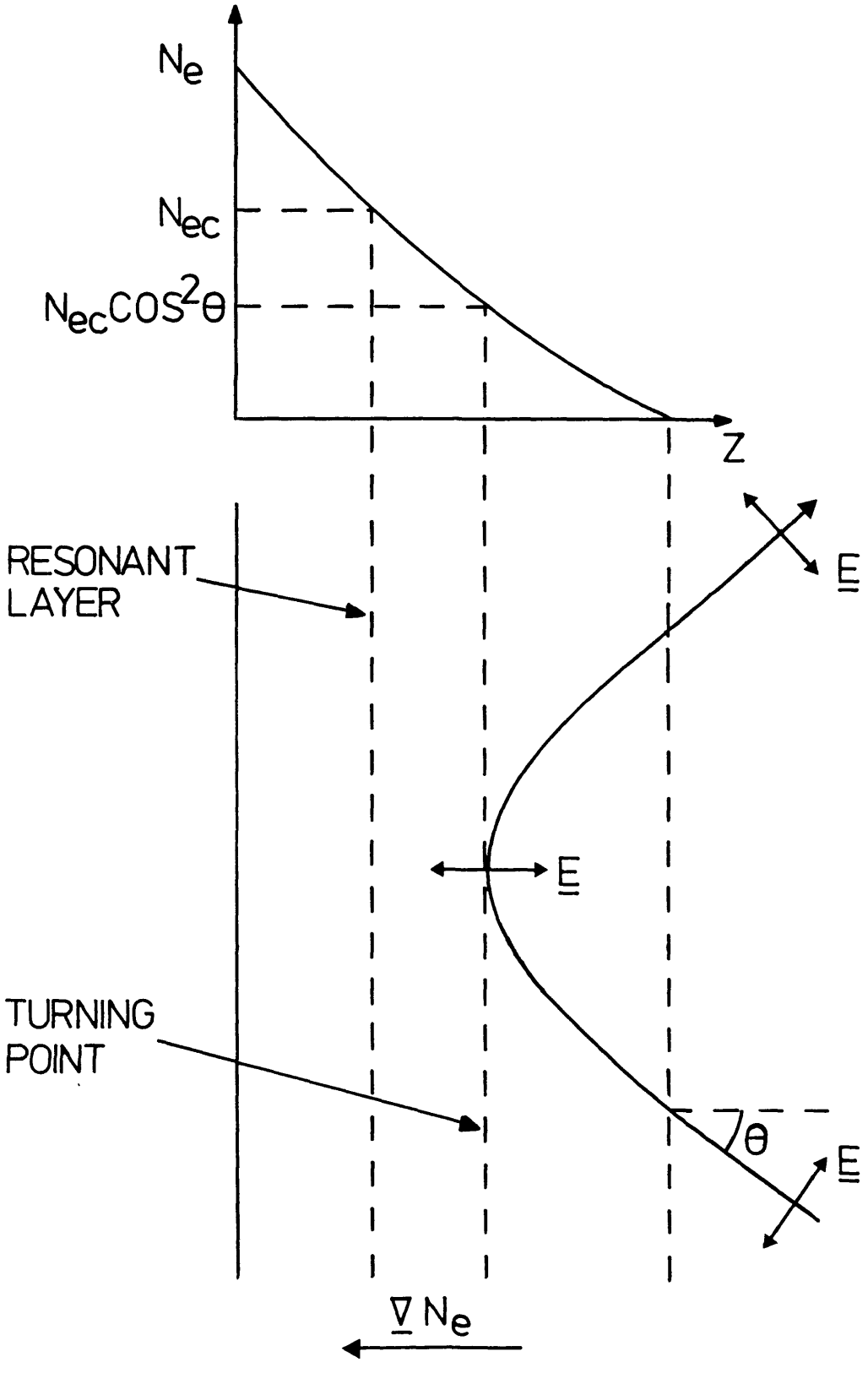


Figure 1.1 The mechanism of resonance absorption.

processes, energy is effectively transferred from the incident laser beam to the thermal energy of the plasma. Resonance absorption will not occur for s−polarization, since at the turning point there will be no component of the laser electric field in the direction of ∇n_e and so plasma oscillations cannot be driven.

The level of resonance absorption which occurs depends critically on the angle of incidence, θ, of the laser beam. This is because the electric field must tunnel the distance between $n_e = n_{ec}\cos^2\theta$ and $n_e = n_{ec}$. If θ is large then this distance also becomes large and the wave will have to tunnel too far to effectively drive the plasma oscillations. Alternatively if θ is small the component of the electric field parallel to ∇n_e near the turning point will be small (it becomes zero for $\theta = 0$), again causing ineffective driving of the plasma oscillations. Hence resonance absorption will be most effectively driven for an intermediate angle of incidence. Clearly the level of resonance absorption will also depend on the density scalelength (L) as this controls the distance between the turning point of the light wave and the critical density surface. The absorbed fraction due to resonance absorption is found to be a maximum for [9,12]

$$\left[\frac{\omega_0 L}{c}\right]^{1/3} \sin\theta \approx 0.8 \qquad (1.8)$$

This angular dependence of resonance absorption has been observed experimentally [13,14]. The level of resonance absorption can be increased by the occurrence of profile steepening near the critical density surface, since this reduces the density gradient and hence the distance the electric field has to tunnel to drive the plasma oscillations. Profile steepening can occur due to the expulsion of material from this region by the ponderomotive force generated by the laser light or the plasma oscillations [9,10]. Overall up to 40 % of the incident laser energy can be absorbed by resonance absorption [15].

Two dimensional particle simulations [16,17] have shown that collisionless wave breaking of the large amplitude plasma waves generated by resonance absorption can result in the production of very high energy electrons. These hot or suprathermal electrons can typically have an energy of EeL (where E is the magnitude of the electric field of the wave), which is many times the average thermal energy of the bulk plasma electrons. The generation of suprathermal electrons is undesirable for laser fusion implosions since they can preheat the target core and consequently not allow the efficient, isentropic compression of the fuel pellet which is required. For this reason inverse bremsstrahlung is the preferred

absorption mechanism, rather than resonance absorption, for I.C.F..

(1.3) Thermal Transport

The laser energy absorbed in the underdense plasma ($n_e \langle n_{ec}$) of a laser fusion target has to be transported to the higher solid density region of the target where it generates the material ablation required to drive the implosion. Since the electron thermal velocity is significantly larger than that of the ions (due to the lower electron mass), it is the electrons which are primarily responsible for this transport of energy. The classical heat flux in a plasma (assuming that the electron mean free path is small compared to the temperature gradient scalelength, and that the electron velocity distribution function is Maxwellian) is given by

$$\underline{q} = -\kappa \underline{\nabla} T \tag{1.9}$$

Where κ is the Spitzer–Härm thermal conductivity [18,19] which is given by

$$\frac{\kappa}{K} = 20 \left[\frac{2}{\pi}\right]^{3/2} \frac{(KT_e)^{5/2} \epsilon \delta_t}{m_e^{\frac{1}{2}} e^4 Z \log\Lambda} \tag{1.10}$$

Where $\log\Lambda$ is the Coulomb logarithm and the parameters ϵ and δ_t are given by Spitzer [18,19].

However in laser produced plasmas in the region between the critical density surface and the ablation surface the electron mean free path can become significant compared to the temperature gradient scalelength. Under such conditions the Spitzer theory overestimates the heat flow. In particular it can predict a heat flow larger than the free streaming limit (which is the energy density of the electrons multiplied by their typical thermal velocity).

$$Q_f = n_e KT_e \left[\frac{KT_e}{m_e}\right]^{\frac{1}{2}} \tag{1.11}$$

Such a result is clearly unphysical. The physical reason for the breakdown of eq(1.9) is that for strong temperature gradients a collisionless regime is entered where electrons simply 'free stream' rather than diffuse. In order to more realistically model the heat flow under such conditions the use of a flux limiter has been widely employed. This restricts the maximum heat flow to some arbitary

fraction of the free streaming limit. Early experiments [20,21] indicated a flux limiter of only 0.03, but these experiments were conducted in a planar geometry where lateral transport of energy can become significant. More recent results [22,23], in spherical geometry have suggested a flux limiter in the range 0.08−0.1. However, even though the use of a flux limiter appears to give a better modelling of the thermal transport in laser produced plasmas there is little direct theoretical justification for its use, and it is widely accepted that the use of a single flux limiter is too simple a parameterization. Consequently there has recently been considerable theoretical effort to solve the full Fokker−Planck equations for the electron thermal transport occurring in laser produced plasmas [24,25].

(1.4) Ablative Compression

In schemes to achieve I.C.F. by the ablative compression of microshell targets the laser energy is deposited in the underdense region surrounding the target, preferrably by inverse bremsstrahlung. This energy is then transported by thermal electron conduction to the solid density surface of the target, as discussed in the last section. The deposition of energy at this point in the target results in the ablation of material from the target surface. The resulting outward flow of material from the target causes the body of the target to be accelerated inwards by the so called 'rocket effect'. The resulting spherically imploded shell compresses the fill gas to the high densities required. In the ideal case preheating of the fill gas is negligible and the compression is isentropic, which minimizes the work required to produce a given compression. However the high pressures produced by ablation (typically 10's of Mbars) result in the generation of shock waves which can preheat the target core. To overcome this problem the use of temporally shaped laser pulses has been suggested [1], so that the compression more closely approaches the adiabatic case. The generation of shocks by shaped laser pulses is the subject of chapter 2 of this thesis and will be more fully discussed there.

(1.5) Instabilities

Several instabilities which can occur in laser produced plasmas may seriously degrade I.C.F. implosions. These instabilities will now be briefly identified.

(1.5.1) Parametric Instabilities

As well as an electromagnetic light wave, ion acoustic and electron plasma waves can also propagate in an underdense plasma. The dispersion relationships for electron plasma and ion acoustic waves are given by eqs (1.12) and (1.13) respectively [10].

$$\omega_e^2 = \omega_{pe}^2 + 3v_{th}^2 k_e^2 \qquad (1.12)$$

$$\omega_i^2 = \left[\frac{ZKT_e}{m_i(1+k_i^2\lambda_D^2)} + \frac{3KT_i}{m_i}\right] k_i^2 \qquad (1.13)$$

Where λ_D is the Debye length, T_i (m_i) the ion temperature (mass), and the subscripts e and i denote electron and ion waves respectively. The resonant coupling of the incident light wave with these plasma waves gives rise to various parametric instabilities [10]. These instabilities are detrimental for I.C.F. since some of them can give rise to significant energy losses by the generation of scattered light waves, and also the production of suprathermal electrons from the collisionless damping of electron plasma waves produced. These instabilities are discussed more fully in chapter 3 of this thesis.

(1.5.2) Filamentation

Intensity hot spots present in the incident laser beams, used to drive implosions, can be enhanced by the filamentation instability. This can make it impossible to achieve the required drive uniformity necessary to produce a symmetric implosion. Again, this instability will be discussed more fully in chapter 3 of this thesis.

(1.5.3) Rayleigh–Taylor instability

The classical Rayleigh–Taylor instability takes place in a fluid when the density and pressure gradients are opposed, for example a heavy fluid on top of a light fluid in a gravitational field. The classical growth rate (γ_c) for the instability, of a small amplitude perturbation between two fluids of densities ρ_1 and ρ_2 ($\rho_1 > \rho_2$) under an effective acceleration (a), is given by [5,8]

$$\gamma_c = (Aka)^{\frac{1}{2}} \tag{1.14}$$

Where $A = (\rho_1 - \rho_2)/(\rho_1 + \rho_2)$ is the Attwood number and k is the wavenumber of the perturbations. It follows from this expression that in general short wavelength perturbations will have faster growth rates.

In ablative compressions the heavy, low pressure shell is accelerated by the high pressure low density ablating plasma and there is a region at the ablation surface where the pressure and density gradients are opposed (see fig(1.2)). Consequently the target shell can be Rayleigh–Taylor unstable. Any density perturbations arising in the target due to non–uniform ablation pressure or target imperfections can act as a seed for the instability. The acclerations involved in I.C.F. implosions are extremely high, typically of the order of 10^{16} cms^{-1}. Consequently the classical growth time for the instability can be as short as 100 ps for a perturbation with a wavelength of 10 μm. Significant growth of the Rayleigh–Taylor instability could significantly disrupt and degrade the symmetry of implosions, and possibly even cause the break up of the target shell before the peak compression is achieved. The target may also be unstable to the Rayleigh–Taylor instability as peak compression is approached, when the shell is decelerated by the fuel.

The growth of a particular mode, due to the Rayleigh–Taylor instability, will saturate when its amplitude is of the same order as the wavelength of the mode [5]. To seriously disrupt the implosion of a shell target a mode must grow sufficiently to have an amplitude comparable with the shell thickness, Δr. Hence the fastest growing mode capable of seriously breaking up the shell will have a wavenumber

$$k \approx 2\pi/\Delta r \tag{1.15}$$

The classical growth rate of this mode will be

$$\gamma \approx (2\pi a/\Delta r)^{\frac{1}{2}} \tag{1.16}$$

For a shell of radius R_0, the implosion time (t) is given by $\frac{1}{2}at^2 = R_0$ and so the final growth exponent for this mode is

$$\gamma t = \left[\frac{4\pi R_0}{\Delta r}\right]^{\frac{1}{2}} \tag{1.17}$$

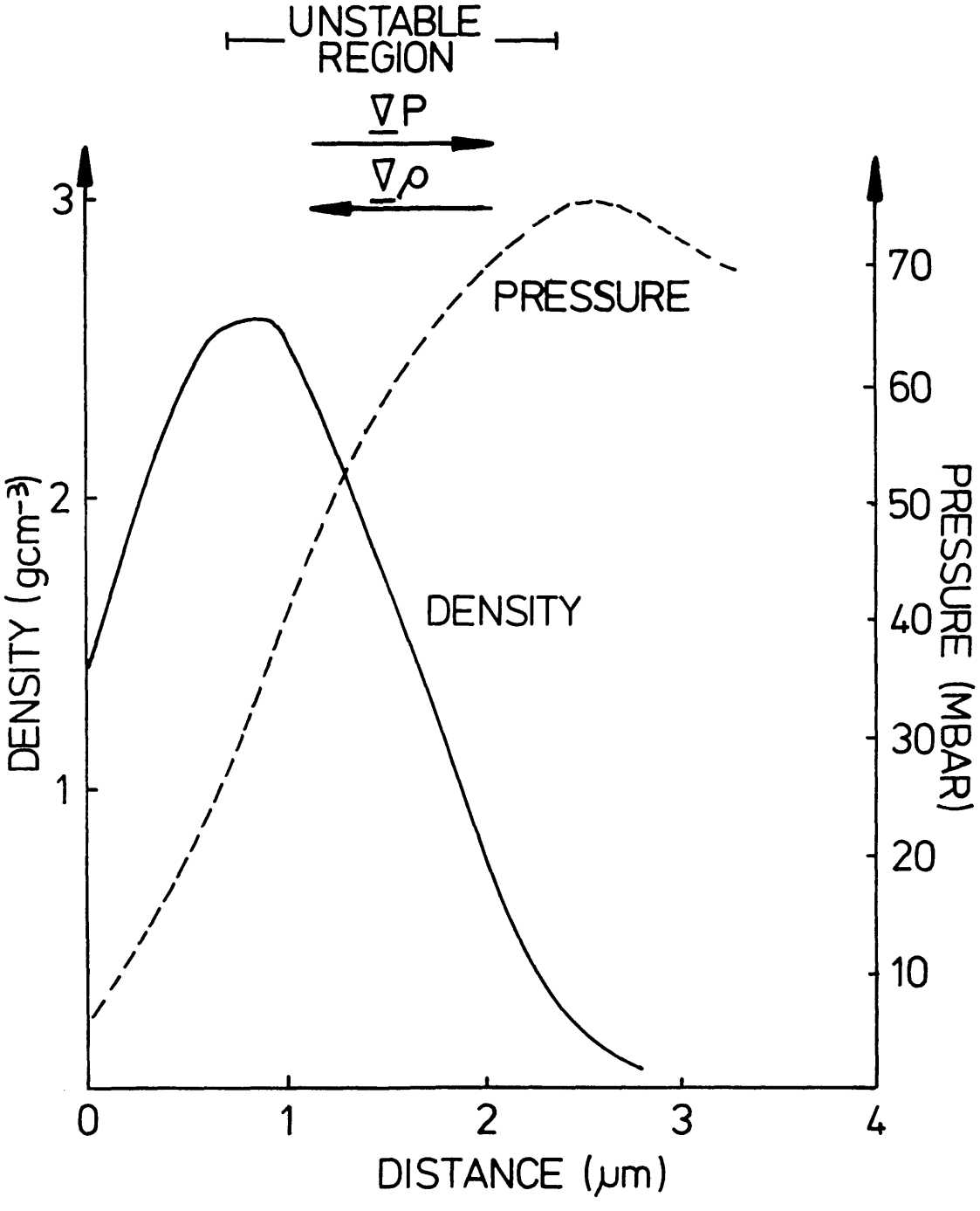


Figure 1.2 Typical density and pressure profiles for a laser irradiated target, which may become unstable to the Rayeigh–Taylor instability.

Hence the overall number of e−foldings in the growth of this mode is dependent only on the aspect ratio ($R_0/\Delta r$) of the shell. Consequently the Rayleigh−Taylor instabilty is expected to impose an upper limit on the aspect ratio which can be used in I.C.F. targets.

Direct experimental observations of the occurrence of the Rayleigh−Taylor instabilty have been obtained by time resolved x−ray back−lighting measurements of accelerated foils [26]. The growth rate of the instability was measured to be 30% of the predicted classical rate.

(1.6) Contents of thesis

This thesis describes experimental work in two areas of importance to proposed laser fusion schemes. Firstly, in chapter 2 an experiment is described to study the coalescence of two shocks generated by a temporally shaped laser pulse. The coalescence of laser generated shocks is a key element of schemes to achieve near adiabatic compression. The main diagnostic used in this experiment was optical streak photography of the shock break out on the rear surface of multiple step targets. The results obtained for both shaped and unshaped laser pulses have been compared with simulations by a 1−D hydrodynamic code.

The remainder of this thesis deals with the study of instabilities in a large underdense plasma. The basic theory of the three instabilities studied, Stimulated Raman Scattering, Stimulated Brillouin Scattering and filamentation is discussed in chapter 3. In chapter 4 details are given of the novel experimental arrangement used to generate a large underdense plasma of a similar scale to those which will surround proposed laser fusion targets. Also the diagnostics used to study these instabilities are described. In chapter 5 results are presented on the interaction of a high power laser beam with this large underdense plasma. In particular this chapter concentrates on measurements made of the break up of the interaction beam due to filamentation and self−focusing. Measurements made of the Raman and Brillouin instabilities were used to determine the plasma conditions, so that the observed filamentary break−up could be compared with theory. In chapter 6 details are given of two beam 'smoothing' techniques which were used in an attempt to suppress the levels of these three instabilities. Quantitative measurements of the reductions in the levels of the Raman and Brillouin instabilities are reported on. Also preliminary measurements showing the effect of these techniques on filamentation are given. Finally, in chapter 7 optical probing

measurements are reported on. These were used to assess the uniformity of the large underdense plasmas generated for these experiments, and also to evaluate the merits of different types of target design.

(1.7) Laser Facility

All the experimental work described in this thesis was carried out at the S.E.R.C. Central Laser Facility at the Rutherford Appleton Laboratory. The high power, multibeam, neodymium glass laser VULCAN was used for these experiments. For all the experiments described in this thesis the output of the laser ($\lambda = 1.052$ μm) was frequency doubled, using KDP crystals, to $\lambda = 0.526$ μm. The output of the laser is delivered in six main beams and one additional backlighting beam which can be fired independently. For the experiments described in chapters 2 and 7 the laser was operational in one of either two possible modes. Either a short pulse mode which produced a maximum of approximately 25 J of green energy (50 J of infra-red) per beam in a 70 ps pulse, or alternatively a long pulse mode producing 70 J of green energy (150 J of infra-red) in a 600-800 ps pulse. In March-May 1988 a major upgrade of the laser increased the available energy output of the laser by almost a factor of 2. This upgraded version of the laser was used for the experimental work described in chapters 5 and 6. Finally a further upgrade of the laser in early December 1988 made available the option of smoothing by induced spatial incoherence on a single beam of the laser. This option was used for the experiment described in chapter 6.

For all the experiments described in this thesis a C.W. argon ion laser, operating at a wavelength of 528 nm, was used in the target areas for alignment purposes. This C.W. beam was expanded and collimated to match the size of the VULCAN laser beams. The argon-ion laser was matched to be co-linear with a C.W. YLF laser which was simultaneously co-linear with the output beams of the VULCAN laser.

(1.8) Role of the author

The experimental results presented in this thesis were all obtained solely by the author, with the following exceptions:-

(1) The stimulated Raman and stimulated Brillouin scattering spectra, presented in

chapters 5 and 6, were obtained by T. Afshar−Rad.

(3) The optical probing data, presented in chapter 7, was obtained jointly with D. Bassett.

(3) The equivalent plane monitor data, presented in chapters 5 and 6, was obtained with assistance from M. Desselberger.

The MEDUSA computer simulations presented in chapter 2 are entirely the work of the author. However, although the computer simulations described in chapter 7 were actually performed by the author, the two dimensional code POLLUX was supplied in a modified form appropriate to the experimental conditions, and in a state ready to use, by J. Edwards. All the remaining data analysis, and the conclusions inferred from this analysis, presented in this thesis are the work of the author. Finally it should be stressed that experimental work on a large facility inevitably involves contributions from a large number of people, and that the work described in this thesis would not have been possible without the support of staff at the Central Laser Facility.

The following refereed publications have resulted from the work described in this thesis:−

(1) 'Study of shock coalescence in laser irradiated targets'
S.E. Coe, O. Willi, T. Afshar−rad and S. Rose, Appl. Phys. Lett. 53, 2383 (1988).

(2) 'Suppression of instabilities in a long scalelength preformed plasma'
S.E. Coe, T. Afshar−rad, M. Desselberger, F. Khattak, O. Willi, A. Giulietti, Z. Lin, W. Yu and C. Danson, Europhysics Letters (accepted for publication).

(3) 'Direct observations of filamentation and self−focusing in a large underdense plasma'
S.E. Coe, T. Afshar−rad and O. Willi, Opt. Commun. (submitted for publication).

CHAPTER 2

STUDY OF SHOCK COALESCENCE IN LASER IRRADIATED TARGETS

(2.1) Introduction

Inertial confinement fusion schemes rely on the fuel pellet being highly and efficiently compressed. The centre of the compressed target must be brought to the ignition temperature of a few keV while the rest of the pellet is highly compressed at the lowest possible temperature [6]. In this way one can ignite a central spark that propagates through the surrounding compressed fuel mass as a thermonuclear burnwave. This approach minimizes the laser energy requirements since it is not necessary to heat the whole fuel pellet to the required temperatures, only to compress it to densities sufficient for ignition and efficient thermonuclear burn. The driving pressure producing the compression is due to material ablation from the dense pellet surface. The energy producing the ablation is transported by hot electrons from the laser deposition region. The velocity of the material ablating off the surface is determined essentially by the local sound speed in the high temperature ablation region. However the speed of sound in the cold fuel region ahead of the ablation front is relatively low. Hence the inward motion of the pellet surface due to the ablation pressure is supersonic with respect to the cold fuel material, and shock waves will necessarily form. It will be seen in section (2.2) that the propagation of a strong shock is a strongly non−adiabatic process and gives a very inefficient compression for a given driving pressure. This is clearly undesirable for I.C.F. implosions since it will result in shock preheating of the fuel pellet and consequently increase the final work which is required to produce the desired compression. It has been proposed [1] that this problem can be overcome by using a tailored laser pulse to generate a series of weak overtaking shocks which coalesce to a stronger shock just before the centre of the target. This ensures that the compression of the target is adiabatic to a maximal degree and that the high temperatures required for ignition are only produced at the pellet centre where the shocks coalesce. It will be demonstrated in section (2.2) that compression by a series of weak shocks approaches the adiabatic case.

The propagation of laser induced shocks has previously been experimentally studied by the use of optical streak photography of the shock breakout on the rear surface of thin planar foil targets. When the laser induced shock reaches the rear surface of the target it causes material to be spalled out. This heated material then emits light as a blackbody and the turn on of this emission can therefore be used to indicate when the shock has traversed the target. This technique has been

used to determine the transit time of a single shock generated by an unshaped (Gaussian) laser pulse [27−29]. The optical emission being imaged onto a streak camera to give the temporal resolution required. These experiments used an optical fiducial split off the main laser beam to give the relative timing of the laser pulse hitting the target. However with a Gaussian laser pulse the rise time of the pulse is not instantaneous and ambiguities arise in the definition of the shock launch time and hence in the shock transit time. This problem has been overcome by using targets with a single step on the rear surface and inferring the shock velocity from the delay in breakout between the step surface and the target base. This technique has recently been extensively used over a wide range of experimental conditions [30−33]. In this chapter, an experiment performed by the author extending this technique to multiple step targets will be reported on. This has allowed the propagation of shocks induced by Gaussian laser pulses to be studied during and after the laser pulse on a single shot. However the main aim of the experiment was to study the coalescence of two shocks generated by a temporally shaped laser pulse. The experimental results have been compared with one dimensional hydrodynamic simulations. As already stated the exact nature of shock coalescence is clearly important to the design of future laser fusion implosions. However shock coalescence also provides a method of generating very dense plasmas which are of significant current interest [34].

In section (2.2) the basic theory of shock propagation will be reviewed and the higher compressions that can be obtained with a shock sequence rather than a single strong shock will be discussed. The experimental arrangement used to study shock propagation and coalescence will be discussed in section (2.3). Section (2.4) will describe the 1−D Lagrangian code used to simulate the experimental results. Finally, results for the case of a single shock and coalescing shocks will be presented in sections (2.5) and (2.6) respectively.

(2.2) Theory of shock propagation

A very simple model [5] shows that the pressure generated by the interaction of a high power laser beam with matter approximately varies with the absorbed irradiance, I_{abs}, according to the following expression.

$$P(\mathrm{TPa}) = 1.05 \left[\frac{I_{abs}(10^{14}\mathrm{Wcm^{-2}})}{\lambda(\mu\mathrm{m})}\right]^{2/3} \qquad (2.1)$$

For typical laser irradiances of 5×10^{13} − 1×10^{15} $\mathrm{Wcm^{-2}}$ (at $\lambda=0.53\mu$m) this

corresponds to pressures in the range 1 − 8 TPa. Hence it can be seen that high power lasers can generate extremely high pressures, and therefore very strong shock waves. These pressures are significantly higher than those attainable by other methods in a laboratory environment such as two stage light gas guns [35]. The basic theory of the propagation of shock waves in a fluid will now be discussed.

(2.2.1) Single shock in planar geometry

Adiabatic compression increases the temperature and the sound velocity in a material. Thus the wave crest in a large amplitude compression wave overtakes the base of the wave to form a discontinuity or shock wave, see fig(2.1). A shock wave can mathematically be treated as a discontinuity across which the equations of conservation of mass, momentum and energy can be applied. We first deal with the case of a planar one dimensional shock. This is discussed in many texts, for example see Zeldovich and Raizer [36].

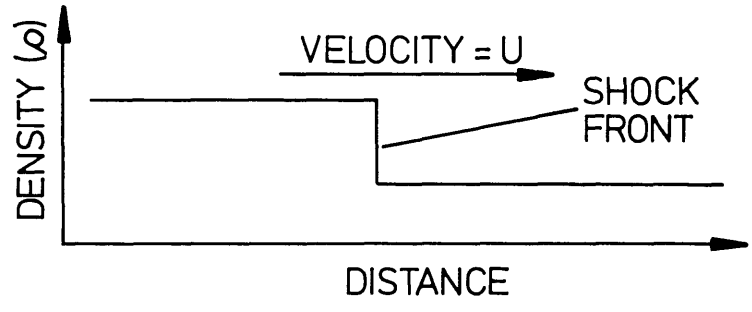


Figure 2.1 Density profile of a shock front.

Consider the steady shockfront in the frame of reference of the shock wave itself as shown in fig(2.2). Where v is the material velocity, P is the pressure and ρ is the density. The subscripts 1 and 2 denote quantities in front of and behind the shock respectively. By conservation of mass the mass flux in and out of the shock front must be equal

$$\rho_1 v_1 = \rho_2 v_2 \tag{2.2}$$

By conservation of momentum the time rate of change of momentum flowing across the shock front must be equal to the net force (due to the pressure) acting on the shock front, giving

$$\rho_1 v_1^2 - \rho_2 v_2^2 = P_2 - P_1 \tag{2.3}$$

By conservation of energy the time rate of flow of energy (kinetic and potential) into the shock front must be balanced by the net work done on the shock front due to the pressure, so we have

$$\{(\tfrac{1}{2}\rho_1 v_1^2+\rho_1 e_1)v_1 - (\tfrac{1}{2}\rho_2 v_2^2+\rho_2 e_2)v_2\} + \{P_1 v_1 - P_2 v_2\} = 0 \tag{2.4}$$

Where e is the internal energy per unit mass. The specific enthalpy is given by $h = e + P/\rho$ so eq(2.4) can be rewritten as

$$\tfrac{1}{2}v_1^2 + h_1 = \tfrac{1}{2}v_2^2 + h_2 \tag{2.5}$$

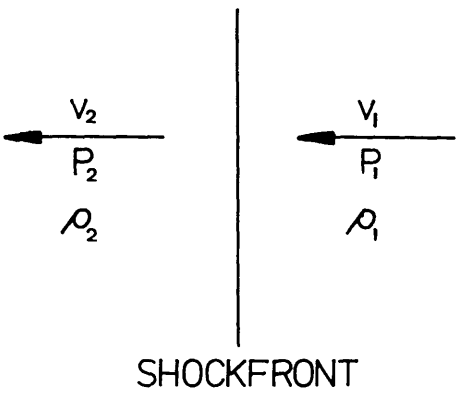


Figure 2.2 Shock front in its own frame of reference.

It should be noted that $v_1 = U$ the velocity of the shock in the lab. frame of reference (assuming the material in front of the shock is stationary), and also that the flow velocity behind the shock in the lab. frame is $U_2 = U - v_2 = v_1 - v_2$. The three equations (2.2),(2.3) and (2.5) can be solved to give the following relationship between the pressure and density before and after the shock.

$$e_1 - e_2 = \tfrac{1}{2}(P_2 + P_1)\left[\frac{1}{\rho_2} - \frac{1}{\rho_1}\right] \tag{2.6}$$

This is the Hugoniot relation. For the case of a perfect gas $e = (1/(\gamma-1))(P/\rho)$, ($\gamma = C_p/C_v$ the ratio of specific heats), and the Hugoniot equation can be rewritten in the following explicit form (assuming $\gamma_1 = \gamma_2$).

$$\frac{P_2}{P_1} = \frac{(\gamma + 1)/\rho_1 - (\gamma - 1)/\rho_2}{(\gamma + 1)/\rho_2 - (\gamma - 1)/\rho_1} \tag{2.7}$$

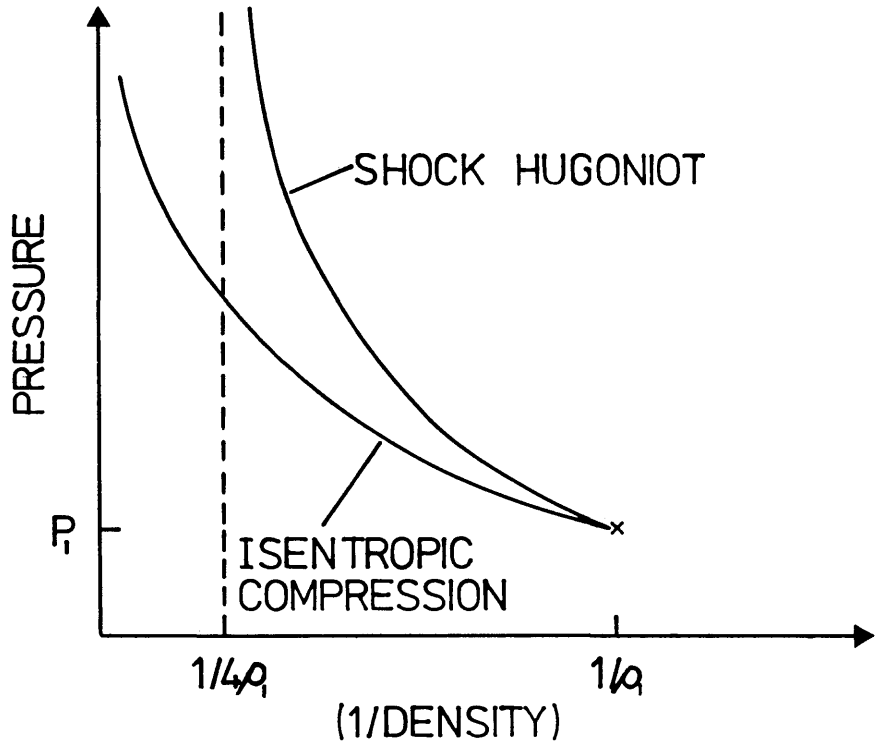


Figure 2.3 Shock Hugoniot for the compression achieved by a single shock.

The curve given by this equation is shown in fig(2.3). For given initial conditions before the shock, P_1 and ρ_1, the curve uniquely determines the density after the shock for any given pressure, P_2, driving the shock. From eq(2.7) the density ratio across the shock can be determined.

$$\frac{\rho_2}{\rho_1} = \frac{(\gamma + 1)P_2 + (\gamma - 1)P_1}{(\gamma - 1)P_2 + (\gamma + 1)P_1} \tag{2.8}$$

Also the temperature ratio across the shock front can be calculated from

$$\frac{T_2}{T_1} = \frac{P_2\rho_1}{P_1\rho_2} \tag{2.9}$$

Combining equations (2.2), (2.3) and (2.8) gives the shock velocity as

$$U^2 = v_1^2 = \frac{1}{2\rho_1}\,[(\gamma + 1)P_2 + (\gamma - 1)P_1] \tag{2.10}$$

and the exhaust velocity as

$$v_2^2 = \frac{1}{2\rho_1} \frac{[(\gamma - 1)P_2 + (\gamma + 1)P_1]^2}{[(\gamma + 1)P_2 + (\gamma - 1)P_1]} \tag{2.11}$$

In the limit of a very strong shock, $P_2 \gg P_1$, these last four equations reduce to

$$\frac{\rho_2}{\rho_1} = \frac{\gamma + 1}{\gamma - 1} \tag{2.12}$$

$$\frac{T_2}{T_1} = \left[\frac{\gamma - 1}{\gamma + 1}\right] \frac{P_2}{P_1} \tag{2.13}$$

$$U = \left[\frac{\gamma + 1}{2}\right]^{\frac{1}{2}} \left[\frac{P_2}{\rho_1}\right]^{\frac{1}{2}} \tag{2.14}$$

$$v_2 = \left[\frac{(\gamma - 1)^2}{2(\gamma + 1)}\right]^{\frac{1}{2}} \left[\frac{P_2}{\rho_1}\right]^{\frac{1}{2}} \tag{2.15}$$

The main result that follows from these expressions is that even for an infinitely strong shock the compression is limited to a maximum value of 4 for $\gamma = 5/3$. This point is illustrated in fig(2.3) where as the pressure tends to infinity, the compression becomes asymptotically constant. This should be compared with the case of adiabatic compression (P/ρ^γ = constant) also shown on the diagram where the compression ratio (ρ_2/ρ_1) continues to increase with pressure and does not tend to a limit. It can be seen that the stronger the shock wave the greater the departure from the ideal adiabatic case. Only a limited compression is obtained with a single strong shock as the shock propagation process is extremely non−adiabatic due to the occurrence of irreversible dissipative processes. These processes can be associated with the presence of viscosity and heat conduction in the fluid. For a perfect gas the entropy is given by $S = C_v \log(P/\rho^\gamma)$ and therefore the entropy change across a shock is

$$S_2 - S_1 = C_v \log\left[\frac{P_2}{P_1}\left[\frac{(\gamma - 1)(P_2/P_1) + (\gamma + 1)}{(\gamma + 1)(P_2/P_1) + (\gamma - 1)}\right]^\gamma\right] \tag{2.16}$$

For a strong shock this becomes

$$S_2 - S_1 = C_v \log\left[\frac{P_2}{P_1}\left[\frac{\gamma - 1}{\gamma + 1}\right]^\gamma\right] \tag{2.17}$$

It clearly follows that as $P_2/P_1 \to \infty$ the entropy increase due to the shock approaches infinity.

The variation of shock velocity with pressure for aluminium calculated from eq(2.14) is shown in fig(2.4). Also shown for comparison is SESAME equation of state data [29,37] for the variation of shock velocity with pressure. It can be seen that over the regime of interest to high power laser generated shocks (ie. pressures of a few TPa) the ideal gas equation of state agrees reasonably well with the SESAME data.

(2.2.2) Shock sequences in planar geometry

From eq(2.16) it can be seen that for a weak shock ($P_2/P_1 \to 1$) the entropy change tends to zero. Hence it follows that a succession of weak shocks will approach the adiabatic case and therefore give a higher compression than a single strong shock for a given final driving pressure. This is illustrated in fig(2.5). We now quantatively determine the compression obtained with a sequence of $n-1$ shocks in one dimension [38]. Consider the simplified case where the density ratio for each shock is constant, ie.

$$x = \rho_2/\rho_1 = - - - - - - - - - - - - - - - = \rho_n/\rho_{n-1} \qquad (2.18)$$

It follows that

$$P_2/P_1 = - - - - - - - = P_n/P_{n-1} = \frac{(\gamma+1)x - (\gamma-1)}{(\gamma+1) - (\gamma-1)x} = Z \qquad (2.19)$$

so $P_n/P_1 = Z^{n-1}$ and $\rho_n/\rho_1 = x^{n-1}$. An effective adiabatic index can now be defined by the relation

$$\frac{P_n}{P_1} = \left[\frac{\rho_n}{\rho_1}\right]^{\gamma_{eff}} \qquad (2.20)$$

Substituting into this expression for P and ρ gives γ_{eff}.

$$\gamma_{eff} = \frac{\log\left[\dfrac{(\gamma+1)x - (\gamma-1)}{(\gamma+1) - (\gamma-1)x}\right]}{\log x} \qquad (2.21)$$

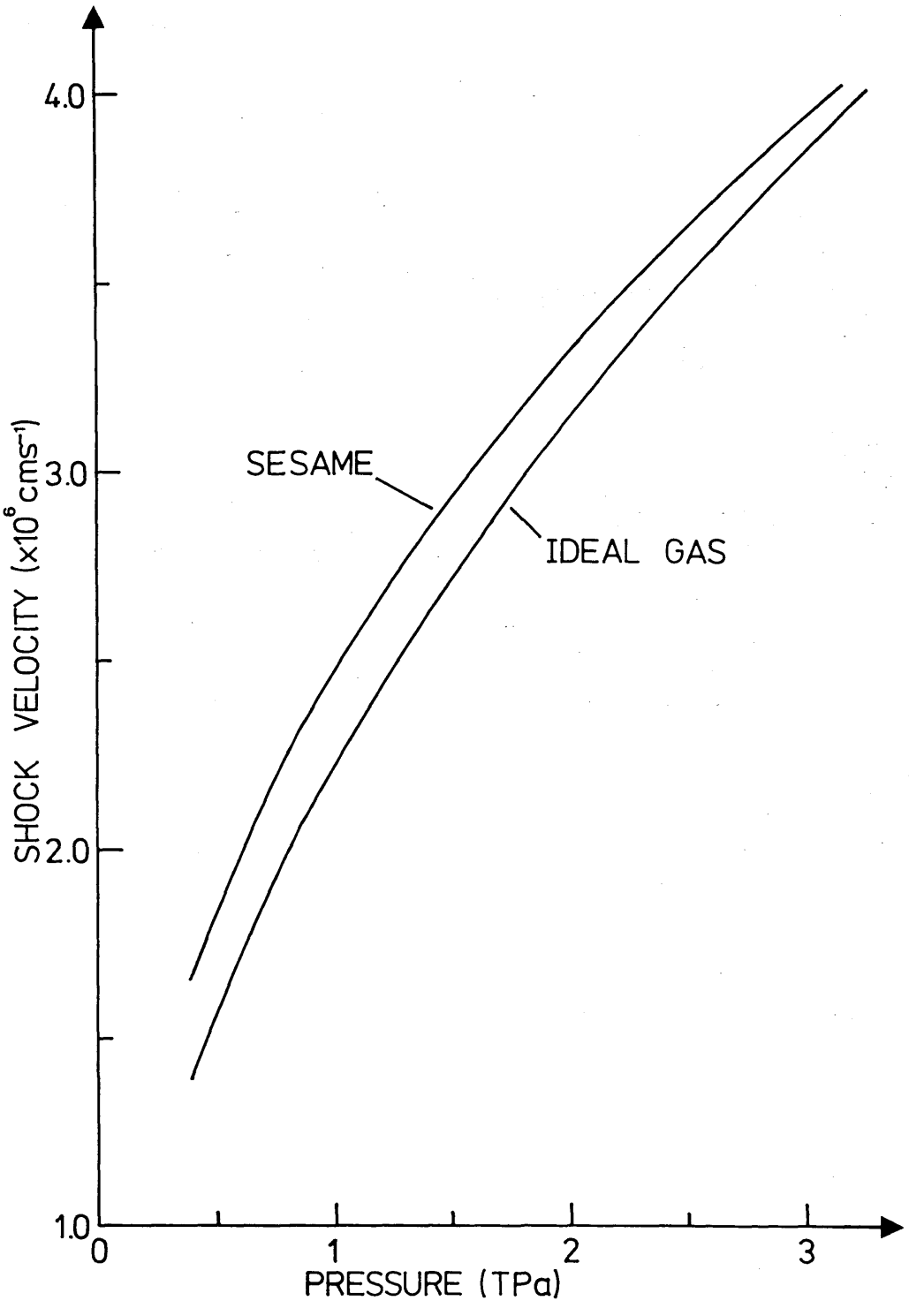


Figure 2.4 Variation of shock velocity with pressure predicted by eq(2.14) and by SESAME equation of state data (for aluminium).

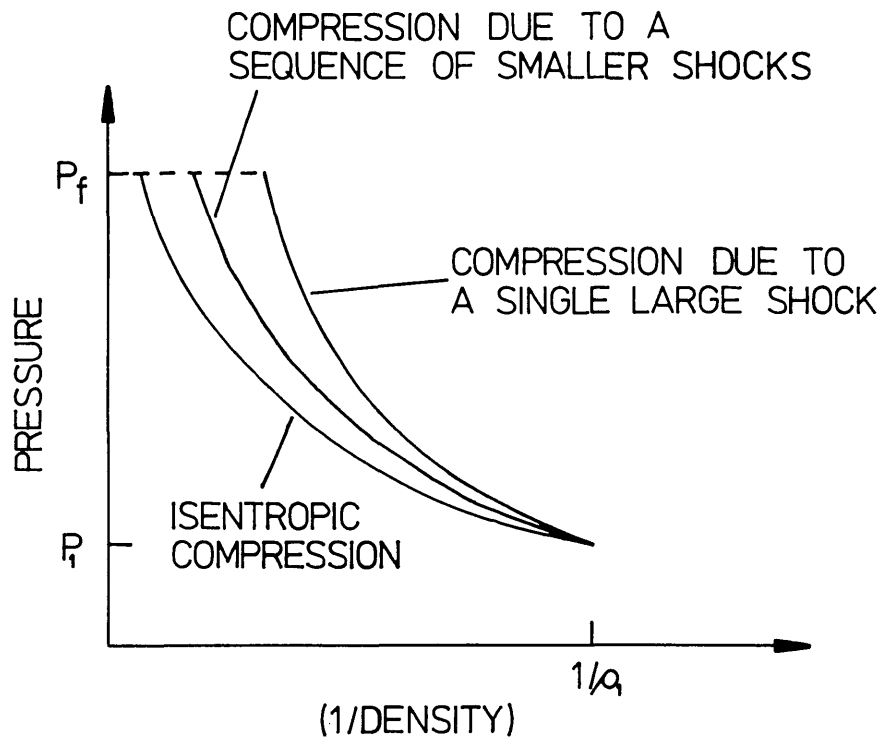


Figure 2.5 Comparison of compression achieved by (a) single strong shock, (b) isentropic compression and (c) sequence of weaker shocks.

Fig(2.6) shows the variation of γ_{eff} with x (for $\gamma = 5/3$). Now since:

$$\frac{\rho_{final}}{\rho_{initial}} = \left[\frac{P_{final}}{P_{initial}}\right]^{1/\gamma_{eff}} \qquad (2.22)$$

It is clear that for a particular final pressure the maximum compression can be achieved when γ_{eff} (and hence x) is as small as possible. In the limit $x = 4$ (ie. strong shock) $\gamma_{eff} \to \infty$ and we have the most inefficient compression possible. Whereas for $x \to 1$, $\gamma_{eff} \approx \gamma$ and the compression approaches the adiabatic ideal. For small x, γ_{eff} is a relatively insensitve function of x and the compression is not far above adiabatic even with a density doubling at each stage.

This analysis is only correct if the shocks do not overtake each other. The n^{th} shock formed at time t_n does not overtake the previous one formed at time t_{n-1}, before time t if

$$v_n(t-t_n) \leqslant v_{n-1}(t-t_{n-1}) \qquad (2.23)$$

if all the shocks are to coalesce at time t then

$$v_1 t = v_2(t-t_2) = - - - - - - - - - - - - - = v_n(t-t_n) \qquad (2.24)$$

Hence the n^{th} shock must satisfy the following condition for all the shocks to coalesce at time t

$$\frac{v_n}{v_1} = \frac{t}{t-t_n} \qquad \text{(taking } t_1 = 0\text{)} \qquad (2.25)$$

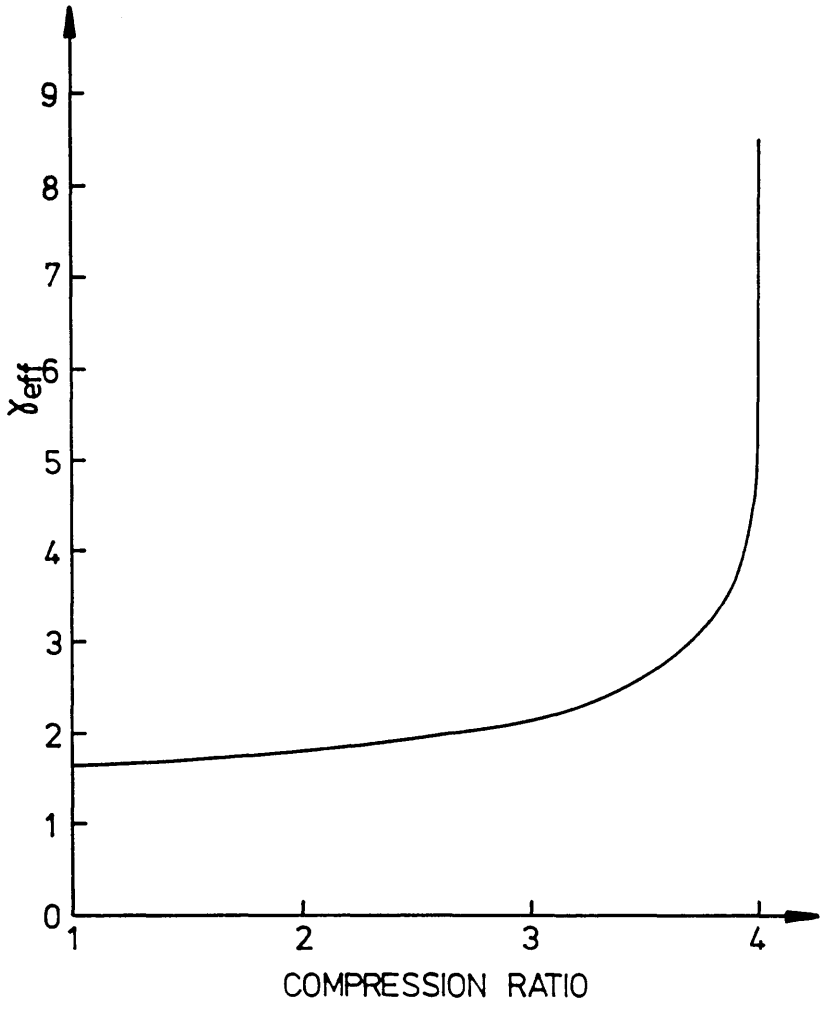


Figure 2.6 Variation of effective adiabatic index (γ_{eff}) with compression ratio.

Of particular interest to the experimental work described later in this chapter is the case of just two coalescing shocks. If the subscript 3 is used to describe quantities behind the second shock than by using eq(2.8) the total compression after the second shock is given by

$$\frac{\rho_3}{\rho_1} = \left[\frac{(\gamma+1)P_3 + (\gamma-1)P_2}{(\gamma-1)P_3 + (\gamma+1)P_2}\right]\left[\frac{\gamma+1}{\gamma-1}\right] \qquad (2.26)$$

The velocity of the second shock, U_3, can be determined by combining eq(2.10), eq(2.12) and eq(2.14) giving

$$U_3 = U_1\left[\frac{2}{\gamma+1} + \frac{(\gamma-1)}{(\gamma+1)}\left[1 + \frac{(\gamma+1)}{(\gamma-1)}\frac{P_3}{P_2}\right]^{\frac{1}{2}}\right] \qquad (2.27)$$

(2.2.3) Shock propagation in Spherical Geometry

Clearly for I.C.F. it is important to study the case of shock propagation in a spherical geometry. In such a geometry the effect of spherical convergence must be taken into account. This results in the pressure driving the shock increasing, due to the decreasing size of the shock surface. This causes the shock to accelerate as it approaches the centre of the sphere. Solutions for the case of a single strong shock in a spherical geometry have been obtained by Guderly [39] and Goldman [40]. These solutions have been discussed in several texts [6,15] and will not be reported on in any detail here. The main result that follows is similar to the planar 1−D case that only a limited compression, which is inadequate for I.C.F., can be obtained by a single strong shock. As in a planar geometry a higher compression can be attained by a sequence of weak coalescing shocks used to approach the adiabatic case. The temporal profile of the laser pulse required to produce an adiabatic compression for a spherical target has been calculated to be [1].

$$I(t) = I_0\left[1 - \frac{t}{t_0}\right]^{-s} \qquad \text{for } t<t_0 \qquad (2.28)$$

Where $s = 3\gamma/(\gamma+1) = 15/8$ for $\gamma = 5/3$, and t_0 is the time taken for the initial shock generated by the laser pulse to reach the centre of the sphere.

(2.3) Experimental Arrangement

(2.3.1) Experimental set−up

The experimental arrangement used to study shock breakout is shown in fig(2.7). The targets were irradiated by six beams of the Rutherford Appleton Laboratory VULCAN glass laser system. The beams were brought to an overlapping focus by using a cluster beam arrangement. This individually focused the six beams onto target via f/10 aspheric singlet lenses arranged around a 16°

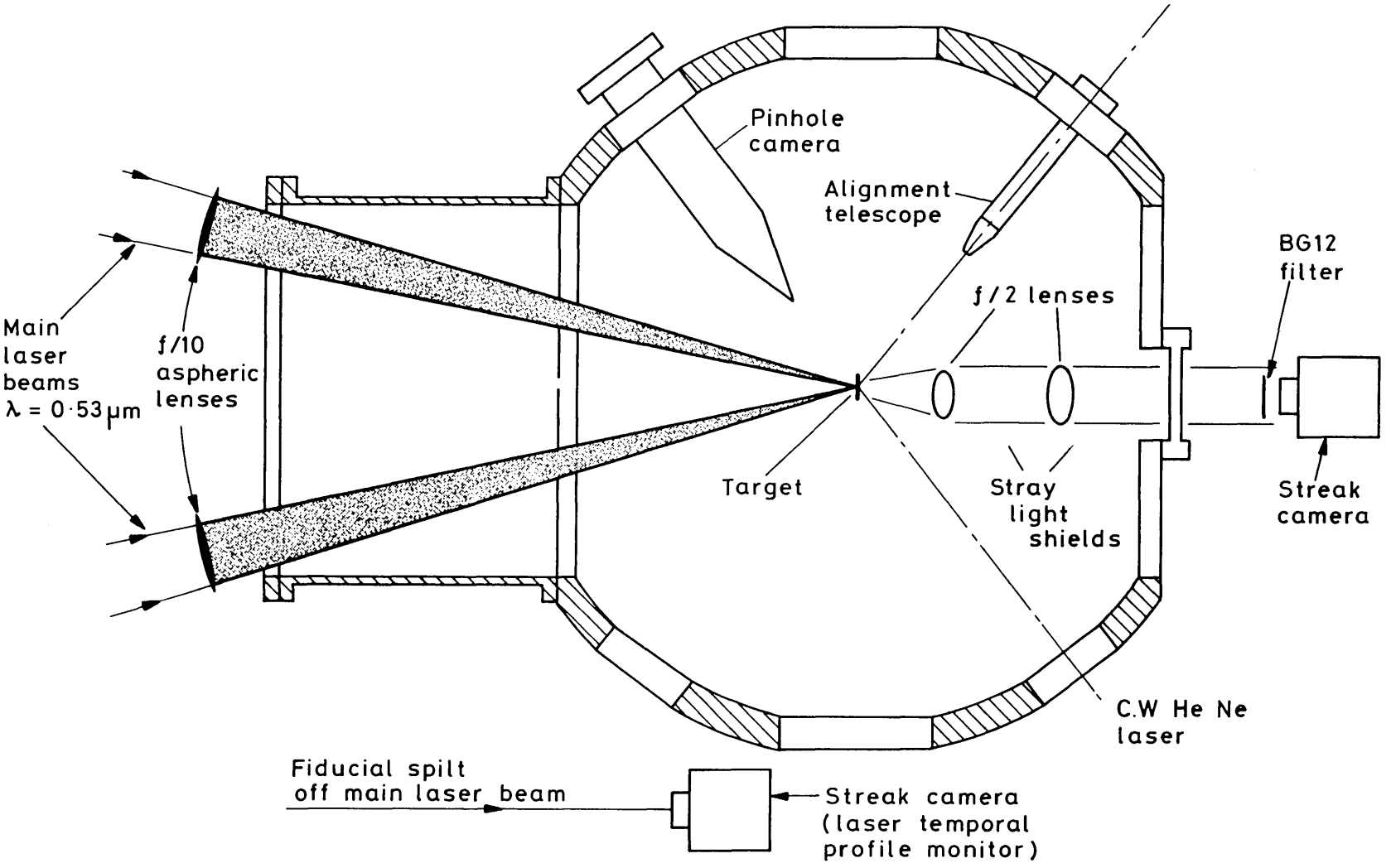


Figure 2.7 Experimental arrangement used to study shock breakout.

half angle cone (this is shown for two of the beams in fig(2.7)). Second harmonic ($\lambda = 0.53$ μm) laser pulses with a 800 ps F.W.H.M. (full width half maximum) were used to irradiate the targets. This allowed irradiances in the range 5×10^{13} – 5×10^{14} Wcm^{-2} to be generated with the VULCAN laser. Temporally shaped laser pulses were generated by bringing one of the six beams early in time (typically by 1 ns) with respect to the other five beams. A small fraction of one of the incident laser beams was split off and directed onto an optical streak camera to measure the temporal profile of the laser pulse. Generally aluminium multiple step targets were used in these experiments. These targets typically had six steps 5 μm thick and 50 μm wide on a 20 μm thick base. This was found to be sufficient to keep radiation preheat of the rear surface of the target to a negligible level (see section (2.3.2)). The laser beams were typically focused to a large 270 μm diameter focal spot on the targets to ensure a planar shock. The actual size and uniformity of the focal spot on each laser shot was measured with an active x–ray pinhole camera. This was positioned at an angle of 55° to the target normal and had an overall magnification of $\times$7.9. The spatial resolution of the pinhole camera was 20 μm.

To observe the shock breakout the rear surface of the targets were imaged onto a Hadland 675 optical streak camera via two f/2 microscpe objectives with an overall magnification of $\times$13. A large 200 μm wide slit was used on the streak camera in order to increase the collection efficiency of the device for the optical signal generated by the shock breakout. The system had a temporal and a spatial resolution of 20 ps and 4 μm respectively. Large shields were mounted around the edge of the targets to prevent any plasma light from the front surface of the targets reaching the streak camera. Coloured glass BG12 filters were placed directly in front of the streak camera to prevent any scattered laser light from reaching the streak camera slit. The system as a whole had a spectral response in the range 380 –470 nm. To align the step targets a C.W. helium neon laser was reflected off the rear surface of the target. The reflected light was then imaged out onto a screen via an alignment telescope with a magnification of approximately $\times$200. The illuminated steps of the target were clearly visible on the screen image. This allowed the target to be positioned to within $\pm$10 μm so that the image of the target steps (generated by the main imaging system) was accurately located on the streak camera slit.

The expected streak records for an unshaped and a shaped laser pulse are shown in fig(2.8) and fig(2.9) respectively. For an unshaped laser pulse generating a single shock, breakout from consecutive steps will be delayed with respect to

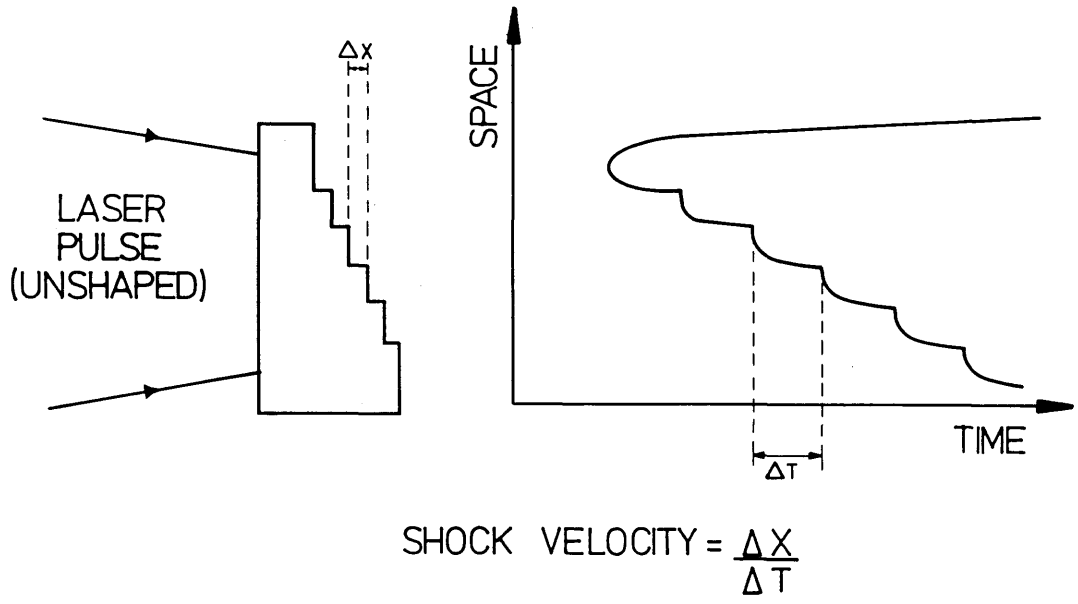


Figure 2.8 Expected streak record for an unshaped laser pulse.

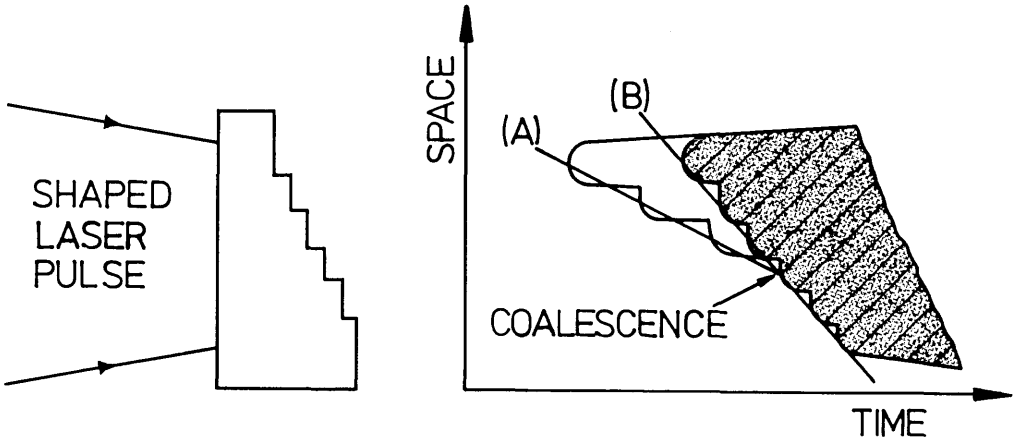


Figure 2.9 Expected streak record for a shaped laser pulse.

each other due to the different target thicknesses traversed by the shock. Clearly if the step thicknesses are known the shock velocity can be calculated. For a shaped laser pulse the first weaker shock generated by the initial leading edge of the laser pulse will break through at the locus of points represented by curve (a) in fig(2.9). The second stronger (and hence faster) shock will break through at some time later at the locus of points represented by curve (b) giving the brighter region on the streak. The crossing of the two curves gives the point at which coalescence occurs.

(2.3.2) Experimental design

In order to perform a 'clean' shock wave experiment it is necessary that the shock is planar, that the shock pressure remains constant during the experiment and that the region ahead of the shock remains unperturbed. These points will now be discussed in detail for conditions relevant to the experiment described in this chapter.

(1) The shock must be planar.

This requires that the size of the laser focal spot generating the shock is significantly larger than the target thickness. Also it is necessary that the driving pressure across the shock front, and hence the laser irradiance across the focal spot is uniform. Two dimensional simulations [41] indicate that for $\lambda = 0.53$ μm irradiation a beam uniformity of ±25% is required to achieve a uniformity of ±2% in the shock front.

(2) The shock pressure should remain constant during the experiment.

In particular it is important that the shock wave does not start to decay, due to the rarefaction wave launched at the end of the laser pulse, before it has reached the rear surface of the target. A simple model has been developed by Trainor and Lee [42] to estimate the distance a laser generated shock will propagate before it starts to decay. The model assumes a laser pulse of constant irradiance I_0 and duration τ. Consider a shock wave propagating into a target with a velocity U, it will impart a velocity V to the material flowing behind the shock, where by combining eqs(2.14) and (2.15) we get $V = (3/4)U$ for a strong shock. The ablation front will follow the shock into the target with a velocity approximately equal to the general flow rate behind the shock. At the end of the

laser pulse ($t=\tau$) a rarefaction wave will propagate into the target with a velocity C_H+V, where C_H is the local sound speed in the shocked material. It follows from this that the rarefaction wave will catch the shock at time, t_d, where

$$t_d = \frac{C_H}{(C_H + V - U)} \tau \qquad (2.29)$$

For a strong shock $C_H \simeq 0.55U$ (by applying the results of section (2.2.1)) and so $t_d \simeq 1.8\tau$. At this time the shock front will be located at a target depth $x_d = Ut_d$. For times $t > t_d$ the rarefaction wave will gradually reduce the pressure driving the shock wave and cause it to decay. It can be shown [42] for aluminium that the pressure, P(x), will vary with distance according to the following relationship.

$$P(x) = P(x_d)\left[1 + \frac{0.0385}{\tau(\text{ns})} [I_0(10^{14}\text{Wcm}^{-2})]^{-0.3}(x-x_d)\right]^{-0.86} \qquad (2.30)$$

Where x is in μm. Although this model assumes a constant laser intensity rather that a Gaussian temporal profile for the laser pulse, it can still be used to estimate the maximum target thickness which can be used for the experiment reported in this chapter. Since $U \propto P^{\frac{1}{2}}$ for a strong shock it follows from eqs(2.29) and (2.30) that for a typical laser irradiance of 2×10^{14} Wcm^{-2} the shock velocity will have decayed by 10% (this corresponds to the likely accuracy to which the shock velocity can be measured) after propagating 49 μm. Clearly for higher irradiances (and hence larger shock velocities) the minimum target thickness allowable will increase (for $I_0 = 4\times10^{14}$ Wcm^{-2}, $x = 63$ μm for a 10% drop in shock velocity). Therefore for the experimental conditions considered here, measurements should only be taken for target thicknesses up to approximately 50 μm if a constant shock velocity is to be assumed.

(3) The region ahead of the shock should remain unperturbed

The region ahead of the shock can be preheated by both suprathermal electrons and x-rays. This needs to be avoided because changing the conditions could potentially effect the propagation of the shock. However preheat is also undesirable since preheating of the rear surface of the target can cause blackbody emission which could swamp the emission due to the shock breakout and make it difficult to detect the arrival of the shock. Hence it is necessary to make the base of the step targets sufficiently thick that preheat of the target rear surface is negligible compared with the shock heating.

The effect of x−ray preheat on the actual shock wave propagation has been studied by computer simulation by Salzmann et. al. [43]. They found that for early times a preheated region (0.1−0.5 eV) ahead of the shock front was formed, which reduced the velocity of the shock at the beginning of its propagation. However as the compressed region, due to the shock, gains width it becomes thicker than the average x−ray mean free path. This causes the x−rays to be absorbed in the compressed region rather than ahead of it. Hence the x−ray energy deposition occurs mainly in the backward portion (the side closer to the ablation surface) of the shock compressed region of the target. Consequently as the x−ray preheat influences only the backside of the shock wave it was not found to induce any measurable difference on the compression, pressure, temperature and velocity of the propagating shock wave; the values of these quantities were found to be the same as for computations without the inclusion of x−ray preheat. Hence it seems reasonable to assume that the x−ray preheat has little detrimental effect on the propagation of the shock wave itself in these experiments.

A very approximate calculation can be performed to estimate the x−ray preheating of the target rear surface. The x−ray flux (I_x) propagating into the target at a distance (x) is given by

$$I_x(x) = I_x(0)\exp(-\mu\rho x) \tag{2.31}$$

Where $I_x(0)$ is the initial x−ray flux, ρ the target density and μ the mass absorption coefficient. Hence the energy absorbed by the target per unit mass (E) at a depth x is

$$E(x) = \frac{-1}{\rho}\frac{dI_x}{dx} = \mu I_x(0)\exp(-\mu\rho x) \tag{2.32}$$

Assuming that, for an aluminium target, 20% of the initial laser energy is converted into x−rays in the range 0.5−1.0 keV (half of which will propagate into the target) then for a typical laser irradiance of 2×10^{14} Wcm^{-2} the incident x−ray flux will be 2×10^{13} Wcm^{-2}. E(x) can then be evaluated by averaging eq(2.32) over the values of μ found in the 0.5−1.0 keV range for cold aluminium. It is required that the x−ray heating is significantly less than the shock heating (typically 1−10 eV). To achieve this it follows from eq(2.32) that a target thickness of 20 μm is required to reduce the absorbed energy per unit mass at the target rear surface to an acceptable level of 4.6×10^{3} Jg^{-1}, which corresponds to a temperature of approximately 0.2 eV.

Preheating of the target rear surface can also occur due to suprathermal electrons. However the threshold for suprathermal electron generation is generally taken as $I\lambda^2 \geqslant 10^{14}$ $Wcm^{-2}\mu m^2$ and consequently the experimental conditions considered here should be just below the threshold. A more detailed estimate of the heating due to suprathermal electrons using the model of Trainor and Lee [42] indicates it will be approximately two orders of magnitude less than the x−ray preheating at an irradiance of 2×10^{14} Wcm^{-2}. Consequently the preheating contribution from suprathermal electrons can be ignored.

It should be noted that it is possible, to some extent, to discriminate in favour of the emission due to shock breakout compared with that due to preheating by observing the optical emission only in the blue region of the spectrum. This is because the blackbody emission due to preheat (temperature typically few×0.1 eV) will have its peak in the I.R. and the emission due to shock breakout (temperature typically 5eV) in the U.V./V.U.V..

To summarize the points considered in this section it is necessary that the bases of the aluminium step targets are at least 20 μm thick and that the maximum target thickness is about 50 μm. Also it is necessary that the focal spot diameter is significantly larger than the total target thickness (ie. $\gg$50 μm). These requirements are clearly met by the actual experimental conditions described in section (2.3.1).

(2.4) Computer simulations

The experimental results obtained were compared with simulations from the 1−D Lagrangian hydrocode MEDUSA [44]. The code describes the plasma by four main dependent variables ρ, U, T_i and T_e which represent the density, fluid velocity and ion and electron temperatures. These variables are functions of the time, t, and a single space variable, r, which in the cases studied here corresponds to distance in a planar geometry. The propagation of the shock front in a plasma can be obtained from the code by following the variation of the position of the quasi−discontinuity in pressure and density associated with the shock front.

Simulations were carried out for an aluminium foil with both boundaries left free. The foil was divided up into 90 cells (the maximum allowable number) in order to give an adequate resolution across the shock front where the physical parameters vary rapidly with position. The Thomas−Fermi equation of state with

modified corrections to give correct solid density for the electrons and a perfect gas equation of state for the ions were used. The initial electron and ion temperatures were both set to 10^4 K. This value is higher than desirable but necessary if this equation of state is to be used in order to prevent excessively rapid temperature changes when the laser is initially incident on the target. For steep temperature gradients a flux limiter of 0.05 of the free streaming limit was imposed.

Two modifications have been made to the standard MEDUSA code by the author to improve the modelling of this experiment.

(1) Instead of the initial cell size being constant throughout the target, it was increased by 4 % per cell with the thinnest cell facing the laser. This approach was found to give a better simulation of the initial formation of the shock wave.

(2) Instead of assuming the temporal profile of the laser pulse was Gaussian the actual experimentally measured laser pulse profile was used in the simulations. The experimental profile was input into the code by measuring the laser pulse intensity at a series of discrete points in time from the streak camera record. The code then calculates the laser intensity at a particular time by interpolating between these points. By adding together two such profiles of different magnitudes, delayed in time with respect to each other it was possible to simulate the case of a shaped laser pulse.

(2.5) Experimental results for an unshaped laser pulse

(2.5.1) Single shocks in foil and slab targets

Initially data was taken on foil and slab targets. This was done to ensure that emission due to preheat and shock breakout could be differentiated between. Fig(2.10) shows a pinhole camera image taken of the focal spot obtained for an unshaped laser pulse irradiating an aluminium foil target. From the microdensitometer trace shown the F.W.H.M. of the focal spot is measured to be 270 μm. Fig(2.11) shows the target rear side emission observed for a 25 μm thick aluminium foil irradiated with an unshaped laser pulse of irradiance 1.2×10^{14} Wcm^{-2}. Emission due to shock breakout can clearly be seen in the central region of the streak. The initial width of the shock breakout corresponds closely to the focal spot size of 270 μm indicating that there is very little two dimensional

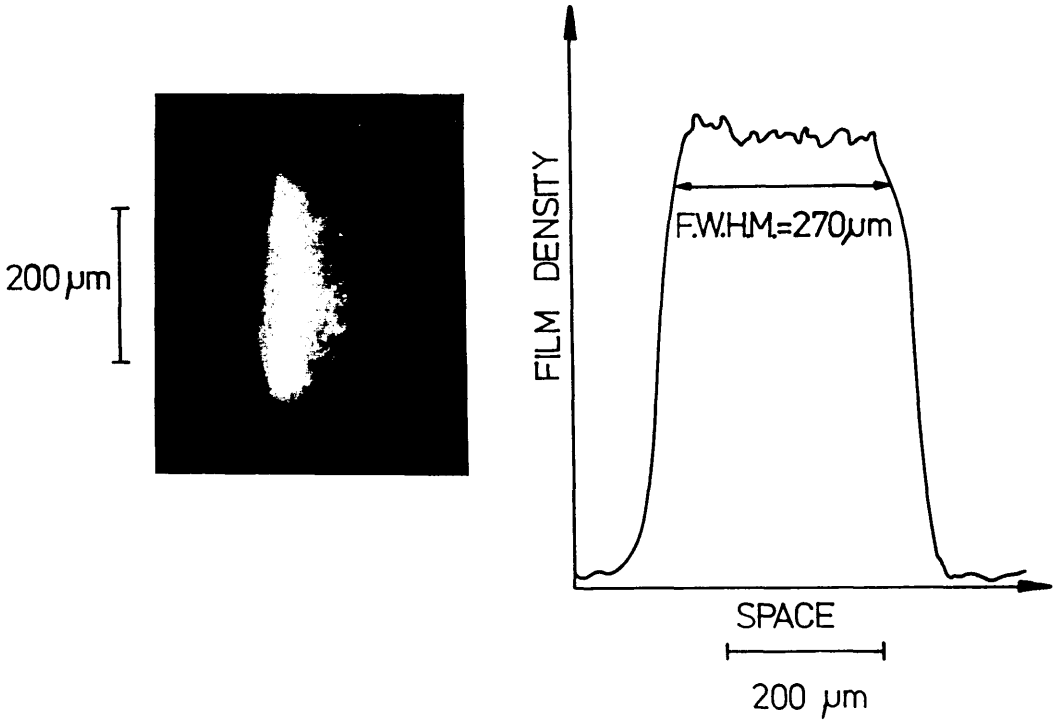


Figure 2.10 Typical pinhole camera image of the focal spot for an unshaped laser pulse.

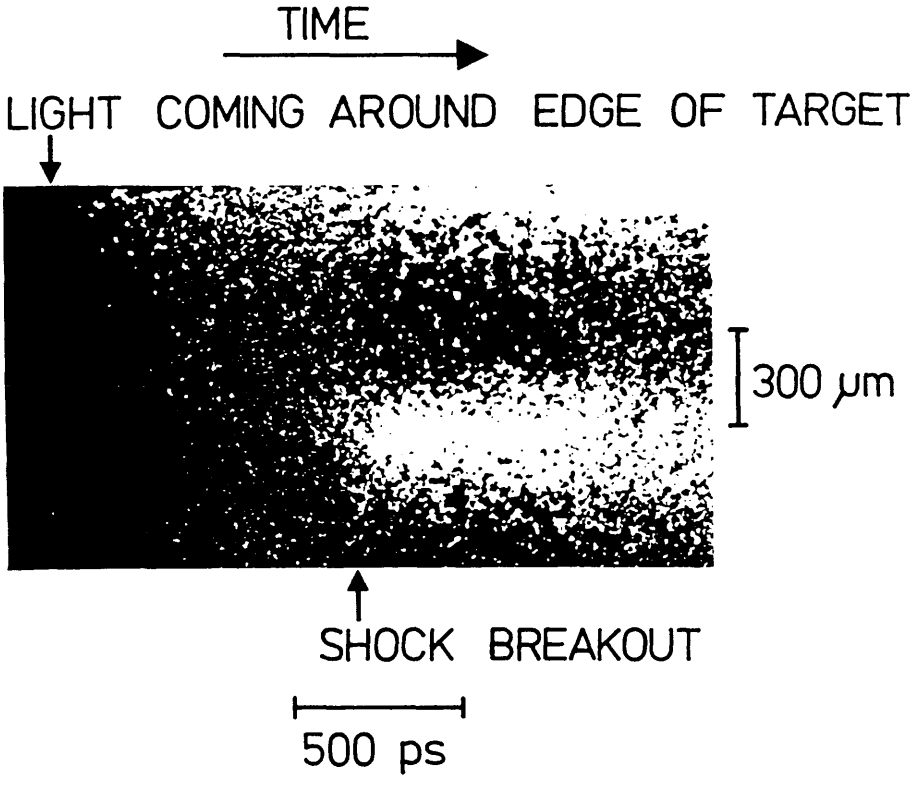


Figure 2.11 Target rear side emission observed for a 25 μm thick aluminium foil (irradiance = 1.2×10^{14} Wcm^{-2}).

expansion of the shock wave in the target. The bright region along the top of the streak is due to stray light coming around the edge of the target. It's turn on can be very approximately used to indicate when the laser pulse hit the target. Hence from the delay of the shock breakout with respect to this stray light the shock velocity can very crudely be estimated. This gives a shock velocity of 2.8×10^6 cm^{-1} which compares well with a MEDUSA prediction of 2.6×10^6 cms^{-1} for this irradiance. It is important to note that there is no evidence of any emission due to radiative preheat of the target rear surface before shock breakout occurs.

The streak record observed for the aluminium foil should be compared with fig(2.12) which shows the target rear surface emission for a 40 μm plastic slab target. The target was irradiated with an unshaped laser pulse of irradiance 2.2×10^{14} Wcm^{-2}. The rear surface of the target was coated with a thin 100 nm layer of aluminium. This was done to block any light from the front surface of the target being transmitted through the target and then imaged onto the streak camera slit. Again, as in fig(2.11), emission due to the shock breakout and stray light coming around the edge of the target can be observed. However emission can now be seen in the region ahead of the shock breakout and this is believed to be due radiative preheat. Also shown in fig(2.12) is a microdensitometer trace taken along the section x−x indicated. It can be seen that initially there is a gradual rise in the emission (and hence the temperature) due to the steady heating of the target rear suface by the incident x−ray flux. In contrast the arrival of the shock causes the temperature, and hence the brightness of the emission, to rise very rapidly as would be expected. The thickness−density product for a 40 μm plastic slab is less than that for a 25 μm aluminium foil and so the aluminium target should more effectively absorb the x−ray flux before it reaches the rear surface of the target. Hence it follows that x−ray preheat should be expected to be more pronounced for the 40 μm plastic slab target than the 25 μm aluminium foil. This clearly agrees with the experimental observations in fig(2.11) and fig(2.12). Also the irradiance for the 40 μm plastic slab target shot was a factor of two higher than for the aluminium foil shot which would further increase the x−ray preheat observed for the plastic target relative to that for the aluminium foil. From the delay of the shock breakout with respect to the stray light observed the shock velocity can be estimated to be 3.4×10^6 cms^{-1}. MEDUSA simulations predict a shock velocity of 4.6×10^6 cms^{-1} which is in rather poor agreement. This discrepancy is presumably due to the very approximate method used to determine the arrival time of the laser pulse.

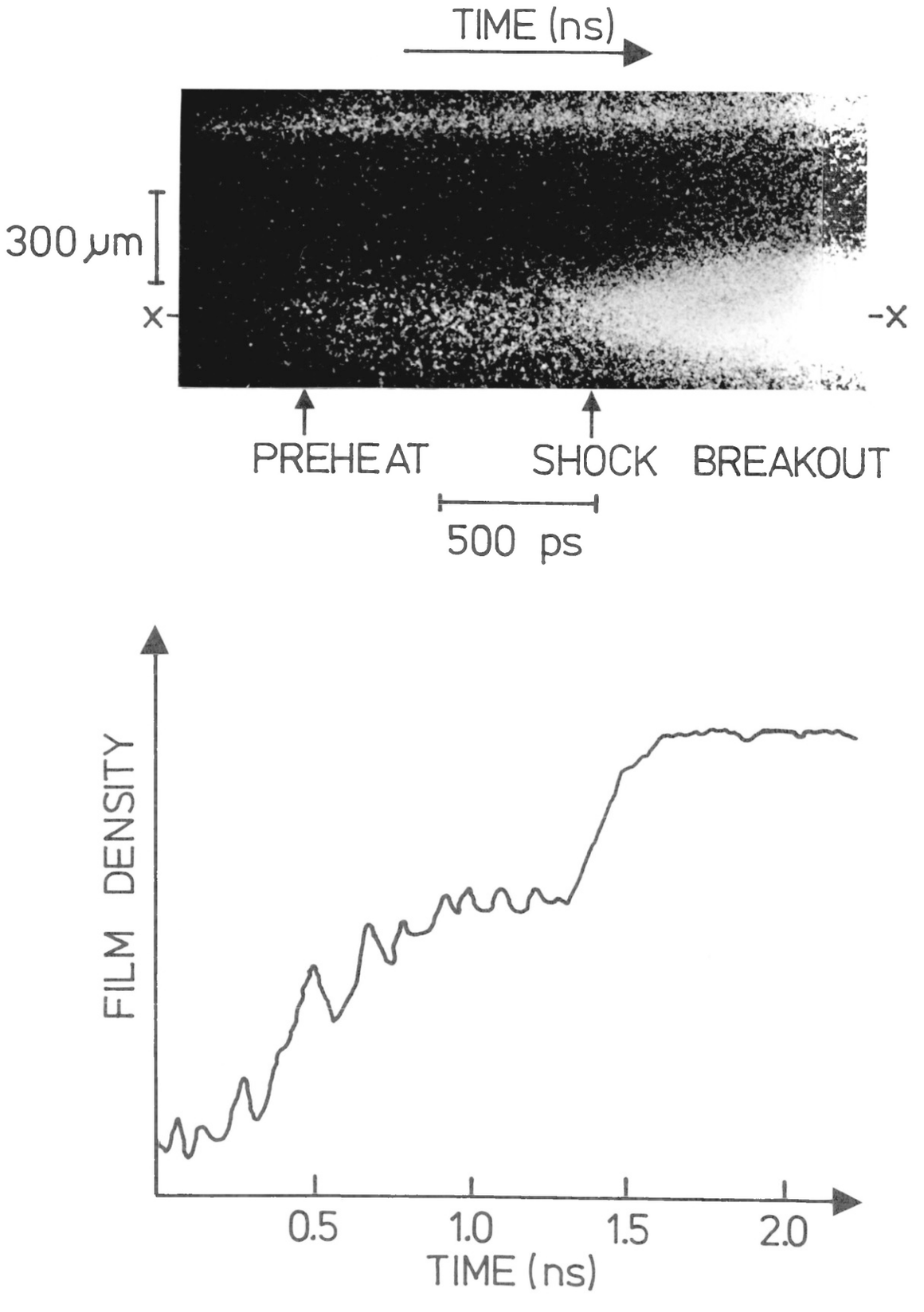


Figure 2.12 Target rear side emission observed for a 40 μm thick plastic slab (irradiance = 2.2 × 10 ^{14} wcm^{-2}).

The reason for irradiating plastic targets was to obtain information on shock propagation in plastic which would be relevant for K−edge spectroscopy measurements of dense plasmas [34]. However due to the large amounts of preheat observed in plastic targets it was not possible to make any detailed measurements of the shock propagation under such conditions. Consequently the results in the experiment reported here were largely restricted to aluminium targets.

It is important to determine the uniformity of the shock front generated in these experiments so that the error in the shock transit time can be estimated. In order to do this a shot was taken on a 25μm thick aluminium foil with a large 550 μm diameter focal spot. By measuring the variation in the breakout time across the shock front it is possible to evaluate the uniformity of the shock front. The streak record obtained is shown in fig(2.13). Analysing the streak in fig(2.13) gives the r.m.s. variation in the shock breakout time as ±38 ps. Assuming a shock transit time of 950 ps (taken from a MEDUSA simulation) this gives a shock front uniformity of ±4.0 %.

(2.5.2) Single shock in Aluminium step targets

Fig(2.14) shows a typical streak image of the shock breakout observed for a Gaussian (unshaped) laser pulse. Breakout can clearly be seen from six consecutive steps. The variation of the shock front position with time deduced from this shot is shown in fig(2.15). The error bars arise from the variation in shock breakout time due to non uniformities in the shock front (estimated from fig(2.13)) and uncertainties in the measurement of the step thicknesses. Also shown are the results of a MEDUSA simulation for this shot. The experimentally measured shock velocity is approximately constant for the duration of the laser pulse and agrees very closely with the simulation. However, after the end of the laser pulse the experimental results show a rapid fall off in shock velocity compared with the gradual decline predicted by the simulation. The shock velocity determined from the linear part of the graph is $(4.3\pm0.3) \times 10^6$ cms^{-1}. This corresponds to a shock pressure of 3.7 TPa.

Fig(2.16) shows the experimentally measured temporal profile of the laser pulse used in the simulation shown in fig(2.15). It was found, that using the real laser profile caused the shock to be generated earlier in the simulation, than if a Gaussian approximation for the temporal profile had been used. This is due to the faster rising edge of the real laser pulse compared with a Gaussian. The

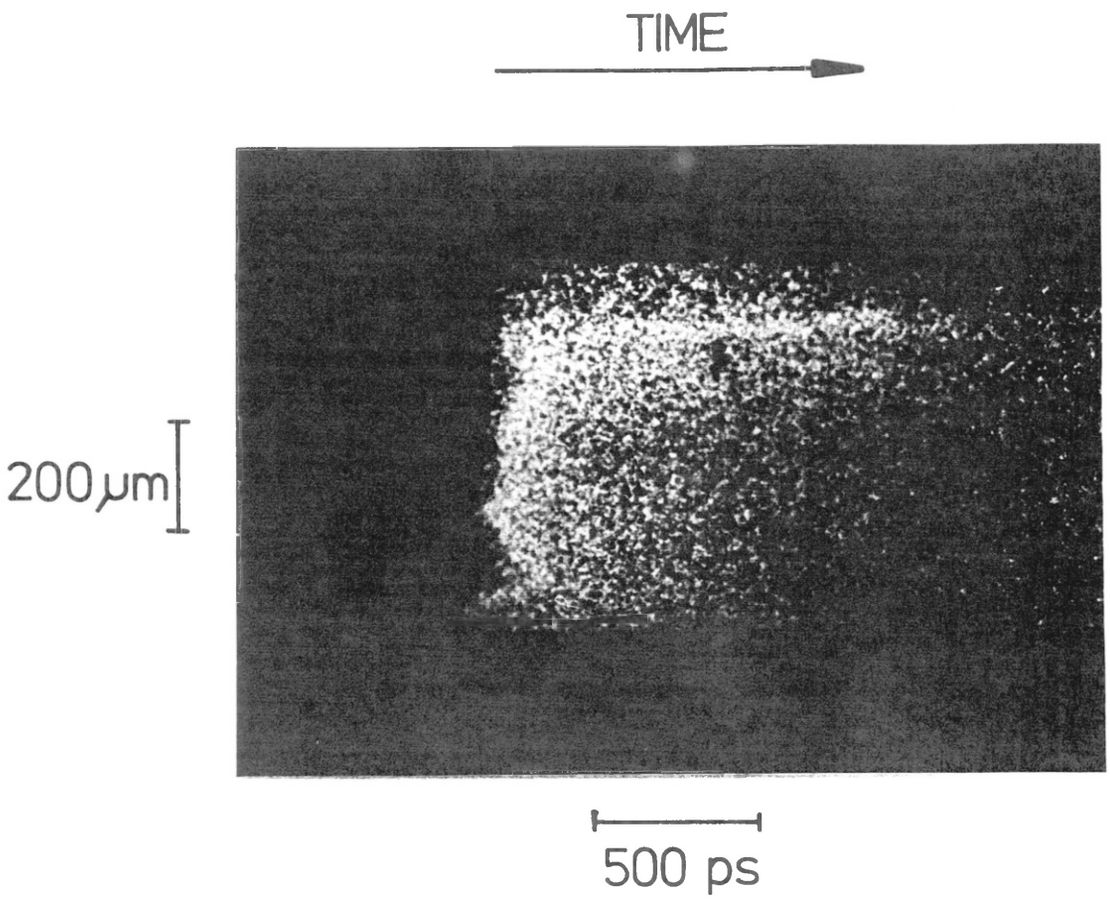


Figure 2.13 Shock breakout observed on a 25 μm aluminium foil with a large 550 μm diameter focal spot. The variation in breakout time is ± 38 ps (irradiance = 1.7×10^{14} Wcm^{-2}).

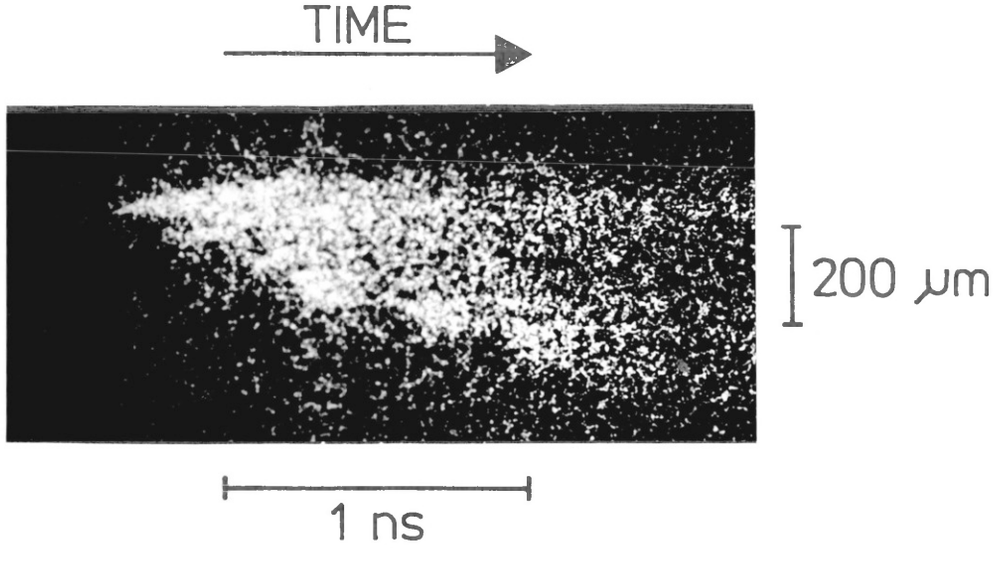


Figure 2.14 Shock breakout from an aluminium step target for an unshaped laser pulse (irradiance = 4.4×10^{14} Wcm^{-2}).

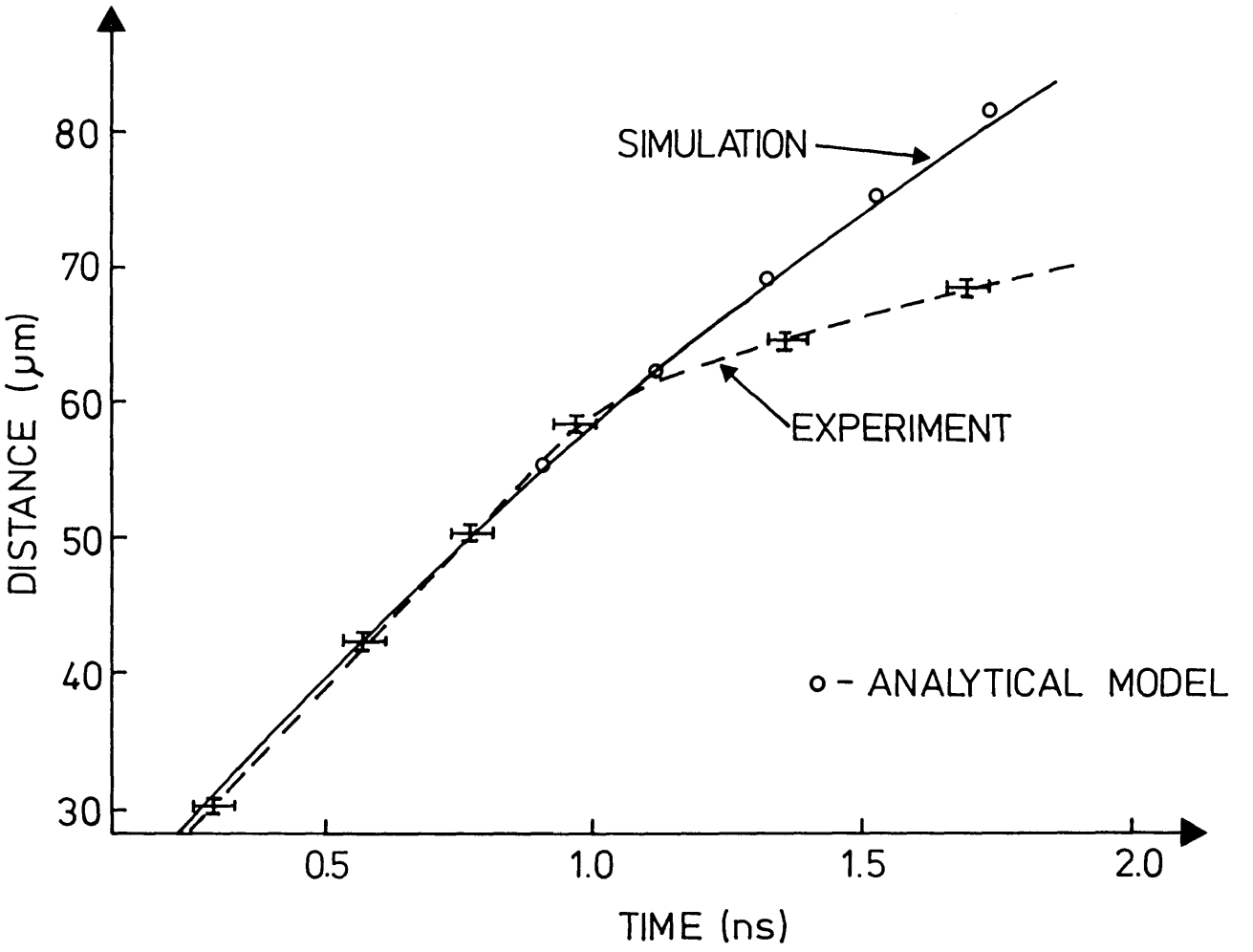


Figure 2.15 Experimentally measured postion of shock front for an unshaped laser pulse (for streak of fig. 2.14) compared with MEDUSA simulation. Also shown is the shock decay predicted by an analytical model.

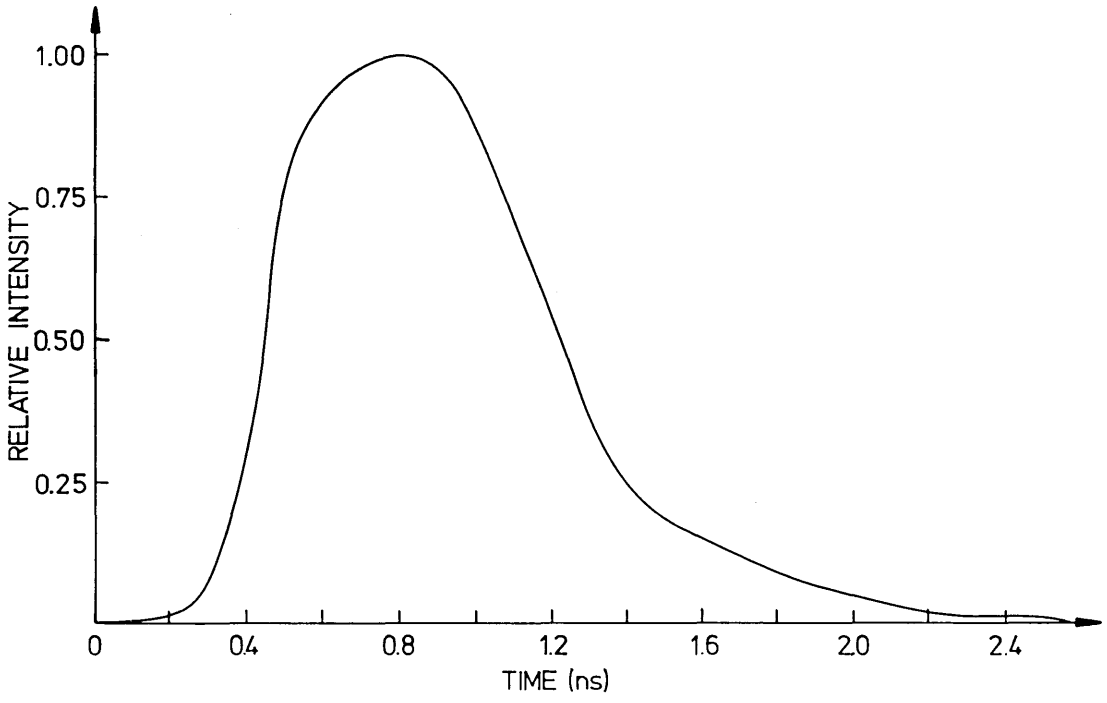


Figure 2.16 Experimentally measured temporal profile of laser pulse (used in the simulation of fig. 2.15).

measured temporal profile of the laser pulse was observed to change to some extent on a shot to shot basis. However these changes were found to have a negligible effect on the shock generation and propagation in the simulations.

The rapid decay of the shock wave measured experimentally after the end of the laser pulse was observed on all the data shots taken. This sudden decrease in the shock velocity cannot simply be explained by the propagation of a rarefaction wave into the target after the end of the laser pulse since this would give a more gradual decay as predicted by the simulations and by various analytical models [42,45]. For comparison the shock decay predicted by the analytical model of Trainor and Lee [42] is also shown in fig(2.15) and it can be seen that it is very similar to that given by the MEDUSA simulation. Even if the value of the sound speed along the Hugoniot is varied from that expected theoretically in this model the experimentally observed decay is not achieved without resorting to an unphysical value for the sound speed. Also it does not seem that the observed shock decay can be entirely due to a drop in laser irradiance at the edges of the focal spot. This is because no delay is observed in the breakout of the shock from the thinnest step. This discrepancy between the experimental results and the

computer simulations may however be due to two dimensional effects. This is because late in the laser pulse the critical density surface, where the laser energy is absorbed, will have moved a significant distance (100−200 microns) out from the target surface. This will cause the shock pressure to decrease for two reasons. Firstly significant lateral transport of energy is likely to occur reducing the pressure driving the shock. Secondly it will cause the six cluster beams to no longer exactly overlap in the region of laser energy deposition. This will reduce the laser irradiance, particularly at the edges of the focal spot, and consequently also reduce the shock pressure. The combination of these two effects will cause a rarefaction wave to propagate into the target earlier than otherwise expected and consequently this may explain the larger than predicted decay of the shock wave. Two dimensional simulations [41] have shown that the two factors just discussed will give rise to a reduction in the shock velocity. Clearly two dimensional spreading of the shock wave itself will also contribute to a reduction in shock velocity at large target thicknesses.

Fig(2.17) shows the variation of shock velocity with irradiance determined from a series of laser shots with unshaped laser pulses. The shock velocity was measured for each shot in the region where it was constant before decay occurs. Also shown on the graph is the MEDUSA predicted scaling of shock velocity with irradiance. Agreement between experiment and the simulation is clearly obtained to within the experimental error. A least squares fit to the experimental results in fig(2.17) gives the scaling of shock velocity with irradiance as

$$V(cms^{-1}) = (2.28\pm0.07) \times 10^{6}[I/10^{14}\ Wcm^{-2}]^{0.35\pm0.03}$$

Assuming an ideal gas equation of state and applying eq(2.14) this gives the variation of shock pressure with irradiance as

$$P(TPa) = (1.06\pm0.08)[I/10^{14}\ Wcm^{-2}]^{0.70\pm0.06}$$

Alternatively using SESAME equation of state data for aluminium [29,37] gives

$$P(TPa) = (0.83\pm0.06)[I/10^{14}\ Wcm^{-2}]^{0.83\pm0.07}$$

The MEDUSA simulations predict the following scalings

$$V(cms^{-1}) = 2.48 \times 10^{6}[I/10^{14}\ Wcm^{-2}]^{0.31}$$

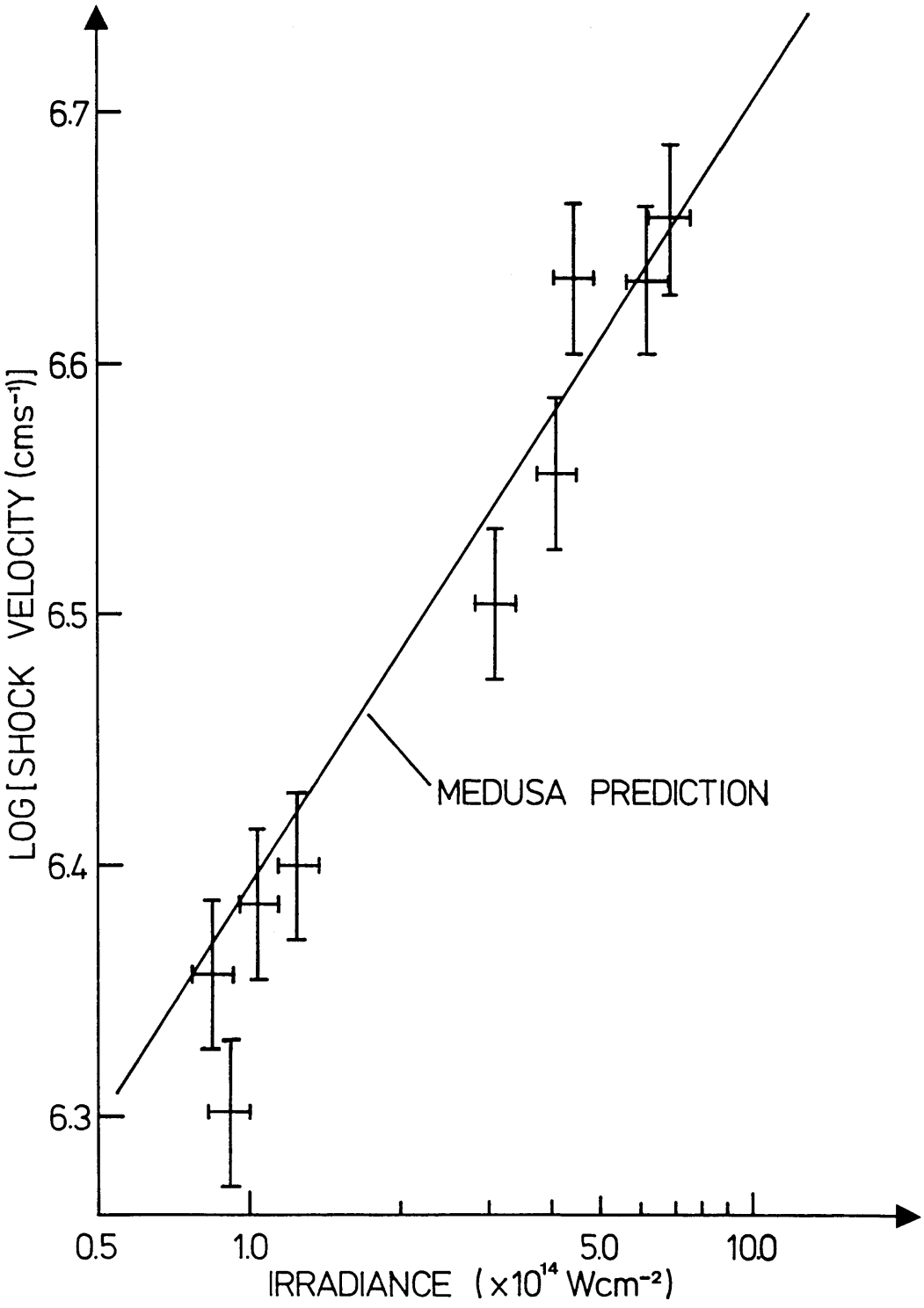


Figure 2.17 Experimentally measured variation of shock velocity with laser irradiance compared with MEDUSA prediction.

$$P(TPa) = 1.32[I/10^{14}\ Wcm^{-2}]^{0.66}$$

Both the experimentally inferred shock pressures and those predicted by the simulations are consistent with previous experimental results [28,29,31,33] and computer simulations [42,46]. Measurements made by Key et. al. [47] of the scaling of the ablation pressure with irradiance (assuming negligible lateral heat flow) give the following result.

$$P(TPa) = 2.2[I/10^{14}\ Wcm^{-2}]^{0.73}$$

This is in approximate agreement with the shock pressures measured here.

(2.6) Experimental results for a shaped lase pulse

Results will now be presented for the case of two coalescing shocks generated by a temporally shaped laser pulse. Fig(2.18) shows a typical example of the shock breakout observed for a shaped laser pulse. The breakout from the first two steps is due to the first (weaker) shock and from the remaining three steps due to the second stronger shock after coalescence has occurred. The breakout due to the two shocks can clearly be differentiated since that due to the second shock is significantly brighter and also has a larger velocity (corresponding to a smaller delay between the breakout from consecutive steps). The shaped laser pulse was generated by bringing one of the laser beams early in time by 1.2 ns compared with the other five beams. This created an intensity ratio of 1:4.3 between the leading and main pulses.

Measurements made with the pinhole camera of the focal spot size for a shaped laser pulse give the F.W.H.M. as 270 μm which is identical to that measured for an unshaped laser pulse. This is important because it shows that there is negligible refraction of the main part of the shaped laser pulse by the plasma generated by the initial leading edge of the shaped pulse. If refraction had occurred it could have increased the effective size of the focal spot for the main part of the shaped pulse and thereby reduced the irradiance generating the second shock.

Fig(2.19) shows the variation of shock front position with time deduced from the streak in fig(2.18). Also shown is the result of a computer simulation for this shot. Two distinct slopes to the graph can be seen corresponding to the first and

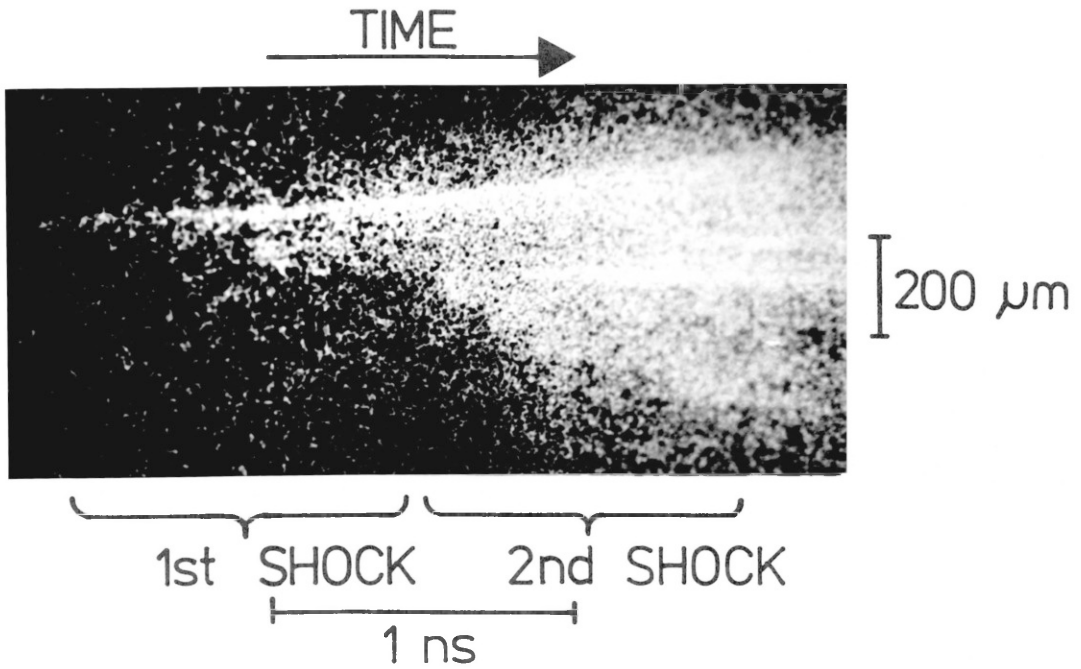


Figure 2.18 Shock breakout observed from an aluminium step target for a shaped laser pulse. Pulse ratio of 1:4.3 and irradiance of first pulse of $8.6\times10^{13}\ Wcm^{-2}$.

second shocks. The velocity of the first shock is 2.0×10^6 cms^{-1} whereas the velocity of the shock front after coalescence is 3.2×10^6 cms^{-1}. The velocity of the first shock is in agreement with the simulation, however the measured velocity of the shock front after coalescence is significantly lower than the MEDUSA prediction of 4.4×10^6 cms^{-1}. Also there is a discrepancy as to at which point in the target coalescence between the two shocks occurs. The simulation predicts coalescence at a target depth of 42 μm whereas the experimental results show that coalescence occurs at a target depth of 38 μm. This disagreement can be explained by the first shock decaying after the end of the initial laser pulse in a similar way to that observed for a single shock driven by a Gaussian laser pulse in section (2.5.2). This causes coalescence to occur at a smaller target depth than predicted by the simulation. It also explains why the second shock is observed to be weaker than predicted by the simulation.

Fig(2.20) shows the variation of the position of the shock front with time for a similar shaped laser pulse shot except that the delay between the two laser pulses was reduced to 1 ns. Here coalescence has occured before the first shock has started to decay and a good agreement is obtained with the simulation. The

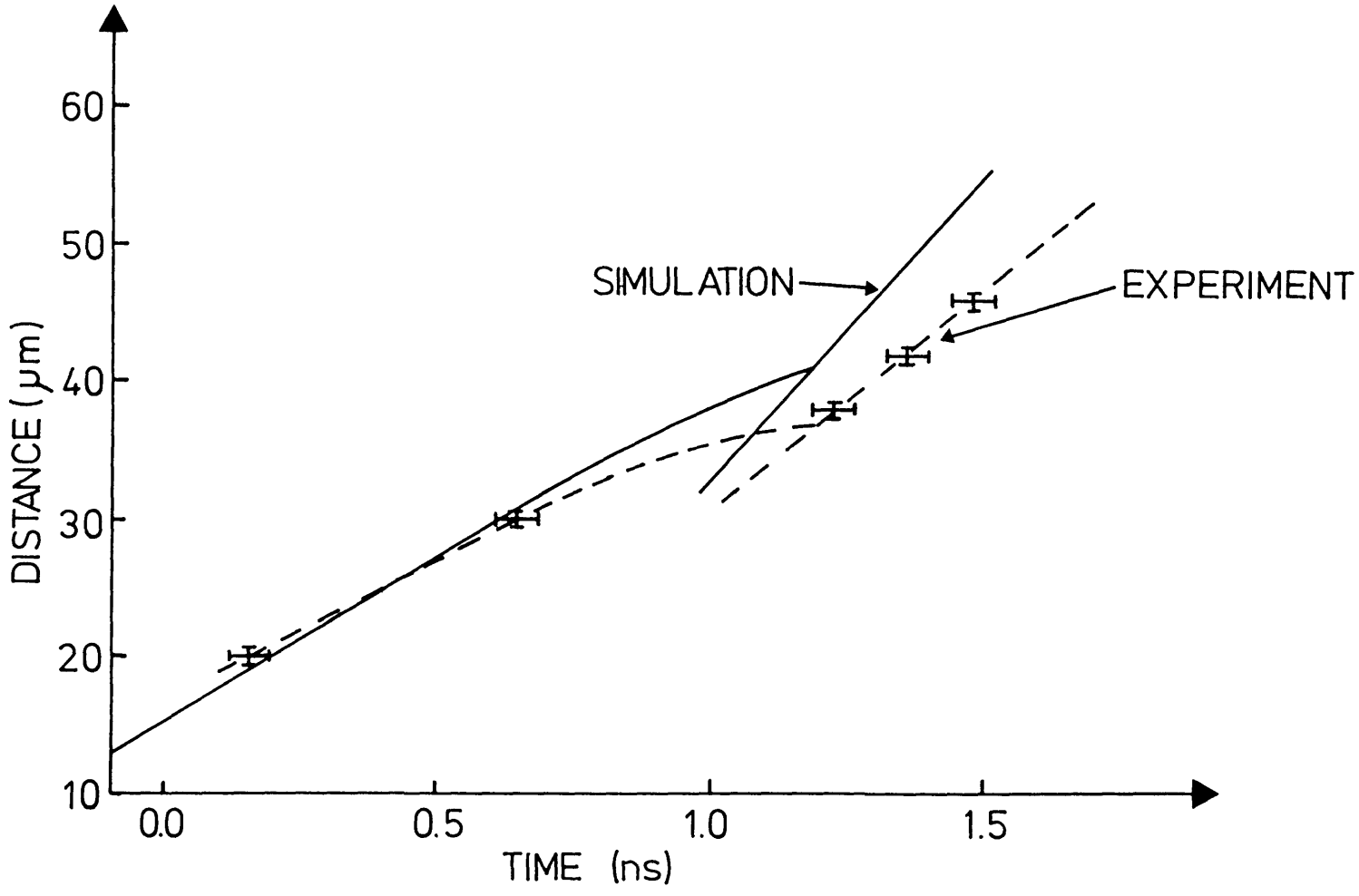


Figure 2.19 Experimentally measured position of shock front for a shaped laser pulse (for streak of fig. 2.18) compared with MEDUSA simulation ($\Delta T = 1.2$ ns).

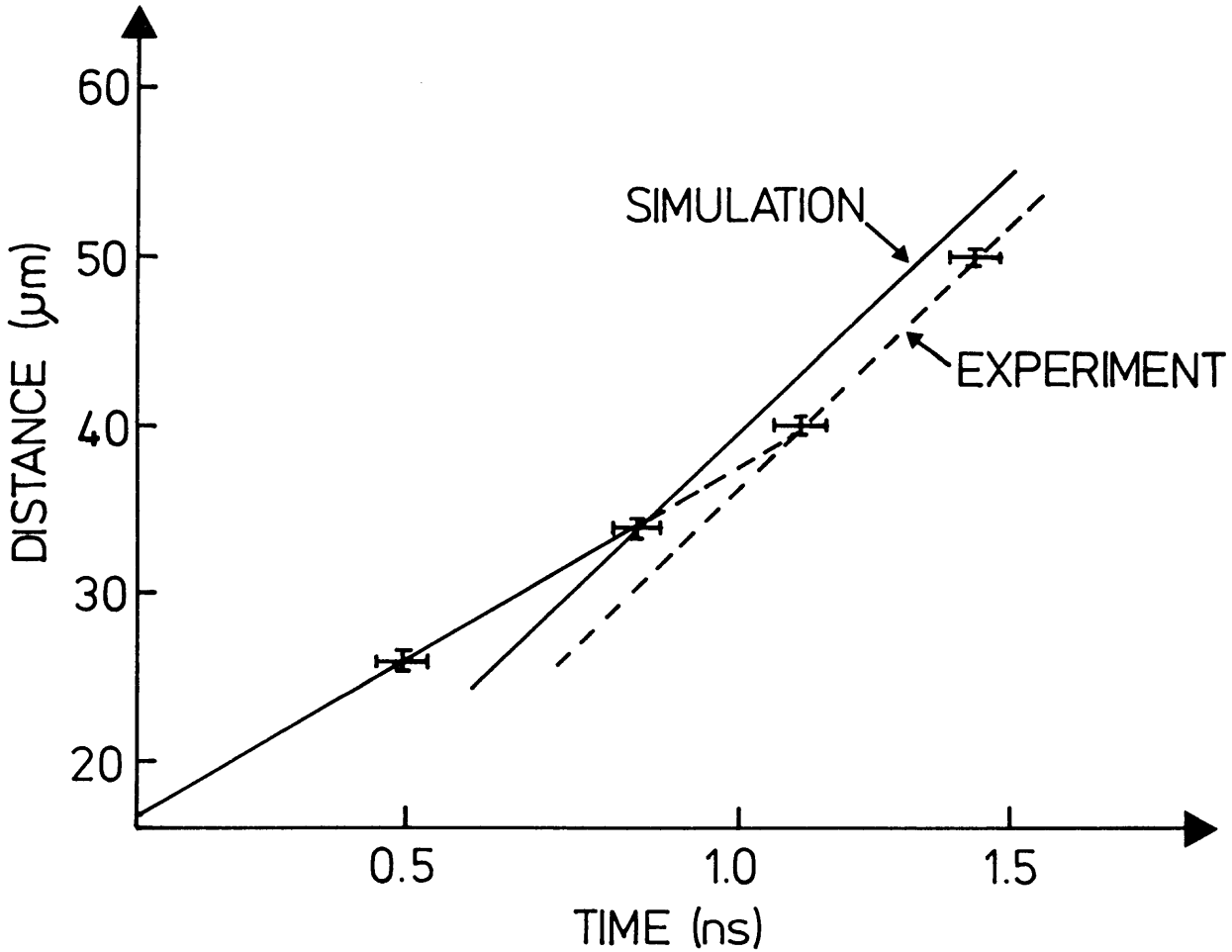


Figure 2.20 Experimentally measured position of shock front for a shaped laser pulse ($\Delta T = 1.0$ ns) compared with a MEDUSA simulation. Pulse ratio of 1:4.3 and irradiance of first pulse of 7.9×10^{13} Wcm^{-2}.

experimentally measured velocities of the first and second shocks are 2.3×10^6 cms^{-1} and 3.9×10^6 cms^{-1} respectively. Both these velocities agree to within 3% with the MEDUSA predictions.

The pressures determined from the experimentally measured velocities of the two shocks in fig(2.19) are 0.8 TPa and 2.2 TPa for the first and second shocks respectively. From these pressures a simple calculation using the results of section (2.2) yields a value for the overall compression ratio of the two shocks of ×7. This is, as expected, higher than the maximum fourfold compression which can be obtained with a single strong shock. This result is also consistent with MEDUSA which predicts a compression ratio of ×6.6 after the second shock.

Finally measurements were also made of the shock breakout observed from 25 μm aluminium foils irradiated by shaped laser pulses. The experimental conditions were controlled so that the first shock broke out of the rear surface of the target before the second shock had caught it up. The second shock is then observed to break out of the target rear surface some time later. Results obtained provide useful information to supplement the measurements taken with step targets. This is because they give details of the propagation of the second shock, in the already shocked target material, before coalescence occurs. For step targets it is not possible to clearly detect the arrival of the second shock in regions where the first shock has already broken out. This is because the emission due to the second shock is largely blocked by the cool dense plasma already spalled out by the first shock. However on a foil target the material spalled out by the second shock is not restricted at the sides and is free to expand out around the edges of the material ejected by the first shock. Hence it is easier to detect the arrival of the second shock under such conditions on a foil target rather than a step target.

Fig(2.21) shows the shock breakout observed on a 25 μm thick aluminium foil irradiated by a shaped laser pulse. The breakout observed on separate shots for two different delays between the leading and main parts of the shaped pulse are shown. In both cases the intensity ratio between the leading and main part of the shaped laser pulse was approximately 1:4. The breakout due to the first and second shocks can clearly be differentiated between on both streaks. Reducing the delay between the leading and main part of the shaped laser pulse is observed to reduce the delay between the first and second shocks breaking out as would be expected.

Fig(2.22) and fig(2.23) show the results of simulations of the variation of

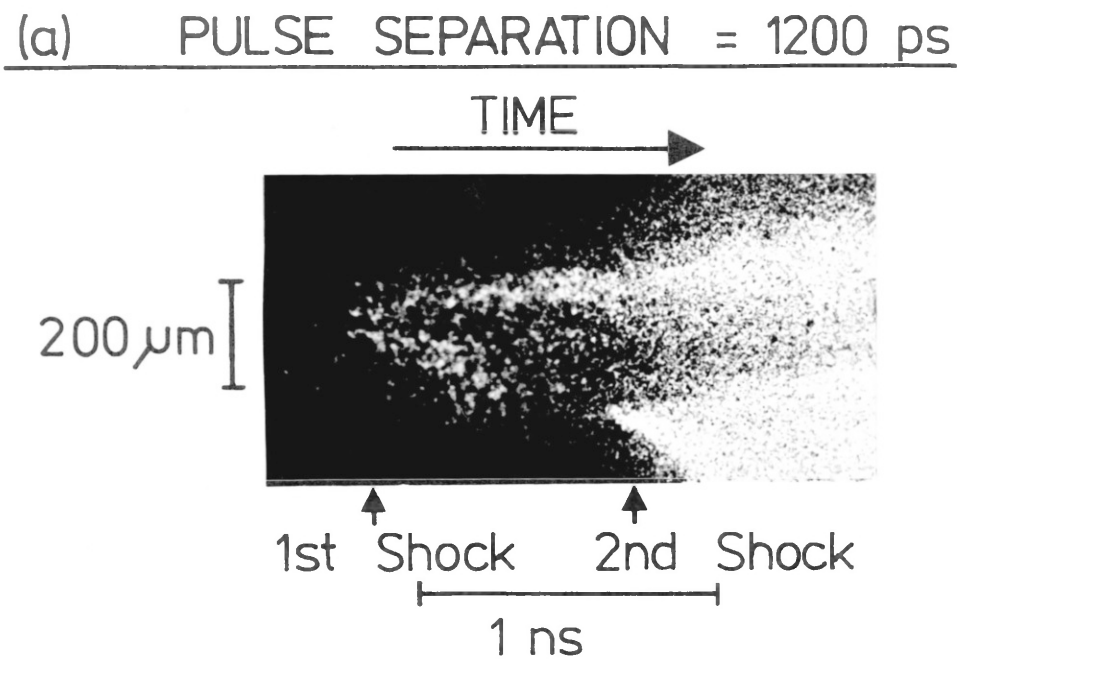


Figure 2.21 Shock breakout observed from a 25 μm thick aluminium foil for a shaped laser pulse, (a) Pulse separation = 1200 ps, pulse ratio of 1:4.5 and irradiance of first pulse of 9.8×10^{13} Wcm^{-2}, (b) Pulse separation = 950 ps, pulse ratio of 1:4.0 and irradiance of first pulse of 8.7×10^{13} Wcm^{-2}.

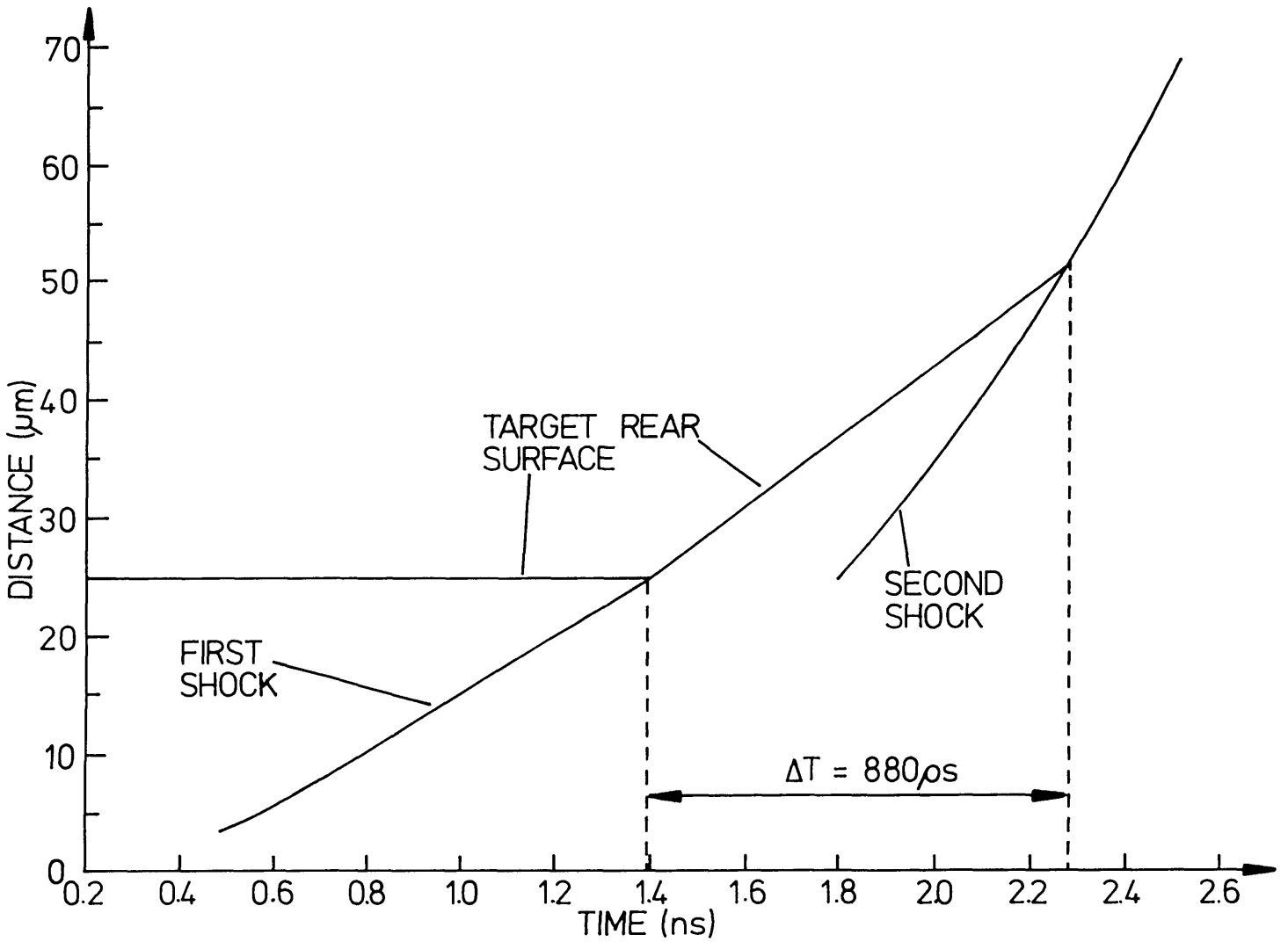


Figure 2.22 MEDUSA simulation of streak of fig. 2.21 (a).

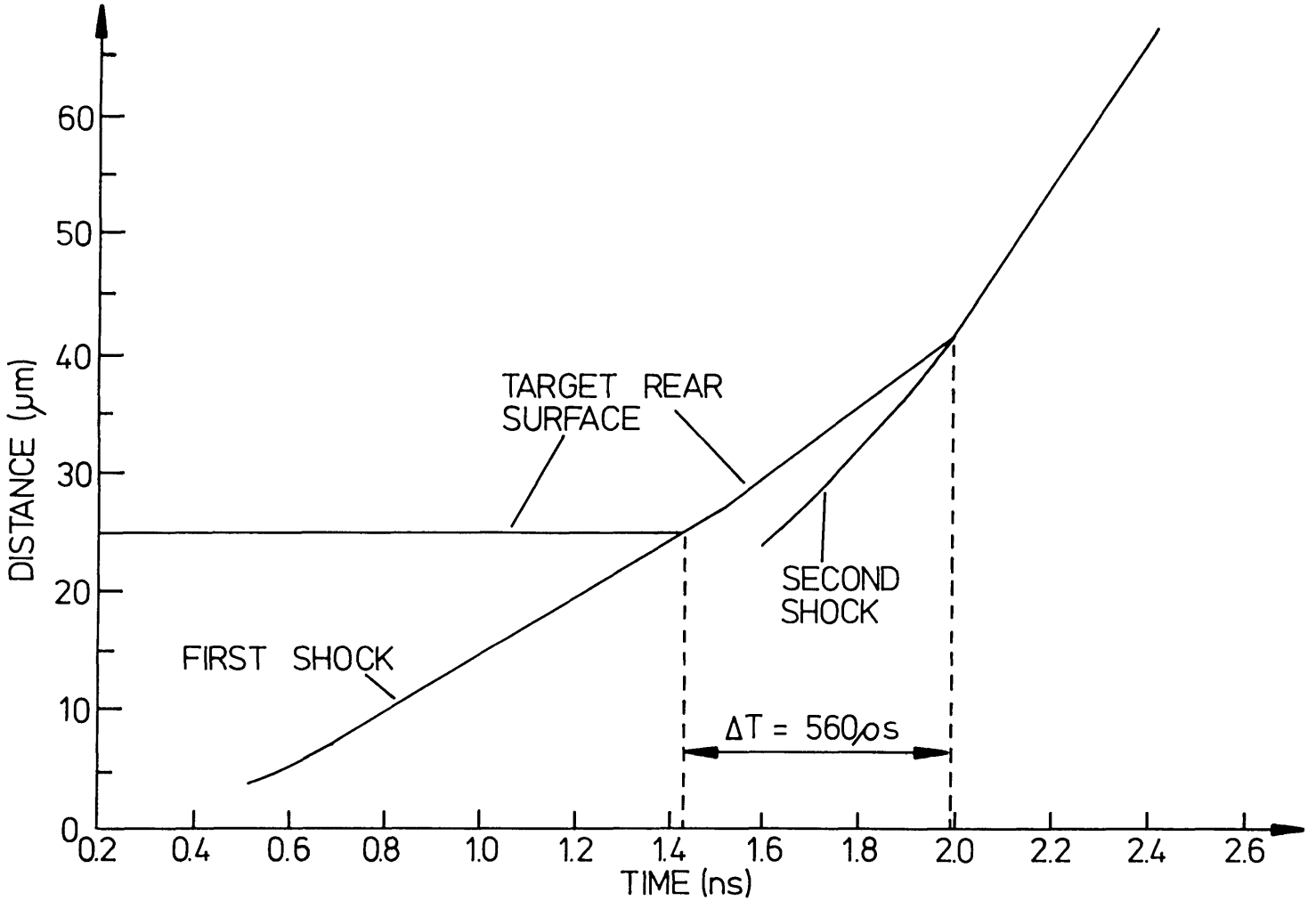


Figure 2.23 MEDUSA simulation of streak of fig. 2.21 (b).

the positions of the shock fronts with time for the streaks in fig(2.21)(a) and fig(2.21)(b) respectively. It can be seen that the situation is complicated by the fact that the rear surface of the target starts to accelerate, in the direction of propagation of the shocks, once the first shock has broken out. The breakout of the first shock also results in a rarefaction wave propagating back into the target. Both these processes affect the time taken for the second shock to reach the rear surface of the target. Firstly, the rarefaction wave causes the plasma conditions ahead of the the second shock to change and thereby effect its velocity. Secondly, the movement of the target rear surface increases the distance the second shock must propagate before it breaks out. The simulations give the delays between the breakout of the first and second shocks as 880 ps and 560 ps for the cases of laser pulse separations of 1200 ps and 950 ps respectively. This agrees well with the experimental measurements of 850±60 ps and 590±60 ps. This suggests that MEDUSA realistically models the initial propagation of the second shock (in the already shocked material) and also the various processes which occur after the first shock breaks out.

(2.7) Conclusion

In summary, the propagation of shocks generated by Gaussian and tailored laser pulses has been studied. In particular the first direct experimental observation of the coalescence of two laser induced shocks has been made by the use of optical streak photography on multiple step targets. The results obtained were generally in good agreement with 1−D computer simulations except that after the end of the laser pulse the shock was found to decay far more rapidly than predicted. It seems likely that this discrepancy is due to two dimensional effects. From the experimental results it has been possible to calculate the compression achieved with a shaped laser pulse and confirm that it is higher than that which can be achieved by a Gaussian laser pulse generating a single shock.

(2.8) Possible future work

The accuracy of the experimental results presented in this chapter could be improved by the use of laser beam smoothing techniques such as induced spatial incoherence [48], a random phase plate [49] or a fly−eye lens [50]. This would generate a more uniform laser focal spot and hence improve the uniformity of the shock front generated. This would allow more accurate measurements to be made

of the shock front position before and after coalescence occurs. Consequently the results obtained would provide a more rigorous test of the computer codes used to simulate the experiment. Also this would potentially allow shock velocities to be determined to the ±2% accuracy which is required if equation of state parameters are to be determined from shock velocity mesurements in impedance mismatch experiments [32].

Further useful future work would be to extend the measurements made for a shaped laser pulse to a wider range of experimental conditions. In particular the effect of varying the intensity ratio between the leading and main parts of the shaped pulse could be studied. Also it would be useful to take measurements with larger focal spots than those used here, so that the shock propagation more closely approximates the one dimensional ideal. Such measurements would confirm whether or not the discrepancies observed between the experimental results and the simulations are indeed due to 2−D effects.

CHAPTER 3

THEORY OF CORONAL PLASMA INSTABILITIES

A number of potentially harmful instabilities can occur in the underdense coronal plasmas which will surround laser fusion targets. Of these instabilities Stimulated Raman Scattering, Stiumlated Brillouin Scattering and filamentation give the greatest cause for concern. In this chapter the basic theory of these three instabilities will be briefly discussed as a background to the experimental results presented in chapters 5 and 6 of this thesis.

(3.1) Parametric Instabilities

A variety of plasma instabilities can be driven by intense laser light in an underdense plasma ($n_e < n_{ec}$). Most of these instabilities can be regarded as the resonant decay of an incident light wave into two other waves [10]. If we consider a high intensity, externally driven wave at a frequency ω_0 in a plasma. Then, if the plasma has an existing mode of oscillation at ω_1 (which may initially be of low power), beats will occur with the wave at ω_0 and side bands are generated. These will be at the frequencies $\omega_2 = \omega_0 - \omega_1$ and $\omega_3 = \omega_0 + \omega_1$. If ω_2 is another lightly damped mode of the plasma then this will beat with ω_0 at $\omega_1 = \omega_0 - \omega_2$. Thus the mode at ω_1 is enhanced and will beat more strongly with the mode at ω_0 to give a stronger ω_2 mode. If this process continues the plasma modes at ω_1 and ω_2, which may have initially been very weak, can reach high levels as the instability grows. It should be noted that for the driven modes to grow they must receive energy faster than they lose it by damping. This results in a threshold 'pump wave' amplitude at ω_0 for the instability to grow. Processes of this type which occur in an underdense plasma are termed Parametric instabilities and four are of particular interest:

(1) The Ion Acoustic (or Parametric) Instability.
incident light wave → ion acoustic wave + electron plasma wave

(2) Stimulated Brillouin Scattering.
incident light wave → ion acoustic wave + scattered light wave

(3) Stimulated Raman Scattering.
incident light wave → electron plasma wave + scattered light wave

(4) Two Plasmon Decay.

incident light wave → electron plasma wave + electron plasma wave

The regions where these instabilities can occur in a laser produced plasma are illustrated in fig(3.1). Of these four processes, Stimulated Brillouin Scattering (S.B.S.) and Stimulated Raman Scattering (S.R.S.) are potentially the most undesirable for laser fusion implosions, since they can result in a large fraction of the incident laser light wave being lost from the plasma as a scattered light wave. Also S.R.S. can result in the production of hot electrons from the damping of the electron plasma wave generated by the instability. These hot electrons could then preheat the target core in a laser fusion implosion [51]. For these reasons considerable experimental [51−60] and theoretical [61−67] effort has been put into studying S.R.S. and S.B.S.. These two processes will now be discussed in more detail.

(3.1.1) Stimulated Brillouin Scattering

S.B.S. involves the conversion of the incident light wave ($_0$) into a lower frequency light wave (sc) and an ion acoustic wave (i). Energy and momentum conservation require that the following conditions are met:

$$\omega_0 = \omega_{sc} + \omega_i \tag{3.1}$$

$$\underline{k}_0 = \underline{k}_{sc} + \underline{k}_i \tag{3.2}$$

The dispersion relationships for each wave require also that:

$$k_0^2 c^2 = \omega_0^2 - \omega_{pe}^2 \tag{3.3}$$

$$k_{sc}^2 c^2 = \omega_{sc}^2 - \omega_{pe}^2 \tag{3.4}$$

$$k_i^2 \left[\frac{ZKT_e}{m_i (1+k_i^2 \lambda_D^2)} + \frac{3KT_i}{m_i} \right] = \omega_i^2 \tag{3.5}$$

Where T_e (T_i) is the electron (ion) temperature, m_i (Z) is the ion mass (charge) and λ_D is the Debye length. These matching conditions are illustrated in fig(3.2) for the case of backscatter. It follows from these expressions that S.B.S. can potentially occur for all densities up to n_{ec}. Since in general $\omega_0 \gg \omega_i$ the

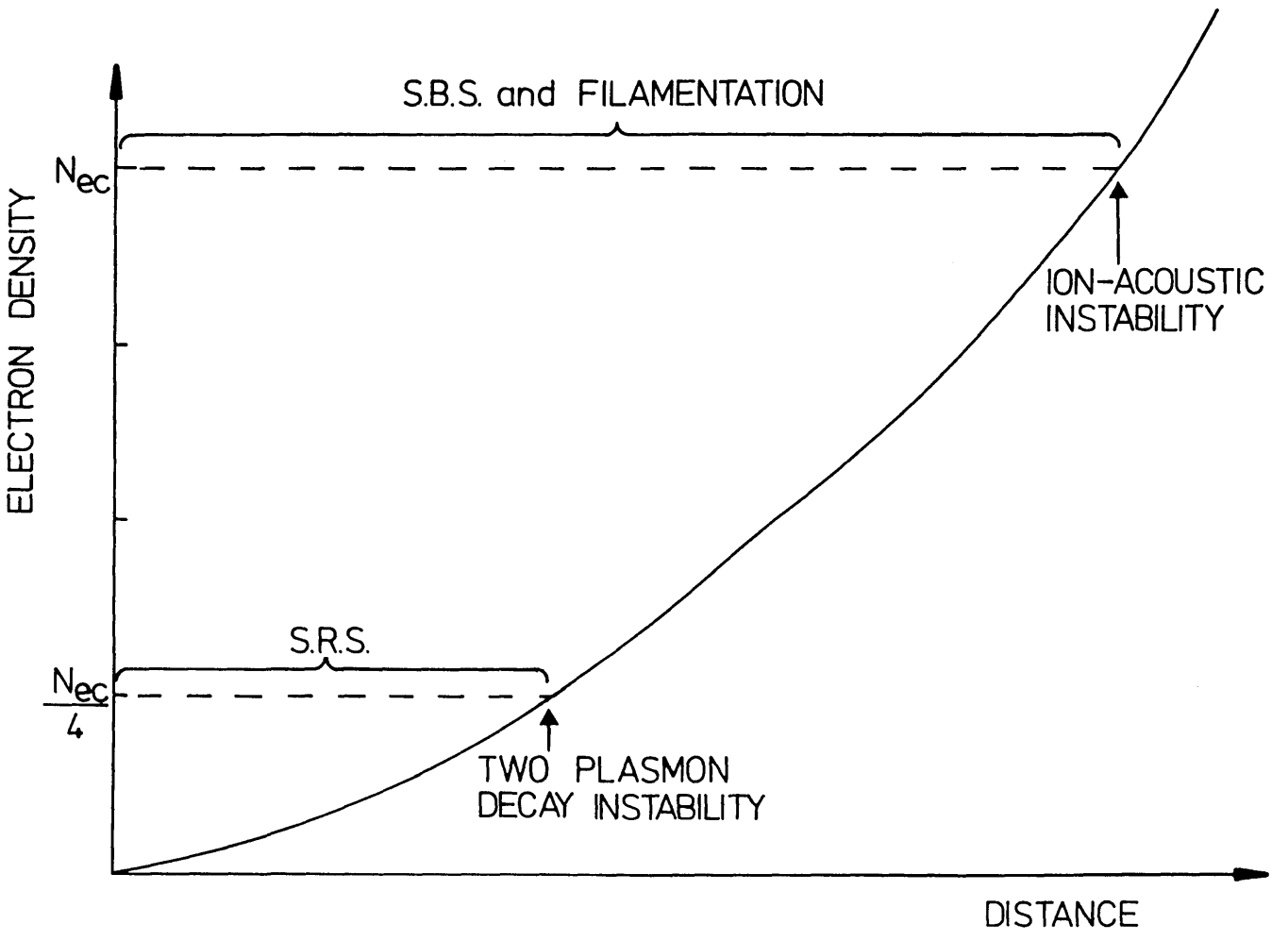


Figure 3.1 Locations of instabilities in an underdense plasma.

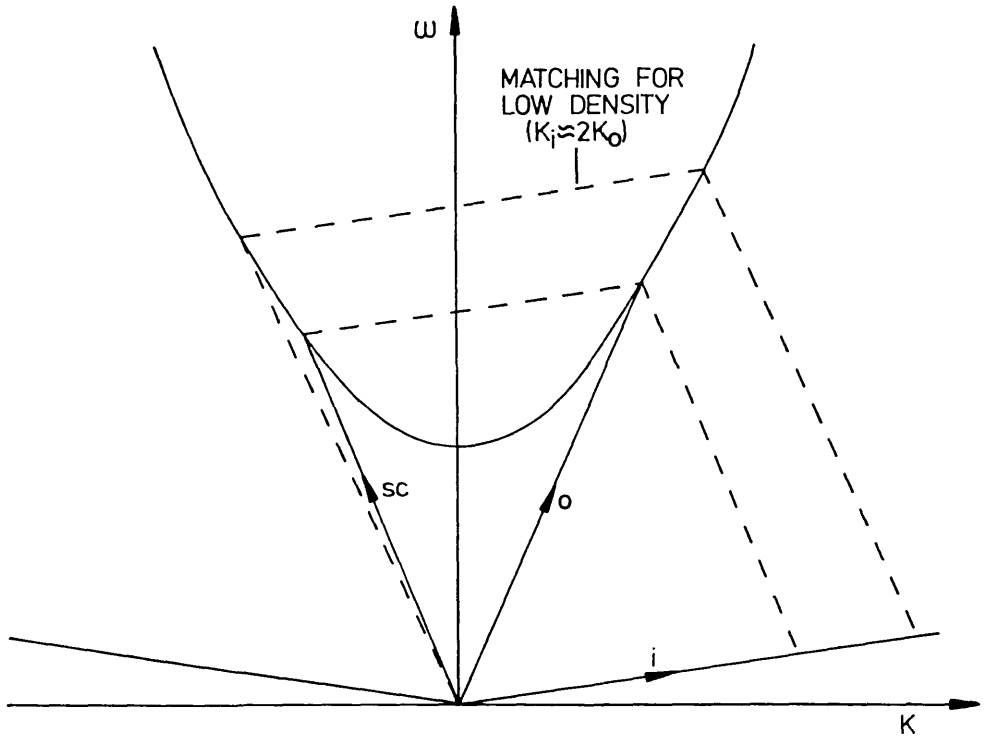


Figure 3.2 Matching conditions for backward stimulated Brillouin scattering.

scattered light wave is only slightly shifted in frequency compared with the incident light wave. If eqs(3.1)−(3.5) are solved for the case of backscatter the wavelength shift ($\Delta\lambda$) of the scattered light can be calculated in terms of the plasma conditions [68].

$$\frac{\Delta\lambda}{\lambda_0} = -2(C_s/c)\ \frac{(1-n_e/n_{ec})^{1/2}}{(1+4k_0{}^2\lambda_D{}^2)^{1/2}} \qquad (3.6)$$

$$= \frac{-2.06\times10^{-3}(Z/A)^{1/2}T_e{}^{1/2}[\text{keV}](1-n_e/n_{ec})^{1/2}}{\{1+7.85\times10^{-3}(n_{ec}/n_e-1)T_e[\text{keV}]\}^{1/2}}$$

Where C_s is the ion sound speed, n_e the electron density, n_{ec} the critical electron density and A the mass number of the ions. The important point to note about this expression is that for $\Delta\lambda/\lambda \leqslant 10^{-3}$ and $n_e \leqslant 0.1n_{ec}$, the wavelength shift is very insensitive to the electron density and effectively only depends on the plasma temperature. It follows from the Manley−Rowe relations [69] that S.B.S. can potentially result in nearly all the incident laser light being transferred to the scattered light wave and lost from the plasma, since $\omega_i/\omega_0 \ll 1$.

(3.1.2) Growth rates and thresholds for S.B.S.

There are numerous [61−64] reports of theoretical treatments to determine the growth rates and thresholds for S.B.S.. Here we will only briefly summarize the derivation and results given by Kruer [70]. The growth rate for S.B.S. in a homogeneous plasma can be determined by considering the feedback loop illustrated in fig(3.3). Consider an initial small (thermal level) low frequency density fluctuation (δn) associated with an ion acoustic wave present in the plasma. The incident light wave (E_ϱ) will then create a transverse current ($\delta j \propto \delta n E_\varrho$) oscillating electrons in the presence of these low frequency density fluctuations. This current will then generate an electric field wave (ie. the scattered light wave) with amplitude, $\delta E \propto \delta n E_\varrho$. Finally this electric field beats with the incident light wave to reinforce the initial density fluctuation via the ponderomotive force ($\delta n \propto E_\varrho \delta E$). Hence the ion acoustic and scattered light waves grow at the expense of the incident light wave, as the instability develops. We now obtain expressions describing the coupling mechanisms between the various waves, from which the growth rate for the instability can be calculated.

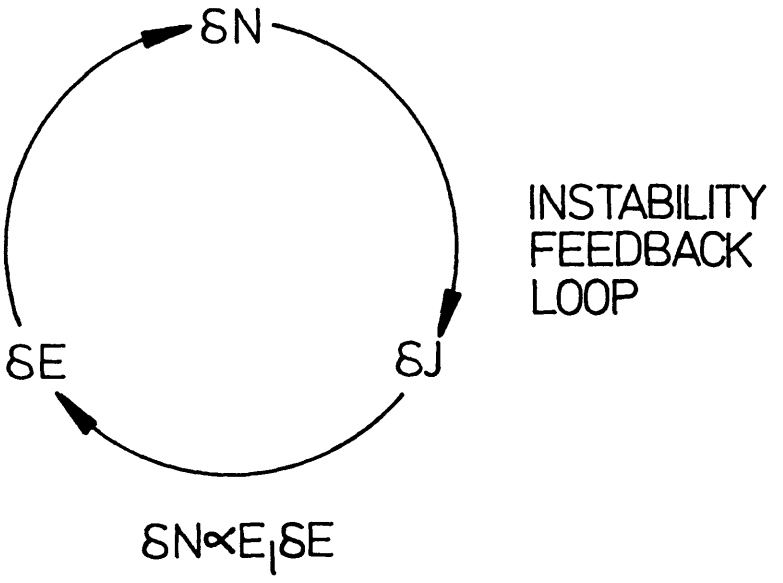


Figure 3.3 Instability feedback loop for stimulated Brillouin scattering.

From Maxwell's equations an expression can be obtained for the propagation of an electromagnetic wave in a plasma.

$$\left[\frac{\partial^2}{\partial t^2} - c^2\nabla^2 + \omega_{pe}^2 \right] \underline{E} = 0 \qquad (3.7)$$

If backscatter is considered, the problem can be reduced to 1−D. Then by splitting the density into a uniform value n_0, plus a low frequency component δn which couples the incident light wave (E_i) to a reflected light wave (E_r), eq(3.7) becomes:

$$\left[\frac{\partial^2}{\partial t^2} - c^2\frac{\partial^2}{\partial x^2} + \omega_{pe}^2 \right]E_r = -\omega_{pe}^2\frac{\delta n}{n_0}E_i \qquad (3.8)$$

The physical interpretation of this equation is that, in the presence of a low frequency density fluctuation the oscillation of electrons in the electric vector of the incident light wave gives rise to a transverse current, which generates the reflected light wave.

We now consider the growth of the density fluctuations due to the two light waves present. By considering a 2−fluid plasma and combining the linearized equations of force for the electrons and ions with the ion continuity equation the following expression is obtained:

$$\left[\frac{\partial^2}{\partial t^2} + \upsilon_i\frac{\partial}{\partial t} - C_s^2\frac{\partial^2}{\partial x^2}\right]\delta n = \frac{Zn_0e^2}{m_em_i\omega_0^2}\frac{\partial^2(E_iE_r)}{\partial x^2} \qquad (3.9)$$

Where υ_i is a damping rate introduced to model Landau damping [10]. The term on the right hand side of the equation is due to the ponderomotive force generated by the fields E_i and E_r beating together. Hence it follows that the physical interpretation of this expression is that the incident and reflected light waves beat together to produce a fluctuation in field intensity, which drives an ion density fluctuation (ie. ion acoustic sound wave) via the ponderomotive force. The dispersion equation governing the instability can be readily obtained by Fourier analysis, and combination of eqs (3.8) and (3.9), which describe the feedback mechanisms. This gives:

$$\omega^2 + i\omega\upsilon_i - k^2C_s^2 = \frac{\omega_{pi}^2k^2v_{os}^2}{4}\left[\frac{1}{D(\omega-\omega_0,k-k_0)} + \frac{1}{D(\omega+\omega_0,k+k_0)} \right] \qquad (3.10)$$

Where $D(k,\omega) = \omega^2 - k^2c^2 - \omega_{pe}^2$, ω_{pi} is the ion plasma frequency and v_{os} is the oscillation velocity of the electrons in the electric field of the laser. For the case of backscatter and densities significantly less than critical (so that $k \triangleq 2k_0$) the unstable root of this equation can be solved, giving the growth rate for S.B.S. as:

$$\gamma = \frac{k_0 v_{os} \omega_{pi}}{2\sqrt{2}(\omega_0 k_0 C_s)^{1/2}} \qquad (3.11)$$

Now if it is assumed that the reflected light wave is collisionally damped (amplitude damping rate γ_L) and that the ion wave undergoes Landau damping (amplitude damping rate $\gamma_i = \upsilon_i/2$), then for the instability to grow it is required that.

$$\gamma > (\gamma_i \gamma_L)^{\frac{1}{2}} \qquad (3.12)$$

Now $\gamma_L = \frac{1}{2}(\omega_{pe}^2/\omega_0^2)\upsilon_{ei}$ where υ_{ei} is the electron–ion collision frequency [10]. Hence the threshold for S.B.S. in a homogeneous plasma becomes:

$$\left[\frac{v_{os}}{v_{th}}\right]^2 \approx 2 \frac{\upsilon_{ei}}{\omega_0} \frac{\upsilon_i}{k_0 C_s} \qquad (3.13)$$

Where v_{th} is the electron thermal velocity. In practice the threshold is generally determined by gradients in the plasma density and expansion velocity rather than by collisional and Landau damping. This is because any gradient in the plasma limits the region over which the waves can resonantly interact. Consequently propagation of wave energy out of this region introduces a loss mechanism which must be overcome. If a density gradient in the direction of propagation (z–axis) is considered then we can define $k(z) = k_i(z) - k_0(z) - k_{sc}(z)$, where at $z=0$, $k=0$ and the waves are resonantly coupled. Away from this region a mismatch develops and we can estimate the size, ℓ_{int}, of this resonant interaction region by the expression:

$$\int_0^{\ell_{int}} k(z)\, dz \approx 0.5 \qquad (3.14)$$

This integral can be solved by use of a Taylor expansion at the point $z=0$, giving $\ell_{int} = 1/\sqrt{k'}$. The effective damping rates for the ion acoustic and scattered light waves are V_{gi}/ℓ_{int} and V_{gsc}/ℓ_{int}, where V_{gi} and V_{gsc} are the respective group velocities of the two waves. Putting these damping rates into eq(3.12) gives the Rosenbluth condition [71] for amplification in an inhomogeneous plasma.

$$\frac{\gamma^2}{|k' V_{gi} V_{gsc}|} > 1 \qquad (3.15)$$

For backscatter in a linear density profile (scalelength L) then $k' = \omega_{pe}^2/c\omega_0 L$. As $V_{gi} \approx C_s$ and $V_{gsc} \approx c$ the threshold becomes:

$$\left[\frac{v_{os}}{v_{th}}\right]^2 \approx \frac{8}{k_0 L} \tag{3.16}$$

A similar approach can be used to calculate the expression for the threshold for S.B.S. in a parabolic density profile (ie. of the form $n_e = n_0(1-x^2/L_1^2)$) [72], which is relevant to the experimental results presented in chapter 6. For a parabolic density profile the threshold is:

$$\left[\frac{v_{os}}{v_{th}}\right]^2 \approx \frac{6}{k_0^{2/3} L_1^{4/3}} \left[\frac{c}{\omega_{pe}}\right]^{2/3} \tag{3.17}$$

(3.1.3) Stimulated Raman Scattering

S.R.S. involves the conversion of an incident light wave ($_0$) into a lower frequency scattered light wave (sc) and an electron plasma wave (e). Energy and momentum conversion require that the following conditions are met.

$$\omega_0 = \omega_{sc} + \omega_e \tag{3.18}$$

$$\underline{k}_0 = \underline{k}_{sc} + \underline{k}_e \tag{3.19}$$

The dispersion relationships for each wave require also that:

$$k_0^2 c^2 = \omega_0^2 - \omega_{pe}^2 \tag{3.20}$$

$$k_{sc}^2 c^2 = \omega_{sc}^2 - \omega_{pe}^2 \tag{3.21}$$

$$k_e^2 v_{th}^2 = (\omega_e^2 - \omega_{pe}^2)/3 \tag{3.22}$$

These matching conditions are illustrated in fig(3.4) for the case of backscatter. For the instability to occur, it is required that both the scattered light wave and the electron plasma wave can propagate, ie. $\omega_{sc} \geqslant \omega_{pe}$ and $\omega_e \geqslant \omega_{pe}$. Hence it follows that $\omega_0/2 \geqslant \omega_{pe}$ and therefore S.R.S. can only occur at densities less than $n_{ec}/4$. Consequently the scattered light wave will have a wavelength in the range $\lambda_0 < \lambda_{sc} < 2\lambda_0$. By solving eqs(3.18)−(3.22) the dependence of the scattered

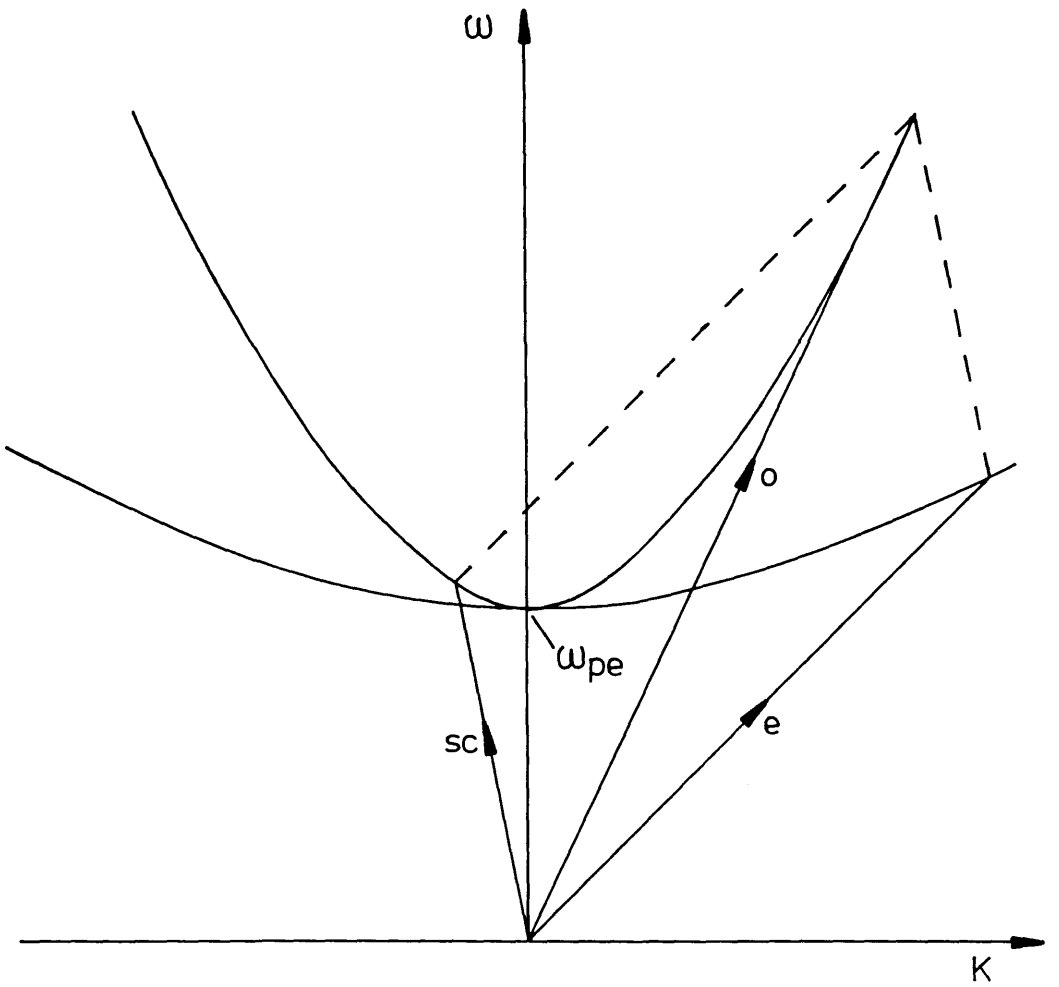


Figure 3.4 Matching conditions for backward stimulated Raman scattering.

wavelength on the plasma conditions can be determined [73]. For the case of backscatter this gives:

$$\lambda_{sc} = \frac{\lambda_0}{1-(\omega_{pe}/\omega_0)(1+3k_e{}^2\lambda_D{}^2)^{1/2}} \tag{3.23}$$

where

$$\frac{k_e}{k_0} = \frac{1 + \left[\frac{1-2\sqrt{N}}{1-N}\right]^{1/2}\left[1 - \frac{3}{2}\left[\frac{v_{th}}{c}\right]\frac{(2-\sqrt{N})(1-\sqrt{N})}{(1-2\sqrt{N})}\right]}{1 + 3\left[\frac{v_{th}}{c}\right]^2\left[\frac{1}{\sqrt{N}} - 1\right]}$$

and $N = n_e/n_{ec}$

The variation of the backscatter wavelength with plasma conditions for a low density plasma is shown in fig(3.5). It can be seen that for low temperatures

($T_e \lesssim 500$ eV) the wavelength of the scattered light is mainly a function of the plasma density. The regimes indicated with a dotted line correspond to the situation where $k_e\lambda_D > 0.4$ and heavy Landau damping of the electron plasma wave is expected, which will suppress the instability [10,73]. Since the plasma frequency (and hence the frequency of an electron plasma wave) is much greater than the frequency of an ion acoustic wave, it follows from the Manley–Rowe relations that S.R.S. will be less effective than S.B.S. at scattering light from a plasma. However S.R.S. is potentially still extremely damaging to I.C.F., as hot electrons which would preheat the fuel pellet, can be produced from the damping of the electron plasma wave generated [51].

(3.1.4) Growth rates and thresholds for S.R.S.

The feedback mechanism for S.R.S. to grow is similar to that for S.B.S.. The incident light wave generates a current by oscillating electrons in a plasma with a high frequency density fluctuation associated with an electron plasma wave. This current then generates a scattered light wave, which beats together with the electric field of the incident laser light to enhance the initial electron density fluctuation via the ponderomotive force. In a similar manner to the case for S.B.S. already discussed expressions can be determined describing these feedback mechanisms. Combining these equations together yields the dispersion relation for the instability from which the growth rate γ can be calculated [74].

$$\gamma = \frac{k_e v_{os}}{4}\left[\frac{\omega_{pe}}{\omega_0-\omega_{pe}}\right]^{1/2} \qquad (3.24)$$

Where k_e can be calculated from eq(3.23). For a homogeneous plasma the threshold for S.R.S. is determined by collisional damping of the scattered light wave and Landau damping of the electron plasma wave. For densities, $n_e \ll n_{ec}/4$ this gives the threshold as:

$$\left[\frac{v_{os}}{c}\right]^2 = 2\left[\frac{\omega_{pe}}{\omega_0}\right]^2 \frac{\gamma_e}{\omega_{pe}} \frac{\upsilon_{ei}}{\omega_0} \qquad (3.25)$$

Where γ_e is the Landau damping rate for the electron plasma wave. In practice, like S.B.S., a density gradient usually introduces a more stringent threshold condition than eq(3.25). By taking the same approach as described earlier for S.B.S. the following thresholds can be calculated for the case of a linear density

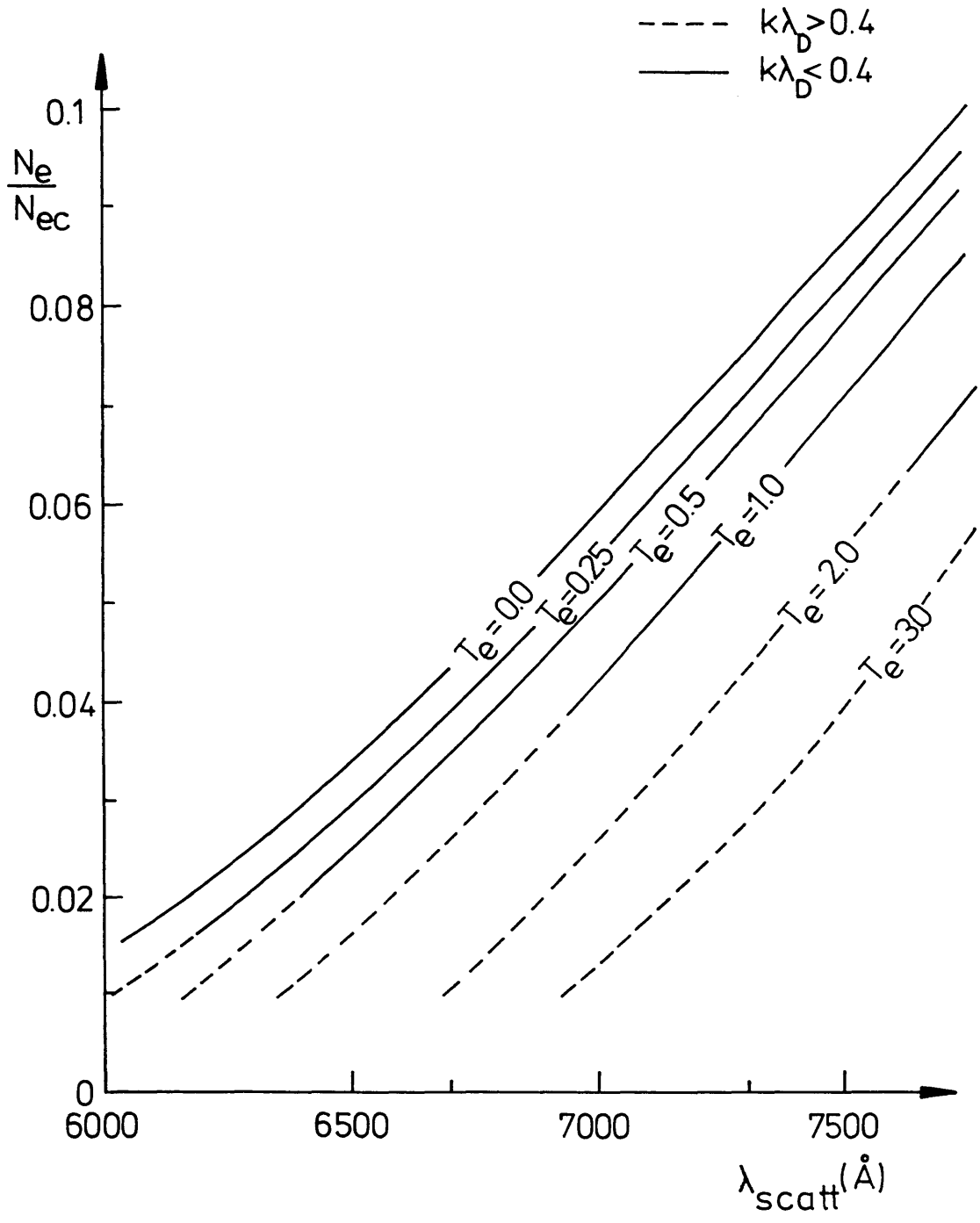


Figure 3.5 Variation of backscatter wavelength with plasma conditions for stimulated Raman scattering (λ_0 = 526 nm).

profile (eq(3.26)) and a parabolic density profile (eq(3.27)) [72].

$$\left[\frac{v_{os}}{c}\right]^2 \approx \frac{2}{k_0 L} \tag{3.26}$$

$$\left[\frac{v_{os}}{c}\right]^2 \approx \frac{3.6}{k_0^{2/3} L_1^{4/3}} \left[\frac{v_{th}}{\omega_{pe}}\right]^{2/3} \tag{3.27}$$

Finally it is worth noting that at a density of $n_e = n_{ec}/4$, S.R.S. can become an absolute rather than a convective instability (ie. temporally rather than spatially growing). It has also been suggested that S.R.S. can become absolute at density maxima and minima in laser produced plasmas [57].

(3.2) Filamentation

The filamentation instability causes perturbations in the intensity profile of an incident laser beam to grow in amplitude, resulting in the break up of the beam into intense filaments. The feedback mechanism for this process is either the ponderomotive force or thermal expansion. The case of ponderomotive filamentation [75,76] is illustrated in fig(3.6). If a laser beam incident on a plasma is more intense in one region (ie. a hot spot), then a ponderomotive force exists which pushes electrons out of the region of highest laser intensity causing a local depletion in the electron density. This results in the refractive index being increased locally in this region (since $\mu = (1 - n_e/n_{ec})^{1/2}$). The phase velocity of the incident light is then reduced in the density depression and consequently the region acts like a 'lens' and focuses down the initial hot spot, increasing its intensity. Hence the initial intensity perturbation is enhanced allowing the process to grow further. Thermal filamentation or self-focusing [77] is similar to this except that the density depression is created by enhanced collisional absorption and subsequent thermal expansion in the the region of the intensity hot spot. Both these processes can potentially result in the break up of an incident laser beam into intense filaments whose irradiance is many times higher than the average beam irradiance. Whole beam self-focusing is the analogous process to filamentation where the whole beam acts as the intensity perturbation and focuses down. Like S.R.S. and S.B.S., filamentation becomes more effective in large, underdense, long scalelength plasmas where the plasma size is much larger than the instability growth length.

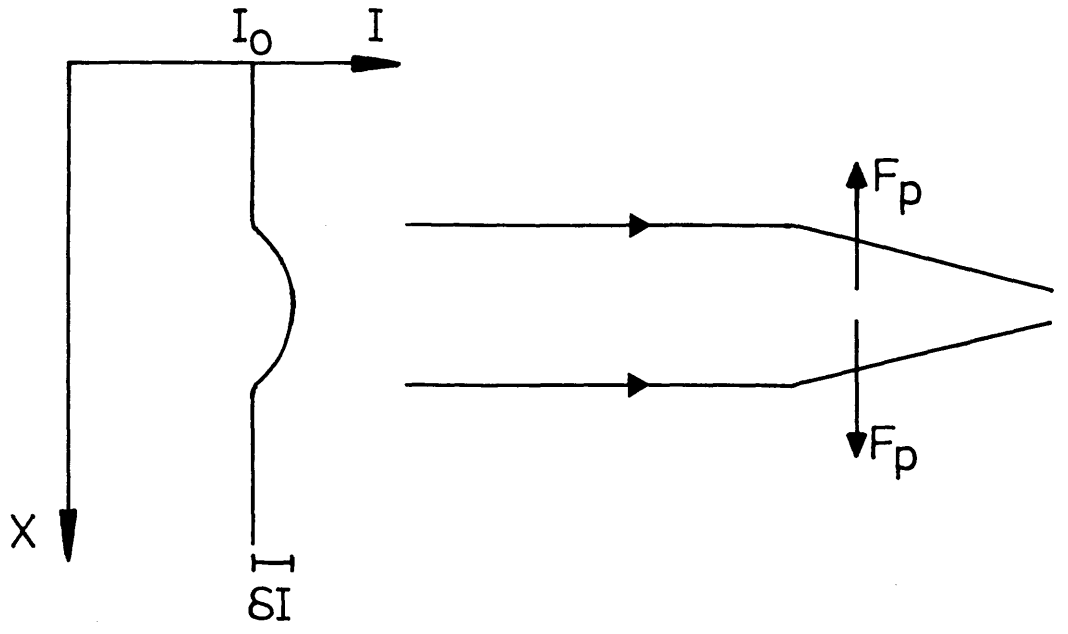


Figure 3.6 Schematic of ponderomotive filamentation.

The filamentation instability presents a potentially serious threat to the achievement of successful laser fusion implosions. The break up of the incident laser beam due to filamentation and self−focusing would result in non−uniform absorption of energy into a fusion target. This would seriously degrade the implosion. It has been estimated [7] that an irradiation uniformity of ±4% is required to successfully drive an implosion and clearly any filamentation occurring in the large underdense plasma surrounding the fuel pellet will make this impossible to achieve. Also filamentation may result in the enhancement of other undesirable processes, such as S.R.S. and S.B.S., by the higher irradiances present in individual filaments.

(3.2.1) Growth rates for filamentation

A simple model has been developed by Kruer [78] to predict the scalelength of the intensity perturbations which will be unstable to ponderomotive or thermal filamentation. The results of this model will be presented here.

For ponderomotive filamentation the dispersion relationship describing the instability is found to be

$$4k_i^2k_0^2 + k_r^4 - k_r^2\frac{\omega_{pe}^2}{c^2}\frac{v_{os}^2}{2v_{th}^2} = 0 \qquad (3.28)$$

Where k_r is the wavenumber of the initial intensity perturbation (ie. wavelength of perturbation = $2\pi/k_r$) and k_i is the growth rate for the instability. The maximum growth rate will occur for $\partial k_i/\partial k_r = 0$, when

$$k_r = \frac{1}{2}\left[\frac{v_{os}}{v_{th}}\right]\frac{\omega_{pe}}{c} \tag{3.29}$$

and

$$k_i = \frac{1}{8}\left[\frac{v_{os}}{v_{th}}\right]^2\frac{\omega_{pe}^2}{k_0 c^2} \tag{3.30}$$

For thermal filamentation the dispersion relation becomes:

$$4k_i^2k_0^2 + k_r^4 - \frac{v_{os}^2}{14v_{th}^2}\frac{\omega_{pe}^2}{c^2\lambda_{ei}^2} = 0 \tag{3.31}$$

Where λ_{ei} is the electron–ion mean free path. The growth rate is now a maximum for large scalelengths so that

$$k_r \ll \left[\frac{\omega_{pe}}{3.6c}\frac{v_{os}}{v_{th}}\frac{1}{\lambda_{ei}}\right]^{1/2} \tag{3.32}$$

when the growth rate becomes

$$k_i = \frac{\omega_{pe}}{7.5k_0c}\left[\frac{v_{os}}{v_{th}}\right]\frac{1}{\lambda_{ei}} \tag{2.33}$$

These results are consistent with other estimates for filamentation growth rates [75–77]. It can be seen that the maximum growth rate for thermal filamentation exceeds that for ponderomotive filamentation when $(c/v_{os})(\upsilon_{ei}/\omega_{pe}) > 1$. Therefore thermal filamentation would be expected to dominate in denser, more collisional plasmas. As an illustrative example consider typical experimental conditions of 0.53 μm laser light in a low density ($n_e = 0.1n_{ec}$) aluminium plasma at a temperature of 500 eV. For an irradiance of 1×10^{15} Wcm^{-2} and Z=13 this gives a minimum growth length of 30 μm for a perturbation wavelength of 7 μm for ponderomotive filamentation. For thermal filamentation any perturbation wavelength significantly greater than 10 μm will be unstable to self–focusing with a growth length of 50 μm. Hence filamentation can be expected to be active in such a plasma if it is of a reasonable size (ie > 100 μm). In general ponderomotive filamentation will be more effective for short wavelength

perturbations whilst thermal self−focusing will dominate for large wavelengths.

For small wavelength perturbations where $2\pi/k_r \approx \lambda_0$ diffraction effects will become important [79]. These will tend to increase the size of the intensity perturbation and thereby oppose the filamentation process. Hence diffraction places an ultimate limit on the minimum size to which a filament can focus down.

(3.2.2) Time scales for filamentation

The time scale for ponderomotive filamentation is determined by the ion acoustic transit time across the filament r_0/C_s (where r_0 is the filament radius). For the conditions in the example in section (3.2.1) this gives a typical time scale of 30 ps for a filament with radius $r_0 = 5$ μm. For thermal self−focusing, the growth time is determined by the larger of the ion acoustic transit time across the filament or the thermal conduction transit time, $n_e r_0^2/\kappa$ (where κ is the electron thermal conductivity). The ion acoustic transit time will be larger for [80]:

$$\frac{1.35\times10^{-5}(n_e/n_{ec})r_0(\mu m)\log\Lambda}{[T_e(keV)]^2[\lambda_0(\mu m)]^2}\,\frac{Z(1+0.24Z)(Z+1)^{\frac{1}{2}}}{(Z+0.24)A^{\frac{1}{2}}} < 1 \qquad (3.34)$$

Where $\log\Lambda$ is the Coulomb logarithm. In general the ion acoustic transit time will be longer except for cool, short wavelength plasmas with large filaments.

CHAPTER 4

EXPERIMENTAL ARRANGEMENT FOR STUDY OF INSTABILITIES IN A LARGE UNDERDENSE PLASMA

(4.1) Introduction

Proposed laser fusion targets will be surrounded by large, underdense, long scalelength coronal plasmas. Under these conditions it follows from the results of chapter 3 that S.R.S., S.B.S. and filamentation should become particularly effective, due to the large density scalelengths present. Until now experimental results on these instabilities have been largely restricted to short scalelength plasmas [52,53,55,59]. This is due to the limited energy output of present day lasers. Clearly it is desirable to experimentally determine the behaviour of these instabilities in a long scalelength plasma before the next generation of high power lasers ($\geq$1MJ), suitable for driving I.C.F. implosions are built. Consequently an experimental arrangement has been developed at R.A.L. [81] to generate long, approximately cylindrical plasmas. This makes it possible to simulate the case of an intense laser beam interacting with a small section of a large coronal plasma generated by a Megajoule laser, as illustrated in fig(4.1).

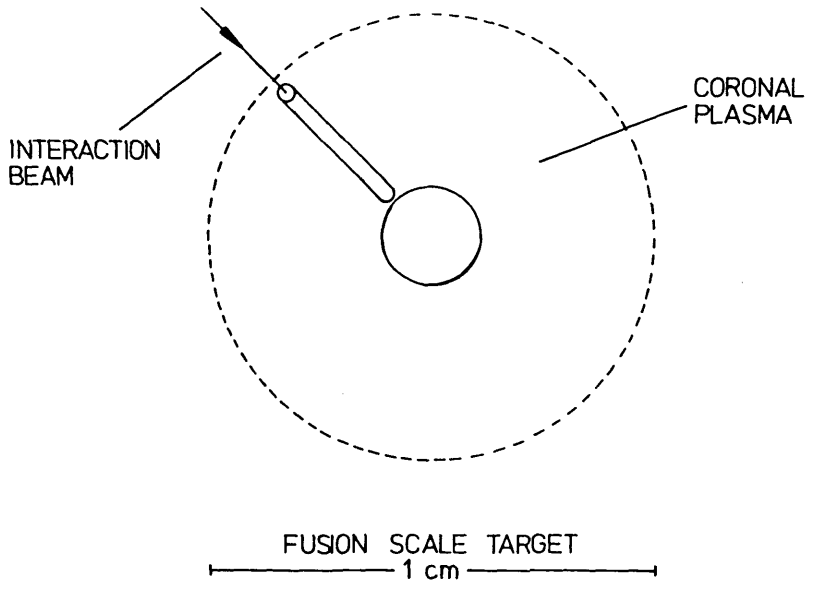


Figure 4.1 The use of a Kilojoule laser to simulate the coronal plasma which would be generated by a Megajoule laser.

In this chapter the experimental arrangement used to produce the large underdense plasma will be described. Also detailed descriptions of the diagnostics used to study the instabilities occurring under such conditions will be given. Details of the experimental arrangement used to generate the large underdense plasma are described in section (4.2). The detailed target design required to generate the desired plasma conditions is discussed in section (4.3). Section (4.4) describes the diagnostics used to study the S.R.S., S.B.S. and filamentation instabilities occurring in the experiment.

(4.2) Experimental Arrangement

The large underdense plasmas were generated by irradiating thin foil stripe targets by four frequency doubled ($\lambda = 0.53$ μm) beams of the VULCAN glass laser. The beams were focused onto target in two opposing pairs by a line focus geometry. The line focus for each beam was generated by an off axis spherical mirror, as illustrated in fig(4.2). The mirror can be considered as part of a spherical surface centered at C with an optical axis along the line CP. An object at the point P will be imaged by the spherical surface to a line focus at Q (lying along the optical axis). This is due to the spherical abberation of the mirror [82]. The length of the line focus (L) is approximately given by the expression [83]

$$L/D \approx 1.4 \times 10^{-4} \theta^2 \qquad (4.1)$$

Where D is the illuminated length on the mirror surface and θ is the tilt angle of the mirror. The point source for each beam at P is generated by a f/2.5 aspheric doublet lens. This scheme generates a high quality line focus, and since the optical components all lie off axis, it has the advantage that many individual beams can be overlapped onto the final line focus formed. The overall arrangement is shown in fig(4.3) for two of the opposing line focus beams. Another major advantage of this arrangement is that the length of the line focus can easily be changed by varying the tilt angle of the mirror. This scheme was originally developed to produce line foci 7mm long for x−ray laser experiments. For the long scalelength plasma experiments described here a shorter line focus was required and so the tilt angle of the mirror was reduced to 13.0°. This gave a line focus approximately 2.4 mm long. The far field width of the line focus is given by $w = \beta R(A/D)$ where A is the original beam diameter and β is the laser beam divergence. Taking $\beta \approx 100$ μRad, R= 25 cm and A≈D this gives a width of 25 μm. To generate the large underdense plasmas required for these instability

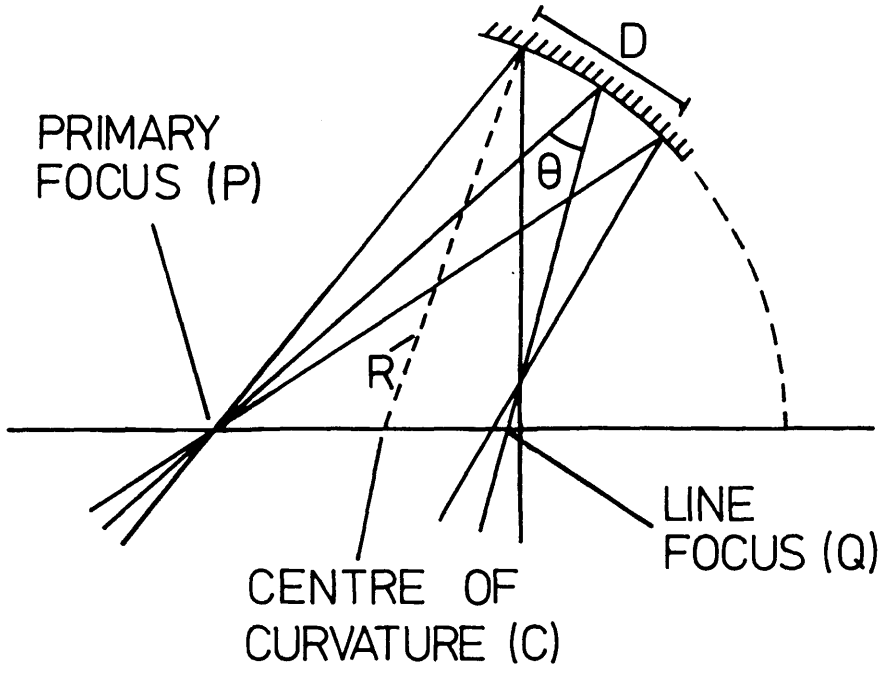


Figure 4.2 Principle of line focus generation.

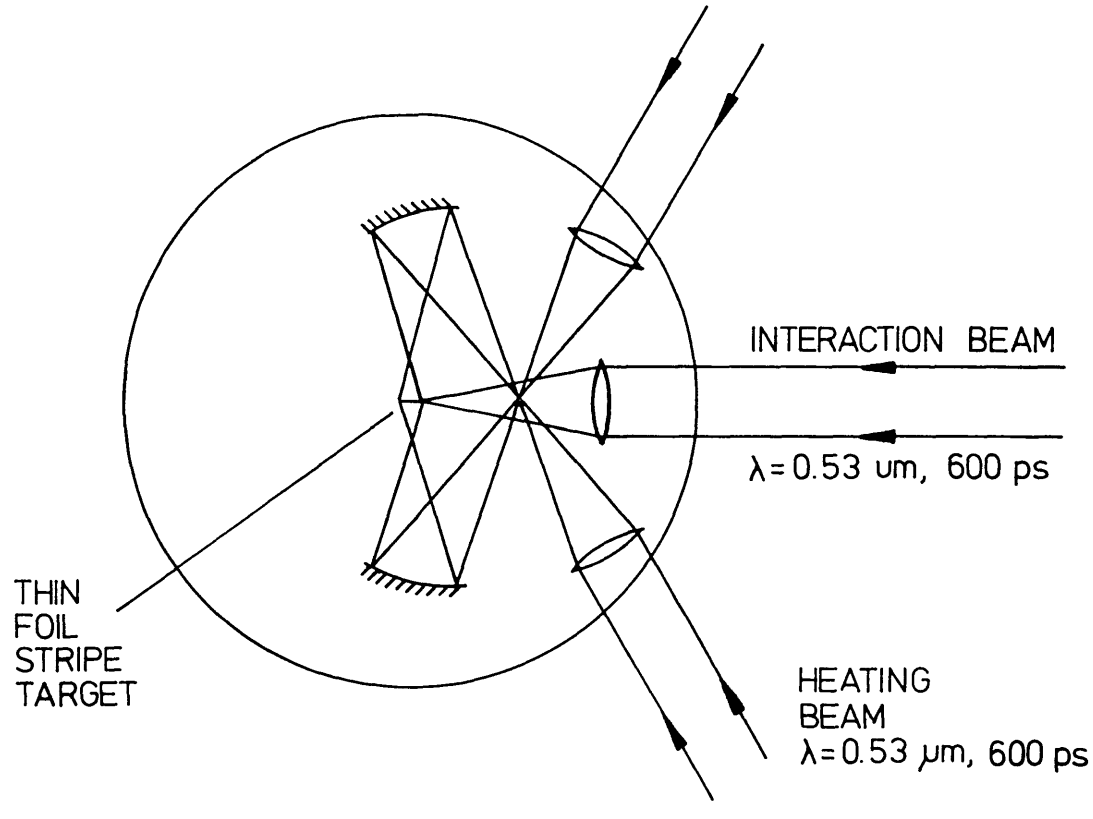


Figure 4.3 Experimental arrangement for generating a large underdense preformed plasma.

experiments a line focus approximately 300 μm wide was required, consequently it was necessary to work in the quasi−near field of each of the four heating beams.

The four line focus beams were superimposed onto the target resulting in a typical irradiance of 10^{14} Wcm^{-2} in a 600 ps laser pulse. The targets consisted of thin metal (normally aluminium) stripes supported on a 100 nm formvar substrate, see fig(4.4). The metal stripes were typically 300 μm wide and 0.8 mm long. A delayed second harmonic, 600 ps F.W.H.M., laser beam was then interacted axially with the preformed plasma generated, as shown in fig(4.3). Consequently the delayed beam interacts with the plasma over a distance of about 800 μm along which the plasma temperature and density are approximately constant. The interaction beam was focused into the preformed plasma with either a f/2.5 aspheric doublet lens or a f/10 aspheric singlet lens. Typically the interaction beam irradiance was 10^{15} Wcm^{-2}. By varying either the thickness of the target stripe or the interaction beam delay it was possible to vary the plasma conditions. This will be discussed in more detail in section (4.3). Typically the interaction beam delay was in the range 1−4 ns.

(4.3) Target design

In order to estimate the thickness of the target foils, and the interaction beam delay which should be used to produce particular plasma conditions the model of Rosen and London was used [84]. This simple 1−D model is based on an isothermal, homogeneous expansion similarity solution of the ideal hydrodynamic equations. The model predicts the conditions in the foil plasma (eg. density and temperature) at a particular time, given the experimental parameters (eg. laser intensity, laser duration, target thickness and target composition). The model assumes irradiation of the foil from both sides. After the end of the laser pulse the plasma will expand adiabatically and the model predicts that the plasma temperature (T), density (N_e), and scalelength (L) vary with time (t) according to the following relationships

$$N_e(cm^{-3}) = \frac{5.46\times10^{20}Z^{5/8}\left[\frac{m}{10^{-4}gcm^{-2}}\right]^{7/6}}{A^{17/24}\Lambda^{1/12}\left[\frac{I}{10^{14}Wcm^{-2}}\right]^{1/3}\left[\frac{\lambda}{\mu m}\right]^{1/6}\left[\frac{t_l}{ns}\right]^{1/4}\left[\frac{t}{ns}\right]} \qquad (4.2)$$

$$T(keV) = T_{trans}\left[\frac{t}{t_l}\right]^{-2/3} \qquad (4.3)$$

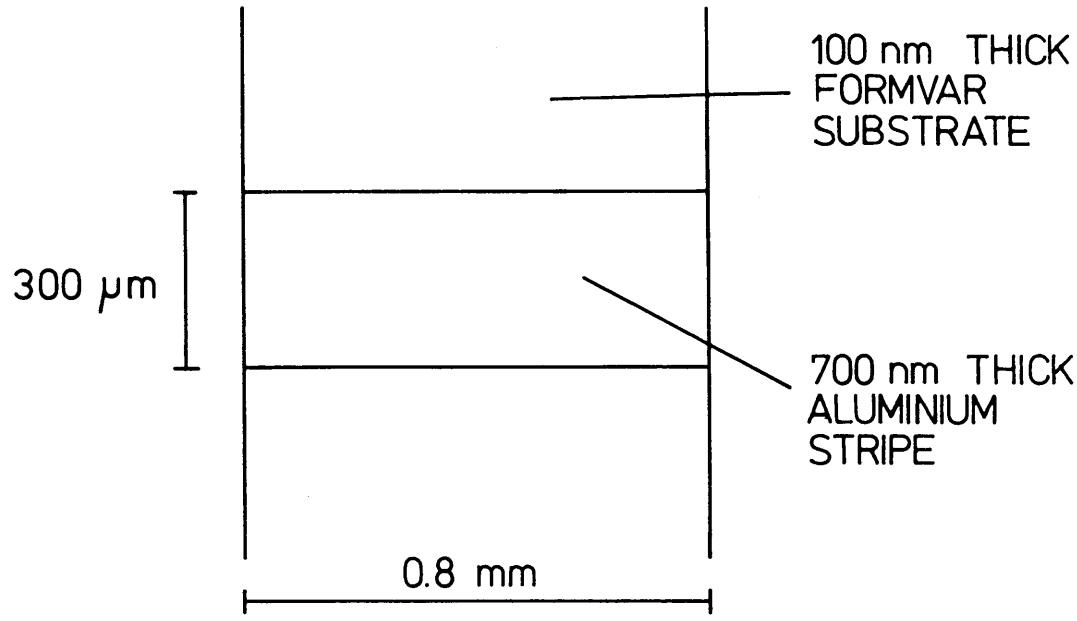


Figure 4.4 Target design.

Where

$$T_{trans}(keV) = \frac{0.645Z^{1/2}\Lambda^{1/3}\left[\frac{I}{10^{14}Wcm^{-2}}\right]^{1/3}\left[\frac{\lambda}{\mu m}\right]^{2/3}\left[\frac{m}{10^{-4}gcm^{-2}}\right]^{1/3}}{A^{1/6}}$$

$$L(cm) = \frac{4.38\times10^{-2}Z^{3/8}\Lambda^{1/12}\left[\frac{I}{10^{14}Wcm^{-2}}\right]^{1/3}\left[\frac{\lambda}{\mu m}\right]^{1/6}\left[\frac{t_l}{ns}\right]^{1/4}\left[\frac{t}{ns}\right]}{A^{7/24}\left[\frac{m}{10^{-4}gcm^{-2}}\right]^{1/6}} \quad (4.4)$$

Where t_l is the duration of the laser pulse, Z is the ion charge, A is the atomic mass of the element present, m is the foil column density, Λ is the Coulomb logarithm, I is the laser irradiance and λ is the laser wavelength. The main requirement regarding the target design is that the foil becomes transparent to the laser beams, when they burn through the target, before the end of the laser pulse. This ensures that the preformed plasma produced is completely underdense and that no solid target material remains. However it is also desirable for the laser beams to burn through the foil as late as possible in the laser pulse in order to maximize the plasma temperature. The model predicts that the foil becomes transparent to the laser beams at a time, t_{trans}, given by

$$t_{trans}(ns) = \frac{0.186 Z^{3/2} \Lambda^{1/3} \left[\frac{\lambda}{\mu m}\right]^{2/3} \left[\frac{m}{10^{-4} g cm^{-2}}\right]^{4/3}}{A^{7/6} \left[\frac{I}{10^{14} W cm^{-2}}\right]^{2/3}} \qquad (4.5)$$

Typically during routine operation the VULCAN glass laser can be expected to produce about 80J of green energy on target per beam. For the line focus arrangement used here this corresponds to a total irradiance of approximately 7.5×10^{13} Wcm^{-2} for all four beams. Hence using eq(4.5) a maximum target thickness can be estimated through which the laser beams will burn through. For a 600 ps duration laser pulse and an aluminium target, the maximum target thickness is found to be 700 nm. Consequently targets of this thickness were used in the actual experiment.

From eqs(4.2) and (4.3) the variation of plasma density and temperature with time after the end of the laser pulse can now be estimated. The results for an aluminium foil 700 nm thick are shown in fig(4.5) and fig(4.6), for the density and temperature respectively. In the actual experiment the interaction beam delay was 1.7 ns and this gives an electron density of 11% of critical and a temperature of 860 eV. This is a reasonable approximation to the plasma conditions which may be expected in the outer coronal plasma of a laser fusion target. It should be stressed that the model used here is only one dimensional and that in reality the plasma expansion will be two dimensional, particularly at late times (ie $t \gg t_l$). The actual plasma is likely to cool more rapidly than predicted by the model due to this two dimensional expansion. However for the purposes of initial target design this model was found to be adequate.

(4.4) Diagnostics

The overall experimental arrangement used, including diagnostics, is shown in fig(4.7). Shown in the centre of the diagram is the target chamber containing the target with its axis in the vertical direction of the page. Two of the line focus heating beams are shown. The interaction beam was directed into the preformed plasma as shown. The diagnostics used include time resolved measurements of the transmitted interaction beam to look for filamentary break up of the beam, time resolved measurements of the S.R.S. and S.B.S. backscatter spectra, quantitative measurements of the levels of S.R.S. and S.B.S. backscatter and characterization of the incident interaction beam profile by an equivalent plane monitor. These

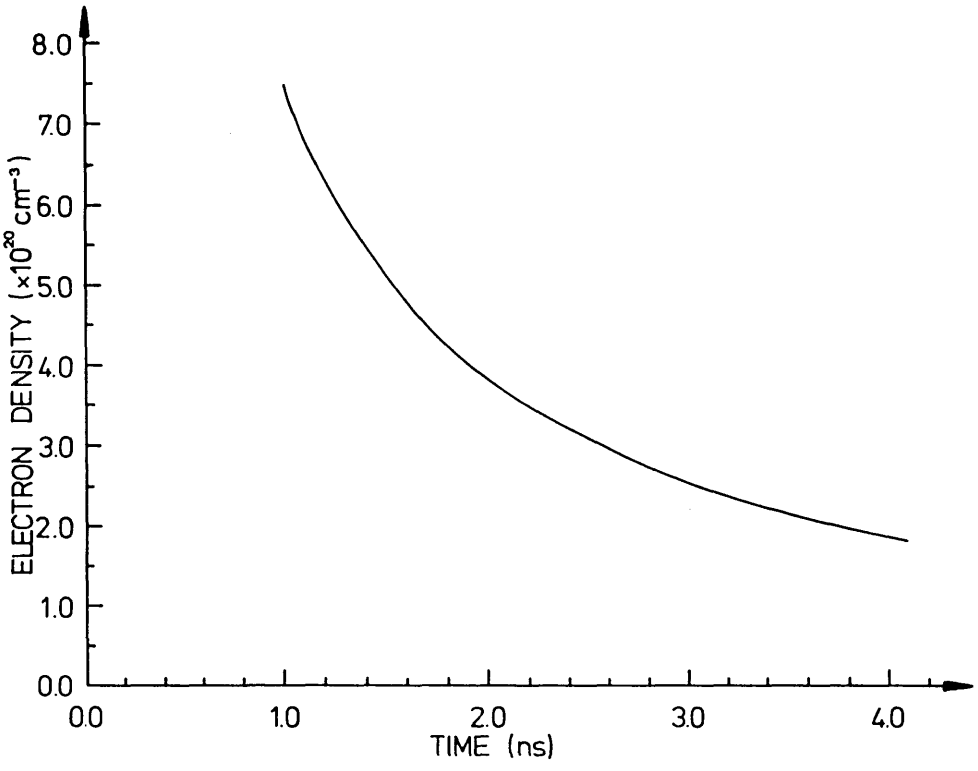


Figure 4.5 Prediction of the Rosen and London model for the variation of density with time (700 nm thick aluminium stripe, irradiance = 7.5×10¹³ Wcm⁻²).

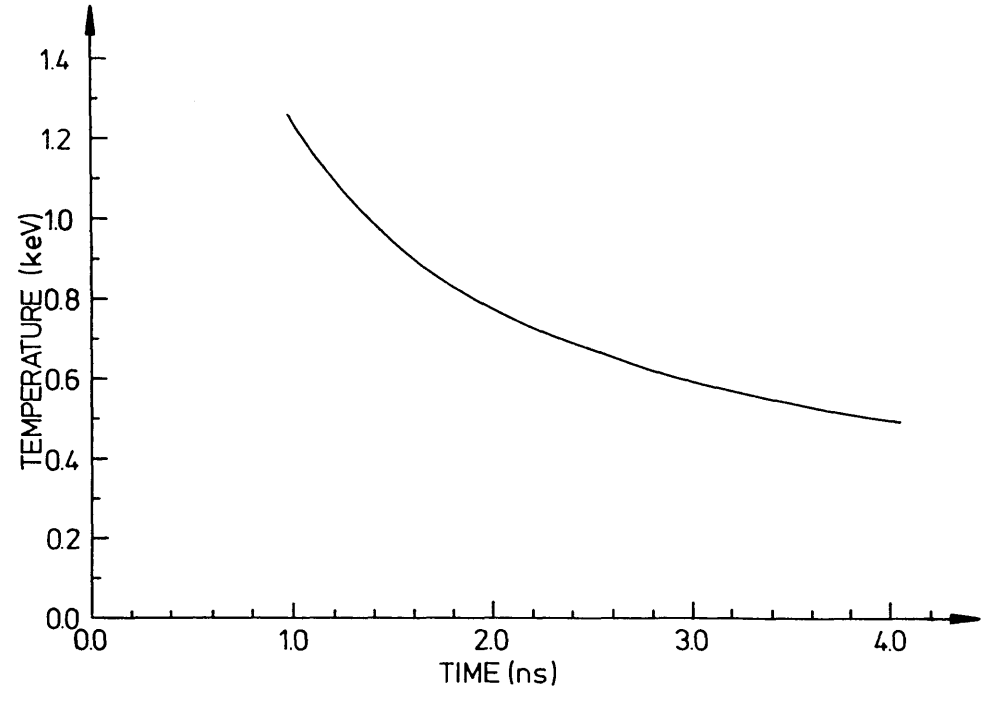


Figure 4.6 Prediction of the Rosen and London model for the variation of temperature with time.

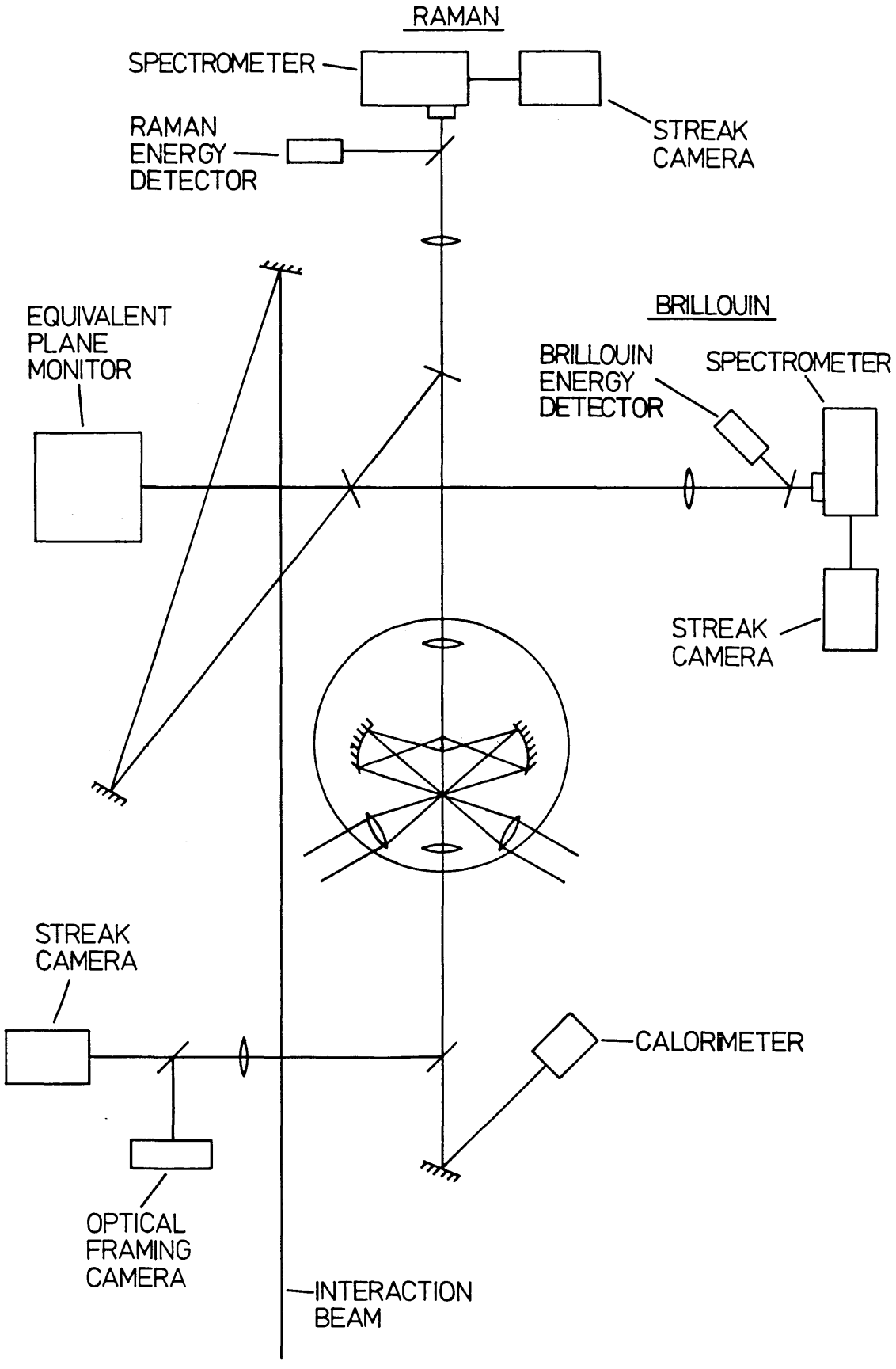


Figure 4.7 Overall experimental arrangement.

diagnostics will now be discussed individually.

(4.4.1) Measurements of the transmitted interaction beam

Time resolved measurements were made of the spatial profile of the transmitted interaction beam after it had propagated through the preformed plasma. This was done to measure any break up of the beam due to filamentation. The transmitted interaction beam was imaged out from the exit plane of the preformed plasma with an f/2.5 aspheric doublet lens. A small fraction (approx. 4%) of the beam was then split off with a BK7 glass blank. This fraction of the transmitted beam was then relayed with a f/2 doublet lens onto the input slit of a Hadland 675 optical streak camera. A further fraction of the transmitted beam was split off with a 50:50 quartz beam splitter onto an optical framing camera. The framing camera was positioned so that its input was in the equivalent image plane to that of the streak camera slit. The optical framing camera takes a single 2−D image with a duration of 120 ps, it will be described in more detail in section (4.4.2). By taking a series of images with the framing camera at different times during the interaction beam pulse from a series of similar laser shots, it was possible to see how the whole 2−D beam profile developed with time. The optical streak camera was used to simultaneously study the evolution with time of a particular cross−section across the interaction beam profile on a single laser shot. The overall magnification of the imaging optics used was ×50. The spatial resolution for both the streak camera and the optical framing camera was approximately 3.5 μm in the target plane. The temporal resolution of the streak camera was 5 ps. High quality neutral density filters were placed in front of the relay lens to avoid damage to the remaining optics in the system by the focused down transmitted beam. Further filters were placed directly in front of the streak camera and optical framing camera in order to obtain a reasonable exposure on film for the outputs of each device, and also to eliminate any stray light.

The remaining transmitted interaction beam not split off by the original glass plate, was directed into a calibrated calorimeter. This was done to measure the fraction of the interaction beam absorbed by the preformed plasma. Several full laser shots were taken without a preformed plasma present in order to cross calibrate this calorimeter to the calorimeter measuring the original interaction beam energy. This allowed measurements made with the transmitted beam calorimeter to be corrected for losses due to the optics in the interaction beam path.

(4.4.2) Optical framing camera

In this section the basic design and construction of the optical framing camera or G.O.I. (gated optical imager) used to study filamentation will be discussed. This device was built and initially tested by the author.

The G.O.I. [85] is a microchannel plate itensified single frame camera with a shortest gate time of 120 ps F.W.H.M. over a full 18 mm diameter cathode aperture. The spatial resolution of the device is typically 10 lp mm^{-1} and it has a temporal jitter of less than 50 ps if triggered from a reliable source. A diagram of the construction of the device is shown in fig(4.8). The incident light signal is coupled by the input fibre optic onto the photocathode of the intensifier tube. The intensifier wafer tube has a S25 photocathode, giving a spectral response in the range 350−900 nm. The intensifier is gated on and off by the indirect application of a high voltage ultrashort electrical pulse to the photocathode. The intensifier tube has a P20 output phosphor which is coupled by a fibre optic to a standard 612 Polariod camera back.

The electrical connections to the intensifier tube are shown in fig(4.9). The intensifier is biased off by means of a small positive potential applied to the photocathode with respect to the microchannel plate input. To gate the camera on a short duration, negative pulse is applied to the photocathode making it −ve with respect to the microchannel plate input. This causes photoelectrons emitted from the photocathode to be accelerated towards the microchannel plate. The microchannel plate consists of a large number of small channels approximately 50 μm in diameter. The inside surface of each channel is coated with a resistive material. Photoelectrons colliding with this material result in the emission of secondary electrons thus producing an overall gain of the signal. The gain of the microchannel plate can be varied by changing the voltage potential between its input and output. The electrons leaving the miocrochannel plate then collide with the earthed phosphor resulting in the emission of photons, and the consequent generation of an optical image which can be recorded on film. The intensifier relies on proximity focusing of the electrons between its various stages. Consequently the photocathode−microchannel plate in, and the microchannel plate out−phosphor distances must be small. The spread of electron transit times between the photocathode and the microchannel plate input provides the ultimate limit as to how fast the intensifier can usefully be gated on and off. This distance is about 250 μm and the acceleration voltage between the photocathode and the microchannel plate, for the device to be biased on, is typically 100 volts. This

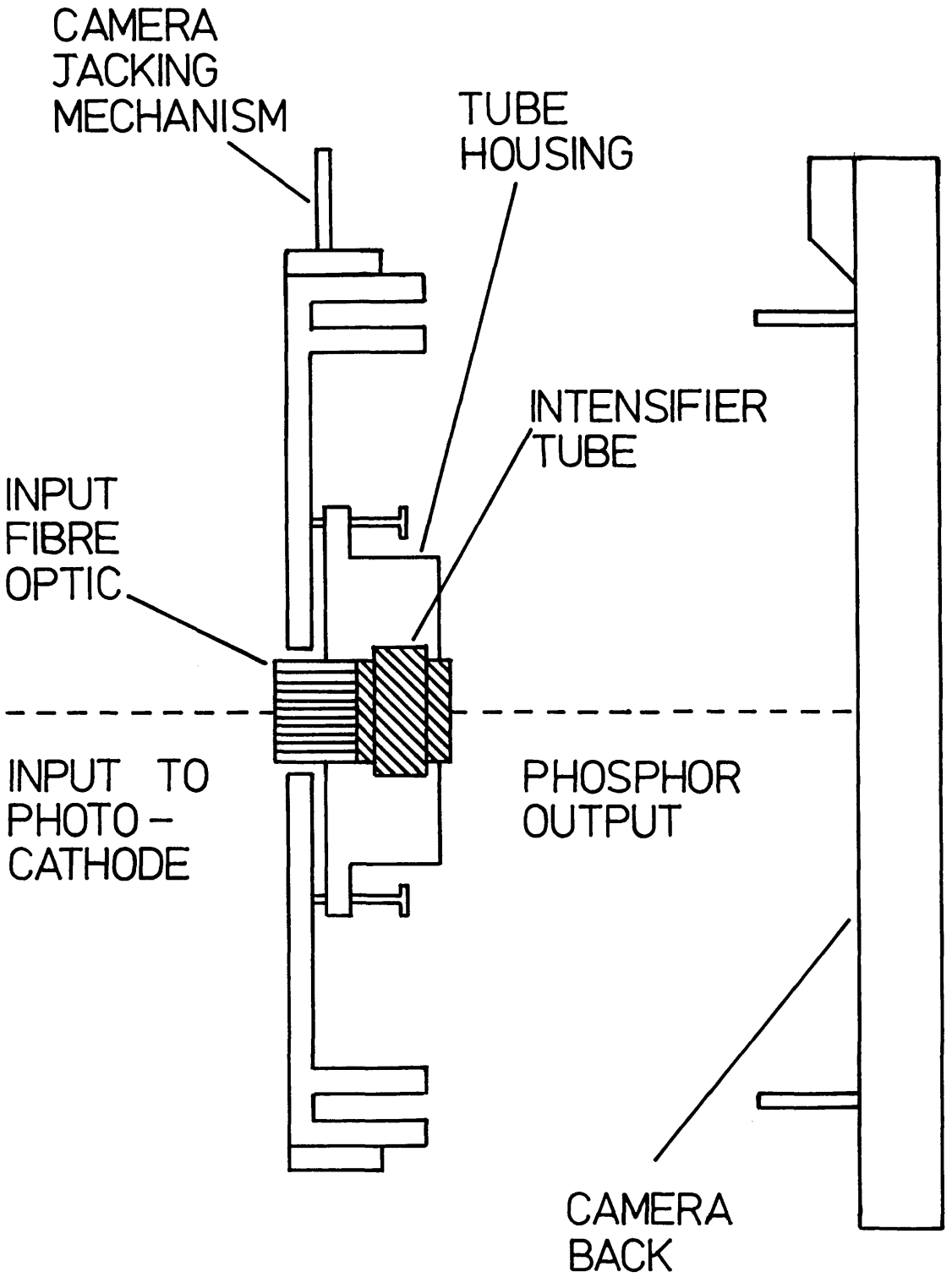


Figure 4.8 Mechanical design of optical framing camera.

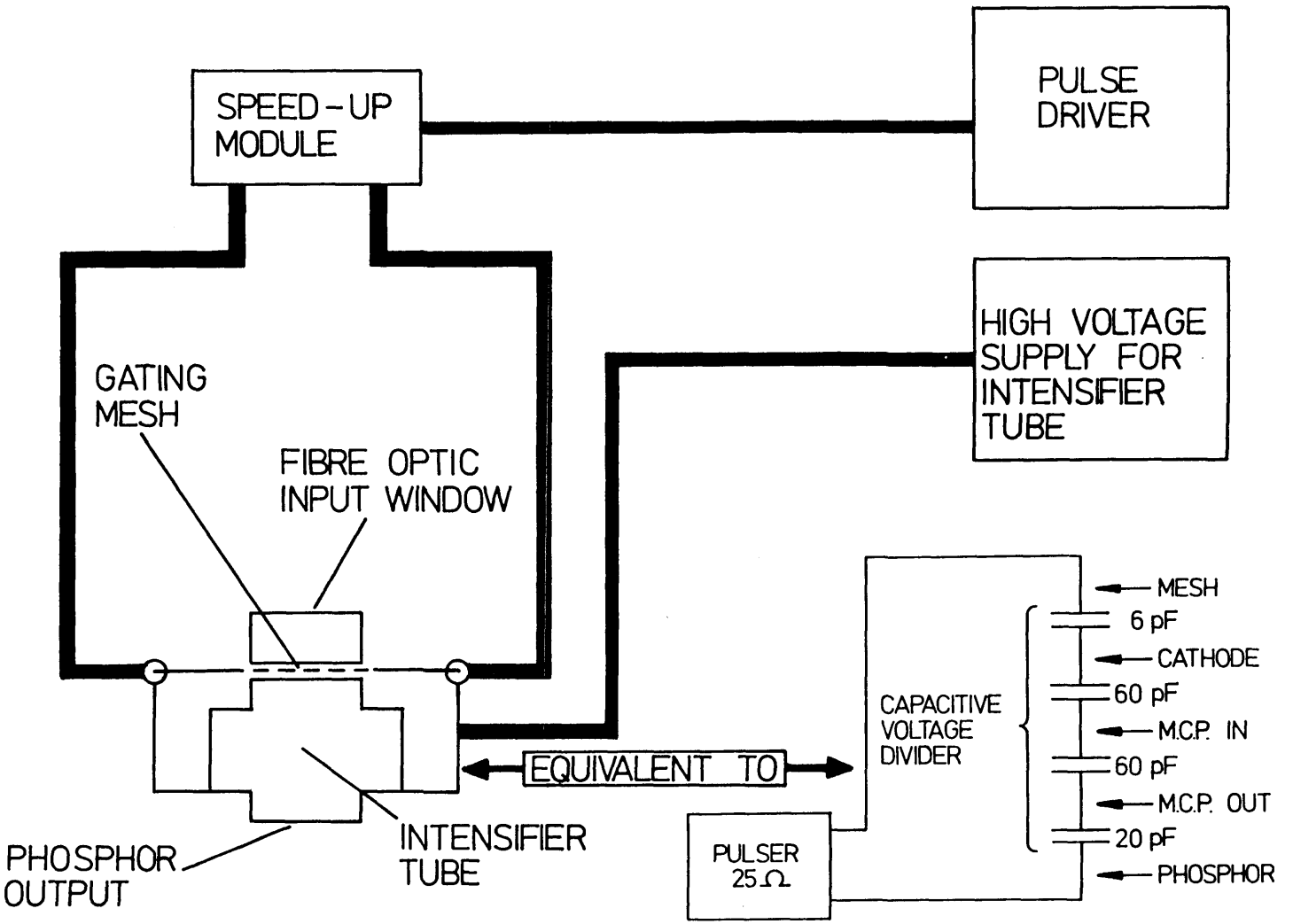


Figure 4.9 Electrical connections to optical framing camera.

gives an electron transit time of approximately 80 ps which potentially allows very fast gating of the device.

The gating pulse applied to the camera is supplied by two 50 Ω cables giving an effective source impedance of 25 Ω. However it is not possible to directly gate the photocathode. This is because the photocathode is capacitively coupled to earth via the microchannel plate and phosphor as illustrated in fig(4.9). This would cause it to represent a significant capacitative load (approximately 12 pF) if directly coupled to the 25 Ω impedance source. This would result in an electrical risetime of order 300 ps which would not allow ultrafast gating of the camera. To overcome this problem the gating pulse is connected to a fine copper mesh which lies next to the photocathode. The mesh is capacitively coupled to the photocathode due to its close proximity. Consequently the cathode forms the centre plate in a capacitive divider as illustrated in fig(4.9). This causes the capacitative load seen by the pulser to be reduced to approximately 4 pF, and this results in a faster electrical risetime of only 100 ps, allowing very fast gating. The disadvantage of this approach is that the capacitative divider will also act as a voltage divider and consequently reduce the voltage actually seen by the photocathode. However, the gating electronics for the camera are capable of supplying a very high voltage output (typically producing a total voltage pulse applied to the copper mesh of −1.6 kV). Consequently even voltage division ratios in excess of 10:1 will still result in a sufficiently large voltage pulse being applied to the actual photocathode to gate the camera on. The off bias applied to the photocathode can be varied, which allows some control of the duration of the framing time for a given electrical gate pulse.

The electronics used to generate the gating pulse consists of two stages, see fig(4.9). An initial pulse driver produces a −1.6 kV pulse with a risetime of < 0.5 ns and a duration of approximately 10 ns as shown in fig(4.10). The pulse driver relies on the use of avalanche transistors to produce its output pulse, since these devices are capable of very high switching speeds. In order to produce the necessary high voltage output a number of these devices are connected in series in the pulse driver. When triggered this chain of transistors undergoes avalanche breakdown. This causes the high voltage initially applied across the whole chain of transistors to be transferred to the output of the device, and thereby produces the output pulse shown in fig(4.10). The suitability of avalanche transistors for the production of short, high voltage pulses has been discussed elsewhere [86]. The ouput of the pulse driver is then connected to a pulse forming speed up module. The basic design of the speed up module is shown in fig(4.11) [86,87]. The

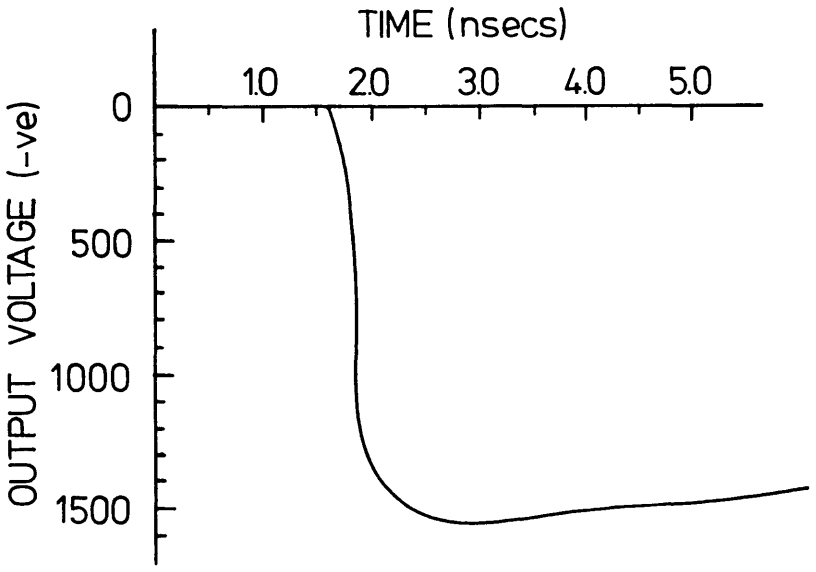


Figure 4.10 Voltage ouput of pulse driver.

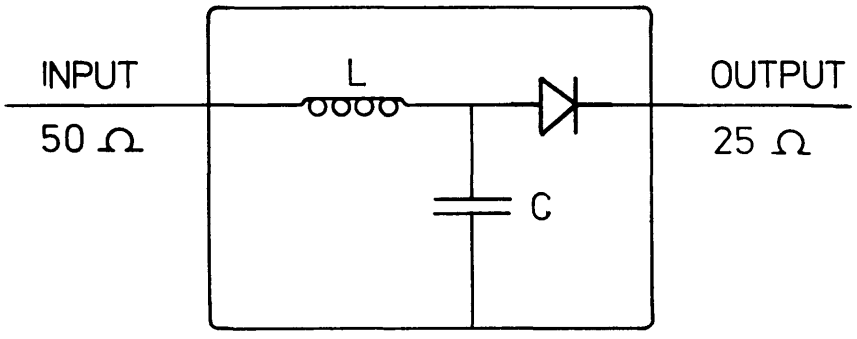


Figure 4.11 Pulse forming speed up module.

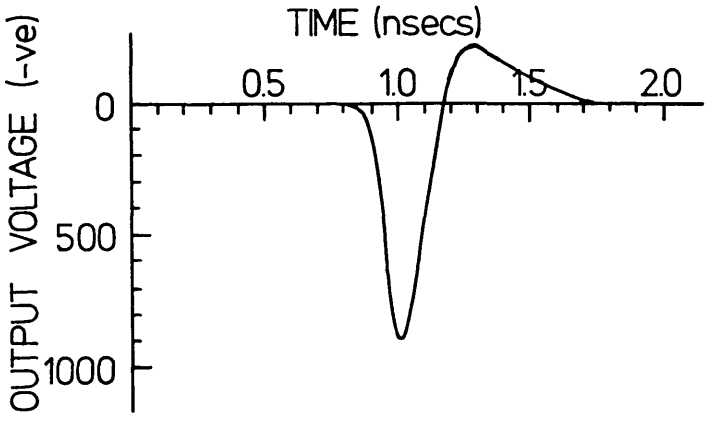


Figure 4.12 Voltage output of speed up module.

incident voltage pulse causes the avalanche breakdown of a reverse biased p−n junction. This dramatically sharpens the voltage edge of the pulse and provides the output pulse shown in fig(4.12). The decay time of the pulse is determind by the capacitance, C, and the load impedance. The output of the speed up module is connected to two 50 Ω cables in parallel to give the required 25 Ω source necessary to gate the camera. By varying the components in the speed up module it is possible to alter the duration of the output pulse. For the camera used in the experiments described in this thesis a speed up module with an output pulse of 120 ps F.W.H.M. was used. The G.O.I. can also be used in a D.C. mode with the gating electronics disconnected and the photocathode permanently biased on.

Initial tests of the G.O.I. were carried out using a Hamamatsu C1308 laser diode with an output pulse duration of 70 ps (at a wavelength of 850 nm) as a light source. The diode and the G.O.I. were both triggered from the same source. By varying the relative delay of the trigger to the G.O.I. and the laser diode it was possible to time the camera to gate at the arrival time of the diode pulse. This was initially done approximately with a long ($\approx$4 ns) gate, produced by connecting the output of the main pulse driver unit (suitably attenuated) directly to the camera. The camera was then accurately timed by using the fast speed up module to provide the gating pulse. By varying the relative delay of the framing camera it was found that the minimum optical gate width corresponded closely to the electrical pulse width of 120 ps F.W.H.M.

(4.4.3) Measurements of S.R.S. and S.B.S. Backscatter

The backscattered Raman and Brillouin signals generated by the interaction beam were imaged out via the incident focusing lens. The interaction beam final turning mirror into the target chamber was angled so that it was highly reflecting ($\geqslant$99 %) for wavelengths less than 570 nm, but had a transmission of $>$90% for wavelengths significantly longer than this. Hence the Brillouin scattered light is reflected by the mirror and the Raman scattered light is transmitted. The Brillouin scattered light then propagates back down the interaction beam path until it reaches a BK7 glass blank which splits off a small fraction of the light, which is directed towards the S.B.S. diagnostics. The Brillouin scattered light was then relayed, with a f=1.0 m singlet lens onto the slit of a Spex 0.5 meter focal length spectrometer. A high dispersion 1200 lines/mm reflection diffraction grating was used in first order in the spectrometer giving a dispersion of 1.66 nm/mm at the spectrometer output. The output of the spectrometer was then magnified onto the

slit of a Hadland 675, S20 optical streak camera. This allowed temporally and spectrally resolved measurements of the Brillouin scattered light to be made. The final dispersion of the system at the output of the streak camera was 0.286 nm/mm. The overall temporal and spectral resolutions were 80 ps and 0.1 nm, respectively.

To measure the S.B.S. level, further fractions of the scattered Brillouin light were split off with two pellicles and directed onto a Gentec calorimeter and a calibrated BPX65 photodiode. The BPX65 photodiode allowed a limited temporal resolution (approximately 1 ns) of the scattered light level. This was found to be important at low scattered light levels since it allowed the genuine signal to be temporally separated from various stray light signals caused by the reflection of the interaction beam off lenses and chamber windows. The detailed design of the photodiode detector is shown in fig(4.13). A diffuser was placed a small distance in front of the photodiode. This considerably eased the requirements on the alignment of the photodiode for it to give a reproducible output for a given input signal. Calibration measurements of the photodiode indicated that it had an accuracy of better than ±25% over its whole range of operation. The output of the photodiode was connected to a fast 7104 Tektronix oscilloscope in order to gain the necessary temporal resolution. By placing calibrated neutral density filters in front of the photodiode it was possible to extend its linear range of response over many orders of magnitude. The Gentec provided a complimentary measurement of the S.B.S. level at high scattered light levels.

The Raman scattered light, after being transmitted through the interaction beam final turning mirror, was focused down onto the slit of another Spex 0.5 meter spectrometer. A low dispersion 100 lines/mm grating was used in first order in the Raman channel giving a spectrometer output dispersion of 20 nm/mm. To give temporal resolution the spectrometer was coupled to a Hadland 675, S1 optical streak camera. The system had an overall temporal and spectral resolution of 20 ps and 2 nm. The S.R.S. scattered light level was measured with an identical photodiode detector to that used for the Brillouin channel. However in addition to neutral density filters, OG570 orange/red glass filters were also placed in front of the Raman photodiode detector. This was done to block any scattered Brillouin or green laser light from reaching the photodiode. The reflectances and transmissions of all the appropriate splitters, lenses and mirrors in both the Raman and Brillouin channels were measured so that the absolute levels of the Brillouin and Raman scattered light could be determined from the measurements made.

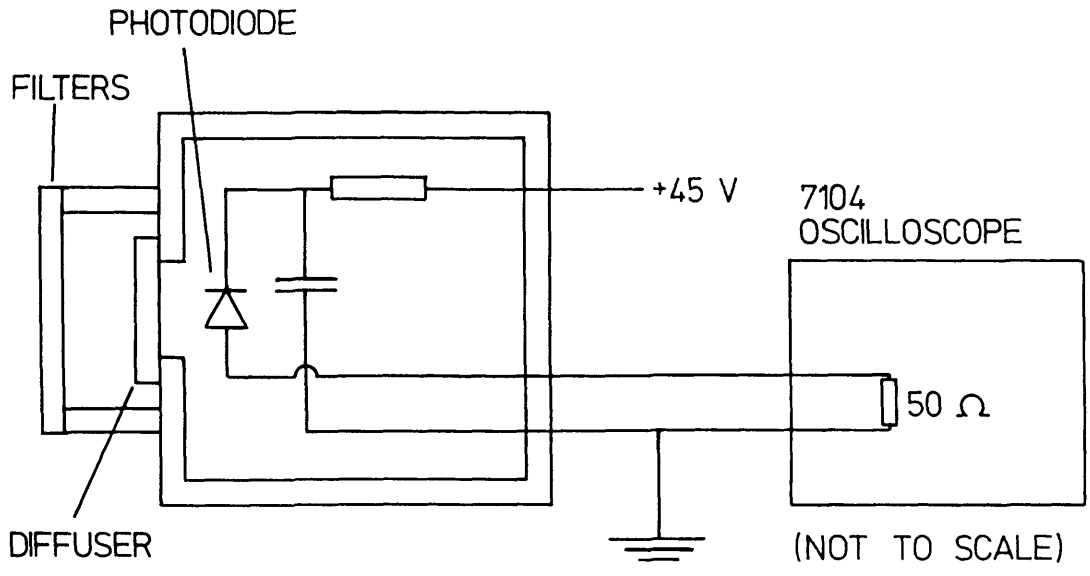


Figure 4.13 Energy detector used to measure S.B.S. and S.R.S. scattered light levels.

(4.4.4) Equivalent plane monitor

A multiple image far field camera (equivalent plane monitor) was used to record the incident interaction beam focal spot distribution at various planes thoughout the length of the preformed plasma. This allowed the size and relative intensity of any hot spots and non−uniformities present in the incident interaction beam to be measured. Also it allowed the size of the interaction beam focal spot, and hence the beam irradiance, to be accurately determined along the whole length of the preformed plasma.

A small fraction of the incident interaction beam was split off by a BK7 blank and directed into the equivalent plane monitor (E.P.M.) as shown in fig(4.7). The detailed design of the E.P.M. is shown in fig(4.14). The incident beam is focused down by a f/100, 10 m focal length lens. A large F/# lens is used so that distortion, due to spherical abberation of the lens, of the images obtained with the E.P.M. is negligible. Hence the E.P.M. images should provide a reasonable representation of the actual focal spot distribution in the preformed plasma. In order to generate a series of multiple images, on a single laser shot of the focal spot distribution at different planes in the far and quasi−near field, the beam was reflected from an echelon at near normal incidence as shown in fig(4.14). The echelon consisted of a 50:50 splitter and a high reflectance green mirror. The echelon splits the beam into a series of beamlets which are spatially separated, and

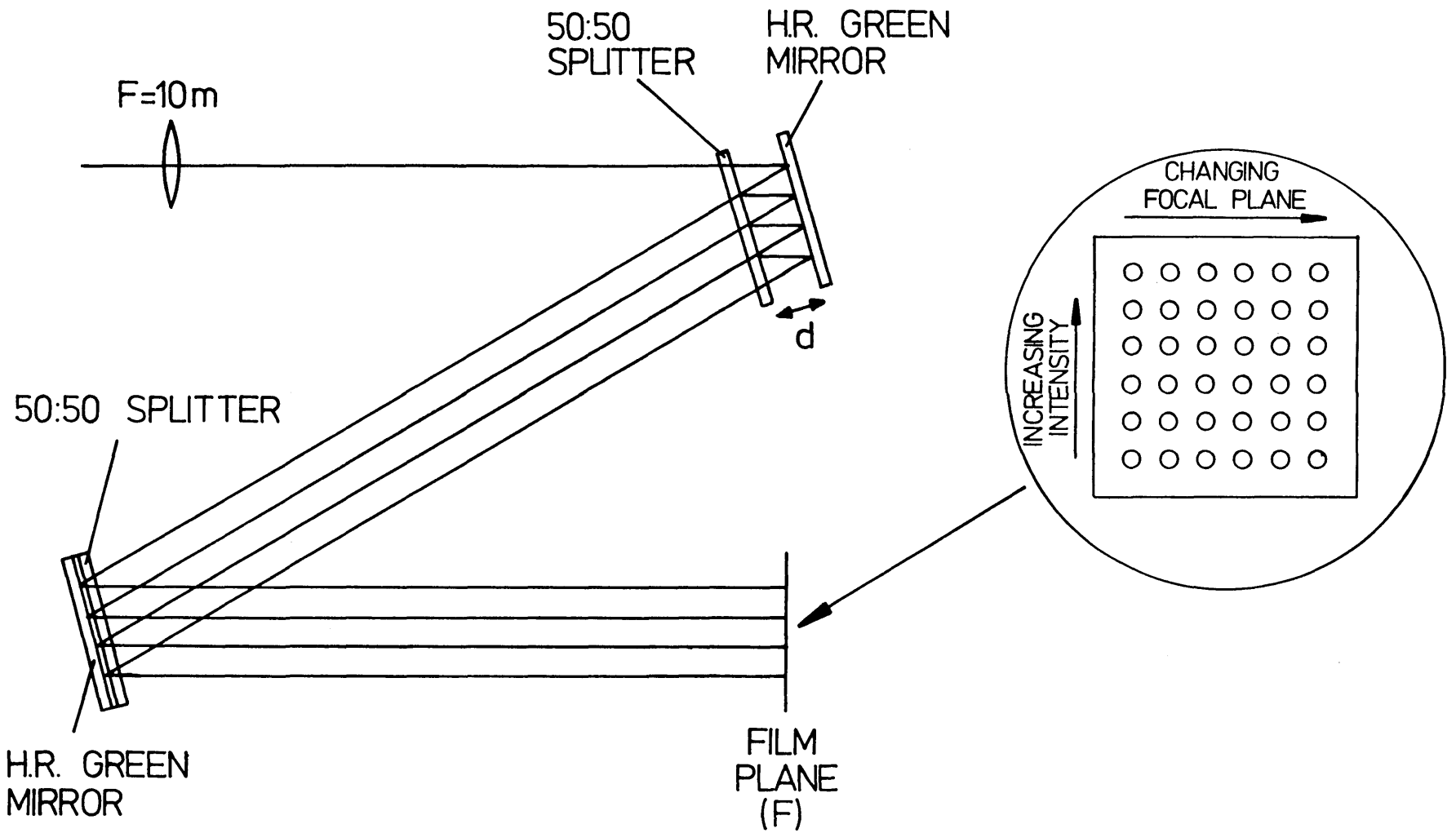


Figure 4.14 Equivalent plane monitor.

also incrementally delayed with respect to each other by a distance 2d. This causes a series of images to be generated in the film plane (f). Due to the optical path differences imposed between the beamlets these images correspond to the focal spot distribution at different planes in the far and quasi−near field. It is straightforward to show that the equivalent separation between the focal spot images in the actual preformed plasma is given by

$$d' = 2d(f'/f)^2 \qquad (4.6)$$

Where f is the focal length of the E.P.M. lens, f' is the focal length of the lens used to focus the interaction beam into the preformed plasma and d is the separation between the two reflecting surfaces of the echelon. The value of d was set to produce a series of images (typically 6) at planes equivalent to a 200 μm separation throughout the length of the preformed plasma. Hence for the cases of a f/2.5 (f'=25 cm) or a f/10 (f'=100 cm) main focusing lens for the interaction beam, d was set to 16 cm or 1 cm respectively. The magnification of the E.P.M. images is simply given by f/f' (ie. ×40 for a f/2.5 focusing lens and ×10 for a f/10 lens).

After being reflected from the initial echelon the beamlets were reflected from two surfaces inclined at a small angle to each other. Again the first surface was a 50:50 splitter and the second a high reflectance green mirror. These two inclined surfaces were orientated so as to split each incident beamlet up into its own series of images (of decreasing intensity) in the film plane, in a direction perpendicular to the original array of images created by the first echelon. The pattern then recorded in the film plane is illustrated in fig(4.14). A series of columns of images is obtained with each column corresponding to a particular plane in the far or quasi−near field of the interaction beam. Along each column is a series of images of different intensities, of the same focal spot distribution. This ensures that at least one image in each column is reasonably exposed on film. Consequently the E.P.M. allows a complete characterization of the focal spot distibution throughout the whole length of the preformed plasma, on a single laser shot.

CHAPTER 5

OBSERVATIONS OF INSTABILITIES IN A LONG SCALELENGTH PLASMA

(5.1) Introduction

The experimental arrangement described in chapter 4 was used to study the interaction of a normal coherent laser beam with the preformed plasma generated. The interaction beam (delayed by 1.7 ns with respect to the main heating beams, unless otherwise stated) was focused into the preformed plasma by a f/2.5 lens. The main aim of this experiment was to determine the degree of filamentation of the interaction beam occurring, due to the propagation of the beam through the preformed plasma. In section (5.2) the S.R.S. and S.B.S. spectra observed under such conditions will be described. These spectra were primarily used as density and temperature diagnostics in this experiment. Time resolved measurements of the transmitted interaction beam showing filamentary break−up and whole beam self−focusing will be reported on in sections (5.3) and (5.4) respectively.

(5.2) Spectroscopic observations of S.R.S. and S.B.S.

One of the main advantages of the experimental arrangement used here is that the plasma expansion is mainly in a direction perpendicular to that of the interaction beam. The plasma flow towards the interaction beam is negligible. Consequently the Brillouin scattered light is not Doppler shifted and the wavelength dependence of the scattered light is simply given by eq(3.6). This means the plasma conditions, in particular the temperature, can be directly inferred from the observed Brillouin spectra. In previous experiments [55,59] it has been necessary to de−convolve the Doppler shift from the S.B.S. spectra before information about the plasma conditions could be inferred. Since the Doppler wavelength shift is normally of the same order as the S.B.S shift this significantly reduced the accuracy of the predictions of the plasma conditions obtained in these experiments. Fig(5.1) shows the expected variation of the S.B.S. wavelength shift with plasma temperature for a fully ionized aluminium plasma, determined from eq(3.6). It can be seen that for the plasma densities present in this experiment (ie. $N_e \leqslant 0.1N_{ec}$) the wavelength shift is dominated by the temperature and is only weakly dependent on the plasma density. Hence the S.B.S. spectra can be used as a reliable temperature diagnostic provided the temperature is not too high (<2 keV).

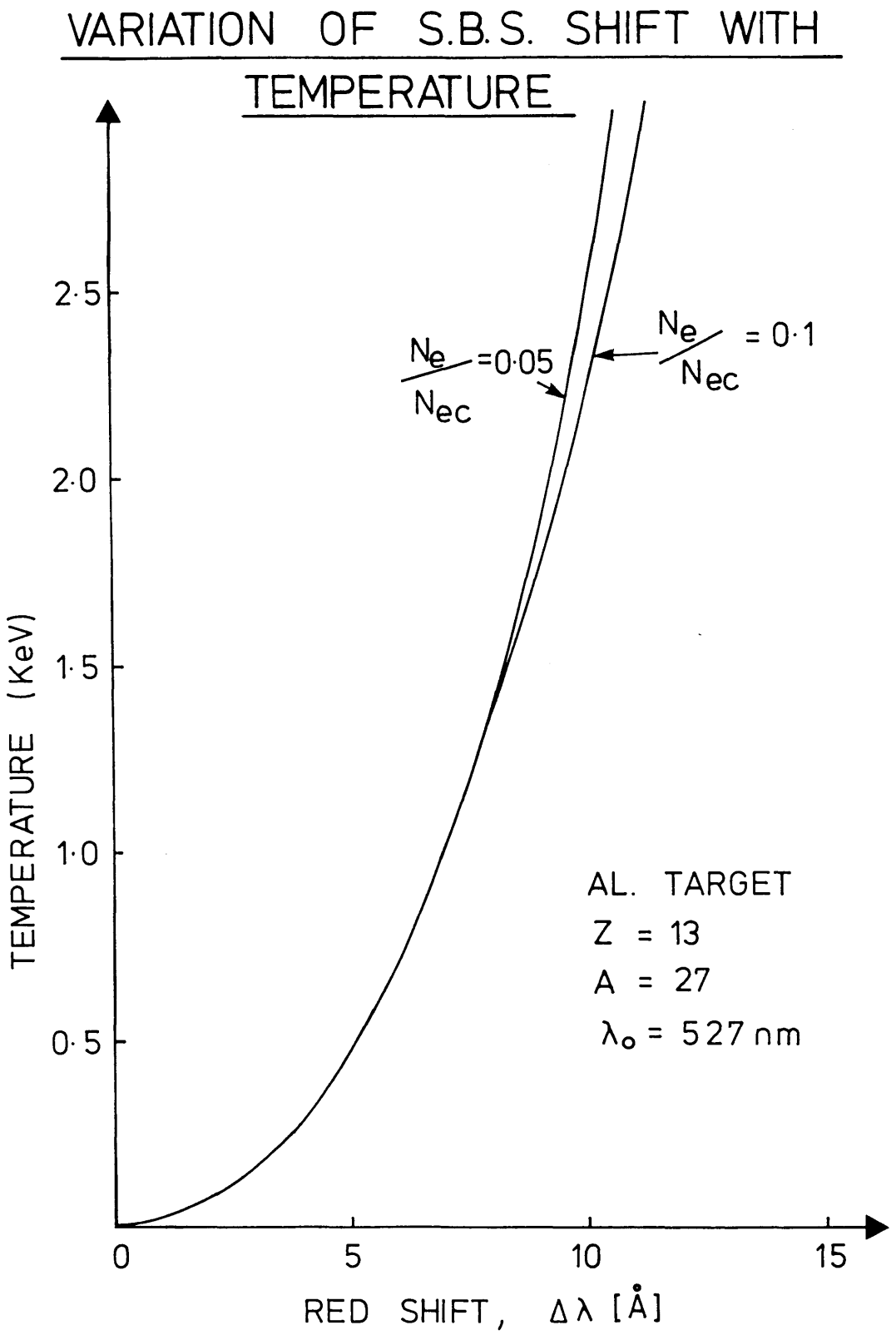


Figure 5.1 Variation of S.B.S. wavelength shift with temperature for an aluminium plasma (λ_0 = 526 nm).

Fig(5.2) shows an example of a typical S.B.S. backscattered spectrum observed. The line along the bottom of the streak is a fiducial, split off from the incident interaction beam, and aligned on to the input slit of the spectrometer. It serves as both a wavelength and a time reference. The remaining signal observed on the streak is due to S.B.S. It can be seen that the S.B.S. spectrum is broken up into a series of individual components. The smallest shifted component corresponds to a temperature of about 500 eV (assuming $N_e \approx 0.08N_{ec}$) which would appear to be a reasonable estimate of the background temperature of the homogeneous plasma. This is somewhat lower than the temperature of 860 eV predicted by the 1−D model of Rosen and London [84]. This is not however, unreasonable since the actual plasma expansion will be two dimensional and so the plasma can be expected to cool more rapidly than predicted by the model. The remaining larger shifted components of the S.B.S. spectrum correspond to considerably higher temperatures of 1−1.6 keV and 3 keV. It is difficult to account for such high temperatures unless it is assumed that the plasma is strongly locally heated in certain regions by filamentation.

Fig(5.3) shows a typical S.R.S. spectrum observed under similar plasma conditions. It should be noted that this streak was taken with a f/10, rather than a f/2.5, focusing lens for the interaction beam. However the general features of the S.R.S. spectra observed were found to not depend on the focusing lens used. A wavelength and time fiducial can again be seen along the bottom of the streak. The S.R.S. spectrum is extremely non−uniform and pronounced temporal modulations can be seen. Similar observations of temporal modulations in S.R.S. spectra have been reported elsewhere [53,72]. Again, as with the S.B.S. spectrum, it seems possible that filamentation could be responsible for these modulations in the spectrum. In particular certain features in the spectrum are observed to shift rapidly to shorter wavelengths with time. This could be due to the creation of lower density regions in the plasma by filamentation (since the S.R.S. wavelength shift decreases with density).

Assuming a temperature of 500 eV for the homogeneous plasma (as indicated by the S.B.S. spectrum) the electron density can be estimated from the Raman spectrum by using eq(3.23). This gives a peak density of $0.08N_{ec}$ (3.2×10^{20} cm^{-3}), by taking the maximum wavelength shift. Again this is somewhat lower than the predictions of the Rosen and London model, which gives a density of $0.11N_{ec}$. As with the discrepancy over the temperature, it seems likely that the cause of this disagreement is the 2−D nature of the expansion which occurs in reality. It can be seen that emission is observed over a reasonably wide range of

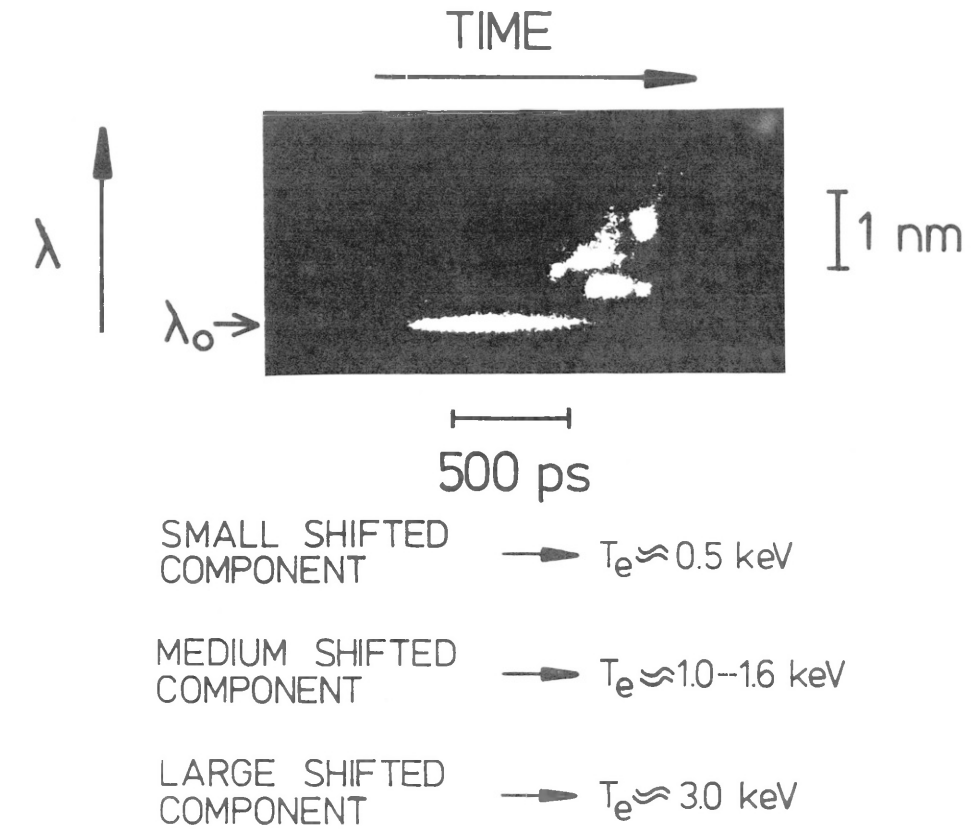


Figure 5.2 Typical S.B.S. spectrum observed with a normal coherent interaction beam (irradiance = 4.5 × 10^{14} Wcm^{-2}). The fiducial shown is 470 ps earlier than the actual interaction laser pulse.

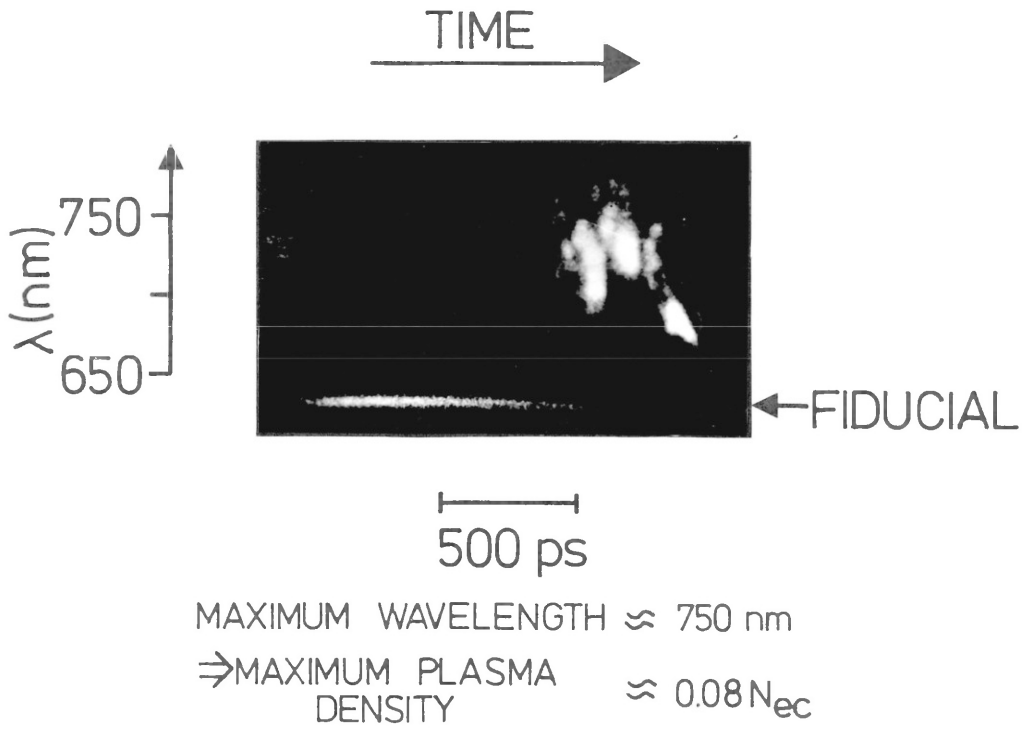


Figure 5.3 Typical S.R.S. spectrum observed for a normal coherent interaction beam (irradiance = 1.0 × 10^{15} Wcm^{-2}).

wavelengths down to 680 nm. The presence of wavelengths as short as 680 nm indicates that densities at least as low as $0.05N_{ec}$ (2.0×10^{20} cm^{-3}) were present in the plasma. It is unclear if these lower densities are generated by filamentation, or that they are simply present around the edges of the preformed plasma (in particular at the entrance plane of the plasma). The actual levels of S.R.S. and S.B.S. which were observed will be discussed in detail in chapter 6.

(5.3) Observations of the filamentary break up of the interaction beam

Previous experimental observations of filamentation have largely been restricted to indirect methods such as x−ray emission [88,89] and optical probing measurements of the plasma non−uniformities created by filamentation [90]. In particular, recent results [91] have shown evidence of the growth of filamentation from intensity perturbations purposely imposed on the laser beam profile. Although these results provide strong evidence of the occurrence of filamentation they give little quantitative information on the extent to which this instability occurs and to what degree the intensity in each individual filament is enhanced. Also these results have largely been restricted to short scalelength plasmas. The advantage of the experimental arrangement described in chapter 4 is that it allows direct quantitative information to be obtained on the level of filamentation occurring (ie. it allows the actual enhancement in intensity in an individual filament to be measured). Also the filamentation process is occurring in a large underdense plasma, the conditions of which are well defined. In particular the plasma density and temperature are restricted to a narrow range of values in the region of interaction. This makes it easier to compare the experimental results with theoretical predictions.

Fig(5.4) shows a series of three images taken at different times during the interaction beam laser pulse, with the optical framing camera (for an aluminium plasma). The interaction beam delay was 1.7 ns. Also shown in fig(5.4) are typical 1−D microdensitometer scans taken across each beam profile. It can clearly be seen that at early times the beam profile is uniform but that it breaks up into a series of intense hot spots later in the laser pulse. It seems likely that this break up is due to filamentation. In order to quantify the uniformity of the beam profiles measured in this experiment the quantity I_{max}/I_{av} (the peak to average intensity ratio from a typical 1−D scan across the beam profile) has been used. From the results shown in fig(5.4) I_{max}/I_{av} increases from 1.3 in the early frame to 3.9 and 7.4 at times +150 ps and 350 ps respectively, where time zero

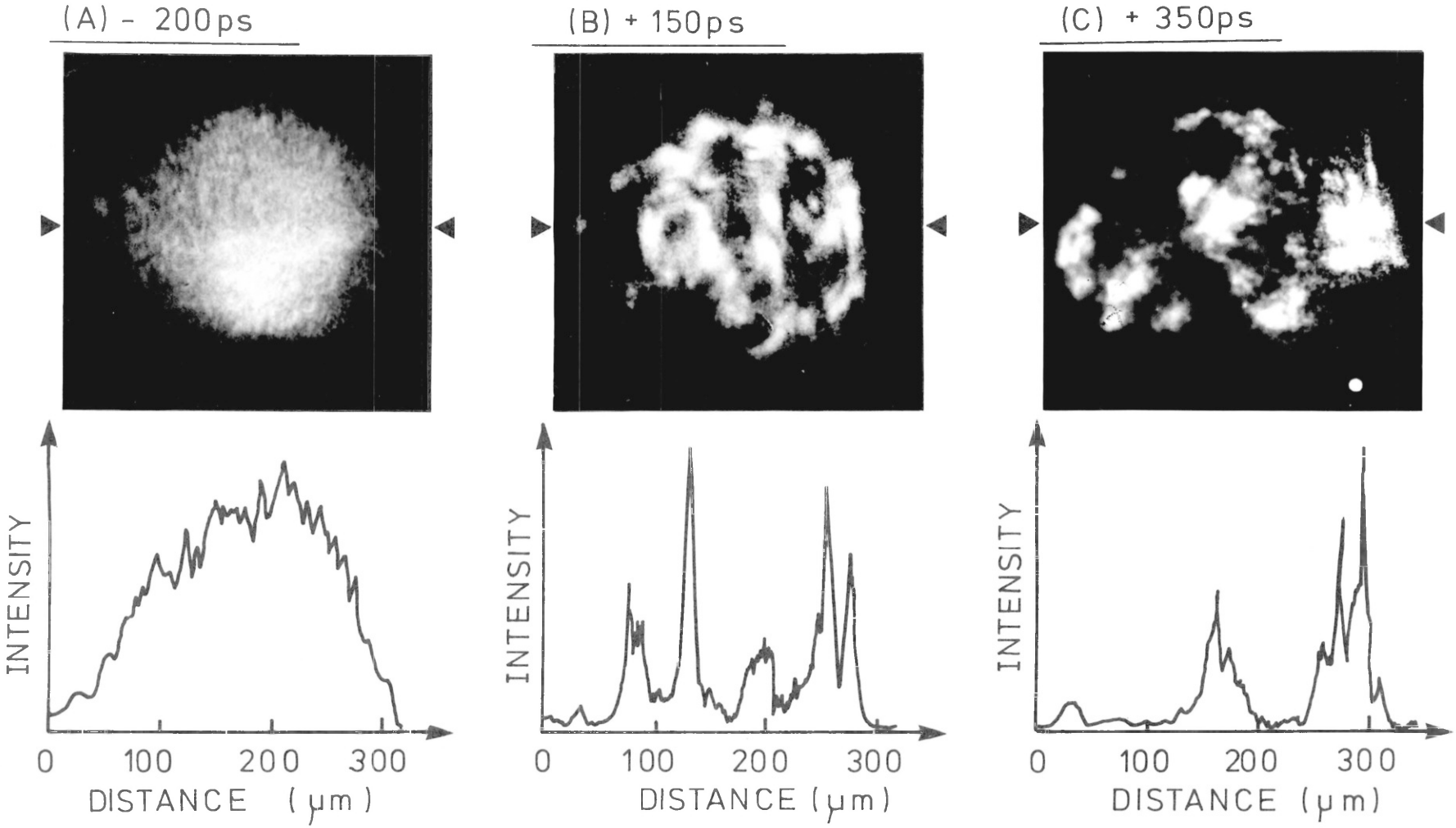


Figure 5.4 A series of three images of the interaction beam recorded at different times during the laser pulse. Time zero refers to the peak of the laser pulse. (a) irradiance = 8.3 × 10^{14} Wcm^{-2}, (b) irradiance = 8.0 × 10^{14} Wcm^{-2} and (c) irradiance = 4.5 × 10^{14} Wcm^{-2}. The arrow heads indicate the sections across which the microdensitometer traces were taken.

is taken as the peak of the laser pulse. For the frame taken at time +350 ps the maximum to minimum intensity ratio across the beam was found to be approximately 50:1. The intense hot spots in fig(5.4)(b) and fig(5.4)(c) have typical sizes of 9−15 μm and 6−10 μm (F.W.H.M.) respectively. This is consistent with them decreasing in size with time as the filaments focus down further.

Fig(5.5) shows a streak image of the transmitted interaction beam observed under similar conditions to the framing camera images in fig(5.4). It can be seen that the beam is observed to break up in a similar fashion to that observed with the framing camera images. This confirms that this observed break up of the interaction beam is not due to shot to shot variations. It can be seen from the streak that the beam structure does not vary significantly on time scales less than 120 ps (ie. the G.O.I. frame time). Hence temporal smearing of the framing camera images shown in fig(5.4), due to the finite gate time of the camera, should be small.

To confirm that the break up of the beam observed was due to filamentation in the plasma, and not an effect of the laser itself, images of the interaction beam were also taken with no preformed plasma present. Fig(5.6) shows a framing camera image taken 350 ps after the peak of the interaction beam pulse (ie. at the same time as the final image in fig(5.4)). Also shown is a microdensitometer trace across the beam profile. The beam is clearly considerably more uniform than that observed in fig(5.4)(b) or (c). I_{max}/I_{av} was found to have a typical value of 1.9. Also streak records of the interaction beam with no preformed plasma present show that there was no significant variation of the beam profile with time. Fig(5.7) shows the streak camera image of the transmitted interaction beam taken on the same laser shot as the framing camera image of fig(5.6). The beam diameter remains constant and no growth of the hot spots, which can be seen present in the beam, is observed. The streak record is rather noisy as the camera intensifier was run at maximum gain on this particular shot. Hence it can be concluded that the break up of the interaction beam observed in fig(5.4) and fig(5.5) must occur in the preformed plasma and not elsewhere. Consequently on the basis of these observations it seems reasonable to conclude that the break up of the interaction beam into intense hot spots is indeed due to filamentation.

The image taken in fig(5.4) 200 ps before the peak of the laser pulse was found to be significantly more uniform than that of the beam with no preformed plasma present. This smoothing effect of the plasma at early times in the laser

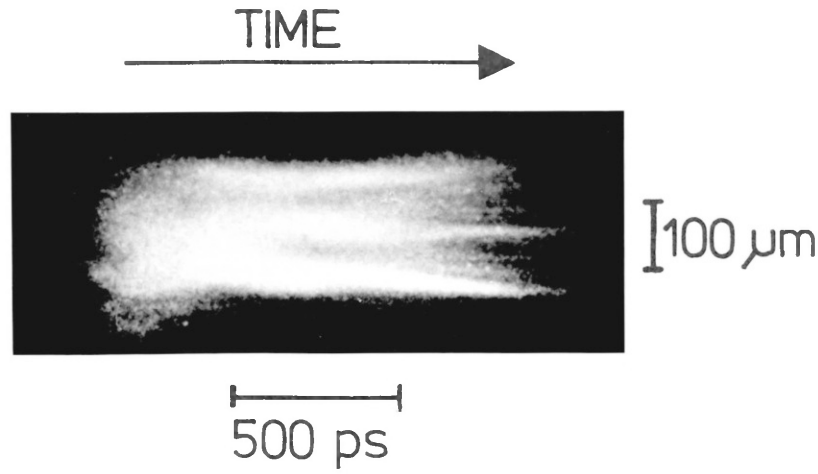


Figure 5.5 Streak of the transmitted interaction beam indicating filamentary break up of the beam (irradiance = 1.0 × 10^{15} Wcm^{-2}).

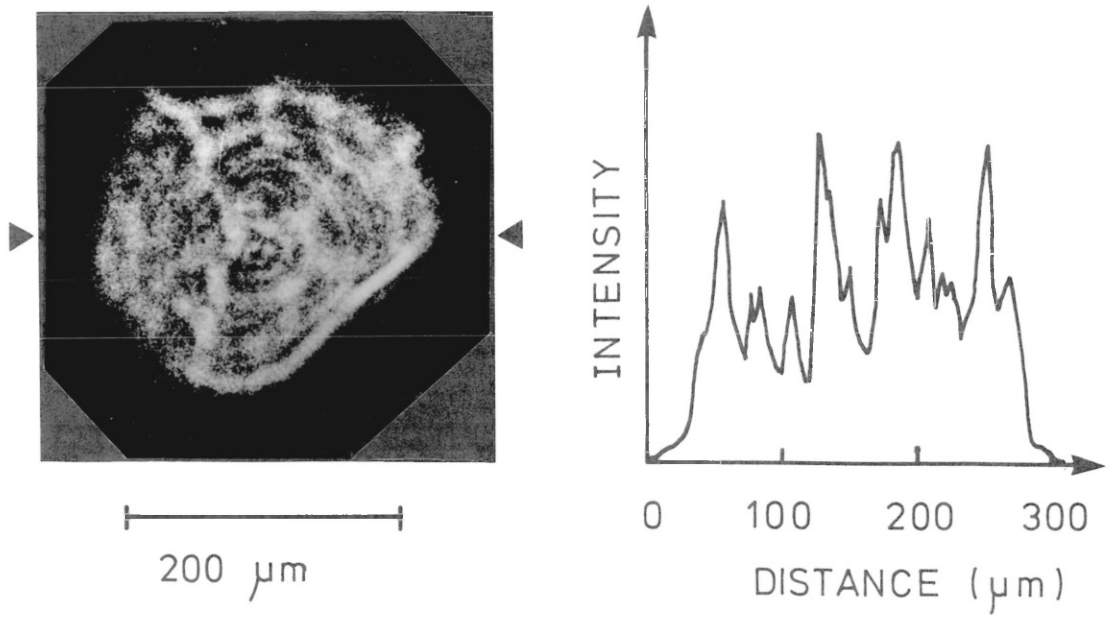


Figure 5.6 Framing camera image of the transmitted interaction beam (350 ps after the peak of the laser pulse) with no plasma present (irradiance = 9.6 × 10^{14} Wcm^{-2}).

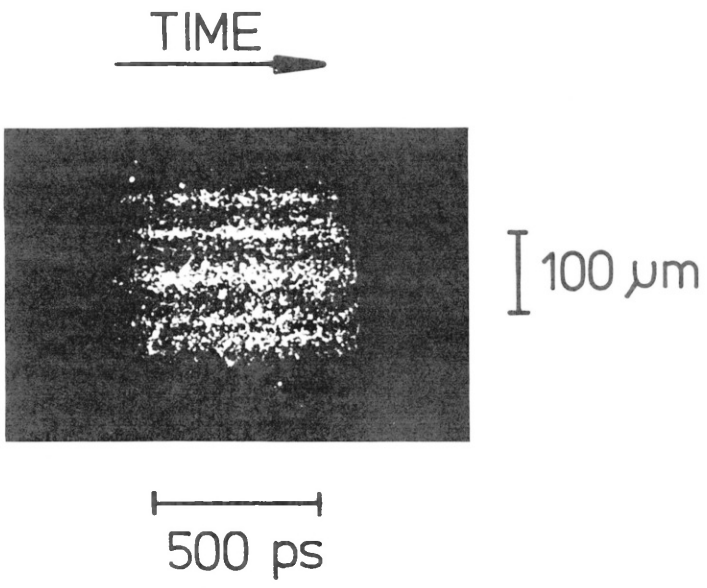


Figure 5.7 Streak of the transmitted interaction beam with no plasma present (for the same shot as the framing camera image of fig. 5.6).

pulse was consistently observed on all shots taken. To investigate this effect further a short (70 ps F.W.H.M.) interaction beam was used instead of the longer (600 ps F.W.H.M.) pulse used previously. Otherwise the experimental conditions were identical. Images taken of the interaction beam with and without a preformed plasma are shown in fig(5.8). It can be seen that with no plasma present the beam is extremely non−uniform (I_{max}/I_{av} = 3.8). This is due to the difficulty of propagating short pulse beams in high power laser systems [92]. However with the plasma present the transmitted beam is observed to be considerably more uniform (I_{max}/I_{av} = 1.4). This clearly demonstrates that propagating a high power laser beam through an underdense plasma can dramatically smooth out any hot spots in the beam over short time scales ($\lesssim$100 ps). It is unclear what the mechanism responsible for this smoothing of the laser beam profile is. Previous observations have been made of the smoothing of laser beams due to plasmas [93−95], but these experiments all dealt with the beam reflected from the critical density region in a dense plasma. In these cases this effect was explained [95−96] by the nature of the reflection process of the beam from the critical density region in the plasma. Clearly such arguments cannot be applied to the experimental conditions considered here since the preformed plasma is entirely underdense. The process leading to beam smoothing clearly occurs on very short time scales ($\lesssim$70 ps) and so is unlikely to be due to any hydrodynamic motion of the plasma. One possible explanation is that the effect may be due to

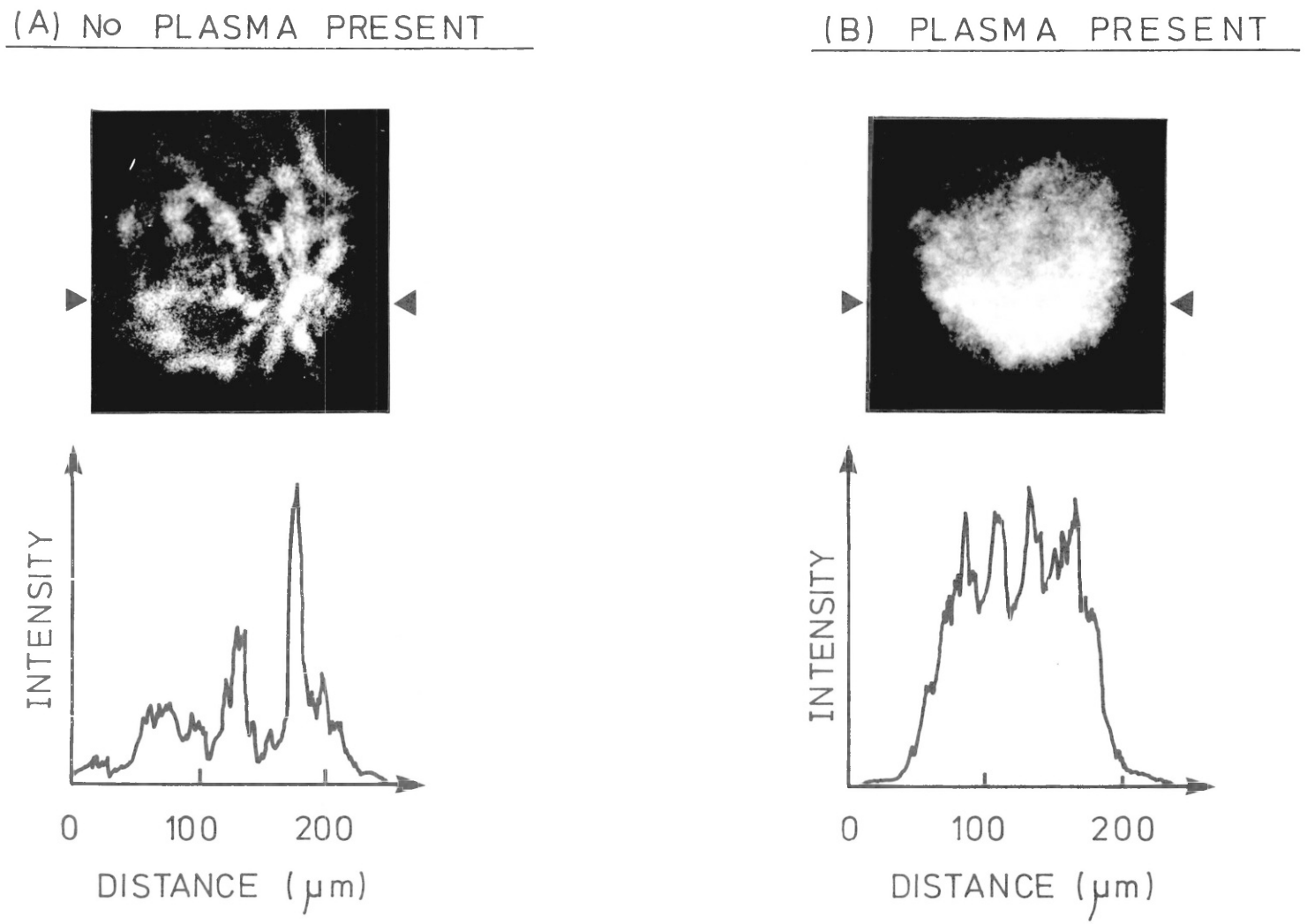


Figure 5.8 Framing camera images of a short pulse (70 ps) interaction beam. (a) No plasma present (irradiance = 6.7×10^{14} Wcm^{-2}) and (b) plasma present (irradiance = 1.5×10^{15} Wcm^{-2}).

refraction from local density perturbations present in the plasma. Experimental evidence for the existence of a certain degree of density non−uniformities in plasmas, generated by a similar experimental arrangement to that used here, will be presented in chapter 7 of this thesis. In order to determine if refraction from density non−uniformities is able to give a sufficient magnitude of deflection to account for this smoothing effect, a calculation was performed with a ray tracing program (see Appendix A). In the calculation a 20% perturbation was superimposed on a uniform density profile of $0.08N_{ec}$. The perturbation had a Gaussian profile with a F.W.H.M. of 40 μm. It was found that this size of density perturbation gave rise to an angular deflection of the incident light rays of up to 0.8°. Over a length of 800 μm (ie. the length of the preformed plasma) an angular deflection of this size would result in a lateral displacement of the light rays of 11 μm. This is of a comparable size to the laser beam hot spots observed in fig(5.6). Consequently it seems plausible that refraction from a number of such density non−uniformities may be able to account for this smoothing effect. Other possible scattering processes, such as Thomson scattering are unlikely to be able to account for this smoothing effect due to the extremely small cross−section for this process. With a long pulse interaction beam it is reasonable that smoothing is not observed for times greater than 100−200 ps because of the growth of filamentation, which can clearly dominate the smoothing effect over long time scales.

As discussed in chapter 3 filamentation and self−focusing are expected to grow from the initial intensity perturbations in the laser beam profile. In order to calculate the expected theoretical thresholds for filamentation to occur in this experiment (using the results of chapter 3) it is necessary to know the size of the intensity perturbations present in the beam. Unfortunately the experimental arrangement considered here is complicated by the use of a f/2.5 focusing lens for the interaction beam. This means that the beam diameter, and also the size and level of hot spots, is not constant through the whole length of the preformed plasma. However from the results shown in fig(5.8) it appears that the plasma has a natural tendency to smooth the beam profile. Consequently it would seem reasonable to assume that the hot spots would be most pronounced at the entrance plane of the plasma before any smoothing has occurred. It follows that these will be the hot spots from which filamentation is most likely to grow. Hence estimates on the thresholds for filamentation have been based on the intensity perturbations present in the beam at the entrance plane of the plasma. Fig(5.9) shows a typical equivalent plane monitor image of the interaction beam at the entrance plane of the preformed plasma. The typical wavelength of the perturbations present in this

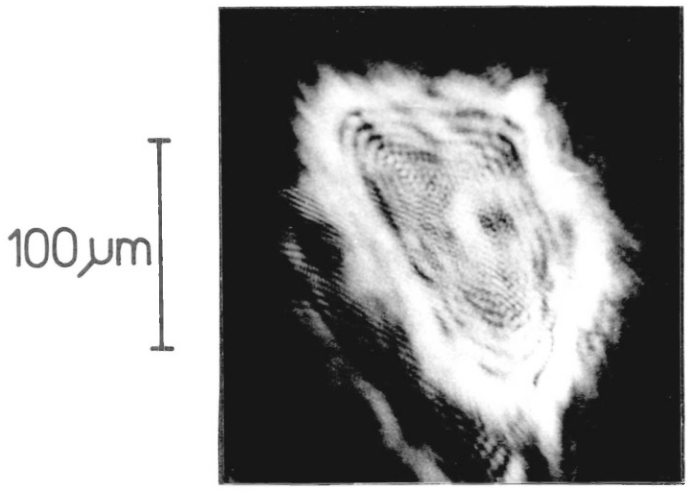


Figure 5.9 Equivalent plane monitor image of the interaction beam profile at the approximate entrance plane of the preformed plasma.

image, and in other similar images, are found to be on a 14−24 μm scalelength.

Fig(5.10) shows the variation of growth rate with perturbation wavelength predicted by the results of chapter 3 for both thermal and ponderomotive filamentation, for an irradiance of 4.5×10^{14} Wcm^{-2} (this corresponds to the conditions for image (c) in fig(5.4)). These estimates of the growth rates have assumed an electron density of 8% of critical and a plasma temperature of 500 eV, as inferred from the S.B.S. and S.R.S. spectra. For a plasma 800 μm long the threshold growth rate for filamentation can be taken as $k_{threshold} = 1250$ m^{-1} (corresponding to a one e−fold growth of the filament). Hence it can be seen from fig(5.10) that both thermal and ponderomotive filamentation can generate filaments from the 14 to 24 μm wavelength perturbations present in the beam. However for perturbations less than 20 μm in size the growth rate for ponderomotive filamentation is significantly larger than the thermal case and so it seems probable that the filamentation observed is mainly due to the ponderomotive force. Even filaments initially formed from larger size perturbations due to thermal effects will soon be dominated by ponderomotive filamentation as they focus down to sizes of less than 20 μm.

Fig(5.11) shows an image taken late in a long pulse interaction beam with the optical framing camera, but with a low interaction beam irradiance of only 7.9

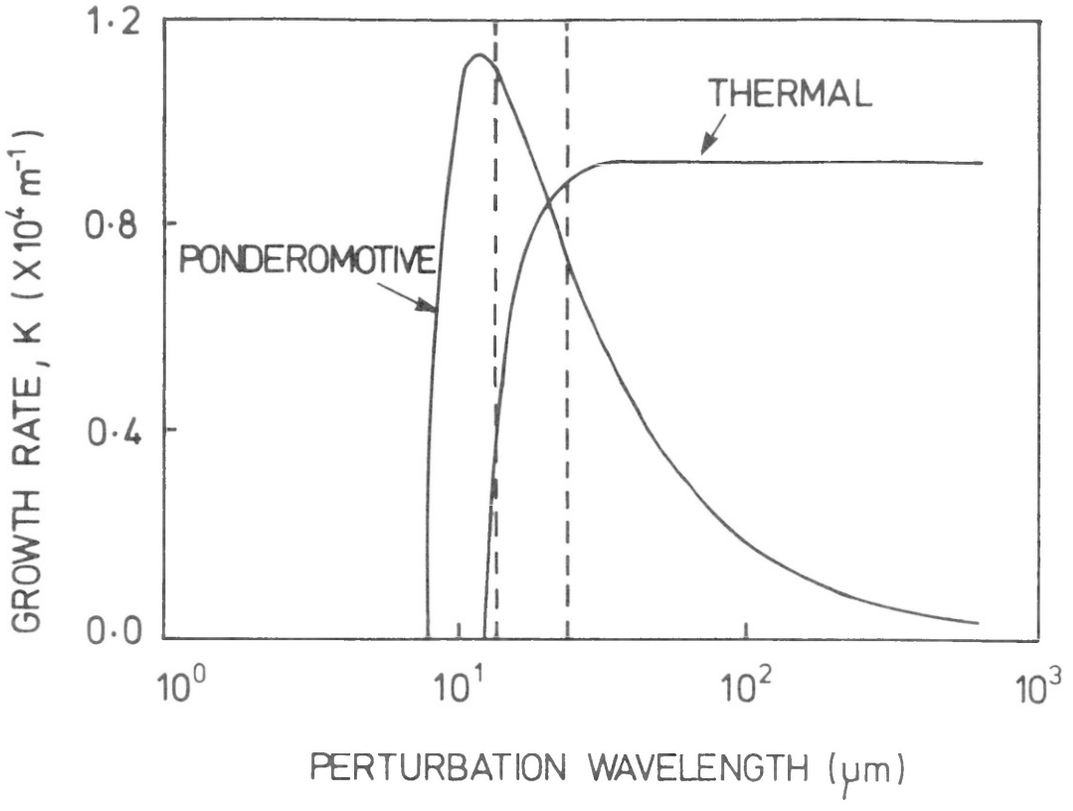


Figure 5.10 Predicted growth rates for ponderomotive and thermal filamentation for $n_e = 0.08n_{ec}$, $T_e = 500$ eV and an irradiance of 4.5×10^{14} Wcm^{-2}. The broken lines indicate the range of perturbation wavelengths present in the interaction beam.

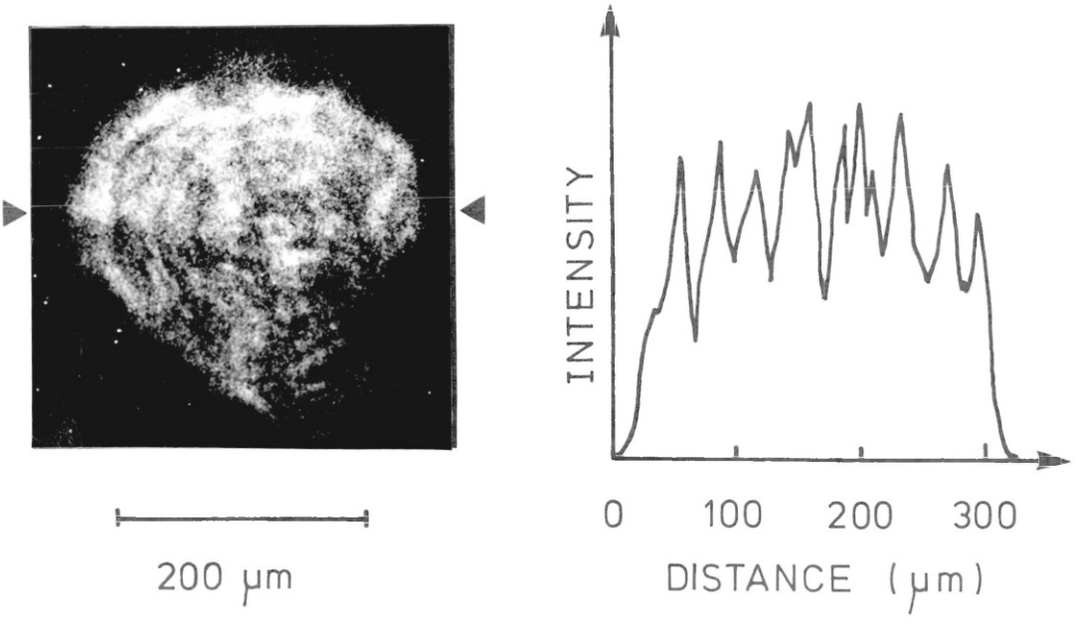


Figure 5.11 Framing camera image of the transmitted interaction beam (350 ps after the peak of the laser pulse) at a low irradiance of 7.9×10^{13} Wcm^{-2}.

$\times 10^{13}$ Wcm^{-2}. No break up of the interaction beam is observed and I_{max}/I_{av} has a value of 1.6. This should be compared with the framing camera image in fig(5.4)(c) taken at the same time in the laser pulse where the irradiance was 4.5 $\times 10^{14}$ Wcm^{-2} and I_{max}/I_{av} = 7.4. This strongly suggests that an irradiance of 7.9 $\times 10^{13}$ Wcm^{-2} is below the threshold for filamentary break-up of the interaction beam, for these plasma conditions.

The results of chapter 3 can be used to estimate the threshold irradiance for filamentation under these conditions. Fig(5.12) shows the variation of the minimum perturbation wavelength which will be unstable to filamentation as a function of irradiance. For the 14 to 24 μm wavelength perturbations present in the interaction beam this gives thresholds of between 1×10^{14} Wcm^{-2} and 2×10^{14} Wcm^{-2} for both ponderomotive and thermal filamentation. This is consistent with the experimentally observed threshold of between 7.9×10^{13} Wcm^{-2} and 4.5×10^{14} Wcm^{-2}, although fig(5.12) does indicate that longer wavelength perturbations should still be unstable to thermal filamentation.

Measurements made of the fraction of the interaction beam absorbed by the preformed plasma under these conditions (from a series of laser shots) give an absorption of (60±6) %. An estimate of the expected absorption can be made by considering inverse bremsstrahlung. The inverse bremsstrahlung absorption coefficient given in chapter 1 can be rewritten in the following approximate form [10]:

$$a_w(\mu m^{-1}) = 74 \frac{Z(n_e/n_{ec})^2}{T_e(eV)^{3/2}\lambda(\mu m)^2(1-n_e/n_{ec})^{\frac{1}{2}}} \qquad (5.1)$$

Where λ is the laser wavelength and Z the ion charge. Again assuming $N_e \approx 3.2\times10^{20}$ cm^{-3} and $T_e \approx 500$ eV this gives an absorbed fraction of 80.9% for a plasma 800 μm long. It is not surprising that this estimate is higher than the actual absorbed fraction. This is because late in the interaction beam pulse the plasma will become heated to temperatures significantly higher than 500 eV. This will be particularly true in regions of strong localized heating due to filamentation, as indicated by the S.B.S. spectrum in fig(5.2). In these strongly heated regions the inverse bremsstrahlung absorption will be reduced (since $a_w \propto T_e^{-3/2}$). Consequently the overall absorption of the interaction beam will be lower than predicted by a simple estimate based on the initial plasma conditions. Also for these experimental conditions, the two non-linear modifications for inverse bremsstrahlung described in chapter 1 may cause some reduction in the inverse bremsstrahlung coefficient, from the value given by eq(5.1).

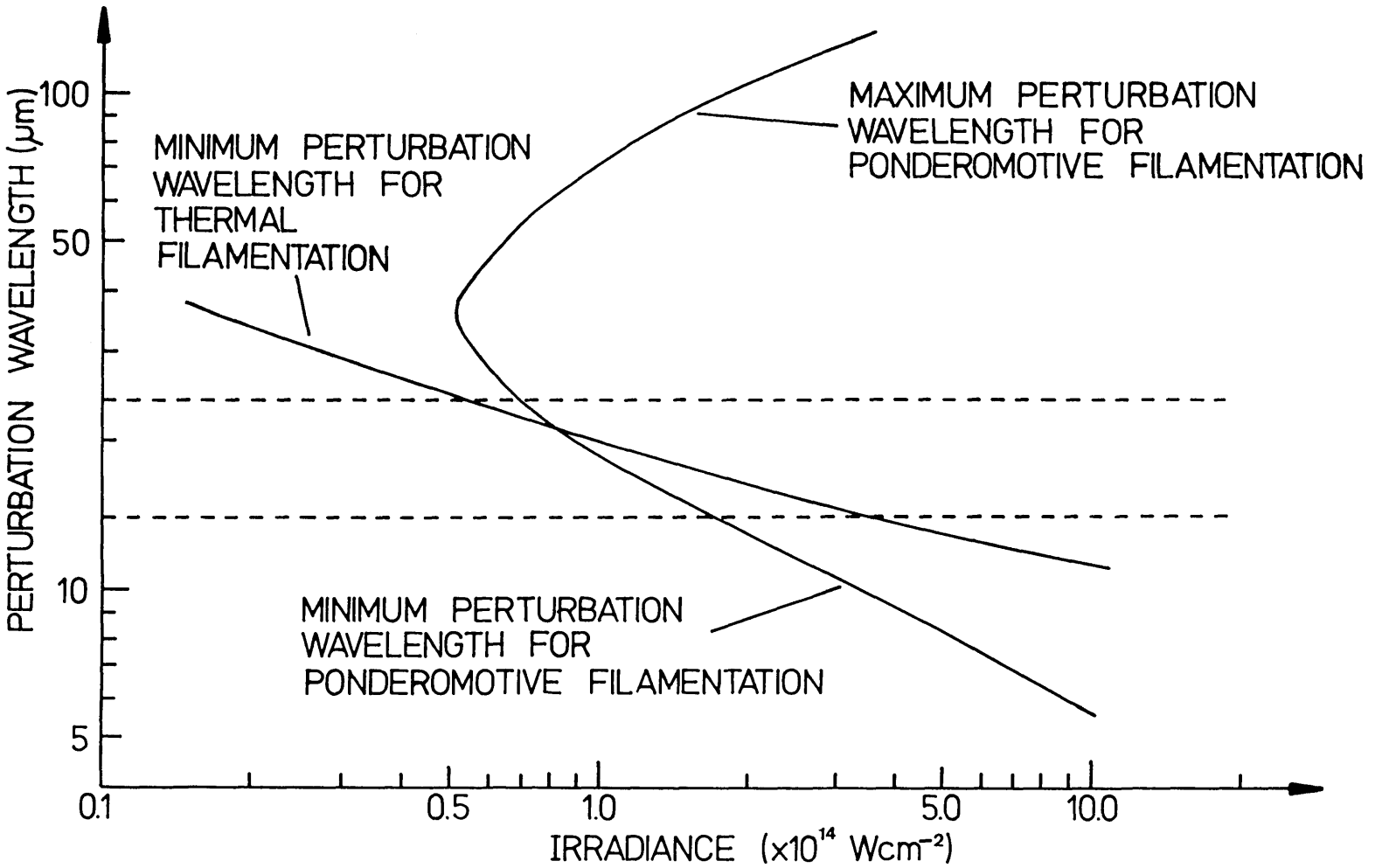


Figure 5.12 Variation of minimum perturbation wavelength unstable to filamentation, with irradiance (assuming $n_e = 0.08\ n_{ec}$ and $T_e = 500$ eV).

(5.4) Observations of whole beam self−focusing

Due to the higher growth rates associated with large scalelength perturbations for thermal filamentation, it has been suggested that this process can result in whole beam self−focusing. Although numerous observations have been made consistent with the break up of laser beams due to filamentation, there has been little evidence reported of whole beam self−focusing [97]. However 2−D hydrodynamic simulations have provided strong evidence that whole beam self−focusing can occur in a laser produced plasma [79,98].

Thermal self−focusing is expected to be particularly significant in a highly collisional plasma. Hence in order to create such a plasma, high Z (atomic number) bismuth stripe targets were used. These targets were 250 nm thick and an interaction beam delay of 4.2 ns was used. Fig(5.13) shows a streak record taken of the transmitted interaction beam after propagating through the preformed plasma. The diameter of the beam can clearly be seen to decrease to about half its original value late in the laser pulse. As already stated (see fig(5.7)) no reduction in beam diameter with time was observed on laser shots with no preformed plasma present and consequently this effect must be due to processes occurring in the plasma. The obvious explanation of this effect is thermal whole beam self−focusing. As well as whole beam self−focusing some finer scale break up of the beam can also be observed in fig(5.13). Presumably this is due to ponderomotive filamentation.

The electron density of the bismuth plasma estimated from the S.R.S. spectrum measured on this laser shot gives a value of 3.5×10^{20} cm^{-3}. If an ionization state of 35 is assumed, the S.B.S. spectrum observed gives a temperature of 850 eV. This appears to be too high to be the true temperature of the preformed plasma before interaction. This is because the Rosen and London model predicts a temperature of only 600 eV even for an ideal 1−D expansion. Consequently it seems likely that there is significant heating of the plasma by the early part of the interaction laser pulse, before the Brillouin scattered light is produced. This is not unreasonable since the inverse bremsstrahlung absorption coefficient is proportional to Z (for a fixed electron density), and so for a high Z bismuth plasma strong absorption of the interaction beam can be expected. Consequently the temperature deduced from the S.B.S. spectrum does not necessarily correspond to the true value of the temperature of the preformed plasma before interaction. It does however give an indication of the temperatures present in the plasma during the early stages of whole beam self−focusing,

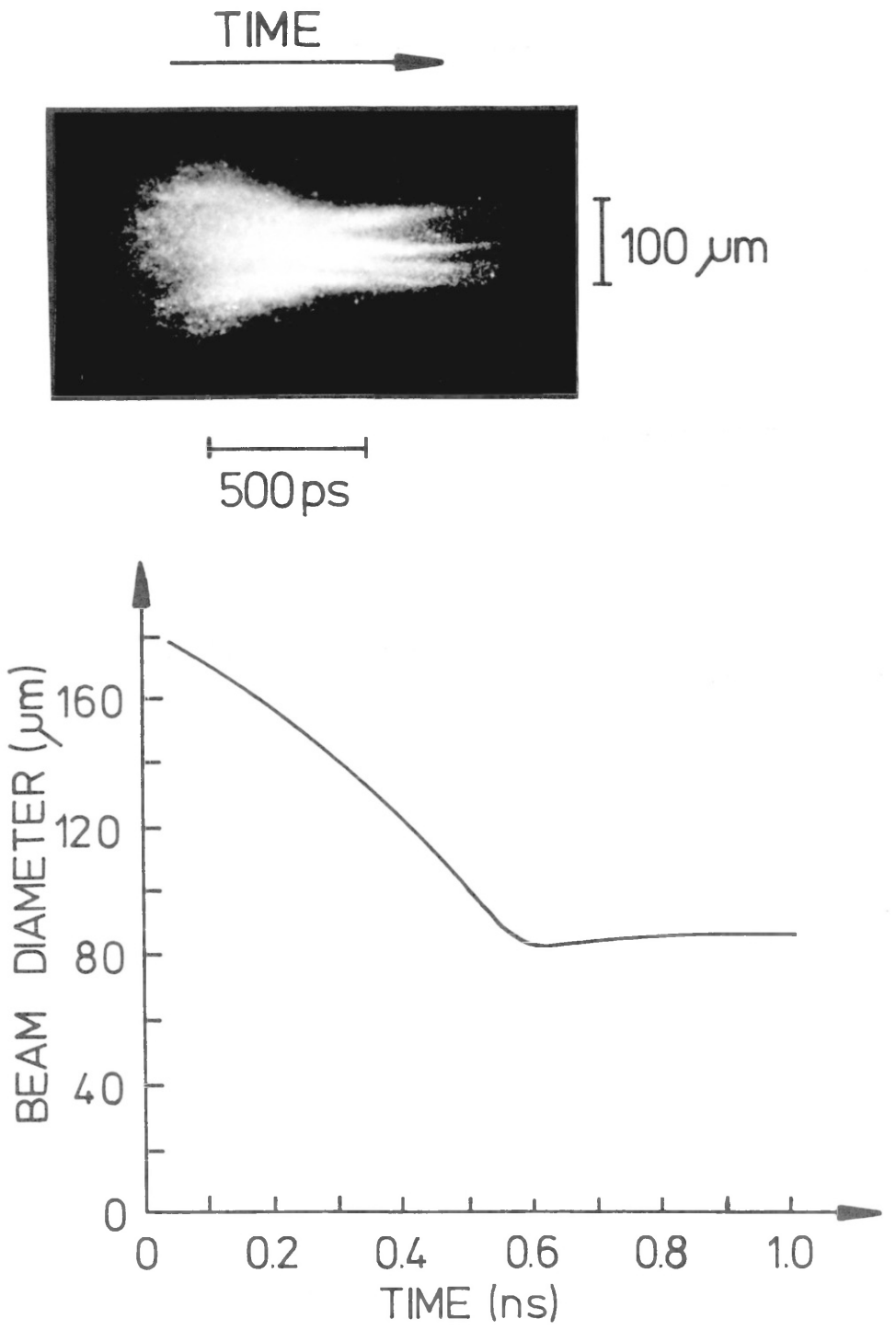


Figure 5.13 Streak of the transmitted interaction beam showing evidence of whole beam self-focusing in a bismuth plasma. The graph shows the variation of beam diameter with time determined from the streak (irradiance = 8.7×10^{14} Wcm^{-2}).

observed in fig(5.13).

From measurements made on the variation of beam diameter with time shown in the graph in fig(5.13) it can be seen that the beam focuses down to about half its initial diameter in about 500 ps. For the conditions estimated, the growth time for whole beam self−focusing will be dominated by the ion acoustic transit time across the beam. This gives a time scale of 790 ps for complete self−focusing of the beam. This is clearly consistent with the time scale of 500 ps observed experimentally for partial self−focusing of the beam.

Whole beam self−focusing was also observed for aluminium plasmas. The experimental conditions were identical to those described in sections (5.2) and (5.3) except that the interaction beam delay was reduced from 1.7 ns to 1.2 ns. This produced a hotter, denser plasma. Measurements made of the S.B.S. and S.R.S. spectra under these conditions give an electron density of 4.5×10^{20} cm^{-3} and a plasma temperature of 800 eV. Fig(5.14) shows a framing camera image taken late in the laser pulse under these conditions which shows the beam significantly reduced in size from its original diameter. The average F.W.H.M. across the beam profile is 125 μm which is 61% of the original average beam diameter of 205 μm. Also shown is the variation of beam diameter with time deduced from the streak record for this shot. The expected time scale for whole beam self−focusing determined by the ion acoustic transit time across the beam is approximately 500 ps in this case. As with the bismuth plasma, this is consistent with the time scale of 300 ps observed experimentally for partial self−focusing of the beam. The approximate time of the framing camera image is indicated on the graph. It can be seen that at the time of the framing camera image the beam diameter is reasonably constant. Consequently over the finite duration (120 ps) of the framing camera image the beam size did not significantly change. Hence there should be no significant temporal smearing of the framing camera image in fig(5.14) due to the finite gate width of the camera.

The framing camera image shows that the beam is not perfectly circular. This illustrates that following the evolution of a single cross−section across the beam with the streak camera can be misleading, since the beam diameter measured is dependent on the cross−section followed. The framing camera image provides considerably more reliable evidence of the occurrence of whole beam self−focusing, since it clearly demonstrates reduction in the beam diameter across any cross section. The non−uniformity of the beam shape probably explains why the initial diameter of the beam measured from the streak of 225 μm is slightly larger than

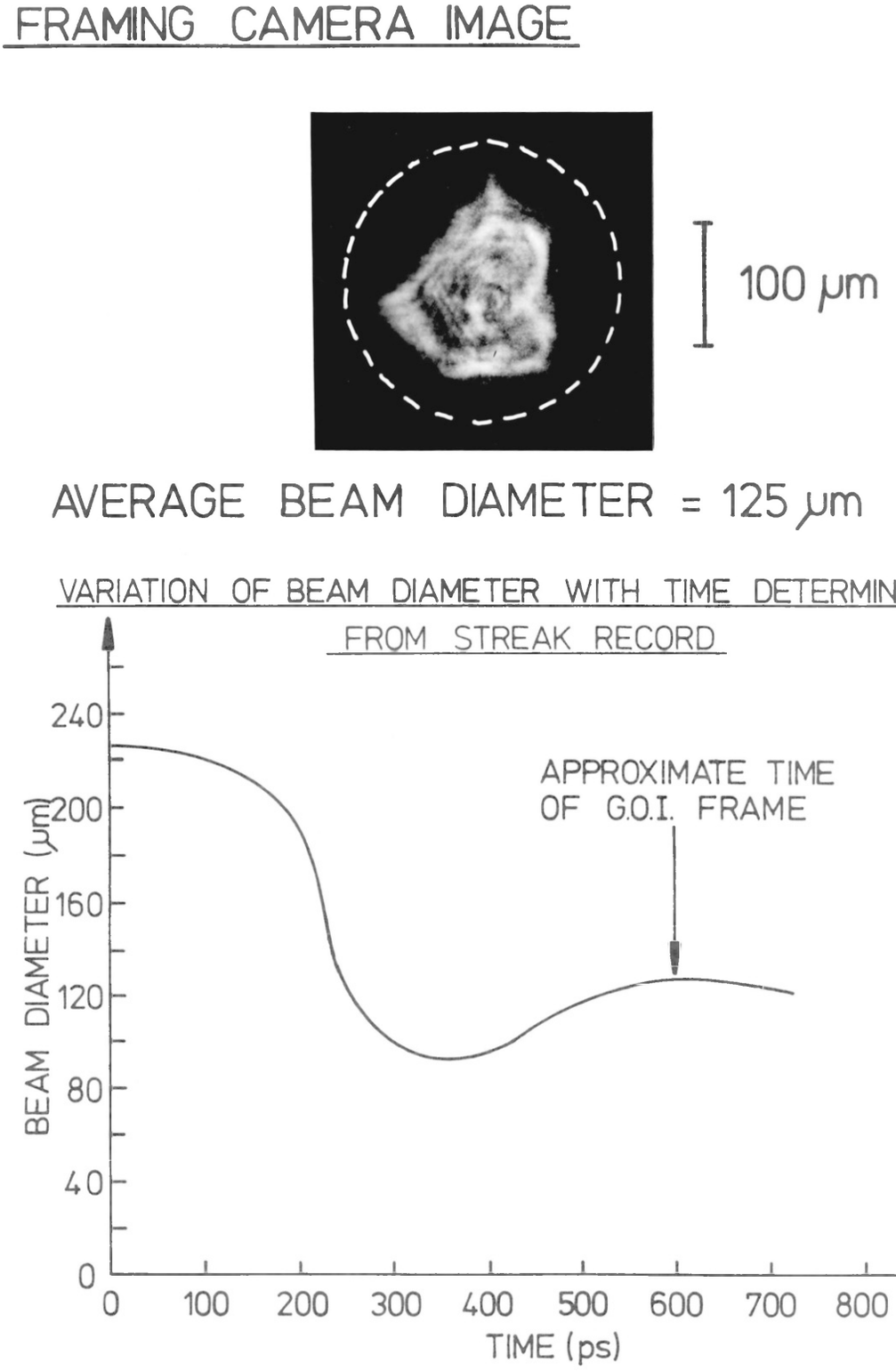


Figure 5.14 Framing camera image late in the laser pulse for an interaction beam delay of 1.2 ns (aluminium plasma and an irradiance of 1.0 × 10^{15} Wcm^{-2}). The beam diameter is clearly reduced from its original size which is indicated by the broken line superimposed on the image. Also shown is a graph of the variation of the beam diameter with time, determined from the streak record for this shot.

the actual initial average beam diameter of 205 μm (determined from E.P.M. data and measurements made of the interaction beam diameter by the framing camera with no preformed plasma present).

The filamentation theory of chapter 3 can be applied to the whole beam self-focusing by taking the beam diameter as the relevant scalelength for the intensity perturbation. For such large scalelengths the growth rate for thermal filamentation is found to dominate that for ponderomotive filamentation by approximately an order of magnitude. For the bismuth plasma, if it is again assumed that $Z=35$, $N_e=3.5\times10^{20}$ cm^{-3} and $T_e=850$ eV, then the theory predicts that any perturbation with a scalelength significantly greater than 20 μm will seed filamentation with a growth length of only 85 μm. Similarly for the aluminium plasma (taking $N_e=4.5\times10^{20}$ cm^{-3}, $T_e=800$ eV and $Z=13$) any perturbation with a wavelength greater than 30 μm will seed self-focusing with a growth length of 140 μm. The plasma length (0.8 mm and 1.0 mm for the bismuth and aluminium plasmas respectively) for both these cases is many times larger that this predicted growth length. Consequently the interaction beam should be expected to focus down significantly more than observed experimentally. The reason for this discrepancy is that the theory assumes only small perturbations of the plasma density and temperature. This assumption is not valid under the experimental conditions considered here, as the plasma density and temperature are significantly modified by the interaction beam. It is found that the temperature of the plasma is now self-consistently determined by the laser beam [98] and this modifies the self-focusing growth lengths. Hence although the perturbation filamentation theory of chapter 3 provides a good indication that the interaction beam is unstable to whole beam self-focusing (under these conditions), it does not provide reliable information about the expected growth lengths.

A better estimate of the expected growth length can be given by the simple model of Estabrook, Kruer and Bailey [98]. This model considers the case of cylinderical geometry and assumes that the intensity profile of the beam remains Gaussian as it self-focuses, ie. $I=I_0(z)\exp(-r^2/2r_0^2(z))$ for a beam propagating in the z direction. Where $r_0(z)$ is the radius of the beam at a distance z into the plasma. The temperature profile of the plasma is then estimated by balancing the classical radial heat flux with the inverse bremsstrahlung absorption. This gives

$$\left[\frac{T}{T_0}\right]^7 = 1 + A\exp\left[\frac{-r^2}{2r_0^2(z)}\right] \qquad (5.2)$$

where

$$A \approx \frac{\left[\frac{v_{osc}}{v_{th}}\right]^2 \left[\frac{r_0^2(0)}{\lambda_{ei}^2}\right]}{8\delta(z)}$$

Here λ_{ei} is the electron−ion mean free path of the unperturbed plasma, v_{th} is the electron thermal velocity, v_{os} is the oscillation velocity of electrons in the field of the laser beam and $\delta(z)$ is given by Spitzer [19]. The density profile can be easily obtained from eq(5.2) by assuming pressure balance ($n_0 T_0 = nT$) in the radial direction. The refraction of a light ray in the plasma is governed by the equation

$$\frac{\partial^2 r}{\partial z^2} = -\frac{1}{2}\frac{\partial(n_e/n_{ec})}{\partial r} \qquad (5.3)$$

for $n \ll n_{ec}$ and gradual deflections of the ray. By substituting the expression for the density into eq(5.3) and solving, the self−focusing distance can be determined. This is the distance for a ray initially at $r = r_0(0)$ to be refracted to $r = 0$. For the case of an initially parallel laser beam this gives a solution:

$$\frac{L_0}{r_1(0)} = 5\left[\frac{\omega_0}{\omega_{pe}}\right]\frac{(1 + 0.6A)^{4/7}}{A^{\frac{1}{2}}} \qquad (5.4)$$

Where $r_1(0) = 1.18 r_0(0)$ is the initial radius of the beam at its half intensity point, ω_0 is the frequency of the incident laser light and ω_{pe} is the plasma frequency. For the conditions relevant to fig(5.13) this gives a self−focusing distance of $L_0 = 1530$ μm. For the case of the aluminium plasma considered in fig(5.14) the self−focusing distance is $L_0 = 1300$ μm. In both cases the results appear to be consistent with the experimental observations of partial self−focusing for a plasma 800 μm long. Clearly under these conditions, the predictions of this model are more realistic than the predictions of the perturbation theory described earlier. It should be stressed that this model assumes a parallel collimated laser beam and so is not directly applicable to the results presented here, as f/2.5 focusing optics were used. However it does give a reasonable estimation of the degree of self−focusing which can be expected under these plasma conditions.

For the experimental conditions considered here we are in a regime where the plasma is strongly perturbed by the interaction beam and $A \gg 1$. Consequently in eq(5.4) L_0 depends only very weakly on A. This means that the self−focusing length is effectively only dependent on the plasma density and laser wavelength. This explains why the degree of self−focusing observed in both the aluminium and

bismuth plasmas is similar, even though they have significantly different ionization states. It is interesting to note that for the transmitted beam for an aluminium plasma with an interaction beam delay of 1.7 ns (compared with 1.2 ns here) reported on in section (5.3), no signs of whole beam self−focusing were observed. From eq(5.2) it follows that the degree of whole beam self−focusing is expected to decrease as the plasma density decreases. Substituting the measured values for the plasma conditions into eq(5.4) gives a whole beam self−focusing distance, at an interaction beam delay time of 1.7 ns, which is 30 % larger than the value of 1300 μm estimated for a delay time of 1.2 ns. Consequently the model predictions go some way towards explaining the experimental observation that significant whole beam self−focusing only occurs for aluminium plasmas at short interaction beam delay times, when the plasma density is relatively high.

Unfortunately the use of f/2.5 focusing optics makes a clear interpretation of the experimental observations by the model of Estabrook, Kruer and Bailey difficult. It seems likely that the actual variation of beam diameter with distance which occurs in the experiment will be similar to that shown in fig(5.15). The self−focusing, results in the beam being initially focused down slightly more rapidly than if no plasma were present. After the focus, when the beam expands, the self−focusing tends to limit the degree of the beam divergence and causes it to be recollimated. Presumably if the plasma were sufficiently long, the self−focusing process would eventually result in the beam being focused down again. In order to try and quantify this process, and to see if the degree of self−focusing observed in the experiments was reasonable, eq(5.3) was solved for the case of converging and diverging beams. For the aluminium plasma conditions relevant to fig(5.14) it

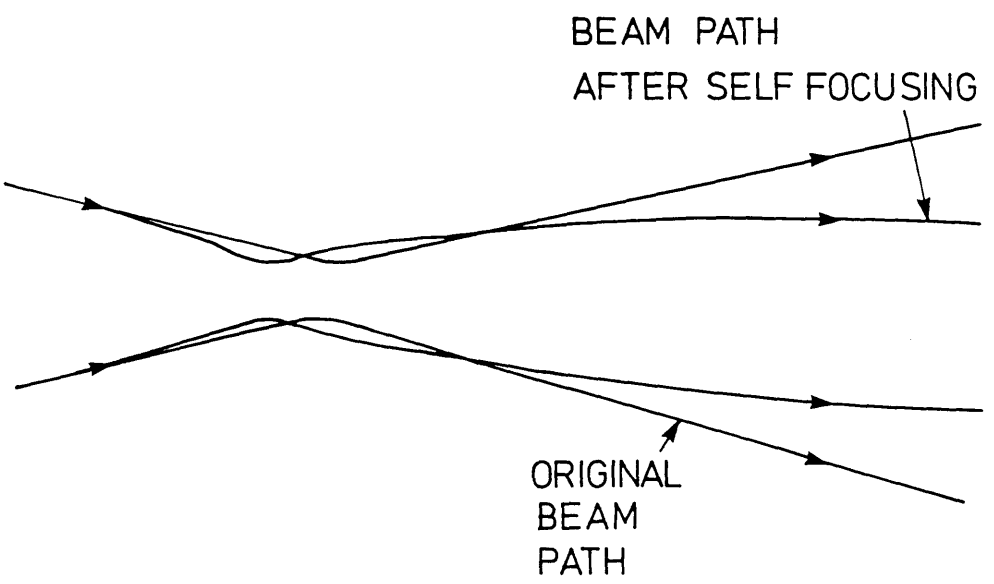


Figure 5.15 Probable beam path due to self−focusing.

was found that the self−focusing process caused the beam to focus down about 50 μm earlier in the plasma than it would otherwise do. The expansion of the beam, after the focus, predicted by the model is shown in fig(5.16). The model predicts that the beam diameter at the end of the preformed plasma ($\approx$650 μm after the focus) will be only 110 μm, compared with the original diameter of 205 μm. This clearly agrees well with the actual F.W.H.M. beam diameter measured from the framing camera of 125 μm. The size of the focal spot and the initial beam divergence, used for this calculation, were taken from the E.P.M. data. Clearly, in reality this may not be accurate since the self−focusing of the beam occurring before the focus may cause these parameters to be different. Consequently these values for the focal spot diameter and initial beam divergence can only be regarded as an approximate estimate. Due to this, the agreement obtained between the final beam diameter predicted by the model and that observed by the framing camera may well be fortuitous. However the agreement does at least indicate that the degree of self−focusing observed experimentally is not inconsistent with that expected theoretically.

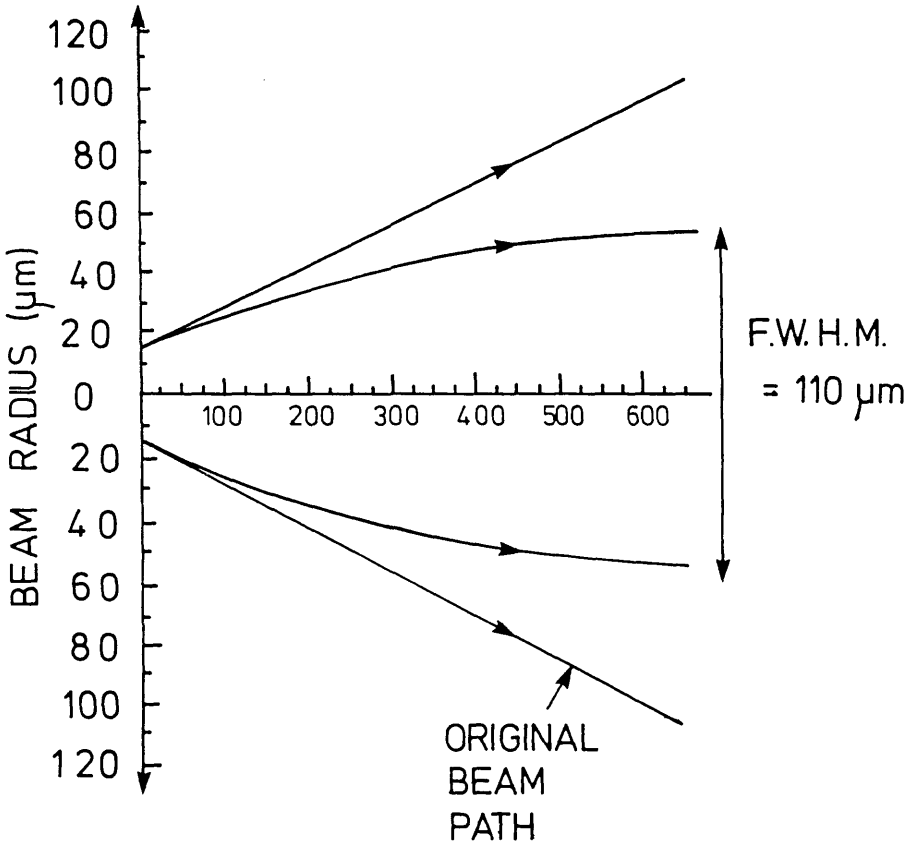


Figure 5.16 Expansion of the interaction beam after the focus predicted by the model of Estabrook et. al. (assuming $n_e = 4.5\times10^{20}$ cm^{-3} and $T_e = 800$ eV).

(5.5) Conclusions

Observations have been made of S.R.S., S.B.S. and filamentation occurring in a large underdense plasma. The S.R.S. and S.B.S. spectra observed were extremely non−uniform. In particular the S.B.S. spectrum indicated that regions of strong localized heating were present in the plasma possibly due to filamentation. From these spectra it was possible to estimate the plasma density and temperature.

Measurements made of the transmitted interaction beam showed considerable break up of the interaction beam due to filamentation, for low density aluminium plasmas. Intensity variations in the beam profile of up to 50:1 were observed due to filamentation. Under these conditions it appears that the dominant mechanism driving the filamentation process was the ponderomotive force rather than thermal effects. At early times before filamentation could grow the plasma was observed to smooth the beam profile. A possible explanation for this smoothing effect is refraction by local density perturbations in the plasma. The threshold for filamentation was experimentally observed to be between 7.9×10^{13} Wcm^{-2} and 4.5×10^{14} Wcm^{-2} which is consistent with theoretical predictions.

Finally, clear evidence has been obtained of the occurrence of whole beam self−focusing for bismuth plasmas, and aluminium plasmas at relatively short interaction beam delay times when the plasma density was higher. The degree of whole beam self−focusing observed appears to be consistent with predictions based on a simple analytical model. Unfortunately the use of f/2.5 focusing optics for the interaction beam made it difficult to directly compare the experimental results with the theoretically expected level of whole beam self−focusing. Useful future work would be to repeat these measurements using f/10 focusing optics so that the incident interaction beam more closely approximated the parallel beam case. Clearly whole beam self−focusing can be expected to be even more effective in higher density plasmas than those studied here. In conclusion, the significant levels of filamentation (both ponderomotive and thermal) observed here in a large underdense plasma, appear to present a serious threat to the success of proposed laser fusion implosions.

CHAPTER 6

SUPPRESSION OF INSTABILITIES IN LARGE UNDERDENSE PLASMAS

(6.1) Introduction

It has been widely recognized that intensity hot spots present in high power laser beams may enhance the levels of S.B.S. and S.R.S. observed. Also these hot spots may act as a seed for the filamentation instability. Consequently several beam smoothing techniques have been developed to remove these hot spots, and give some control over the gross laser beam profile. As well as giving suppression of harmful instabilities it is hoped that these techniques will give the beam uniformity required to drive successful I.C.F. implosions. The two main approaches which have been developed to provide beam smoothing are the Random Phase Plate (R.P.P.) technique [49,99] and the use of an Induced Spatial Incoherence System (I.S.I.) [48,100]. The R.P.P. technique breaks the incident laser beam up into a large number of individual beamlets which are then randomly shifted in phase. These beamlets are then overlapped onto the target by a focusing lens. The resulting interference pattern produced eliminates any gross, long scalelength non−uniformities from the laser beam profile, but introduces pronounced short scalelength intensity fluctuations, which remain frozen in the focal spot distribution throughout the laser pulse. An I.S.I. system is similar to this except that a broadband laser is used so that the coherence time of the laser, t_c, is shorter than the incremental delay between indivdual beamlets. This causes the instantaneous interference pattern produced to be averaged out over times which are long compared to t_c. This results in a smooth time averaged focal spot profile.

Recent results [101,102] have demonstrated that an I.S.I. system can significantly reduce the levels of S.R.S. and S.B.S. observed in laser plasma interactions. In this chapter an experiment will be reported on to determine the effectiveness of both an I.S.I. system or a R.P.P. to suppress instabilities in a large underdense plasma generated by the experimental arrangement described in chapter 4. In section (6.2) detailed descriptions of the R.P.P. and I.S.I. beam smoothing techniques used will be described. In section (6.3) the measurements made of the effectiveness of these two techniques, to reduce the observed levels of S.R.S. and S.B.S., will be reported on. Finally results will be presented in section (6.4) on the ability of these two techniques to reduce the filamentary break up of a high power laser beam, which was observed in chapter 5.

(6.2) Laser beam smoothing techniques

In order to determine the effectiveness of either a R.P.P. or I.S.I. to suppress S.R.S., S.B.S. and filamentation the experimental arrangement described in chapters 4 and 5 was used. The only difference being that the interaction beam was modified by either the use of a R.P.P. or I.S.I..

(6.2.1) Random Phase Plate

The basic arrangement used for the R.P.P. is illustrated in fig(6.1). The incident interaction beam was broken up into a large number (approximately 2500) of individual beamlets, each 2 mm by 2mm, by the R.P.P.. This was done by the use of a transmitting SiO_2 coating on one surface of the R.P.P.. The coating thickness varied across the R.P.P. and randomly imposed a phase shift of either 0 or Π for each beamlet. The randomly phase shifted beamlets were then overlapped in the target plane by a f/2.5 aspheric doublet lens. For a R.P.P. the resulting intensity distribution produced in the focal plane of the lens is given by the expression [103].

$$I(x,y) = I_0\left[\frac{\sin\Theta_x}{\Theta_x}\right]^2\left[\frac{\sin\Theta_y}{\Theta_y}\right]^2\left[\mathrm{Re}\sum_{k,l}\exp i\left[\Phi_{k,l} + \frac{2\Pi}{f\lambda}(X_k x + Y_l y)\right]\right]^2 \qquad (6.1)$$

Where $\Theta_x = \Pi dx/f\lambda$ and $\Theta_y = \Pi dy/f\lambda$

The indicies (k,l) refer to an individual element of the R.P.P., (X_k,Y_l) is the centre of that element measured from the beam axis, and $\Phi_{k,l}$ is the random static phase shift (in this case Π or 0) imposed on the (k,l) beamlet by the R.P.P.. The focal length of the lens used is denoted by f, d is the width of an individual beamlet, λ is the wavelength of the laser and (x,y) the coordinates in the focal plane. For simplicity this expression has assumed a constant near field amplitude of the beam at the R.P.P.. Eq(6.1) can be broken down into two parts. The first part (the sinc function terms) is just the Fraunhofer diffraction limit of an indivdual beamlet and this gives the envelope function for the focal spot profile. The zero order diffraction square, of the envelope function, bounded by $x_0,y_0 = \pm\lambda f/d$ contains 82 % of the laser energy. The F.W.H.M. of the focal spot is given by $0.886f\lambda/d$. The second part of eq(6.1) (the term in the square brackets) is due to the interference between the individual beamlets overlapping in the focal plane. This term results in pronounced short scalelength intensity

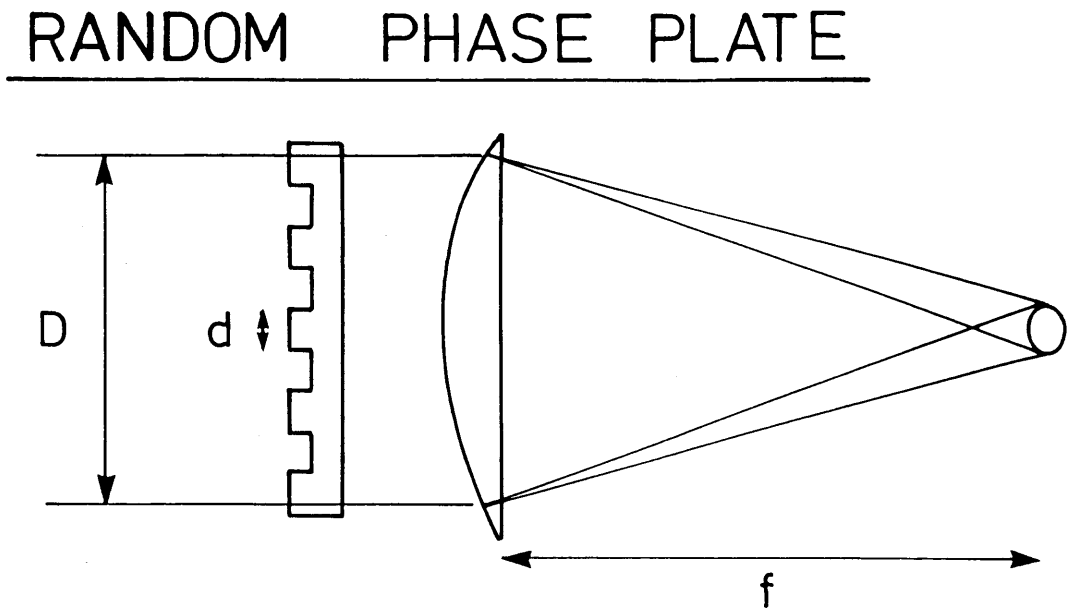


Figure 6.1 Random phase plate (for the experimental conditions used here d ≈ 2 mm, D ≈ 10 cm and f ≈ 25 cm).

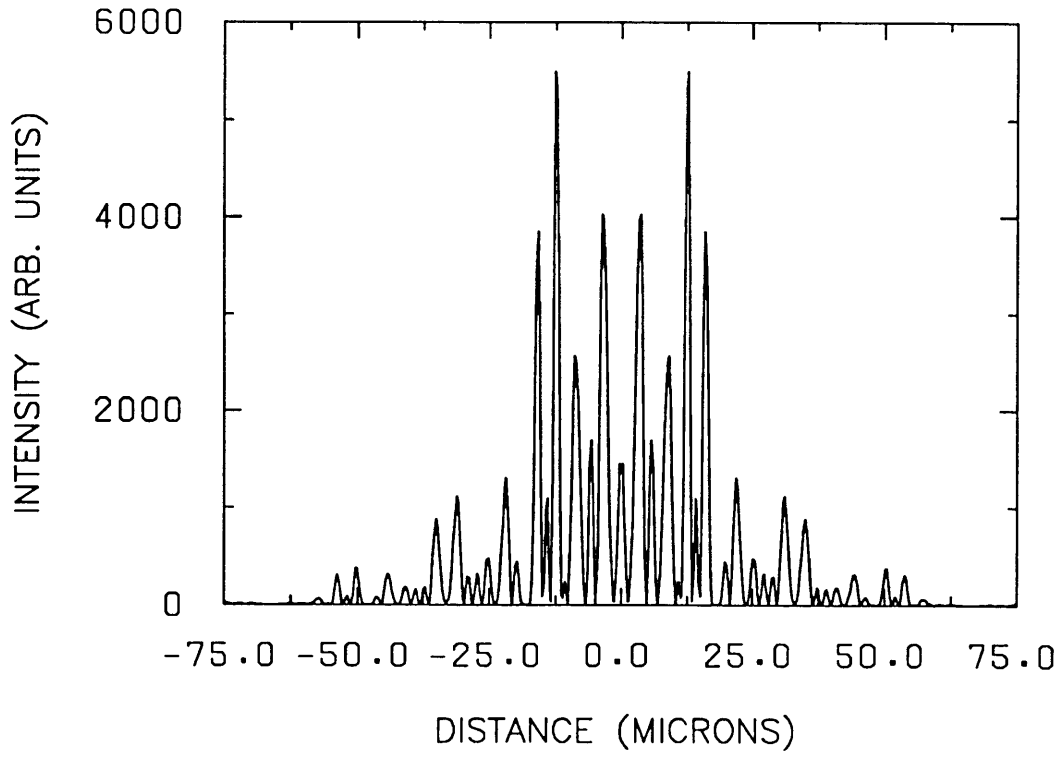


Figure 6.2 Theoretical calculation of the far field intensity distribution generated by the random phase plate.

fluctuations which are superimposed on the smooth envelope function for the focal spot profile. Fig(6.2) shows the intensity distribution calculated from eq(6.1) for the experimental conditions used here (f= 25 cm, d= 2 mm, λ= 0.53 μm and D= 10 cm). The typical dimension of these short scalelength intensity fluctuations (which can clearly be seen in fig(6.2)) is given by $2\lambda f/D$, the diffraction limit for the original laser beam. The principle of a R.P.P. is that these short scalelength intensity fluctuations are on too small a scale for the plasma to respond to. Consequently the plasma will only 'see' the smooth envelope function of the beam profile. However the disadvantage of this scheme is that these small scalelength fluctuations remain frozen in the focal spot distribution throughout the laser pulse. For the experimental conditions used here the expected focal spot F.W.H.M. is 58 μm and the intensity fluctuations should be on a 2.7 μm scalelength. Actual measurements made with the E.P.M. of the interaction beam gave the far field F.W.H.M. to be 70 μm, in reasonable agreement with that expected theoretically.

(6.2.2) Induced spatial incoherence

The basic arrangement of the I.S.I. system used is illustrated in fig(6.3) [104]. The incident broadband ($\Delta\omega/\omega \approx 0.1\%$) laser beam was broken up into a 5×5 array of individual beamlets by transmission echelons consisting of two perpendicular arrays of glass blocks. The first echelon imposed incremental delays of 5 ps between adjacent beamlets and the second echelon incremental delays of 50 ps. Consequently any two beamlets had a minimum delay of 5 ps between them. This is larger than the coherence time, t_c, of 2 ps which was measured for the broadband laser beam used for I.S.I.. When the beamlets are overlapped in the target plane by the focusing lens the resulting instantaneous (ie. $t < t_c$) interference pattern produced is extremely complicated and of a similar nature to that produced by a R.P.P.. This is illustrated in fig(6.3). However for times longer than t_c the individual beamlets are effectively incoherent with respect to each other and the complicated interference pattern is smoothed out. For times significantly longer than t_c only the smooth envelope beam profile will be observed as shown in fig(6.3).

The initial broadband laser pulse was generated by using a high gain phosphate glass rod as the lasing medium in the oscillator, rather than neodymium Y.L.F. which is used in the normal operation of the laser. This allowed the generation of a laser pulse with the necessary 1−2 nm bandwidth. The basic principles of the generation of broadband laser pulses by this technique are

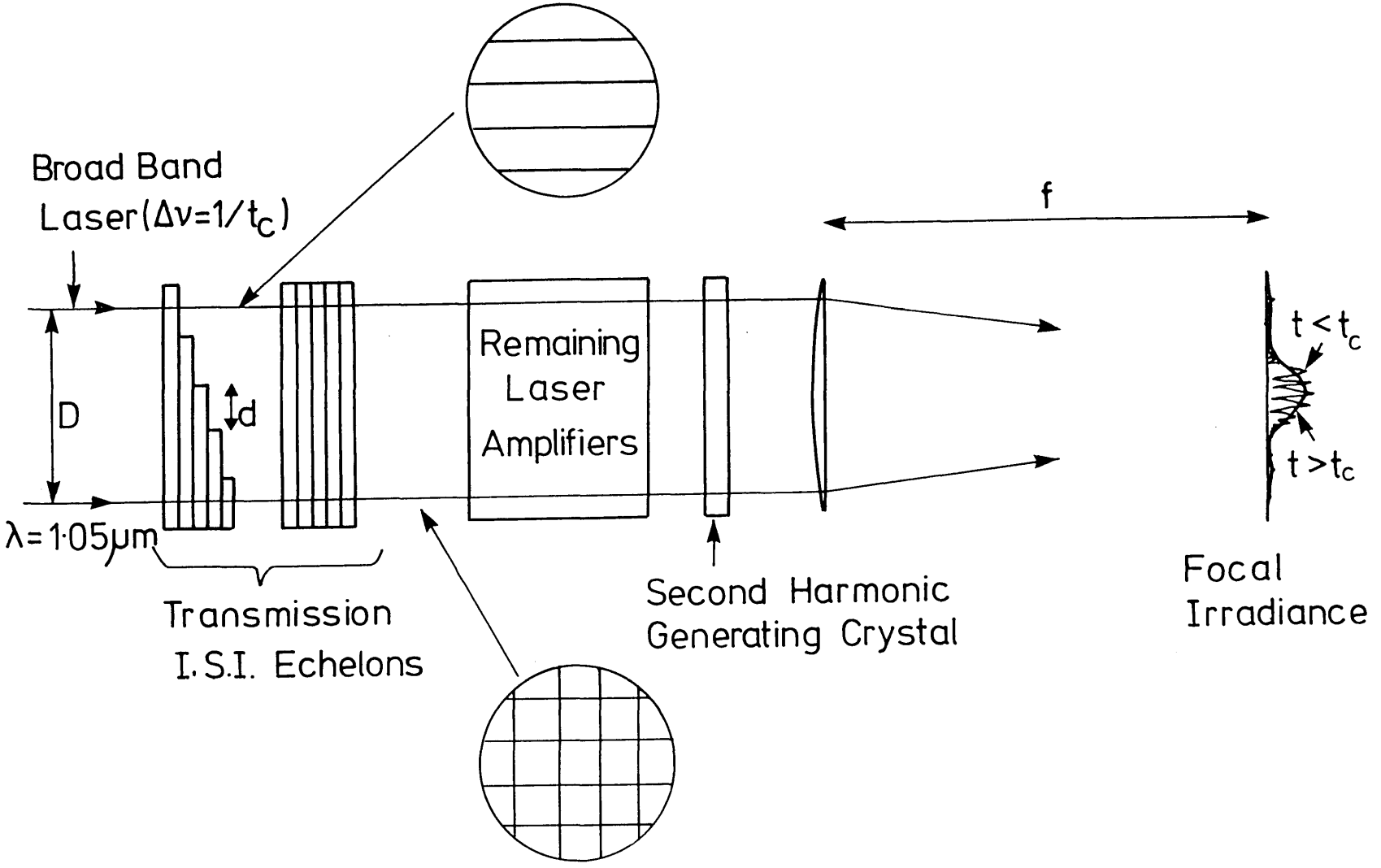


Figure 6.3 The induced spatial incoherence system used in these experiments.

discussed elsewhwere [104,105]. The bandwidth of the standard narrowband Y.L.F. oscillator is 1.1×10^{-4} nm.

The basic principle of the I.S.I. system used here is similar to that developed elsewhere [100] except that the echelons, used to break the beam up spatially into individual beamlets, were placed earlier down the amplifier chain instead of after the second harmonic generating crystals. This is advantageous for future use in multibeam I.S.I. systems, since it allows a single pair of echelons to be placed in a high power laser sytem before the laser pulse is split into individual beams. Consequently it is then no longer necessary to have a separate echelon pair at the output of each beam. The disadvantage of this approach is that it imposes a stricter limit on the maximum total laser power, which can be propagated through the laser system, without causing damage to the optical components of the laser. This is because the near field beam pattern generated by the echelons is very non-uniform. This limited the infra-red energy for the broadband interaction beam to a maximum of about 150 J in this experiment. Due to the poorer second harmonic conversion efficiences which can be obtained with broadband laser beams [104] of typically only 35%, the final energy output of the interaction beam was limited to about 50-60 J of green energy. The other advantage of the I.S.I. sytem used here is the use of transmission echelons rather than the reflectance echelons used elsewhere [100]. This greatly eases the alignment of the beam and also significantly reduces the cost of the echelons. The individual glass blocks in the echelon were all anti-reflectance coated at 1.056 μm so that the overall transmission through both echelons was over 80%.

In order to generate a focal spot of comparable size to the case of a R.P.P. with f/2.5 focusing optics, a f/10 lens was used with the I.S.I. system. This is because with the large, 2 cm $\times$ 2 cm, beamlets used with the I.S.I. system, the focal spot size will be determined by the beam divergence rather than the diffraction limit for each beamlet. The beam divergence of the VULCAN glass laser is typically 100 μrad, and for a 1 m focal length lens this gives a focal spot size of approximately 100 μm. This is comparable with the spot size generated with a R.P.P. and f/2.5 lens.

(6.3) Suppression of S.R.S. and S.B.S. in a large underdense plasma

In this experiment three different situations were studied. Firstly a normal coherent narrowband laser pulse was used as the interaction beam and was

focused onto target by a f/10 aspheric singlet lens. From the E.P.M. data this was found to generate a focal spot of 120 μm diameter (F.W.H.M.). The beam diameter was approximately constant along the whole length of the preformed plasma. Secondly the I.S.I. system was used with the same f/10 focusing lens. From the E.P.M. data no significant difference was found between the I.S.I. focal spot size and that generated by the normal coherent interaction beam. This confirms that the focal spot size was dominated by the laser beam divergence. As stated in section(6.2.2) the reason for using a f/10 focusing lens in these cases was to give a comparable focal spot size to the final situation considered. This was a normal coherent beam with a R.P.P. and f/2.5 focusing optics. This gave a focal spot size of 70 μm F.W.H.M. in the far field of the beam, which was situated to be half way along the preformed plasma. At either end of the preformed plasma the beam diameter increased to 140 μm. The E.P.M. measurements of the beam diameter along the preformed plasmas were used to adjust the average irradiances calculated for each of the three cases studied. This enabled a direct comparison to be made between the results obtained in each of these three situations. This correction has been made for all the data presented in this chapter.

Fig(6.4) shows images taken from the E.P.M. of the far field focal spot distributions for the three cases considered. Also shown are typical microdensitometer traces across each beam profile. For the normal coherent interaction beam pronounced structure with a typical scalelength of 15−25 μm, causing intensity ratios of up to 5:1, can be seen. This gross structure is eliminated with the use of the R.P.P., but the interference pattern produced by the R.P.P. results in a fine scale structure with pronounced intensity fluctuations on a 2−3 μm spatial scalength, as expected. It should be noted the magnification of the R.P.P. image is twice that of the other two cases. It can be seen that the far field image for the I.S.I. beam is observed to have very little structure compared with the other two cases.

Measurements were made of the levels of S.R.S. and S.B.S. observed for the three cases considered using the arrangement described in chapter 4. Fig(6.5) shows the variation with irradiation of the level of S.B.S. observed for each case. It can be seen that the use of a R.P.P. reduces the level of S.B.S. by a factor of 10−20 and that for the I.S.I. beam the level of S.B.S. is reduced below the threshold of detection. This relatively high threshold of detection level was determined by small fractions of the incident laser beam being scattered from chamber windows and lenses etc. Even though this scattered light arrived earlier than the true S.B.S. signal it caused the energy detector diode to saturate at these

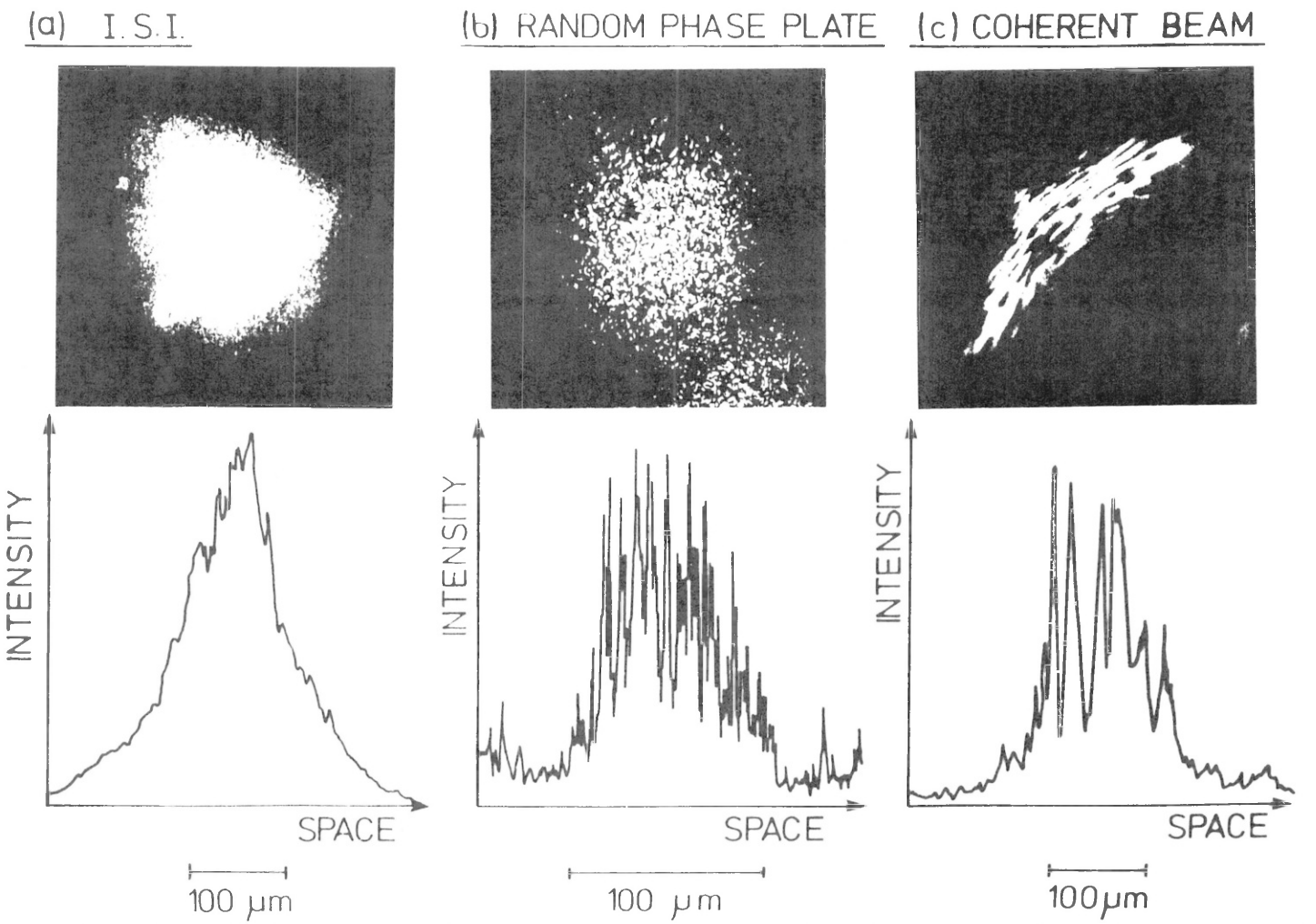


Figure 6.4 Typical far field focal spot distributions measured with the equivalent plane monitor: (a) broadband I.S.I. beam (f/10 lens), (b) narrowband beam with R.P.P. (f/2.5 lens) and (c) normal coherent narrowband beam (f/10 lens). Note that the magnification for the R.P.P. image and micodensitometer trace is twice that of the other two cases.

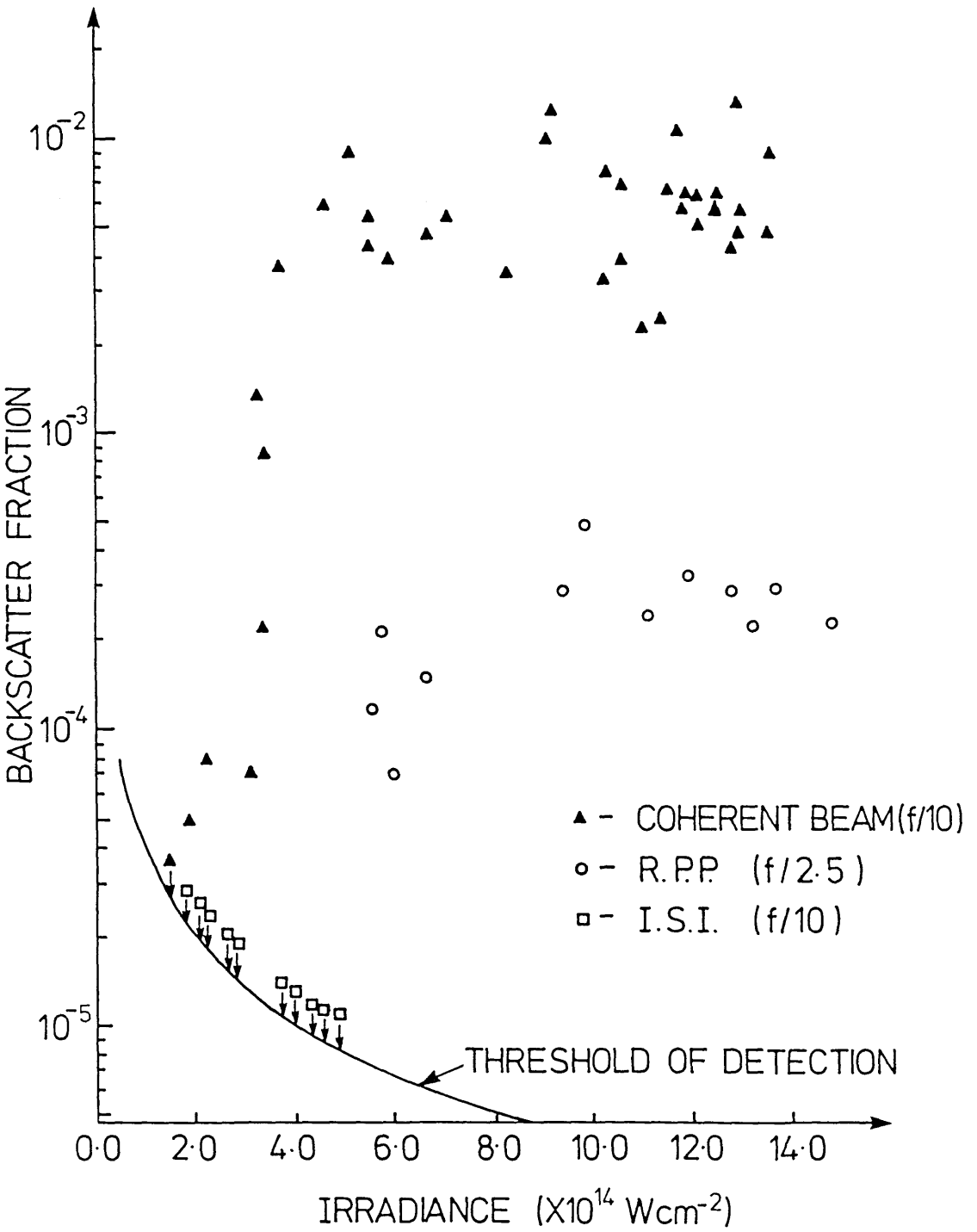


Figure 6.5 Variation of the S.B.S. backscatter fraction with average laser irradiance. An arrow (↓) indicates that the S.B.S. signal was lower than the threshold of detection.

light levels and consequently did not allow measurments to be made of the S.B.S. scattered light level. Due to the small wavelength shift of the S.B.S. signal it was not possible to spectrally separate this scattered light from the true signal. However, for irradiances of $4.0-5.0 \times 10^{14}$ Wcm^{-2} the I.S.I. system can be seen to suppress the S.B.S. level by at least a factor of 500. Unfortunately, as explained in section (6.2.2), the laser output for the I.S.I. beam was limited to 50−60 J of green energy and so it was not possible to take data for higher irradiance shots than this. For the normal coherent interaction beam there appears to be a threshold for S.B.S. at about $1.0-2.0 \times 10^{14}$ Wcm^{-2}. Approaching irradiances of 10^{15} Wcm^{-2} the S.B.S. level seems to saturate at a level of about 1 %. Clearly in a real fusion target, electron densities up to critical would be present, rather than just up to $\approx 0.08\ n_{ec}$ as in this experiment and so much higher levels of S.B.S. could be expected.

Fig(6.6) shows the variation of S.R.S. level with irradiance for the three cases considered in this experiment. Similar reductions are observed for S.R.S., due to the R.P.P. or I.S.I., as in the S.B.S. case. However the level of S.R.S. observed with the I.S.I. beam does not fall below the threshold of detection. This is because scattered green laser light is no longer a problem with the Raman energy detector as it is blocked by the OG570 glass filters used. For the case of a normal coherent interaction beam, a wide variation is observed in the level of S.R.S. for a particular irradiance, on a shot to shot basis. It seems likely that in this case the level of S.R.S. depends critically on the scale and level of the hot spots present in the interaction beam. From the E.P.M. data this is known to vary on a shot to shot basis. It also seems reasonable that for S.B.S. the level of scattered light does not depend so critically on the variation of the hot spots present in the beam. This is because it appears from fig(6.5) that for these plasma conditions the S.B.S. level is close to saturation for irradiances greater than 5×10^{14} Wcm^{-2}. From the measured energy levels of S.R.S presented in fig(6.6) it is not possible to say if any threshold is present for the case of a coherent interaction beam. However from the simultaneously recorded, time resolved measurments made of the S.R.S. spectra it is known that the scattered light level reduced dramatically for irradiances below 2×10^{14} Wcm^{-2}. Hence it appears a threshold was present for S.R.S., as well as for S.B.S., at irradiances of $1-2 \times 10^{14}$ Wcm^{-2}. Unfortunately no measurements were obtained with the S.R.S. energy detector at these irradiances.

Since the preformed plasmas generated in this experiment have long scalelengths in the direction of propagation of the interaction beam, the thresholds

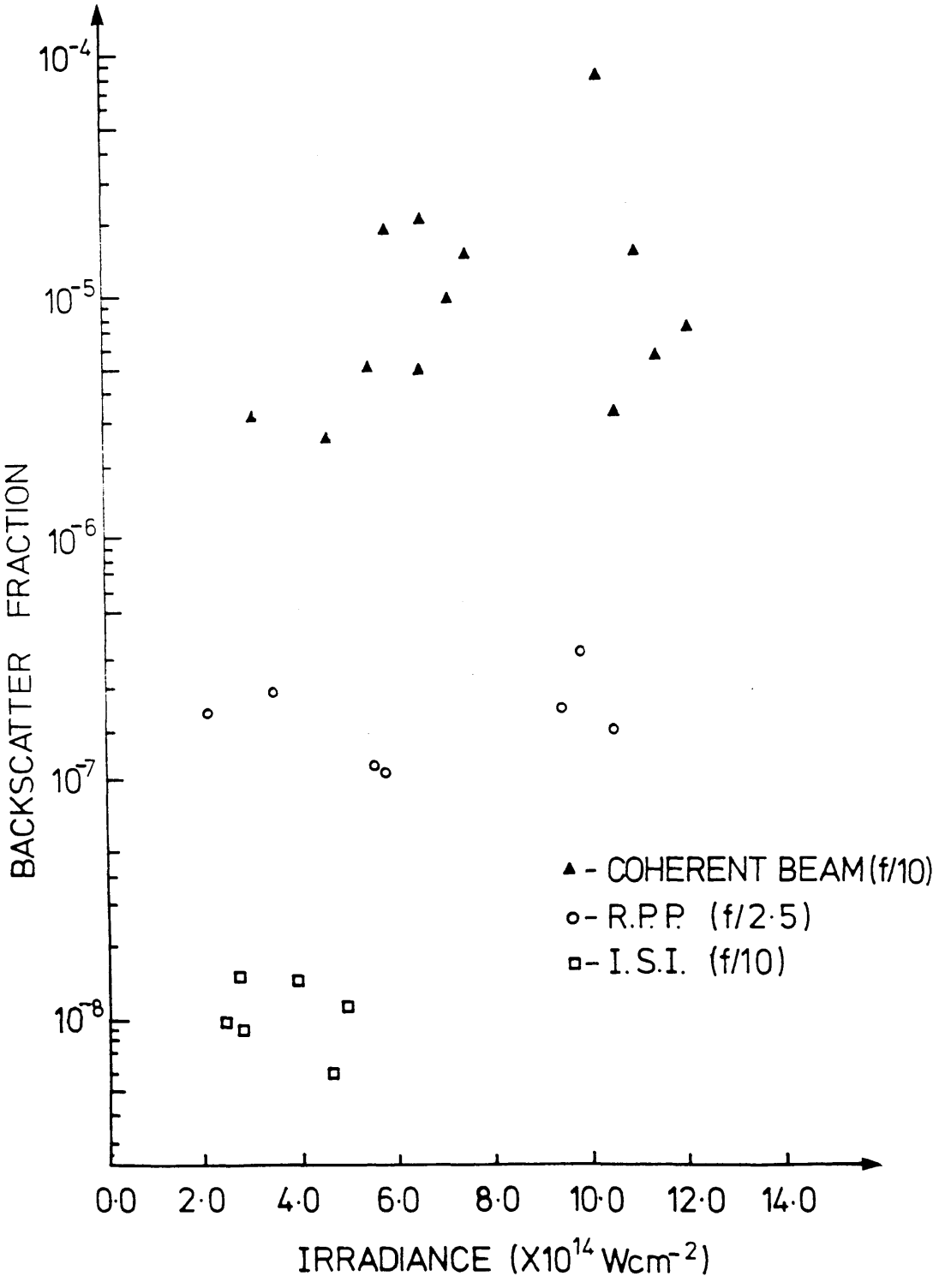


Figure 6.6 Variation of the S.R.S. backscatter fraction with average laser irradiance.

for S.R.S. and S.B.S. should be significantly lower than those expected in other short scalelength experiments [52,55]. If the axial density of the plasma is assumed to be approximately parabolic (ie. of the form $n = n_0(1-x^2/L^2)$) then the threshold for convective S.R.S. can be calculated using eq(3.27). Taking $n_e/n_{ec} = 0.08$ and a plasma temperature of 500 eV (as indicated by the S.R.S. and S.B.S. spectra) and assuming a density scalelength of 500 μm this gives a threshold of only 5×10^{13} Wcm^{-2}. However this estimate of the threshold should be treated with caution as it depends critically on the density profile assumed. For example, if a linear density profile is assumed the threshold becomes 1.7×10^{15} Wcm^{-2} for a 500 μm density scalelength. For these experimental conditions it is found that Landau and collisional damping, place a more stringent restriction on S.B.S. than the density scalelength does. Consequently the homogeneous plasma threshold for S.B.S. of eq(3.13) can be used. This gives a threshold of the order of 10^{12} Wcm^{-2}.

There is clearly a significant disagreement between these theoretical thresholds and those observed experimentally, which for both S.R.S. and S.B.S. appear to be of the order of $1-2 \times 10^{14}$ Wcm^{-2}. Partly, this disagreement may be due to the presence of density non-uniformities in the plasma. These non-uniformities would decrease the effective density scalelength from the ideal value of 500 μm considered above. This would increase the expected thresholds for both S.R.S. and S.B.S.. Observations of the existence of a certain degree of density non-uniformities in plasmas generated by a similar experimental arrangement will be given in chapter 7 of this thesis. For S.R.S., this argument appears to be reasonable, since only a marginal reduction in the density scalelength from the assumed value of 500 μm is required to give agreement with the experimentally observed threshold of $1-2 \times 10^{14}$ wcm^{-2}. However for S.B.S., for the theoretical threshold to be increased to 10^{14} Wcm^{-2} would require a density scalelength of only 33 μm (obtained using eq(3.16)). It seems extremely unlikely that the plasma could be sufficiently non-uniform to give such a short density scalelength. Consequently another explanation is required to reconcile the differences in the expected and observed thresholds for S.B.S..

Using the results of chapter 3 the expected growth rates for S.B.S. and S.R.S. are 3.8×10^{12} s^{-1} and 9.4×10^{12} s^{-1} respectively (for an irradiance of 5×10^{14} Wcm^{-2}). These growth rates should be sufficiently fast to allow significant growth of both instabilities on time scales less than the coherence time of 2 ps for the broadband I.S.I. interaction beam. Consequently both instabilities should still be influenced by the intensity non-uniformities generated by the

instantaneous I.S.I. interference pattern. Hence it appears surprising that I.S.I. is so effective at dramatically reducing the levels of both S.R.S. and S.B.S., as beam smoothing only occurs on a timescale greater then t_c. This seems to suggest that the suppression of both instabilities occurs via some intermediate mechanism which occurs on time scales longer than t_c. Further evidence of the existence of an intermediate mechanism is provided by the magnitude of the reductions in the levels of S.R.S. and S.B.S. caused by the R.P.P. or I.S.I.. These are significantly greater than would be expected from simple intensity averaging of the hot spots present in the normal coherent interaction beam. One possible explanation for both these anomalies is that S.B.S. and S.R.S. are driven by filamentation, which grows from hot spots present in the initial laser beam, rather than directly by the hot spots themselves. The possible enhancement of S.R.S. by filamentation has been considered in depth by Barr, Boyd and Coutts [67]. In general, they concluded that filamentation will enhance S.R.S. unless the density in the filaments becomes sufficiently low that Landau damping becomes significant. Both a R.P.P. and I.S.I. should suppress filamentation under these experimental conditions. For a R.P.P. this is because the filamentation model described in section (3.2) predicts that, for the plasma conditions here, filamentation will only grow on a scalelength larger than 5−6 μm (see fig(5.10)). This is significantly larger than the 2−3 μm intensity variations produced by the R.P.P. with f/2.5 focusing optics. For I.S.I., filamentation should be suppressed since the instantaneous interference pattern is smoothed out over times greater than the laser coherence time, which is significantly shorter than the growth time for filamentation. The suppression of filamentation by both a R.P.P. or I.S.I. has also been demonstrated by numerical simulations [80].

The occurrence of filamentation could also explain the discrepancy between the observed and expected thresholds for S.B.S.. This is because for these plasma conditions filamentation is expected to have a threshold near 10^{14} Wcm^{-2}. Consequently the rapid increase in the level of S.B.S. observed for irradiances of $1.0-2.0 \times 10^{14}$ Wcm^{-2} could be due to the onset of filamentation. For irradiances less than 10^{14} Wcm^{-2}, S.B.S. may still be occurring as predicted by the homogeneous threshold of 10^{12} Wcm^{-2} (or somewhat higher if density non−uniformities are present in the plasma) but at a level too low to be detected by the limited effective sensitivity of the S.B.S. energy monitor. For S.R.S. it is possible that the rapid increase in the level of the instability near 10^{14} Wcm^{-2} may be due to either the onset of filamentation or the actual convective threshold.

Further evidence that filamentation plays a key role in the occurrence of

S.R.S. and S.B.S. is provided by the time resolved spectra of the Brillouin and Raman scattered light. Fig(6.7) shows an example of a typical Raman spectrum observed when an interaction beam with a random phase plate was used. It can be seen that the Raman emission now covers a significantly narrower wavelength range than was previously observed in section (5.2) for the case of a coherent interaction beam. The typical wavelength shift of the Raman emission here (corresponding to an electron density of $0.08N_{ec}$) is similar to the maximum wavelength shift observed in the spectrum for the coherent beam. No Raman emission for shorter wavelengths, associated with lower densities, is now observed. This is consistent with these lower densities being generated by the occurrence of filamentation for the normal coherent interaction beam case, but not being generated when the R.P.P. is used, due to the suppression of the filamentation instability. Fig(6.8) shows a typical Raman spectrum observed when I.S.I. was used. It can be seen to be very similar in nature to that observed when the R.P.P. was used. The narrow spread of wavelengths for the Raman spectra when either the R.P.P. or I.S.I. was used suggests that the electron density inferred from these spectra is a reasonably accurate measure of the homogeneous plasma density.

Fig(6.9) shows an example of a typical S.B.S. spectrum observed when the R.P.P. was used. When compared with the S.B.S. spectrum for a coherent

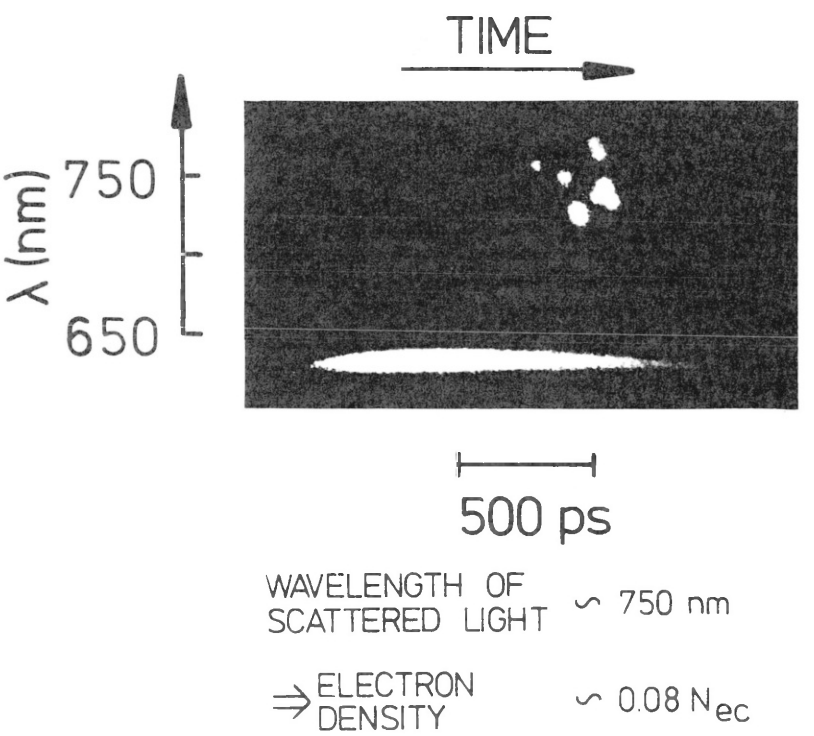


Figure 6.7 Typical S.R.S. spectrum observed for a narrowband interaction beam with a R.P.P. (irradiance = 7.5×10^{14} Wcm^{-2}).

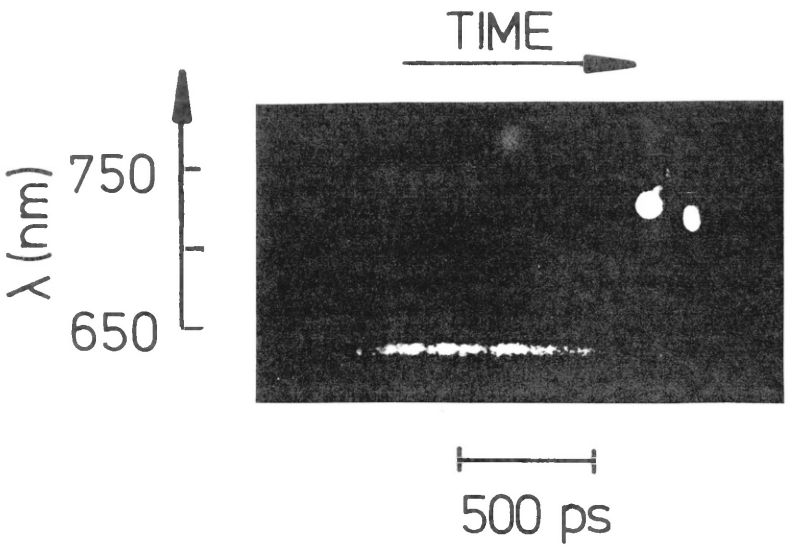


Figure 6.8 Typical S.R.S. spectrum observed for a broadband interaction beam with I.S.I. (irradiance = 3.5 × 10^{14} Wcm^{-2}).

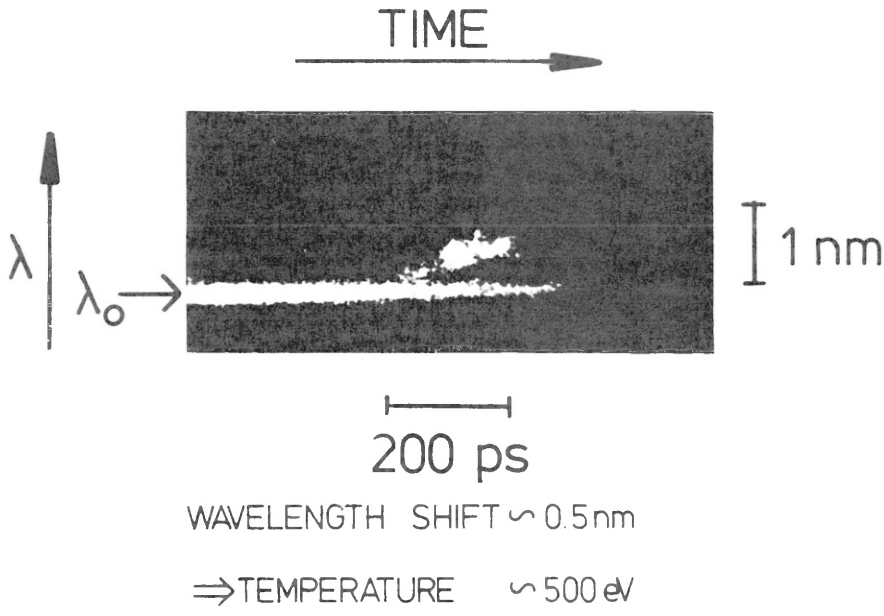


Figure 6.9 Typical S.B.S. spectrum observed for a narrowband interaction beam with a R.P.P. (irradiance = 7.9 × 10^{14} Wcm^{-2}).

interaction beam of fig(5.2) it can be seen that the large shifted components associated with high temperatures (>1 keV) are no longer present. Only a single component is observed to the S.B.S. spectrum corresponding to a plasma temperature of 500 eV. This is in agreement with the small shifted component of the coherent beam S.B.S. spectrum which was associated with the background plasma temperature. This gives further support to the argument that for a coherent interaction beam filamentation occurs, in this case giving rise to regions of strong localized heating and hence large shifted components to the S.B.S. spectrum.

Whereas when a R.P.P. is used filamentation is suppressed and only a single component is observed to the S.B.S. spectrum, corresponding to the background plasma temperature of 500 eV. No measurements were made of the S.B.S. spectra for the case of an interaction beam with I.S.I.. It is doubtful if any useful information could have been obtained from such spectra, since any details in the spectra would have been blurred by the wide bandwidth of the laser.

Finally, data was taken to determine the effectiveness of the I.S.I. system with a f/2.5 focusing lens. Fig(6.10) shows the variation of S.R.S. level with irradiance for f/2.5 focusing optics with and without I.S.I.. The focusing lens was positioned so as to produce the tightest focus approximately midway along the preformed plasma. It can be seen that for these circumstances the use of the I.S.I. system actually increases the level of S.R.S. (by approximately a factor of 100) compared with the normal coherent beam case. The explanation for this is that for a f/2.5 lens the entrance plane of the preformed plasma is no longer in the far field of the interaction beam, but is in the quasi−near field where the individual beamlets no longer significantly overlap. This gives rise to an extremely non−uniform focal spot. This is demonstrated in fig(6.11) which shows an E.P.M. image of the interaction beam with I.S.I. and f/2.5 focusing optics at a plane equivalent to the entrance of the preformed plasma (approximately 400 μm before the tightest focus). The separation of the beamlets, so they no longer significantly overlap, results in pronounced hot spots in the beam with peak intensities up to 5 times the average beam irradiance. Presumably it is these hot spots which directly, or indirectly via filamentation, account for the higher levels of S.R.S. observed.

Studies of I.S.I. systems used elsewhere [48], have found that significant smoothing is only obtained over a distance along the beam of $\pm\Delta z$ (from best focus) given by $\Delta z \approx d'/\theta$. Where θ is the angle of convergence of the outermost beamlets at the beam focus and d' is the total width (zero to zero) of the focal spot. For the I.S.I. system used here this gives an effective smoothed length of the interaction beam of ±2.4 mm or ±150 μm, either side of the focus, for f/10 and f/2.5 focusing optics respectively. Clearly a total effective smoothed length of only 300 μm is completely inadequate for a plasma 800 μm long as used here. This is demonstrated by the resulting observed increase in the level of S.R.S.. Consequently it can be concluded that it is essential to use reasonably slow focusing optics for large plasmas such as those which will surround laser fusion targets to ensure that only the far field region of the laser beam interacts with the plasma. If the quasi−near field of the beam is present in the plasma the beam profile is sufficiently non−uniform to overcome any advantage obtained by the smoothing of

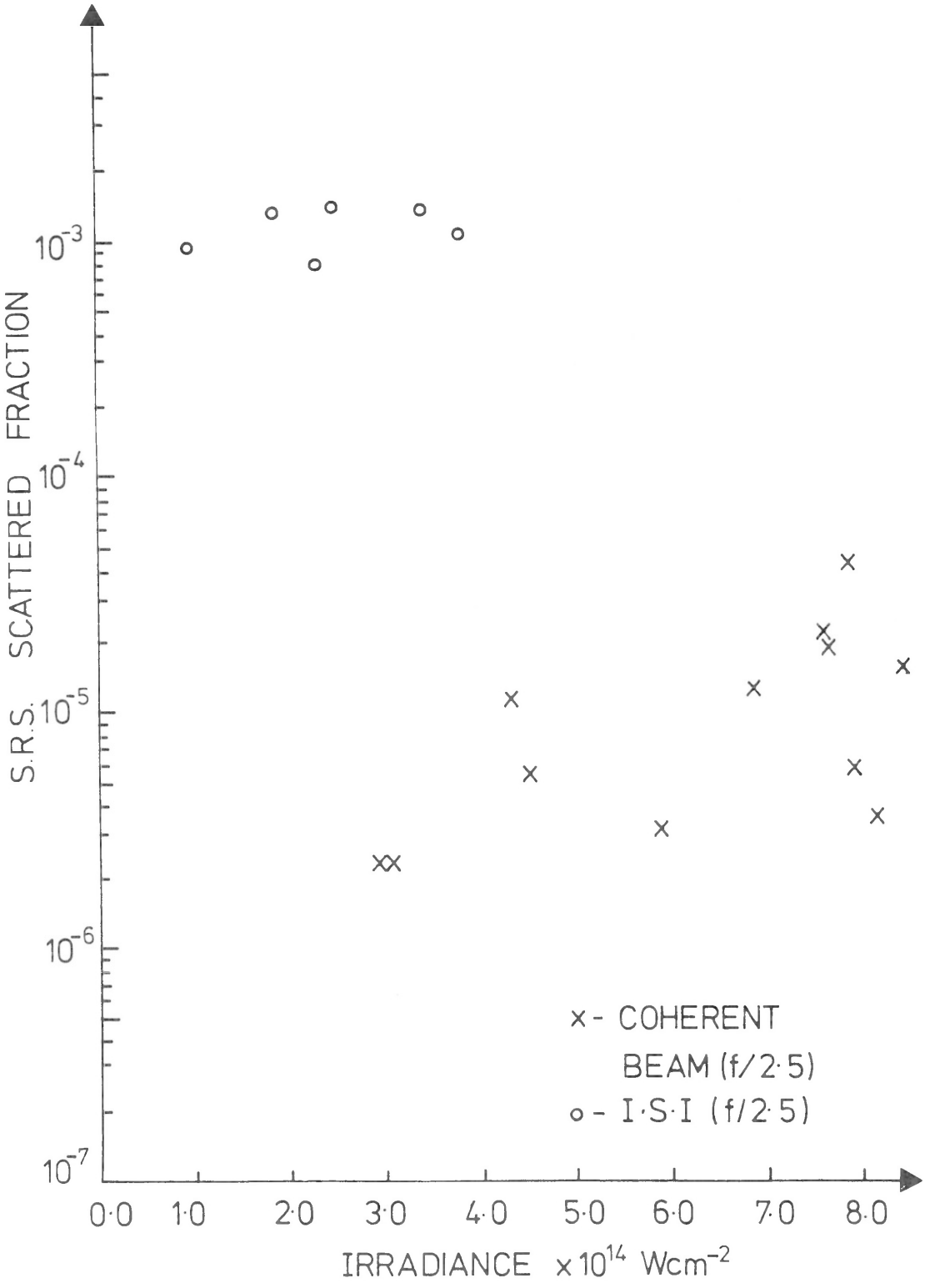


Figure 6.10 Variation of the S.R.S. backscatter fraction with laser irradiance for f/2.5 focusing optics (with and without I.S.I.).

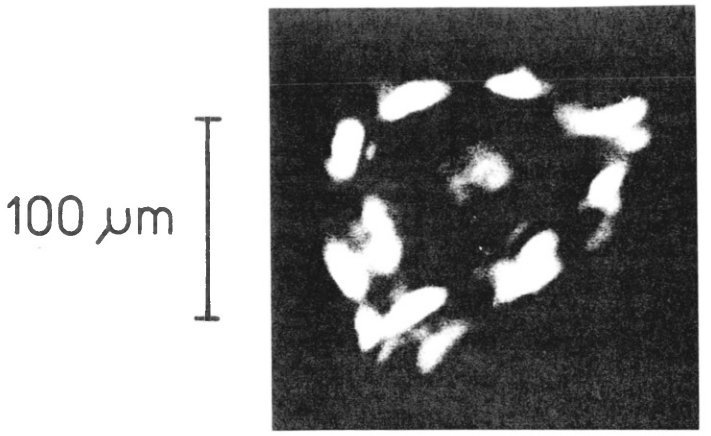


Figure 6.11 Equivalent plane monitor image of the interaction beam profile at the approximate entrance plane to the preformed plasma, for the case of I.S.I. and f/2.5 focusing optics.

the far field of the beam.

Fig(6.12) shows the level of S.B.S observed with an I.S.I. system with f/2.5 focusing optics. No significant increase in the level of S.B.S. is observed with respect to the coherent beam case. This should be compared to the dramatic increase observed for S.R.S.. This provides further evidence that for these plasma conditions the level of S.B.S. saturates at about $1-2$ % no matter how non−uniform a focal spot profile, or high an overall beam irradiance is used. It is interesting to note that this saturation level for S.B.S. is rather modest when compared with higher levels of the instability observed elsewhere [55,58,59,101]. Possible saturation mechanisms for S.B.S. [106,107], such as ion trapping and ion heating are unable to account for such a low level of the instability under these experimental conditions. It seems likely that the relatively low level of S.B.S. observed is connected with the lower plasma density used here, compared with these other experiments. It would appear from the experimental data obtained that the level of S.R.S. is still far from saturation.

It has been theoretically predicted that the use of a wide laser bandwidth, by itself, can suppress S.R.S. and S.B.S. [108,109]. However for such suppression to be effective it is required that $\Delta\omega/\gamma \gg 1$ (where $\Delta\omega$ is the bandwidth of the laser and γ is the growth rate of the instability). For the experimental conditions considered here $\Delta\omega/\gamma$ is of order unity or less for the broadband laser beam used with the I.S.I. system. Consequently any suppression of S.R.S. and S.B.S., due directly to the laser bandwidth, would be expected to be negligible for the I.S.I. beam. No direct comparisons were made between a broad and narrow band

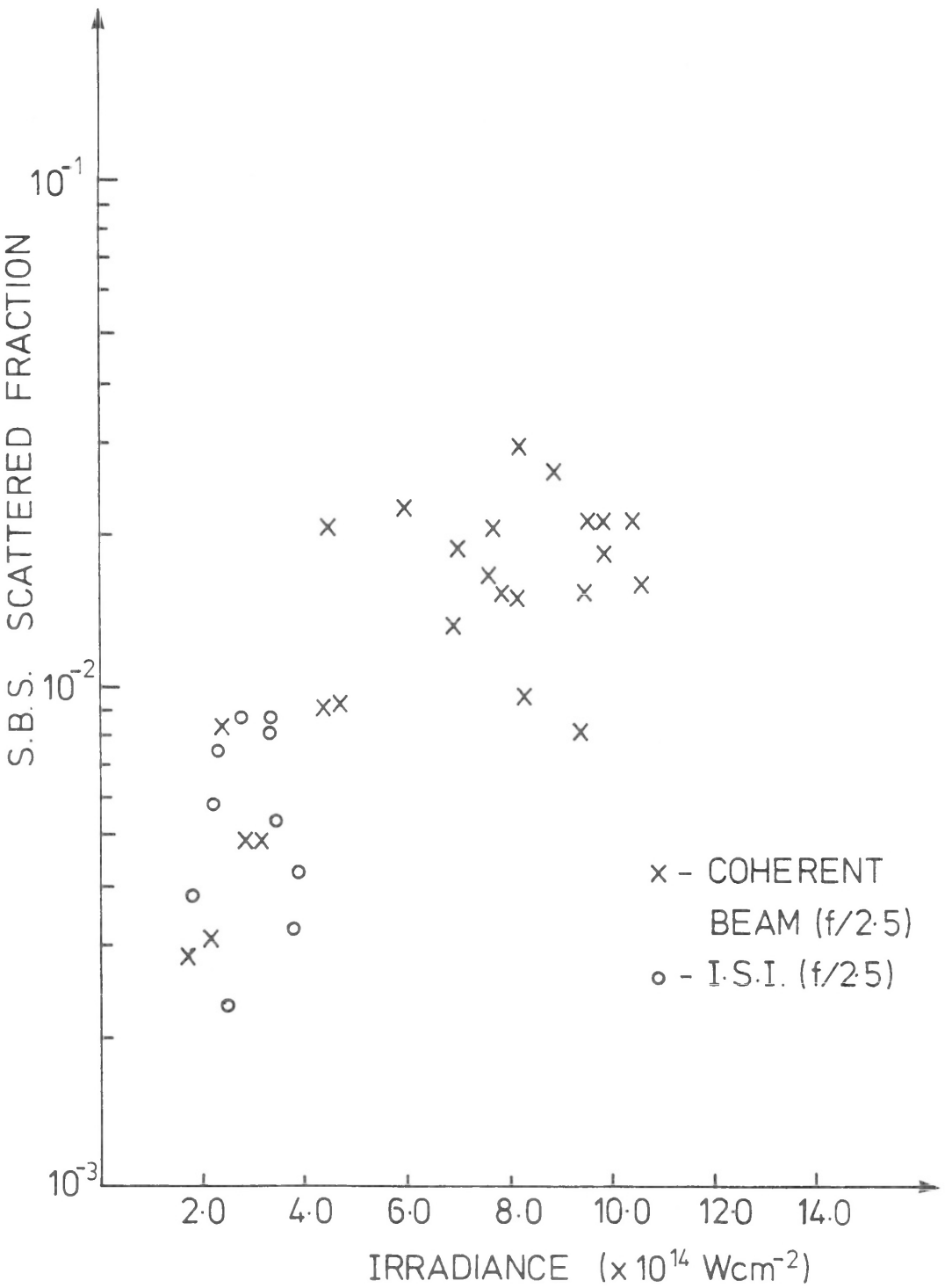


Figure 6.12 Variation of the S.B.S. backscatter fraction with laser irradiance for f/2.5 focusing optics (with and without I.S.I.).

interaction beam (without the I.S.I. echelons present). However from the high levels of S.R.S. and S.B.S. observed in figs. (6.10) and (6.12) for the case of a broadband laser (with I.S.I. echelons present) it seems unlikely that there is any significant suppression due directly to the laser bandwidth. It seems more likely that the level of S.R.S. and S.B.S. is completely dominated by the uniformity and structure of the actual laser beam profile. This is consistent with results from elsewhere [101], which showed no measurable reduction in the observed level of S.B.S. for a broadband laser with a comparable laser bandwidth to that used here.

(6.4) Suppression of filamentation in a large underdense plasma

The effect of a R.P.P. or I.S.I. to suppress the filamentary break up of a laser beam, as observed in chapter 5, was investigated. The results for the case of a R.P.P. and I.S.I. will be discussed in sections (6.4.1) and (6.4.2) respectively.

(6.4.1) Suppression of filamentation by a R.P.P.

To investigate the effect of the use of a R.P.P. on filamentation two focusing conditions were studied. Firstly the f/2.5 lens was aligned so that the tightest focus was obtained at the entrance plane of the preformed plasma. Secondly the tightest focus was positioned to be midway along the preformed plasma. The reason for doing this was to investigate the effect of changing the range of the scalelengths of the irradiation non−uniformities, generated by the R.P.P., which will be present in the preformed plasma.

Fig(6.13) shows three images taken with the optical framing camera of the interaction beam with the R.P.P. present, for the case when the tightest focus of the interaction beam was at the entrance plane of the preformed plasma. The first image is for the case when no preformed plasma is present. The small scalelength irradiation non−uniformities present, generated by the R.P.P., can clearly be seen. These are typically on a scalelength of 8−12 μm. From the microdensitometer trace shown, taken from across the beam profile, it was found that the root mean squared intensity variation ($\sigma_{r.m.s.}$) was 48% (I_{max}/I_{av} = 2.4). Fig(6.13)(b) and (c) show images taken, with a preformed plasma present, early and late in the interacting laser pulse. It can clearly be seen that the irradiation non−uniformities are significantly more pronounced in the late image compared with those in the image taken early in the laser pulse. This becomes even more

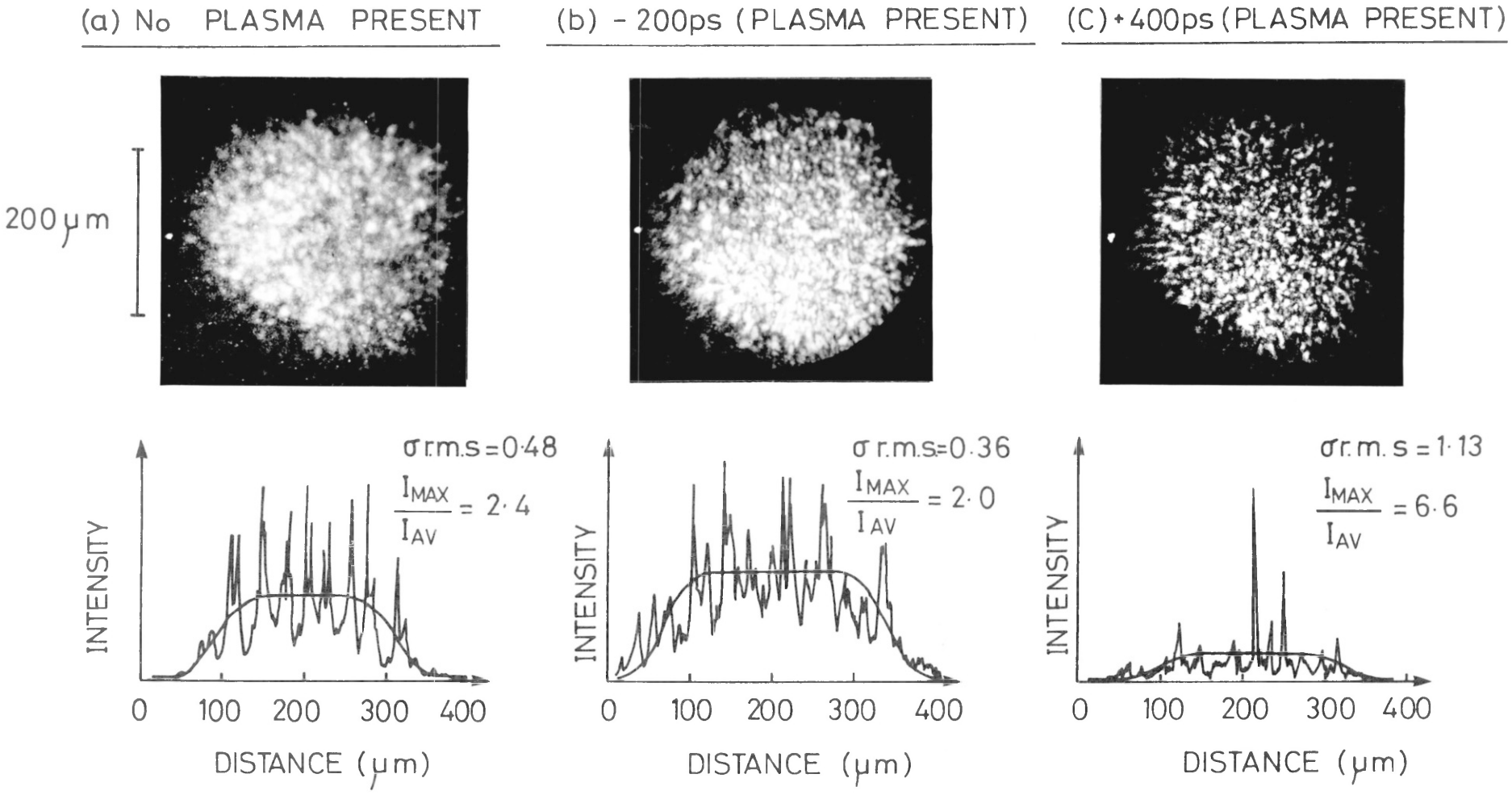


Figure 6.13 Optical framing camera images of the transmitted interaction beam (with the R.P.P. present), for the case when the tightest focus of the interaction beam was at the entrance plane of the preformed plasma. (a) No plasma present (irradiance = 1.0 × 10^{15} Wcm^{-2}), (b) early in laser pulse with plasma present (irradiance = 7.9 × 10^{14} Wcm^{-2}) and (c) late in laser pulse with plasma present (irradiance = 1.0 × 10^{15} Wcm^{-2}).

evident when the microdensitometer traces, across the beam profiles are compared. For the early image $\sigma_{r.m.s.}$ = 36% (I_{max}/I_{av} = 2.0) and for the late image $\sigma_{r.m.s.}$ = 113% (I_{max}/I_{av} = 6.6). Comparing the image early in the laser pulse with that with no preformed plasma present, it appears that there is some marginal smoothing of the laser beam by the plasma as observed in chapter 5 for a normal coherent interaction beam without a R.P.P.. It is possible that this framing camera image was not sufficiently early in the interaction beam pulse to observe the full dramatic level of smoothing observed in chapter 5. The existence of a number of pronounced intensity hot spots present in the microdensitometer trace for the framing camera image late in the laser pulse, when compared to the other two cases, seems to strongly suggest that some of the intensity non−uniformities generated by the R.P.P. have been enhanced by filamentation.

Fig(6.14) shows the variation in growth rate for ponderomotive filamentation expected, under the experimental conditions relevant to the results of fig(6.13), from the filamentation theory of chapter 3. It can be seen that effectively the theory predicts that only intensity perturbations with a wavelength of greater than about 6 μm will be unstable to filamentation. Consequently the intensity variations present in the far field of the interaction beam at the entrance plane of the preformed plasma, which are on a 2−3 μm scalelength, should not be unstable to filamentation. However as the interaction beam propagates along the preformed plasma the beam expands outwards and consequently the scalelength of the intensity non−uniformities also increases. From the E.P.M. data the irradiation non−uniformities will have reached a scalelength of 6 μm, a distance of approximately 400 μm after the tightest focus. At this point they could be expected to become unstable to ponderomotive filamentation. The remaining plasma length of 400 μm should be adequate to give sufficient enhancement of some of the irradiation non−uniformities by ponderomotive filamentation to account for the pronounced hot spots of fig(6.13)(c).

Fig(6.15) shows two microdensitometer traces taken across the interaction beam profile, early and late in the laser pulse, for the second focusing condition considered here, where the beam far field was located midway along the preformed plasma. It is observed that there is little difference between the two traces in the level of the irradiation non−uniformities. Hence it appears that no significant enhancement of the irradiation non−uniformities by filamentation now occurs. This seems reasonable, since in this configuration, the irradiation non−uniformities generated by the R.P.P. are never on a scalelength of greater than 5−6 μm along the whole length of the preformed plasma. Hence from the theoretical predictions

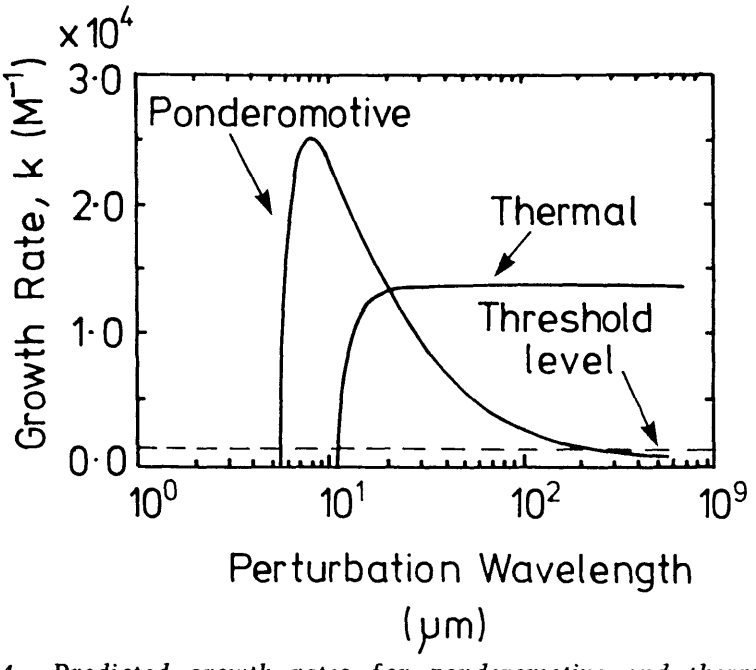


Figure 6.14 Predicted growth rates for ponderomotive and thermal filamentation (for $n_e = 0.08n_{ec}$, $T_e = 500$ eV and an irradiance of 10^{15} Wcm^{-2}).

of fig(6.14) no growth due to filamentation can be expected. However this experimental result should be treated with some caution as the typical scalelength of the irradiation non−uniformities now present in the beam (of 5−6 μm) is only about 50 % greater than the measured resolution of the framing camera and streak camera. Working this close to the resolution of the system may well mean that the intensity non−uniformities observed in fig(6.15) are more pronounced in reality than these measurements would suggest. However the complete lack of any sign of enhancement in the degree of the intensity non−uniformities in the beam profile late in the pulse, compared with early in the pulse, makes it seem unlikely that any significant degree of filamentation is occurring.

Hence it appears from these results that filamentation will be suppressed by a R.P.P. provided appropriate experimental conditions are used. In particular it is necessary that the size of the irradiation non−uniformities generated are on a sufficiently small scale that filamentation will not grow. It seems that the maximum scalelength of the intensity non−uniformities, which can be tolerated without the growth of filamentation, is reasonably accurately predicted by the simple filamentation theory of chapter 3. This conclusion is consistent with the results of numerical simulations carried out elsewhere [80], which suggest that a R.P.P. will suppress filamentation in the laser beam far field, provided fast focusing optics ($\lesssim$f/5) are used (ie. that the typical irradiation non−uniformities generated are on a scalelength <6 μm for $\lambda = 0.53$ μm).

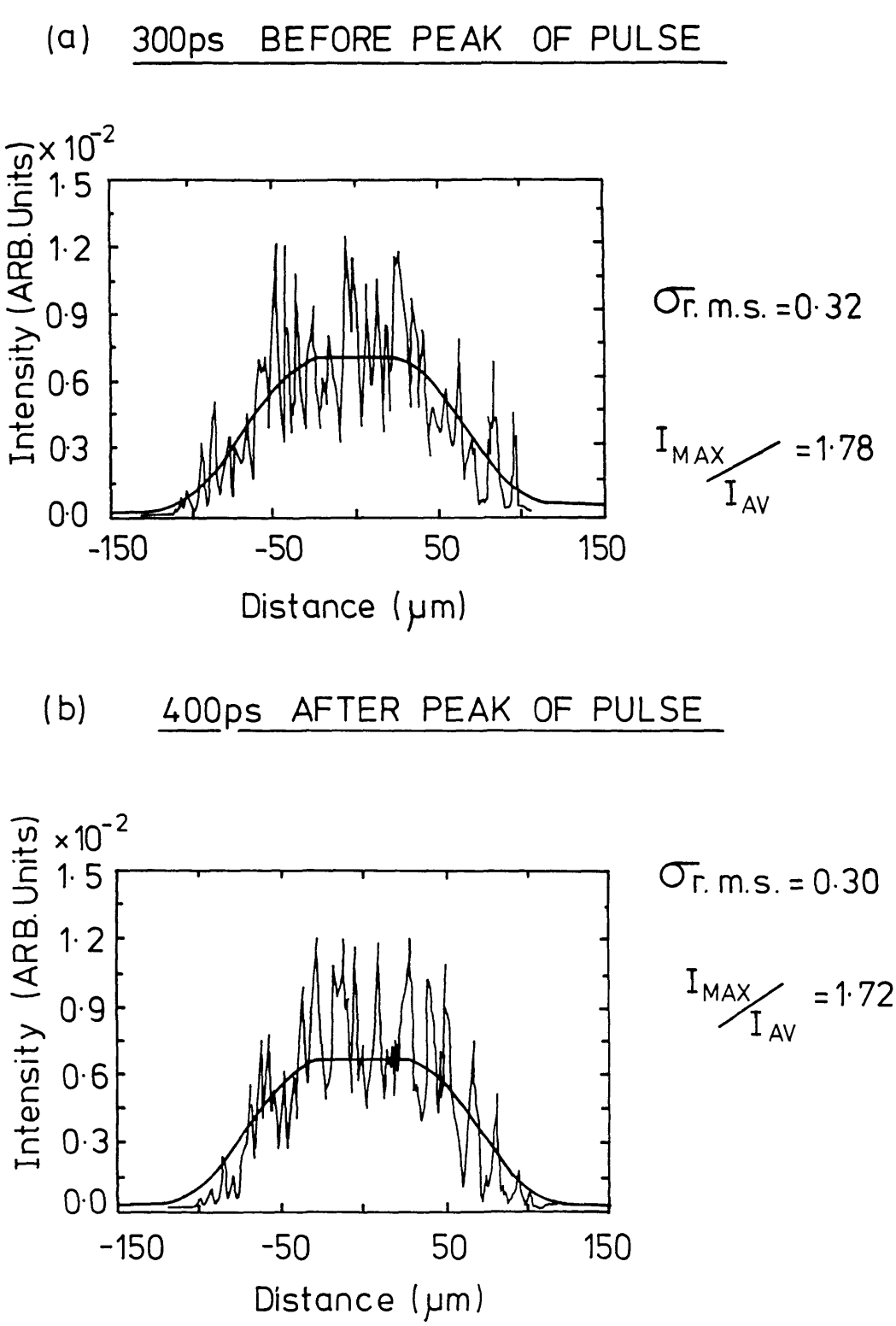


Figure 6.15 Measured profiles of the transmitted interaction beam (with the R.P.P. present) for the case when the tightest focus of the interaction beam was midway along the preformed plasma: (a) 300 ps before the peak of the laser pulse and (b) 400 ps after the peak of the laser pulse (irradiance = 9.8 × 10^{14} Wcm^{-2}).

(6.4.2) Suppression of filamentation by I.S.I.

Fig(6.16) shows a framing camera image, taken late in the laser pulse, of the transmitted interaction beam for the case of I.S.I. with a f/10 focusing lens. It can be seen that the framing camera image is reasonably uniform and no break up of the interaction beam due to filamentation can be observed. Also shown is a streak record of the transmitted beam for a similar shot. It can be seen that the spatial profile of the beam remains constant with time. The slight temporal modulations which can be seen in the streak were found to be present in the incident interaction beam. These modulations are believed to be due to noise present on the initial laser pulse switched out from the broadband I.S.I. oscillator [110].

As already stated earlier in this chapter, the irradiance of the interaction beam was limited to a value of about 5×10^{14} Wcm^{-2} when I.S.I. was used. Clearly it would have been desirable to demonstrate the suppression of filamentation at higher irradiances. However even for an irradiance of 5×10^{14} Wcm^{-2} it can be seen from fig(5.12) of chapter 5, that the beam should still be of a sufficiently high irradiance to be unstable to filamentation. For ponderomotive and thermal filamentation any filaments larger than 8.5 μm and 13 μm respectively, should be able to grow under these conditions. The lack of any break up of the interaction beam suggests that any hot spots present in the I.S.I. beam, on this scale, are not sufficiently pronounced to seed filamentation. The growth time for the minimum size ($\approx$8.5 μm) of perturbation unstable to filamentation (determined by the ion accoustic transit time), for these plasma conditions is approximately 25 ps. Since any non-uniformities present in the instantaneous I.S.I. pattern are smoothed out on a time scale significantly less than this (ie. the broadband coherence time of 2 ps), it is reasonable that no growth of filamentation is observed with the I.S.I. beam. As stated earlier in this chapter the suppression of filamentation by I.S.I has been demonstrated by numerical simulations [80].

(6.5) I.S.I. and R.P.P. hybrid system

It appears from the results of this chapter that the major drawback of the I.S.I. system used here is the necessity of working in the far field of the laser beam. This means that the system is largely restricted to the use of slow focusing optics and, in particular small focal spot sizes ($\lesssim$120 μm). This problem is not so

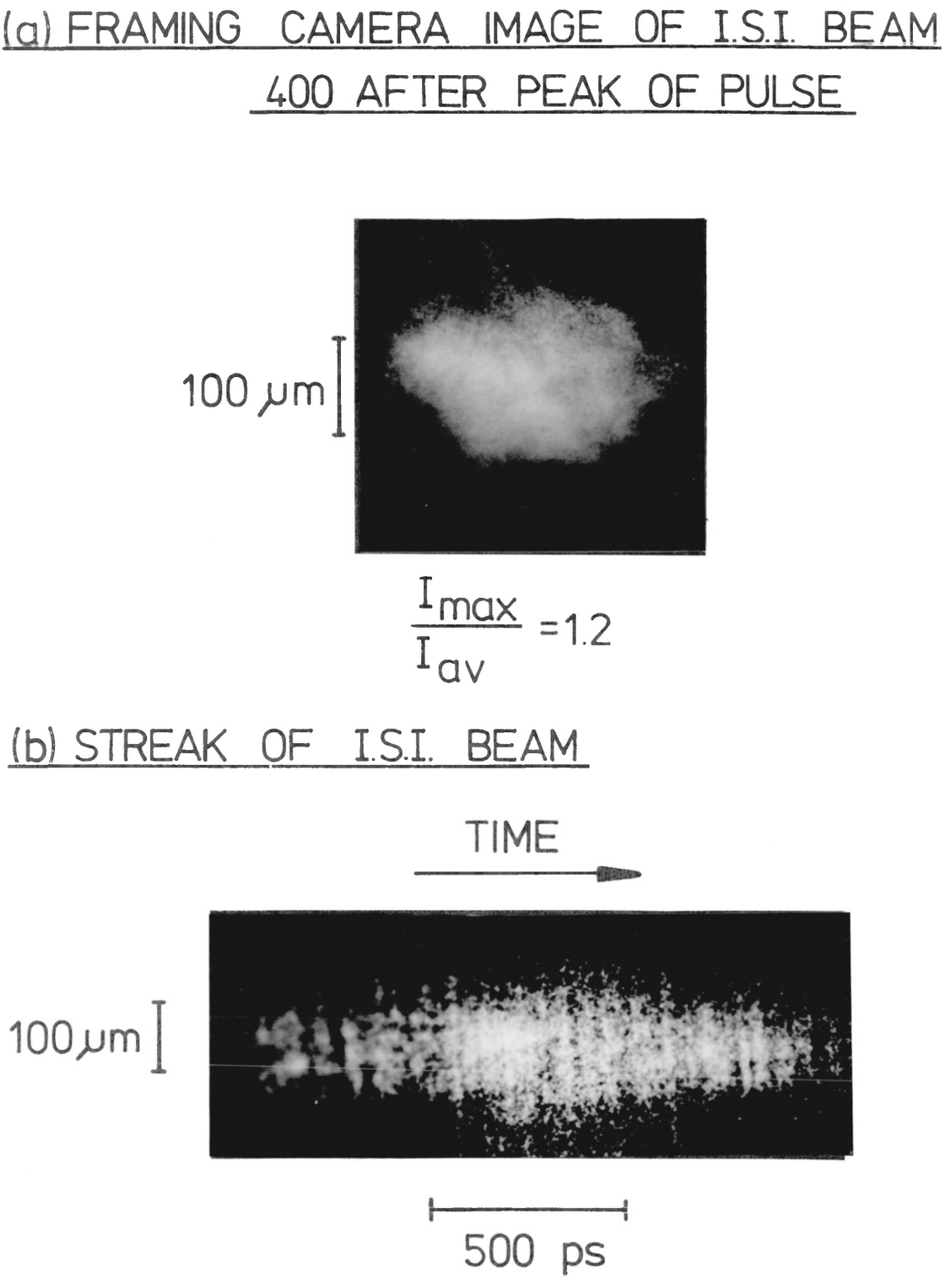


Figure 6.16 (a) Optical framing camera image of the transmitted interaction beam (with I.S.I. and f/10 focusing optics) 400 ps after the peak of the laser pulse (irradiance = 4.5×10^{14} Wcm^{-2}) and (b) streak record of the transmitted interaction beam, for a similar laser shot.

acute for the I.S.I. system developed at N.R.L. (Naval Research Laboratory, Washington, U.S.A.), since they use reflective I.S.I. echelons consisting of two stacks of mirrors. This allows alternate mirrors in the echelons to be tilted to produce four partially overlapping sets of beamlets at the target [100]. This increases the focal spot size which can be obtained and also has the advantage of producing a relatively flat top focal spot distribution. Such an approach is not feasible with the transmission echelons used here. Clearly it is desirable to be able to generate large ($\approx$400 μm) focal spots with the I.S.I. system without having to resort to the use of excessively large focal length lenses or an unreasonably large number of beamlets. To overcome this problem a new approach was tried. This involved using the I.S.I. system in combination with a R.P.P.. The focal spot size is then determined by the diffraction limit of an individual beamlet of the R.P.P.. This allows the generation of considerably larger focal spot sizes than can be obtained by using I.S.I. by itself. For example, for a f/10 lens the focal spot size is 280 μm F.W.H.M.. Fig(6.17) shows an E.P.M. image of the far field of the interaction beam using the I.S.I. and R.P.P. combination, as well as a microdensitometer trace across the beam profile. It can be seen that the beam profile is extremely uniform. Even the small level of intensity fluctuations present in the beam profile for the I.S.I. beam by itself, see fig(6.4), are no longer present. The use of I.S.I. and a R.P.P. together effectively amounts to combining a number (equal to the number of I.S.I. beamlets) of R.P.P. focal spot distributions together in the target plane, each of which are temporally incoherent with each other. It can be seen from fig(6.17) that the use of the two systems in combination gives rise to significant improvements in the uniformity of the far field focal spot distribution, over that which can be obtained when using either a R.P.P. or I.S.I. individually.

Fig(6.18) shows E.P.M. images of the interaction beam profile in a plane 400 μm before the tightest focus for a f/2.5 lens for the cases of a R.P.P./I.S.I. combination and a R.P.P. used by itself. Clearly the use of the I.S.I./R.P.P. combination reduces the degree of the short scalelength non$-$uniformities generated by the R.P.P. by itself. Also comparing the focal spot distribution with that shown in fig(6.11) for I.S.I. by itself, it can be seen that the pronounced hot spots generated by the individual I.S.I. beamlets not overlapping are no longer present. Hence it can be seen that the use of a I.S.I./R.P.P. combination gives significant improvements in the beam quality which can be achieved in the quasi$-$near field, as well in the far field, when compared with that which can be obtained when either system is used individually. Unfortunately no experimental data was obtained on the levels of S.R.S. or S.B.S. which occur with the I.S.I./R.P.P. combination.

However the preliminary measurements made here of the focal spot distribution obtained with such a hybrid system indicate that it is an extremely promising avenue for future research.

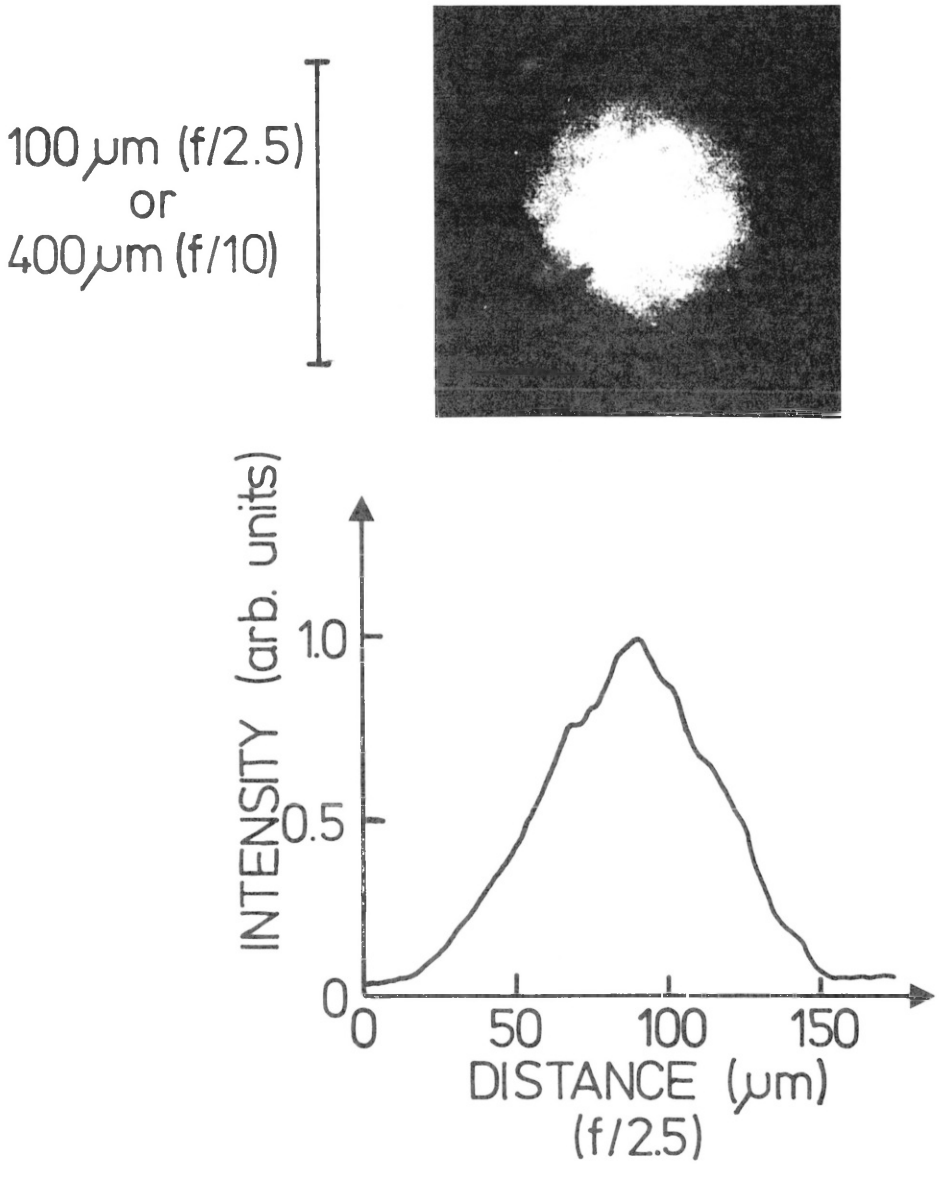


Figure 6.17 Far field focal spot distribution measured with the equivalent plane monitor, for the case of the R.P.P. and I.S.I. combination.

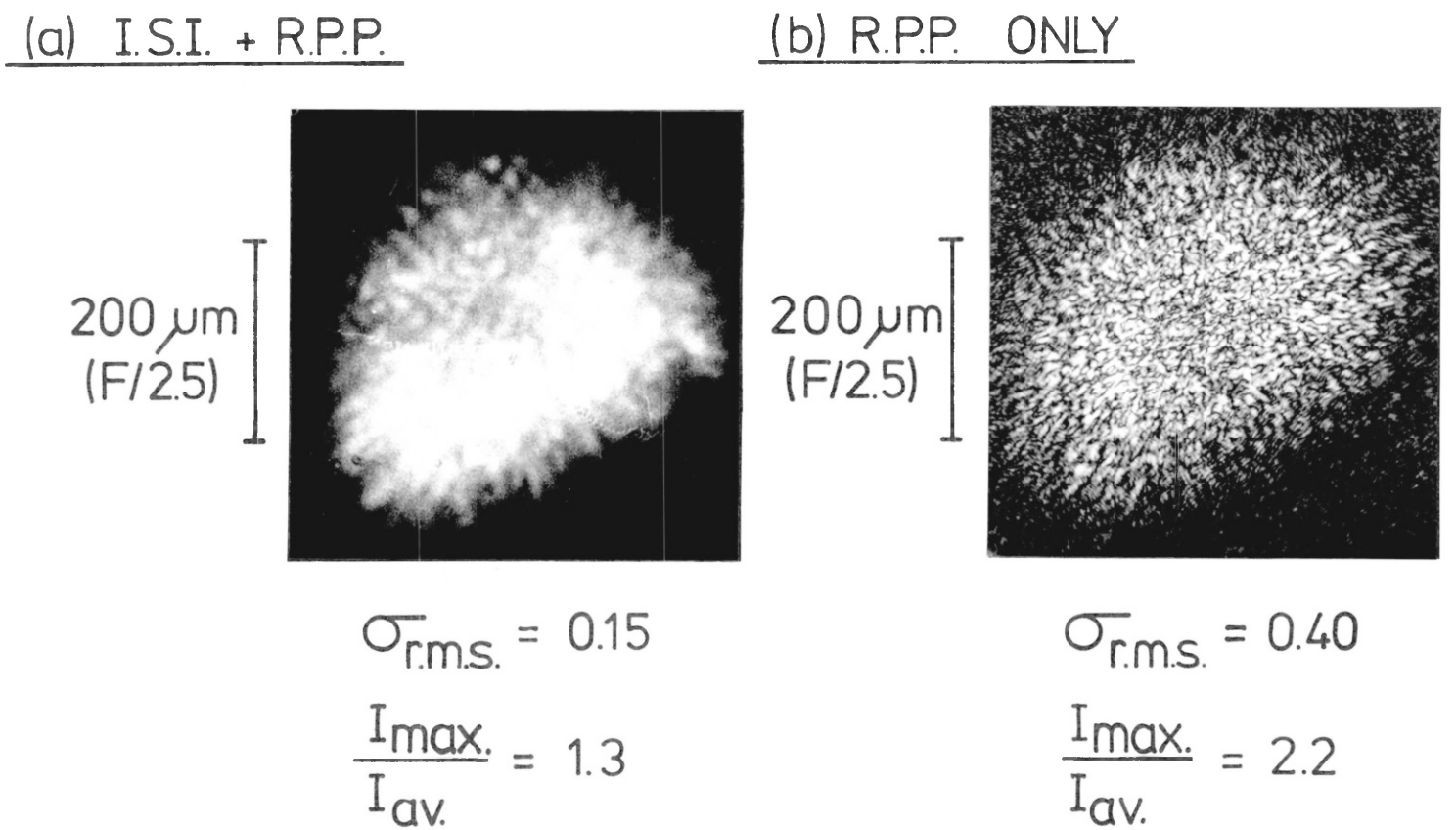


Figure 6.18 Equivalent plane monitor images of the interaction beam profile in a plane 400 μm before the tightest focus (for f/2.5 focusing optics): (a) I.S.I. and R.P.P. combination and (b) R.P.P. by itself.

(6.6) Discussion and Conclusions

(6.6.1) Reproducibility of plasma conditions and results

Clearly it is important that the conditions in the preformed plasma at the time of interaction do not vary significantly on a shot to shot basis. A reasonable reproducibility of the plasma conditions is necessary so that meaningful comparisons can be made between data obtained from different laser shots. In particular this point is relevant for the graphs of S.R.S. and S.B.S. energy levels presented earlier in this chapter. In order to achieve reproducible plasma conditions the irradiance of the four line focus, plasma forming beams were carefully monitored on each shot. Data obtained from shots where the irradiance of these four beams varied significantly from the nominal value of 7.5×10^{13} Wcm^{-2} was discarded. Also the wavelength shifts of the observed S.R.S. and S.B.S. spectra produced during interaction, were found to be a reliable check that the plasma conditions did not vary significantly on a shot to shot basis. In particular the S.R.S. spectra were found to be useful for this purpose, since they give a good measure of the electron density due to the large wavelength shift involved. Again data was discarded from laser shots where the S.R.S. spectrum indicated that the plasma density was significantly different from the normal value (possibly caused by the use of a defective target or faulty target alignment). In general it was found that the plasma conditions were reproducible for both the experiments of this chapter and chapter 5. From the S.R.S. spectra measurements an approximate maximum shot to shot variation in the plasma density of ±15 % can be estimated. This variation is sufficiently small that the levels of S.B.S., S.R.S. and filamentation ocurring should not be significantly effected. This conclusion is consistent with the graphs of S.R.S. and S.B.S. presented earlier in this chapter. Although there are variations in the levels of S.R.S. and S.B.S. observed for similar laser shots, which may be due to variations in the plasma conditions, it seems more likely that these variations are due to the uniformity of the interaction beam varying on a shot to shot basis. In either case the gross changes in the levels of S.R.S. and S.B.S., due to the use of I.S.I. or a R.P.P. are considerably larger than these shot to shot variations. Hence these variations do not invalidate the conclusions inferred from these graphs, in this chapter.

The inferred plasma conditions have been used to determine theoretical estimates for the growth rates and thresholds for S.R.S., S.B.S. and filamentation in both this chapter and chapter 5. Given the approximate nature of these calculations any additional inaccuracies introduced into these estimates by the

relatively minor uncertainties in the plasma conditions are unimportant.

As a final point it should be noted that the preformed plasmas generated for the experiments of chapter 5 were produced from aluminium stripes 200 μm wide (rather than 300 μm wide as used predominately in the experiments reported on in this chapter). In order to produce similar plasma conditions in both sets of experiments lower line focus beam energies were used in the experiments of chapter 5. This ensured that the actual irradiance on target due to the heating beams was similar in both sets of experiments (ie. nominally 7.5×10^{13} Wcm^{-2}). Hence a similar plasma expansion should be observed in both cases. This is confirmed by the S.R.S. and S.B.S. spectra which show no measurable difference in the plasma conditions between the experiments reported on in chapters 5 and 6.

(6.6.2) General discussion

Experiments have been carried out to determine the effectiveness of a R.P.P. or an I.S.I. system to suppress S.R.S., S.B.S. and filamentation. Results from N.R.L. showing the suppression of S.B.S. and S.R.S. by I.S.I. [101,102] have been extended to the case of a large underdense plasma, similar in scale to those which will surround proposed laser fusion targets. As was the case for the N.R.L. results for shorter scalelength plasmas, comprehensive suppression of the levels of S.R.S. and S.B.S were observed by the I.S.I. system (by nearly three orders of magnitude). Unfortunately these measurements with the I.S.I. system were limited to modest laser intensities. Clearly it is important in the future to establish if the same degree of suppression occurs at higher irradiances. The I.S.I. system used in the experiments reported here had several advantages over that developed at N.R.L.. In particular in terms of cost, simplicity of alignment and potential ease of future extension to multibeam operation for compression experiments. The confirmation that such a system, with the advantages of low overall cost and ease of installation, can provide sufficient beam smoothing to substantially suppress parametric instabilities is clearly extremely encouraging.

Also experiments carried out with a R.P.P. have provided the first experimental observations of the suppression of S.R.S. and S.B.S. by such a device. The levels of these instabilities were reduced by a factor of 10−20 by using a R.P.P.. If in the future, it is found that the same degree of suppression occurs at higher plasma densities it may well prove that an I.S.I. system is unnecessary to control parametric instabilities, and that the use of random phase plates would be

adequate.

It was found with the I.S.I. system that it was essential to work near the far field of the beam. In the quasi−near field, where the individual beamlets no longer overlap, high levels of S.R.S. and S.B.S. were observed due to the non−uniformity of the beam profile. This presents a limitation to the maximum focal spot size which can be obtained with the I.S.I. system used here. In order to overcome this problem and allow the generation of larger focal spot sizes preliminary investigations were made of a hybrid system which simultaneously uses a R.P.P. and the I.S.I. system together. The preliminary results obtained on the characterization of the far and quasi−near field beam profiles produced with such a system were extremely encouraging.

Measurements made of the transmitted interaction beam appear to suggest that the use of a R.P.P. can suppress filamentation provided the size of the irradiance non−uniformities generated by the R.P.P. are on a sufficiently small scale. The maximum size of irradiation non−uniformity which can be tolerated without the growth of filamentation appears to agree reasonably well with theoretical predictions. Consequently for filamentation to be suppressed by a R.P.P. reasonably fast focusing optics ($\lesssim$f/5) must be used. With I.S.I. and a f/10 focusing lens no break up of the interaction beam due to filamentation was observed, although measurements made were again restricted to modest irradiances ($\lesssim 5 \times 10^{14}$ Wcm^{-2}). However, even for irradiances of this level filamentation could be expected to grow from a wide range of sizes of intensity perturbations. Clearly the observed lack of any such growth is encouraging. However it is important to investigate if this result still holds for higher irradiances in the future.

Several features of the results obtained indicate that with a coherent interaction beam the occurrence of S.R.S and S.B.S. was strongly influenced by the presence of filamentation. Firstly, a rapid rise in both the levels of S.R.S. and S.B.S. was observed near irradiances of 10^{14} Wcm^{-2}, which is the expected threshold for filamentation under these conditions. Secondly S.B.S. spectra appear to indicate regions of strong localized heating, presumably due to filamentation. Thirdly, S.R.S. spectra show emission from regions of low density, possibly generated by filamentation. None of these features were observed when I.S.I. or the R.P.P. was used, when it is known from the transmitted beam measurements that no filamentation occurs. Finally it seems likely that some intermediate mechanism such as filamentation, is needed to account for the dramatic reduction in the levels of S.R.S. and S.B.S. which occur when I.S.I. or the R.P.P. is used.

This is because such a large reduction cannot just be explained by intensity averaging of the hot spots in the coherent beam. Also the existence of filamentation as an intermediate mechanism may explain how I.S.I. can suppress S.R.S. and S.B.S., when the growth time for both these instabilities is on a significantly shorter time scale than that of the smoothing of the laser beam profile.

The results obtained for the suppression of S.R.S., S.B.S. and filamentation by a R.P.P. are clearly promising. However there are still significant doubts as to whether a R.P.P. system will provide adequate beam 'smoothing' to successfully drive I.C.F. implosions. Nevertheless the use of random phase plates should still significantly enhance present day plasma physics experiments, such as those in chapter 2 of this thesis, where the use of I.S.I. may be prohibited by cost. Although the results obtained (both those in this thesis and those obtained at N.R.L.), for the suppression of parametric instabilities and filamentation by I.S.I. are extremely encouraging, there are still some practical problems with the use of an I.S.I. system. In particular, the requirement of a broadband laser significantly reduces the efficiency of the frequency up−conversion of the laser output which can be achieved. For the experiments reported on here the second harmonic generation efficiences were reduced by about 35 % due to the use of a broad band laser. For frequency tripling (to $\lambda = 0.35$ μm) the requirements for efficient frequency conversion become even more severe, and for a broadband laser only negligible conversion efficiences can be obtained. Clearly this presents a significant problem, since it is widely recognized that shorter wavelength ($\lesssim 0.35$ μm) drivers will be required for successful I.C.F. implosions. One possible solution to this problem is the use of KrF lasers to drive implosions since the wavelength of the laser output ($\lambda = 0.25$ μm) is then sufficiently short that frequency up−conversion is no longer required. KrF lasers are expected to be well suited to the generation of the broad bandwidths which are required for the use of I.S.I. [111]. An alternative approach to this problem is the use of smoothing by spectral dispersion (S.S.D.) which is currently being developed elsewhere [112,113]. This system effectively uses a R.P.P., but the wavelength of the input laser beam is varied across the R.P.P. in a controlled manner so that the resultant far field pattern produced varies with time. In this way temporal smoothing is obtained as in an I.S.I. system. The advantage of this approach is that by careful design of the optics in the beam, near optimum ($\approx 60\%$) conversion efficiences can still be obtained. It remains to be seen how effective such a system will be at suppressing parametric instabilities and filamentation, when compared with I.S.I..

CHAPTER 7

GENERATION OF PREFORMED PLASMAS BY IRRADIATION OF THIN FOIL STRIPE TARGETS

(7.1) Introduction

In order to determine the plasma conditions for the experiments of chapters 5 and 6 the Raman and Brillouin spectra produced during interaction were used. These measurements appear to give reliable estimates of the plasma conditions. In particular the Raman spectra should give a good measure of the electron density due to the large wavelength shift involved. However it is still clearly desirable to be able to independently predict what the plasma conditions will be at a particular time in the expansion of the foil targets. This is necessary firstly for purposes of experimental design, and secondly to confirm that the plasma expansion observed is well behaved. Reliable estimates of the plasma conditions produced by the expansion of thin foil stripe targets are also important for x−ray laser experiments. This is because the use of stripe targets rather than coventional fibre targets, offers the possibilty of considerably increased coupling of the incident laser energy into the target for x−ray laser experiments [114,115]. Also for x−ray laser experiments, as well as for the study of instabilities, it is important to produce homogeneous plasmas, and it is therefore necessary to know how uniform the plasmas produced by the expansion of foil stripe targets are.

In this chapter experimental measurements of the plasma conditions produced by the expansion of thin foil stripe targets are reported on. The results are compared with the predictions of a 1−D model and also a 2−D hydrocode. In section (7.2) measurements made of the plasma conditions produced in the experiments described in chapters 5 and 6 are compared with theoretical predictions. In section (7.3) optical probing measurements of the plasma produced under similar conditions are described. These measurements are used to assess the uniformity of the plasmas generated and also to estimate the plasma conditions. In both sections the effect of varying the construction of the target on the resulting plasma expansion is investigated.

(7.2) Plasma production by long pulse heating beams

(7.2.1) Experimental results

It is interesting to note that the plasma density (of 0.08 N_{ec}) inferred from the S.R.S. spectra of chapters 5 and 6 for a 700 nm thick aluminium target is not that much lower than that predicted by the model of Rosen and London for an ideal 1−D expansion. For the relevant experimental conditions the model predicts a plasma density of 0.11 N_{ec} at the time of interaction (1.7 ns). Consequently it appears that the expansion of the plasma is not as strongly two dimensional as might be expected. One possible reason for this is the presence of the 100 nm thick formvar substrates used to support the targets, which may play a significant role in the expansion of the plasma. Such effects have been noted before [116]. In order to investigate this possibility further a target was used where the aluminium stripe was free standing along almost all of its length, and only supported at each end by two vertical struts. The normal formvar supported target and the new free standing H−target are illustrated in fig(7.1). For otherwise identical experimental conditions to those described in chapters 5 and 6 a 750 nm thick H−target was found to produce S.R.S. emission, during interaction, in the wavelength range 620 − 680 nm. The maximum wavelength observed gives a plasma density of 0.043 N_{ec}, which is just over half that obtained with a stripe target supported on a formvar base under similar conditions. Assuming that the short wavelength cut−off in the emission is due to the onset of Landau damping gives a plasma temperature of approximately 250 eV. Consequently it can be concluded that the presence of a formvar substrate plays an important role in the expansion of the plasma produced. There appear to be two possible mechanisms by which the presence of the formvar substrate can effect the plasma expansion. Firstly, if significant lateral transport of energy occurs from the aluminium plasma into the formvar substrate, then the resulting loss of energy from the aluminium plasma will slow down its expansion and result in higher plasma densities. Secondly the lateral transport of energy into the formvar substrate may cause the generation of a cold dense plasma at either side of the expanding aluminium plasma. This may serve to confine the aluminium plasma and cause its expansion to more closely approximate to the 1−D case.

(7.2.2) Two dimensional simulations

In order to model the expected expansion of the aluminium stripe targets the

2−D Eulerian hydrodynamic code POLLUX [117,118], was used. The code employs a two temperature description of the plasma with a flux limited electron thermal conductivity being used for steep temperature gradients. A perfect gas equation of state was used, which for the low plasma densities relevant to the experimental conditions considered here is expected to be a reasonable approximation. The laser energy is absorbed by inverse bremsstrahlung absorption with a dump at critical density. The output of the code takes the form of the density, temperature and pressure profiles on a two dimensional spatial grid. The mesh can have a maximum of 100 cells in the z direction and 50 cells in the r direction, where the laser is incident along the z axis. The mesh was set to expand at a constant velocity in the z direction during the simulations to allow adequate resolution early in the simulation across the small target dimensions. In order to simulate the experiment described here the code was modified to allow irradiation of the target stripe from both sides. The code was used to predict the evolution with time of the temperature and density profiles across a section perpendicular to the axis of the stripe targets.

Fig(7.2) shows the resulting density profile predicted by the code for a free standing 750 nm thick H−target at the time of interaction, for the experimental conditions of section (7.2.1). For this simulation a flux limiter of 0.1 of the free streaming limit was used for the electron thermal conductivity. The incident laser beam was assumed to have a Gaussian spatial profile with a F.W.H.M. of 230 μm. The laser beam profile was allowed to overlap the target stripe by 40 μm at each edge before being cut off, as approximately occurred in the actual experiment. The expansion velocity of the mesh was set to a value of 4×10^{7} cms^{-1}. It was found that altering the mesh expansion velocity by up to a factor of two from this value did not make any significant difference to the code predictions. The simulation predicts a peak electron density on axis of 0.033 N_{ec} which agrees to within 30 % with the value of 0.043 N_{ec} measured for the density at this time, from the observed S.R.S spectrum. The code predicts a plasma temperature of 180 eV which is consistent with the short wavelength cut−off of the observed S.R.S. spectrum at 620 nm being due to the onset of Landau damping. Over the region of the plasma which the interaction beam passes through the plasma conditions are found to vary by no more than 15% in the simulation. The reasonable agreement between the simulation and the conditions inferred from the S.R.S. spectra suggest that the expansion of a free standing stripe target is well behaved, and as expected.

A significant number of physical effects are omitted from the 2−D code

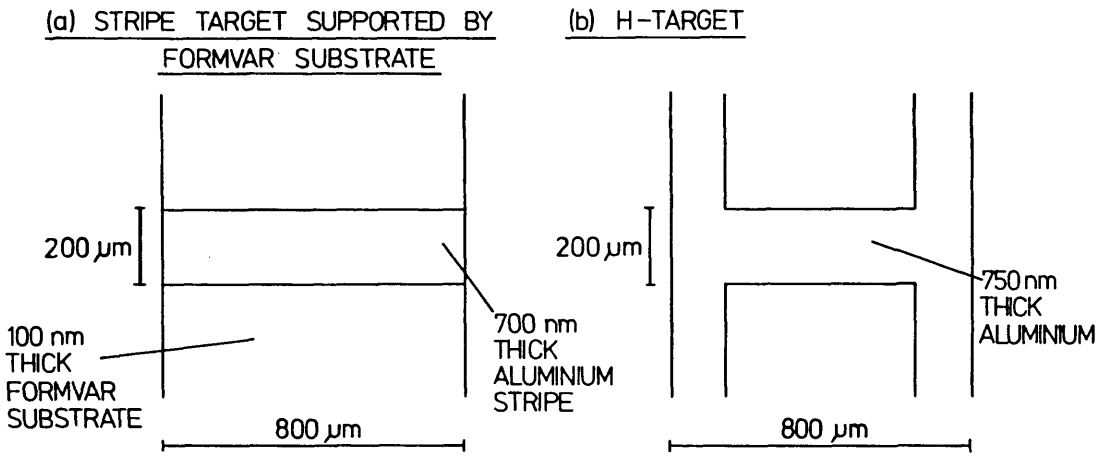


Figure 7.1 Target design: (a) aluminium stripe supported by a 100 nm thick formvar substrate and (b) free standing H–target.

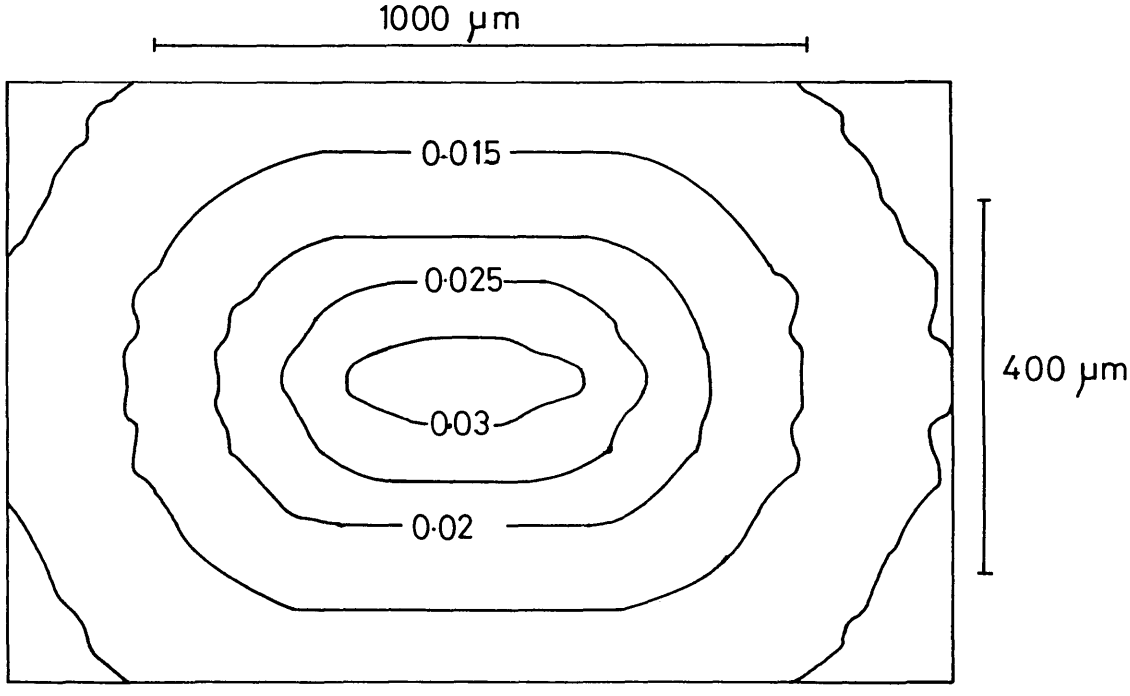


Figure 7.2 POLLUX prediction of the density profile generated from a 750 nm thick H–target, at the time of interaction. The contours are labelled as fractions of the critical electron density (4×10^{21} cm^{-3}).

used here (eg. a real equation of state, calculation of the plasma ionization state and transport of thermally produced x−rays). These omissions may all introduce inaccuracies into the code predictions. Also it is unclear what errors may be introduced by the simple constant velocity expansion of the mesh employed. However, comparisons between the Rosen and London model and the code predictions when it was run in a strongly one dimensional situation (ie. target width $\gg$ depth of plasma) give agreement to within 30 % for relevant experimental conditions. This gives some support for the reliability of the code predictions, and suggests that the simulation described above is of value in at least estimating the importance of two dimensional effects on the plasma expansion.

Unfortunately the code POLLUX is not able to simulate the case of a target with more than one element present. Hence it is not possible to directly simulate the case of a stripe target supported on a formvar substrate. In an attempt to model the case of a stripe target supported on a formvar substrate a further modification was made to the code to allow the inclusion of a low density layer of aluminium next to the main aluminium stripe, to represent the plastic substrate. However the inclusion of such a layer in the simulations was found to not significantly alter the expansion of the central aluminium plasma, with the electron densities present being increased by only about 8%. In these simulations the low density layer remained largely undisturbed and did not significantly interact with the central expanding aluminium plasma. A possible explanation for the failure of the code to predict a significantly modified expansion, due to the presence of a substrate, is that the code significantly underestimates the thermal conduction in the substrate. This is because the Spitzer thermal conductivity (see chapter 1) is inversely proportional to the ion charge. Consequently the conductivity predicted for the low density aluminium substrate, used in the simulation, will be significantly less than that which occurs in reality for a lower Z plastic substrate. This will cause the code to significantly underestimate the flow of heat into the substrate, and hence also the expansion of the substrate. Consequently the use of a low density aluminium layer, instead of a formvar substrate as used in reality, can not be expected to give a realistic modelling of the true physical situation.

As a further attempt to try to estimate the effect of the presence of the formvar substrate, the electron thermal conductivity flux limiter was varied from the value of 0.1 used in the simulation of fig(7.2). Reducing the value of the flux limiter can crudely be regarded as representing the case of significant energy loss due to lateral heat flow. It was found that reducing the flux limiter to a value of 0.03 increased the plasma density at the time of interaction by almost a factor of

two. Hence it appears feasible that the the occurrence of significant lateral heat flow into the plastic substrate (which may not be accurately modelled by the 2−D code), may slow down the expansion of the aluminium foil.

In summary the expansion of a free standing aluminium foil was found to be in reasonable agreement with that predicted by the 2−D code POLLUX. However for a aluminium stripe supported by a formvar substrate the plasma expansion was found to lie midway between that predicted by the 2−D code and by a 1−D model. It seems that the likely reasons for this effect are loss of energy, due to lateral heat transport into the formvar substrate slowing down the expansion, and also the presence of cold, dense plasma at either side of the aluminium stripe confining the plasma expansion to more closely follow the 1−D case.

(7.3) Optical probing measurements of plasma expansion and uniformity

To investigate further the effect of the presence of a formvar substrate on the expansion of an aluminium stripe target an experiment was performed using optical probing as a diagnostic. This allowed the expansion of the plasma generated to be followed, and also the uniformity of the plasma to be assessed. The basic experimental arrangement used to generate the plasma was identical to that described in chapters 4, 5 and 6, except that short 70 ps (F.W.H.M.) laser pulses were used to irradiate the targets. Consequently thinner targets, typically only 350 nm thick, were used so that the laser beams were still able to burn through the target on this shorter time scale. The total irradiance of the heating beams used was typically 1.6×10^{14} Wcm^{-2}.

(7.3.1) Details of the optical probing system

In order to diagnose the plasmas produced a four frame optical probing system was used [119]. Laser beam probing is a very effective technique for observing small scale structures in underdense plasmas due to its high temporal and spatial resolution. Consequently in the past it has been successfully used to make a wide variety of measurements in laser produced plasmas [90,120,121]. The optical probe beam used in this experiment was split off early in the main amplifier chain of the VULCAN glass laser. At this stage the probe pulse had an energy of approximately 100 mJ and a duration of 100 ps (at $\lambda=1.056$ μm). The probe beam pulse was then frequency doubled in a KDP crystal to a wavelength of

526 nm, as illustrated in fig(7.3). This was done to allow probing of higher densities in the plasma, since shorter wavelength light can more effectively penetrate a plasma. The second harmonic probe beam was then focused down into a cell of ethanol to Raman shift it to a wavelength of 622 nm [122]. This was done so that the probe beam was at a different wavelength to the main laser, or any of its harmonics. This allowed scattered green laser light, or harmonic emission, from the plasma to be blocked from the final probe beam images by the use of appropriate filters. The backscattered Raman light from the ethanol cell was used to probe the plasma, and this was automatically re−collimated by the lens used to focus the original beam into the cell. A significant fraction of this backscattered probe pulse then passes straight through the final green turning mirror (which is used to direct the incident beam into the Raman cell) as the mirror is only weakly reflecting at a wavelength of 622 nm. The Raman shifted probe pulse generated by this process has previously been measured to have a pulse length of only 15 ps [119]. This allows good temporal resolution.

In order to allow a series of images to be obtained with the probe beam system on a single laser shot, the probe beam was then split into four separate pulses by the combination of mirrors and splitters shown in fig(7.4). The four individual pulses were then approximately directed towards the target by aluminium mirrors, as shown in the diagram for two of the beams. By varying the positions of the aluminium mirrors it was possible to control the relative time delays of the four probe pulses. For the experiment reported here the delay between the the individual pulses was set to be approximately 450 ps. To accurately overlap the individual probe beams onto the target a four faceted prism was used. After passing through the plasma the four probe pulses were then all collected by a single f/2 microscope objective, as illustrated in fig(7.4). A second four faceted prism was placed directly after the imaging lens. This was done to spatially separate the four images of the plasma, produced by the individual probe beam pulses, in the final image plane. A series of RG610 coloured glass filters and also 622 nm narrow band interference filters were placed directly in front of the camera backs to block any scattered green laser light, or harmonic emission, from the plasma. The probe beam images were all recorded on HP5 film. The overall magnification of the imaging system was measured to be $\times 14$. The theoretical, diffraction limited resolution of the system was 4 μm. This is considerably smaller than any details of interest actually observed in the plasma.

To study the evolution of the plasmas generated either Schlieren photography or interferometry was used with the individual probe beams. The principle of

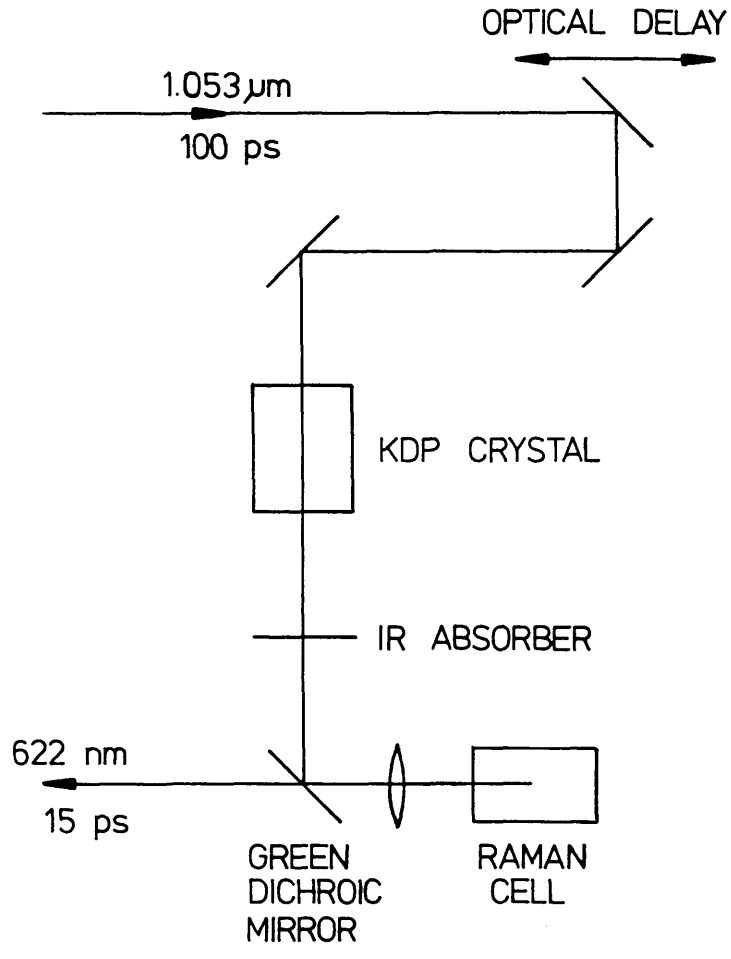


Figure 7.3 Generation of the optical probing pulse (λ = 622 nm and pulse width = 15 ps).

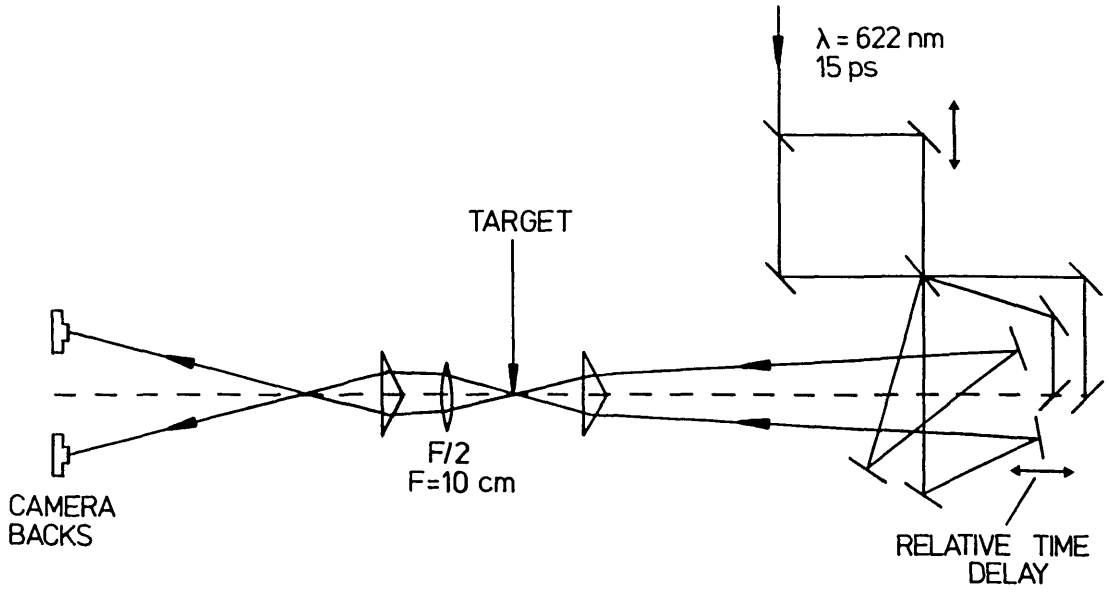


Figure 7.4 Layout of the four frame optical probing system.

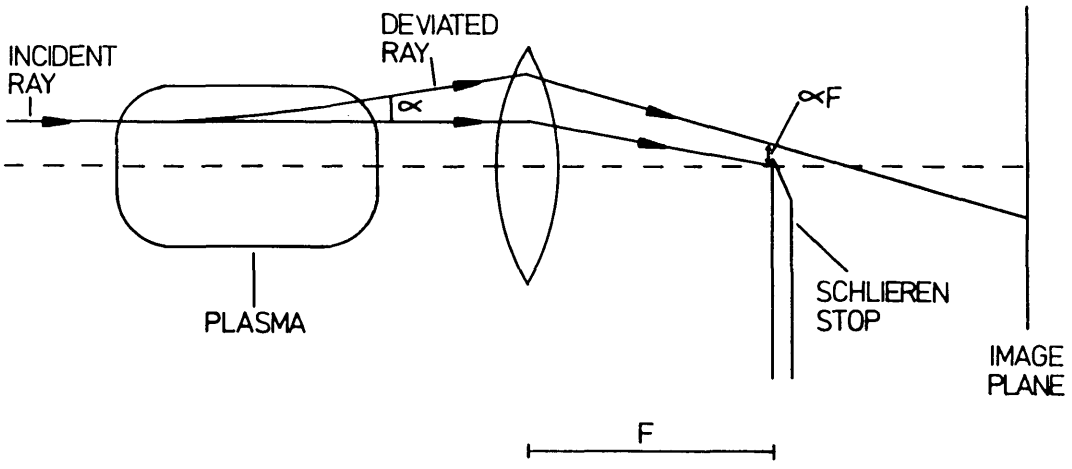


Figure 7.5 The principle of Schlieren photography.

Schlieren photography [123], is illustrated in fig(7.5). A small Schlieren stop is placed at the focus, f, of the imaging lens. Any light rays which are undeviated by the plasma are then blocked by the Schlieren stop, since they are brought to a focus at this point by the imaging lens. However any light rays which are significantly deviated by the plasma, for example by refraction due to density non−uniformities present in the plasma, will not pass through the focus of the lens and consequently will not be blocked. A ray deviated by an angle α due to the plasma will pass through the focal plane at a distance αf from the axis of the system, where f is the focal length of the lens used. Consequently the only rays of light which reach the image plane will be those which are sufficiently deviated by the plasma to miss the Schlieren stop. In general these rays will come from regions of steep density gradients present in the plasma. Consequently Schlieren images are particularly effective at indicating regions of non−uniformity in the plasma. For the measurements reported in this chapter a 300 μm diameter aluminium wire was used as the Schlieren stop. By varying the orientation of the wire used as the Schlieren stop, it was possible to make the system sensitive to density gradients in different directions in the plasma.

As an alternative to Schlieren photography, a Normaski interferometer was used on some of the probe images. The details of the type of interferometer are comprehensively described elsewhere [124].

(7.3.2) Experimental results

Fig(7.6) shows a series of probe beam images of the expansion of a 350 nm thick aluminium H−target, taken on a single main laser shot. Even up until quite late times (1.24 ns) it can be seen that the central region of the plasma is found to be opaque to the probe beam. This is because the electron density in this region must still be high enough to cause sufficient refraction of the probe rays that they are not collected by the f/2 imaging lens. It can be seen that the central region decreases in size with time, as would be expected, due to the decreasing density of the plasma. The plasma observed towards the edge of this central region appears to be reasonably uniform. The four supporting struts of the H−target can still clearly be seen at times up to 1.24 ns. This indicates that the transport of energy into the struts is insufficient to significantly disturb them.

These images should be compared with fig(7.7) which show the results of a similar laser shot, except that the aluminium stripe was now supported on a 100 nm thick formvar substrate. It can be seen that the plasma expansion produced is significantly different from that observed in fig(7.6) for a H−target. Either side of the central opaque region highly non−uniform regions can be observed. These regions are typically 100 μm wide and are presumably caused by the interaction of the expanding aluminium plasma with the relatively cold plastic substrate. Similar effects have been observed before [116], although under conditions with narrower targets and higher irradiances. Under these conditions it was suggested that these regions may become unstable to a form of the Rayleigh−Taylor instability, or possibly even the Bénard instability. Outside these turbulent regions it can be seen that the probe rays become strongly refracted again and are no longer collected by the imaging lens. Presumably this is due to the presence of dense plasma generated from the formvar substrate used to support the aluminium stripes.

Clearly these probe images indicate the presence of significant regions of relatively cold, dense plasma due to the formvar substrate at the edges of the expanding aluminium plasma. Although these outer regions of dense plasma are observed to interact with the expanding aluminium plasma it is not possible to say from these probe images how much this restricts the flow of the expanding aluminium plasma. It does however, appear possible that the plasma expansion may be sufficiently restricted to account for the higher plasma densities which were observed in section (7.2.1) when a formvar substrate was used to support the stripe targets.

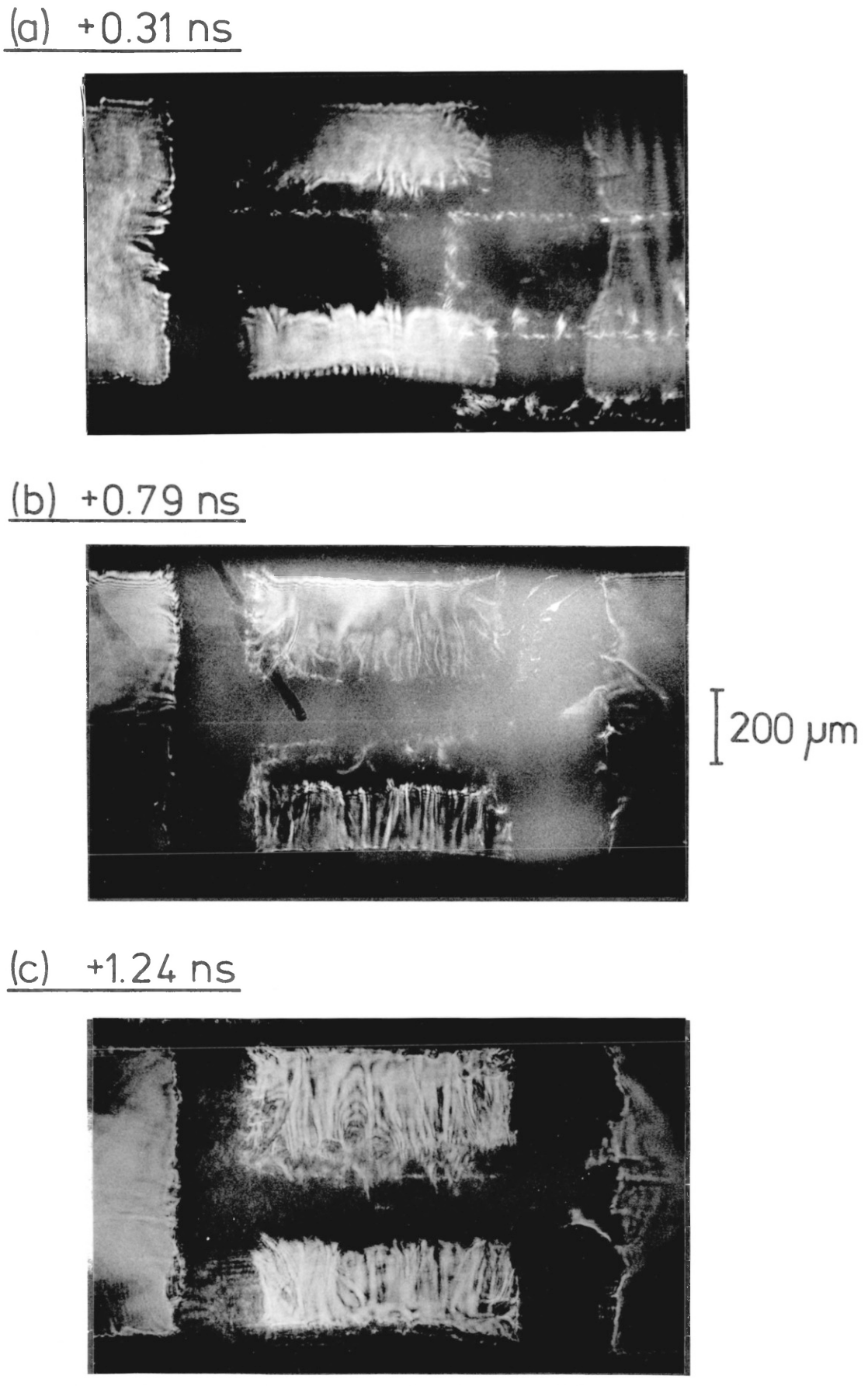


Figure 7.6 Optical probing images of a 350 nm thick aluminium H−target: (a) interferogram (+0.31 ns), (b) Schlieren image (+0.79 ns) and (c) Schlieren image (+1.24 ns). The times quoted are relative to the main plasma forming beams.

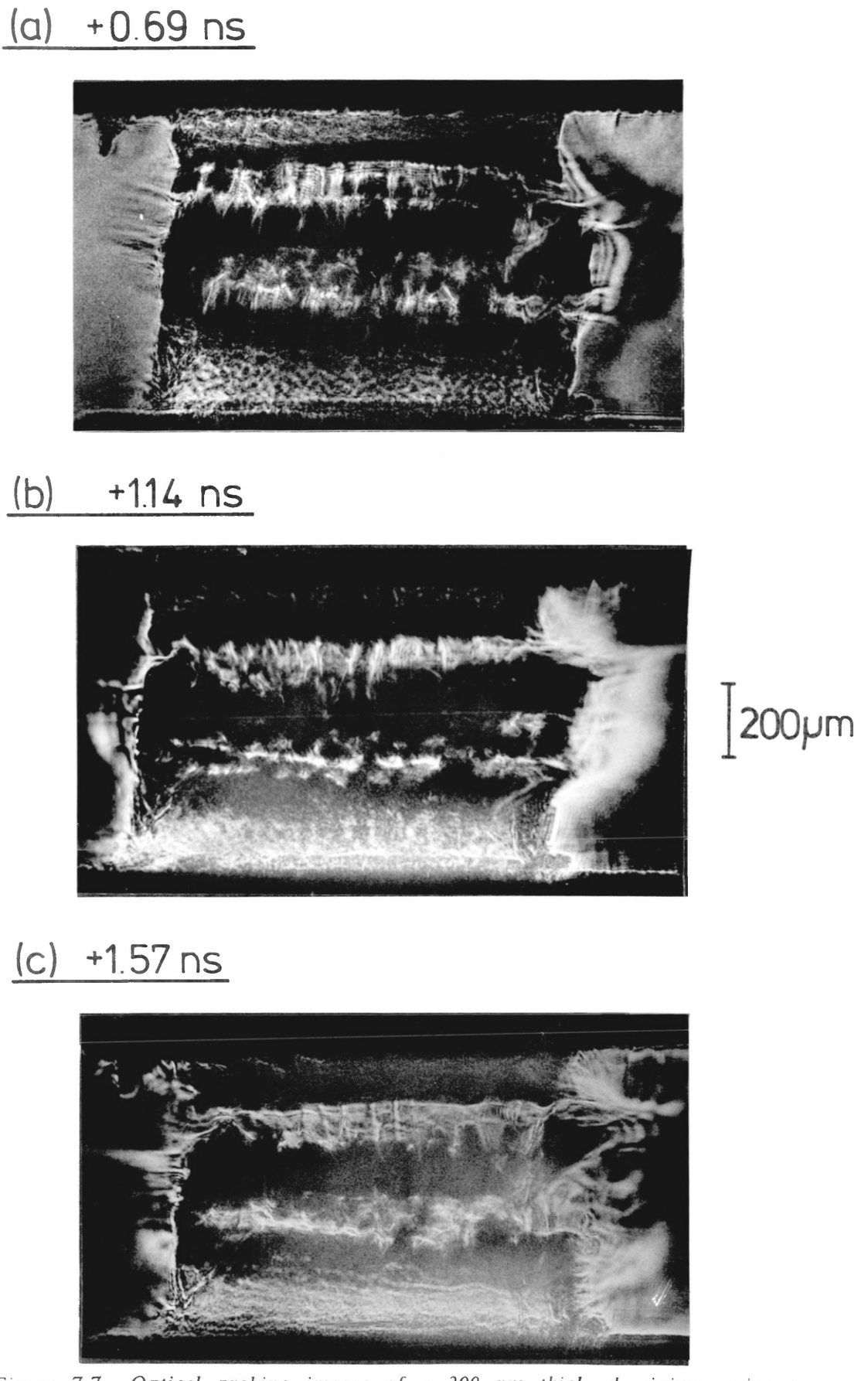


Figure 7.7 Optical probing images of a 300 nm thick aluminium stripe target supported on a 100 nm thick formvar substrate: (a) Schlieren image (+ 0.69 ns) (b) Schlieren image (+1.14 ns) and (c) Schlieren image (+1.57 ns).

Finally fig(7.8) shows a series of probe images obtained for a thinner H−target only 175 nm thick. It can be seen that for the later images the plasma now becomes completely transparent to the probe beam. In particular for the image 0.69 ns after the heating beams it appears that the central region of the plasma has only just become transparent to the probe beam, since the transmission is fairly weak in this region. This is useful since it allows some rough estimates to be made of the plasma density at this time, based on the observed refraction.

The angle a light ray is refracted by after propagating through a length L, of plasma with a transverse linear density gradient ℓ is approximately given by [123],

$$\alpha = 2.21 \times 10^{-14} \, n_e \, \lambda_p^2 \, \frac{L}{\ell} \qquad (7.1)$$

Where n_e is the electron density in cm^{-3} and λ_p the probe wavelength in cm. This expression can be used to make a very crude estimate of the refraction occurring in the plasma illustrated in fig(7.8). The collection optics used in this experiment are effectively f/5 for each individual beam of the probe system. Hence for a probe ray to be collected requires that $\alpha \leqslant 0.1$. Substituting this into eq(7.1) gives the following condition for the light rays to be collected by the lens

$$n_e \, \frac{L}{\ell} \leqslant 1.2 \times 10^{21} \ cm^{-3} \qquad (7.2)$$

The expected length of plasma through which the probe beam propagates can be estimated using the Rosen and London model described in chapter 4. This gives a value for L of 530 μm. Taking the transverse density scalelength as 100 μm (ie. half the width of the target) this gives a density of approximately 2×10^{20} cm^{-3} for the plasma to become transparent to the probe beam. This is consistent with the predictions of the Rosen and London model itself which gives a plasma density of 2.5×10^{20} cm^{-3} (T_e = 300 eV) at a time of +0.7 ns. In reality the plasma density will be less than this as the expansion will be two dimensional. A simulation with the 2−D code POLLUX gives the plasma density as 1.3×10^{20} cm^{-3} at this time (T_e = 160 eV). Clearly the above simple calculation based on eq(7.1) predicts the correct magnitude of the density of the plasma when compared with either the 1−D model or the 2−D code. It is worth noting that at early times after the heating beams (≈200 ps) when the plasma expansion is nearly one dimensional the predictions of the 1−D model and 2−D code agree to within

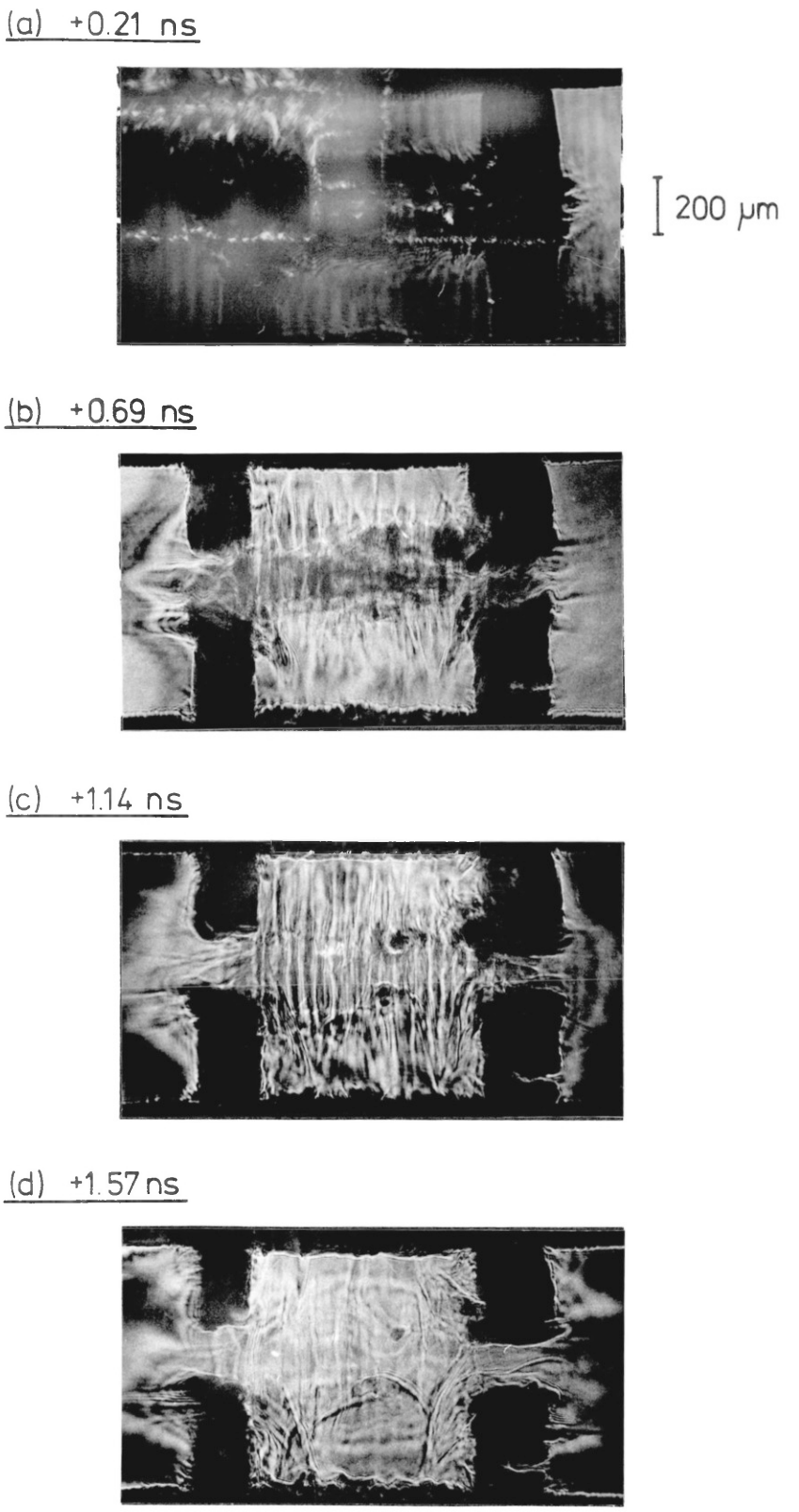


Figure 7.8 Optical probing images of a 175 nm thick aluminium H−target: (a) interferogram (+0.21 ns), (b) Schlieren image with wire horizontal (+0.69 ns), (c) Schlieren image with wire vertical (+1.14 ns) and (d) Schlieren image with wire horizontal (+1.57 ns).

10%.

In order to more carefully compare the POLLUX simulation with the experimental results a ray tracing program, written by the author, was used. Details of this program are given in Appendix A. This program was used to compute the refraction of the probe rays propagating through the density profiles obtained from the POLLUX simulations. Fig(7.9) shows the results of such ray traces at times of +0.6 ns and +0.8 ns for the results of a POLLUX simulation, for the conditions relevant to fig(7.8). At time +0.6 ns the maximum angle of refraction is 0.13 rad., this is reduced to an angle of 0.08 rad. at a time of +0.08 ns. Hence it follows that the code simulation predicts that the maximum refraction of the probe rays will drop below the angle of 0.1 rad. required for the plasma to become transparent to the probe at a time between 0.6 and 0.8 ns after the initial heating beams. This is in good agreement with the experimental observation that the plasma becomes transparent to the probe beam at a time near to 0.7 ns after the heating beams. This provides further evidence to support that presented in section (7.2) that the POLLUX code reasonably models the expansion of a free standing stripe target.

(7.3.3) Uniformity of the plasma produced

The probe beam images in fig(7.8) can be used to assess the uniformity of the central region of the plasmas produced. For the final image at time +1.57 ns where the Schlieren stop was aligned along the axis of the target, the plasma image is observed to be reasonably uniform. This indicates that no significant density non−uniformities were present in the direction perpendicular to the axis of the plasma. However in the image at +1.14 ns, where the Schlieren stop was aligned perpendicular to the target axis, significant structure can be observed. This structure indicates the presence of density non−uniformities with a periodicity of about 40 μm lying along the axis of the plasma. By using eq(7.1) a rough estimate can be made as to how pronounced these non−uniformities must be, to be visible in the Schlieren image. Since the Schlieren stop used was 300 μm wide the probe rays have to be deflected by an angle of 1.5×10^{-3} rad. to pass it. Hence, from eq(7.1) for the probe rays to pass the Schlieren stop it is necessary that

$$\delta n_e \frac{L}{\ell} \geqslant 1.8 \times 10^{19} \text{ cm}^{-3} \qquad (7.3)$$

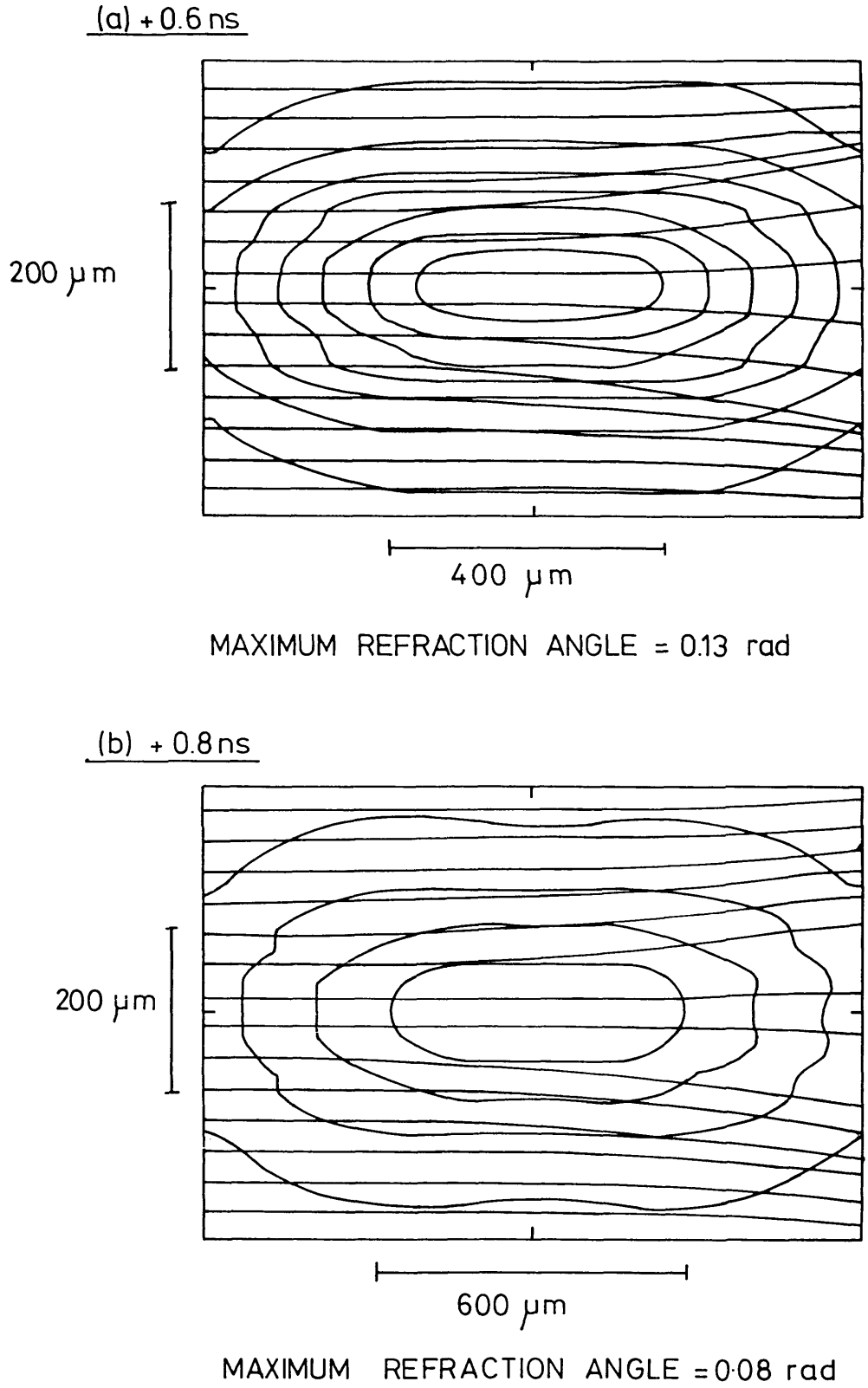


Figure 7.9 Ray traces of the probe beam for the density profiles predicted by POLLUX, for the experimental conditions relevant to fig. 7.8. The density contours are at intervals of 0.005 n_{ec}. (a) 600 ps after the plasma forming beams and (b) 800 ps after the plasma forming beams.

Where δn_e is the size of the density perturbation. The distance that the density non−uniformities extend in the direction of propagation of the probe rays L, can be estimated by assuming that it is comparable to the distance the non−uniformities extend over in the transverse direction shown in fig(7.8)(c). This gives a value of L of 400 μm. The value of the density scalelength can be measured directly from fig(7.8)(c), which gives a value of 40 μm. This gives a minimum density perturbation of $\pm 1.8 \times 10^{18}$ cm^{-3}. Assuming an average electron density of 5.0×10^{19} cm^{-3} (taken from the POLLUX simulation for this time), this gives a minimum density perturbation of approximately ±3%. Although this estimate is very approximate it does give some indication that significant density non−uniformities may be present in the plasmas produced. It would appear that the major causes of these density non−uniformities are likely to be variations in intensity across the profiles of the laser beams used to irradiate the targets, and also irregularities in the original targets.

(7.4) Discussion and Conclusions

The expansion of free standing aluminium stripe targets have been observed to reasonably closely follow predictions of a 2−D code. The experimental measurements of the plasma density were made by the use of S.R.S. spectra produced by the interaction of a high power laser beam with the plasma, and also by optical probing measurements of the expanding foil. However when the aluminium stripe targets were supported on a formvar substrate the plasma densities observed were found to be significantly higher, and to lie midway between the 2−D code predictions and the predictions of a 1−D model. It appears that from the optical probing data the expanding aluminium plasma may be confined at either side by the presence of regions of colder, dense plasma generated from the formvar substrate. This may cause the plasma expansion to more closely approximate the one dimensional case. The loss of energy from the expanding aluminium plasma into the formvar substrate by lateral heat flow may also cause the expansion to slow down, and consequently this may also contribute to the higher plasma densities observed.

For the stripe targets supported on formvar substrates highly non−uniform interaction regions were observed between the expanding aluminium plasma and the outer regions of dense plasma generated from the formvar substrate. For x−ray laser experiments the width of the targets used would be significantly smaller than the value of 200 μm used here. Consequently even stronger interaction could be expected between the central expanding plasma and the formvar substrate. Hence

it appears such targets may be of limited value for x−ray laser experiments and that it may be advantageous to use the better behaved free standing H−targets. However such targets are not easy to manufacture and consequently it is difficult to produce large quantities of them. It is for this reason that the experiments of chapters 5 and 6 used aluminium stripe targets supported on formvar substrates. Since the width of the targets used in these experiments of 200−300 μm was significantly larger than the typical diameter of the interaction beam, which was 100 μm, the presence of these turbulent regions is not expected to be important in these experiments. The only remaining difficulty in the use of these targets is that for the purposes of experimental design it is not straightforward to predict the expansion of the targets. However since from the results of this chapter it appears that the expansion of the targets lie somewhere between the 1−D and 2−D cases, it should still be possible to predict the plasma conditions to sufficient accuracy for the purposes of designing underdense plasma experiments.

Finally from the optical probing measurements it appears that a certain degree of density non−uniformities may be present in the plasmas produced. A crude estimate gives a lower limit for the degree of the non−uniformities of ±3%. It seems likely that the causes of these non−uniformities are hot spots present in the plasma forming laser beams, and also irregularities in the original targets. Although the large underdense plasmas generated in chapters 5 and 6 were produced under different conditions (ie longer laser pulse lengths and thicker targets), it seems possible that a similar degree of non−uniformity may be present in these plasmas also. This is because the likely causes of the plasma non−uniformities (ie. laser beam hot spots and target defects) would also have been present in these experiments.

CHAPTER 8

SUMMARY OF MAIN CONCLUSIONS

This thesis has described two areas of interest to proposed laser fusion schemes. Firstly the study of the propagation of shocks generated by temporally shaped and unshaped laser pulses, and secondly the study of instabilities in a large underdense plasma.

(8.1) Coalescing shock experiment

In Chapter 2 an experiment was described to study the propagation of shocks generated by Gaussian and tailored laser pulses. In particular the first direct experimental observation of the coalescence of two shocks generated by a temporally shaped laser pulse was reported on. This is of relevance to schemes for the adiabatic compression of laser fusion targets. Optical streak photography of the rear surface of aluminium multiple step targets was used to study the breakout of these shocks and observe their behaviour. In general the experimental results were in good agreement with the results of 1−D computer simulations, except that after the end of the laser pulse the shocks were found to decay far more rapidly than predicted. It seems likely that this discrepancy is due to two dimensional effects. Further useful future work in this area could involve the use of laser beam smoothing techniques to generate a more uniform focal spot profile. This would improve the uniformity of the shock front generated and hence allow more accurate shock velocity measurements to be made. Also it would be worthwhile to investigate if the discrepancies observed between the experimental results and the simulations are indeed due to 2−D effects. This could be done by the use of larger focal spots to generate more planar shocks.

(8.2) Study of instabilities in a large underdense plasma

A novel experimental arrangement has been used to generate large underdense plasmas, which are comparable in size and conditions to the plasmas which will be present around the edges of proposed laser fusion targets. The instabilties occurring when a high power laser beam interacts with this preformed plasma have been studied.

In chapter 5 time resolved measurements of the transmitted interaction beam showing its break up due to filamentation were described. The filamentary break up of the interaction beam was found to generate up to 50:1 maximum to minimum intensity variations across the beam profile. This process was found to have a threshold near 10^{14} Wcm^{-2}, which is consistent with theoretical predictions. Over very short time scales it was unexpectedly found that the plasma can actually smooth the laser beam profile. The mechanism for this process is unclear, although it may be due to refraction from density non-uniformities in the plasma. For bismuth and higher density aluminium plasmas whole beam self-focusing was observed. The degree of self-focusing occurring was found to be consistent with predictions of a simple model.

In chapter 6 the use of an I.S.I. system and a R.P.P. to reduce the levels of S.R.S., S.B.S. and filamentation in a large underdense plasma were reported on. It was found that a R.P.P. reduced the levels of S.R.S. and S.B.S. by a factor of 10-20. For an I.S.I. system a reduction of nearly three orders of magnitude in the levels of both these instabilities was achieved. From these results, and also from measurements made of the S.R.S. and S.B.S. spectra it appears that filamentation may play a key intermediate role in the occurrence of both these instabilities. Preliminary measurements made of the transmitted interaction beam when either I.S.I. or a R.P.P. is used appear to indicate some suppression of the filamentation instability by these techniques. Also an initial characterization of a I.S.I./R.P.P. hybrid system was made. The results obtained suggest that it may be a promising option for generating large size focal spots in future experiments. Useful future work in these areas would be to extend the I.S.I. measurements to higher irradiances, and also to make measurements at higher plasma densities where higher levels of these instabilities could be expected.

Finally, in chapter 7 optical probing measurements used to determine the uniformity of the large underdense plasmas generated, appear to suggest that the presence of a formvar substrate to support the targets may play an important role in the plasma expansion. It seems the formvar substrate may result in the generation of regions of cool, dense plasma either side of the central target stripe. This may confine the plasma expansion, and cause it to more closely approximate the 1-D case. Further experimental evidence is provided by plasma density measurements obtained from S.R.S. spectra, which indicate that the expansion of a stripe target supported on a formvar substrate lies midway between the predictions of a 1-D model and a 2-D code. The expansion of a free standing stripe target was found to be reasonably close to the 2-D code predictions.

APPENDIX A

RAY TRACING PROGRAM

The two dimensional ray tracing program used in chapters 5 and 7 calculates the paths followed by an arbitrary number of initially parallel rays in a plasma of varying refractive index. The refraction of each ray is calculated from geometric optics considerations of the effect of the varying refractive index, due to the changing electron density of the plasma. It is assumed that the light rays do not perturb the plasma.

The input to the program takes the form of a electron density profile defined on a rectangular 2−D grid. The program then calculates the density at the centre of each rectangle in this grid. The is done so that a planar density profile can be calculated for each of the individual triangular elements which now make up the grid. The path followed by a light ray in each individual triangular element can than be calculated exactly. This is because in a planar electron density profile the path followed by a light ray due to refraction has an exact solution, which takes the form of a parabola. The coefficients of the parabola can be calculated by considering Snell's law for a continuous medium in which the direction of the density gradient is constant [125], this states:

$$\mu \sin \theta = \text{constant} \tag{A.1}$$

Where θ is the angle between the ray and the density gradient and μ is the refractive index of the medium, which for a plasma is given by [10]:

$$\mu = \left[1 - \frac{n_e}{n_{ec}}\right]^{\frac{1}{2}} \tag{A.2}$$

From eqs (A.1) and (A.2) it is straightforward to show that for a planar density profile of the form $n_e = A+By$, a light ray will follow the path of a parabola given by the expression:

$$y = \frac{1}{\tan\theta_0}\, x - \frac{B\left[1 + \dfrac{1}{\tan^2\theta_0}\right]}{4n_{ec}\left[1 - \dfrac{A}{n_{ec}}\right]}\, x^2 \tag{A.3}$$

Where θ_0 is the angle initially made betwen the ray and the direction of the density gradient at the origin.

The ray tracing program uses eq(A.3) to calculate the path of the light ray in the particular triangular element the ray happens to be in. Once the ray propagates out of that element the program then determines which new triangular element the ray has moved to. The ray path is then determined in this new element. This process is repeated until a ray initially incident from the left hand boundary of the plasma, has passed out of another outer boundary of the plasma. This whole process can be repeated for any number of rays initially incident from the left hand side of the plasma. The output of the program takes the form of graphical plots of each ray path, and also numerical output of the final position and direction of each ray as it passes out of one of the outer boundaries of the plasma.

REFERENCES

(1) J. Nuckolls, L. Wood, A. Thiessen and G. Zimmerman, Nature 239, 139 (1972).

(2) J. Meyer-ter Vehn, in 'Laser Plasma Interactions 3', ed. M.B. Hooper, S.U.S.S.P. Publications Edinburgh 1986.

(3) T.H. Johnson, Proceedings of the I.E.E.E. 72, 548 (1984).

(4) 'Laser Plasma Interactions', S.U.S.S.P. Publications Edinburgh, ed. R.A. Cairns and J.J. Sanderson (1980), ed. R.A. Cairns (1983) and ed. M.B. Hooper (1986).

(5) R.G. Evans, Can. J. Phys 64, 893 (1986).

(6) K.A. Brueckner and S. Jorna, Rev. Mod. Phys. 46, 325 (1974).

(7) S.E. Bodner, J. Fusion Energy 1, 221 (1981).

(8) G.J. Pert, in 'Plasma Physics and Nuclear Fusion Research', ed. R. Gill, Academic Press London 1981.

(9) C.E. Max, 'Theory of the Coronal Plasma in Laser Fusion Targets', course 2, Les Houches summer school 1980.

(10) T.P. Hughes, in 'Laser Plasma Interactions', ed. R.A. Cairns and J.J. Sanderson, S.U.S.S.P. Publications Edinburgh 1980.

(11) A.B. Langdon, Phys. Rev. Lett. 44, 575 (1980).

(12) J.P. Friedberg, R.W. Mitchell, R.L. Morse and L.I. Rudsinski, Phys. Rev. Lett. 28, 795 (1972).

(13) K.R. Manes, V.C. Rupert, J.M. Auerbach, P. Lee and J.E. Swain, Phys. Rev. Lett. 39, 281 (1977).

(14) J.E. Balmer and T.P. Donaldson, Phys. Rev. Lett. 39, 1084 (1977).

(15) M.H. Key, in 'Laser Plasma Interactions' ed. R.A. Cairns and J.J. Sanderson, S.U.S.S.P. Publications Edinburgh 1980.

(16) D.W. Forslund, J.M. Kindel, K. Lee, E.L. Lindman and R.L. Morse, Phys. Rev. A 11, 679 (1975).

(17) K.G. Estabrook, E.J. Valeo and W.L. Kruer, Phys. Fluids 18, 1151 (1975).

(18) L. Spitzer and R. Härm, Phys. Rev. 89, 977 (1953).

(19) L. Spitzer, 'Physics of Fully Ionised Gases', Interscience New York (1956).

(20) R.C. Malone, R.L. McCory and R.L. Morse, Phys. Rev Lett. 34, 721 (1975).

(21) B. Yaakobi and T. Bristow, Phys. Rev. Lett. 38, 350 (1977).

(22) A. Hauer, W.C. Mead, O. Willi, J.D. Kilkenny, D.K. Bradley, S.D. Tabatabaei and C. Hooker, Phys. Rev. Lett. 53, 2563 (1984).

(23) O. Willi, S.D. Tabatabaei, D. Riley, A. Hauer, N. Delameter, C. Chenais-Popovics, A.J. Cole and P.D. Apte, Phys. Rev. A 39, 6090 (1989).

(24) A.R. Bell, R.G. Evans and D.J. Nicholas, Phys. Rev. Lett. 46, 243 (1981).

(25) E.M. Epperlein, G.J. Rickard and A.R. Bell, Phys. Rev. Lett. 61, 2453 (1988).

(26) A.J. Cole, J.D. Kilkenny, P.T. Rumsby, R.G Evans, C.J. Hooker and M.H. Key, Nature 299, 329 (1982).

(27) N. Burnett, G. Josin, B. Ahlborn and R. Evans, Appl. Phys. Lett. 38, 226 (1981).

(28) F. Cottet, J. Romain, R. Fabbro and B. Faral, Phys. Rev. Lett. 52, 1884 (1984).

(29) A. Ng, D. Parfeniuk and L. DaSilva, Phys. Rev. Lett. 54, 2604 (1985).

(30) L. Veeser and J. Solem, Phys. Rev. Lett. 40, 1391 (1978).

(31) R. Trainor, J. Shanar, J. Auerbach and N. Holmes, Phys. Rev. Lett. 42, 1154 (1979).

(32) L. Veeser, J. Solem and A. Lieber, Appl. Phys. Lett. 35, 761 (1979).

(33) R. Trainor, N. Holmes, R. Anderson, E. Campbell, W. Mead, R. Olness, R. Turner and F. Ze, Appl. Phys. Lett. 43, 542 (1983).

(34) D. Riley, S.J. Rose, O. Willi and T. Afshar−rad, To be published in Europhysics Letters.

(35) A.C. Mitchell and W.J. Nellis, J. Appl. Phys. 52, 3363 (1981).

(36) Ya.B. Zeldovich and Yu.P. Raizer, 'Physics of Shock Waves and High Temperature Hydrodynamic Phenomena', (Academic, New York and London, 1966), vol 1, pp. 45−67.

(37) C.E. Ragan III, Phys. Rev. A 25, 3360 (1982), and 29 1391 (1984); SESAME libary, Los Alamos National Laboratory, Los Alamos, Material No. 3712 (unpublished).

(38) Motz, 'The Physics of Laser Fusion', (Academic, London, 1979), pp. 182−183.

(39) Guderly, Luftfahrt Forschung 19, 302 (1942).

(40) E. Goldman, Plasma Phys. 15, 289 (1973).

(41) P.C. Thompson and P.D. Roberts, Laser and Particle Beams 2, 13 (1984).

(42) R. Trainor and Y. Lee, Phys. Fluids 25, 1898 (1982).

(43) D. Salzmann, H. Szichman and A.D. Krumbein, Phys. Fluids 30, 515 (1987).

(44) J. Christiansen, D. Ashby and K. Roberts, Comput. Phys. Commun. 7, 271 (1974).

(45) A. Loeb and S. Eliezer, Phys. Fluids 28, 1196 (1985).

(46) S. Jackel, D. Salzmann, A. Krumbein and S. Eliezer, Phys. Fluids 26, 3138 (1983).

(47) M.H. Key, W.T. Toner, T.J. Goldsack, J.D. Kilkenny, S.A. Veats, P.F. Cunningham and C.L.S. Lewis, Phys. Fluids 26, 2011 (1983).

(48) R.H. Lehmberg and S.P. Obenschain, Opt. Commun. 46, 27 (1983).

(49) Y. Kato, K. Mima, N. Miyanaga, S. Aringa, Y. Kitagawa, M. Nakatsuka and C. Yamanaka, Phys. Rev. Lett. 53, 1057 (1984).

(50) X. Deng, X. Liang, Z. Chen, W. Yu and R. Ma, Appl. Opt. 25, 377 (1986).

(51) R.P. Drake, R.E Turner, B.F. Lasinski, K.G. Estabrook, E.M. Campbell, C.L. Wang, D.W. Phillion, E.A. Williams and W.L. Kruer, Phys. Rev. Lett. 53, 1739 (1984).

(52) K. Tanaka, L.M. Goldman, W. Seka, M.C. Richardson, J.M. Soures and E.A. Williams, Phys. Rev. Lett. 48, 1179 (1982).

(53) R.E. Turner, D.W. Phillion and K.G. Estabrook, Phys. Fluids 26, 579 (1983).

(54) H. Figueroa, C. Joshi and C.E. Clayton, Phys. Fluids 30, 586 (1987).

(55) A.J. Cole, J. Murdoch, S.M.L. Sim and R. Evans, Opt. Commun. 36, 51 (1981).

(56) R.E. Turner, K. Estabrook, R.L. Kaufman, D.R. Bach, R.P. Drake, D.W. Phillion, B.F. Lasinski, E.M. Campbell, W.L. Kruer and E.A. Williams, Phys. Rev. Lett. 54, 189 (1985).

(57) R.P. Drake, E.A. Williams, P.E. Young, K. Estabrook, W.L. Kruer, H.A. Baldis and T.W. Johnston, Phys. Rev. Lett. 60, 1018 (1988).

(58) B.H. Ripin, F.C Young, J.A. Stamper, C.M. Armstrong, R. Decoste, E.A. Mclean and S.E. Bodner, Phys. Rev. Lett. 39, 611 (1977).

(59) M.D. Rosen, D.W. Phillion, V.C. Rupert, W.C. Mead, W.L. Kruer, J.J. Thomson, H.N. Kornblum, V.W. Silvinsky, G.J. Caporaso, M.J. Boyle and K.G. Tirsell, Phys. Fluids 22, 2020 (1979).

(60) G.J. Walsh, D.M. Villeneuve and H.A Baldis, Phys. Rev. Lett. 53, 1445 (1984).

(61) S. Jorna, Phys. Fluids 17, 765 (1974).

(62) J.F. Drake, P.K. Kaw, Y.C. Lee, G. Schmidt, C.S. Liu and M.N. Rosenbluth, Phys. Fluids 17, 778 (1974).

(63) C.S. Liu, M.N. Rosenbluth and R.B. White, Phys. Fluids 17, 1211 (1974).

(64) D.W. Forslund, J.M. Kindel and E.L. Lindman, Phys. Fluids 18, 1002 (1975).

(65) D.W. Forslund, J.M. Kindel and E.L. Lindman, Phys. Fluids 18, 1017 (1975).

(66) A. Simon and R.W. Short, Phys. Rev. Lett. 53, 1912 (1984).

(67) H.C. Barr, T.J.M. Boyd and G.A. Coutts, Phys. Fluids 31, 641 (1988).

(68) S.J. Karttunen, Private Communication (1988).

(69) C.N. Lashmore−Davies, in 'Plasma Physics and Nuclear Fusion Research', ed. R. Gill, Academic press London 1981.

(70) W.L. Kruer, in 'Laser Plasma Interactions', ed. R.A. Cairns and J.J. Sanderson, S.U.S.S.P. Publications Edinburgh 1980.

(71) M.N. Rosenbluth, Phys. Rev. Lett. 29, 565 (1972).

(72) H. Figueroa, C. Joshi, H. Azechi, N.A. Ebrahim and K. Estabrook, Phys. Fluids 27, 1887 (1984).

(73) S.J. Karttunen, Laser and Particle Beams 3, 157 (1985).

(74) W.L. Kruer, in 'Laser Plasma Interactions 2', ed. R.A. Cairns, S.U.S.S.P. Publications Edinburgh 1983.

(75) P. Kaw, G. Schmidt and T. Wilcox, Phys. Fluids 16, 1522 (1973).

(76) B.I. Cohen and C.E. Max, Phys. Fluids 22, 1115 (1979).

(77) V.K. Tripathi and L.A. Pitale, J. Appl. Phys. 48, 3288 (1977).

(78) W.L. Kruer, Comm. Plasma Phys. Contro. Fusion 9, 63 (1985).

(79) R.S. Craxton and R.L. McCory, J. Appl. Phys. 56, 108 (1984).

(80) A.J. Schmitt, Phys. Fluids 31, 3079 (1988).

(81) O. Willi, D. Bassett, A. Giulietti and S. Karttunen, Opt. Commun. 70, 487 (1989).

(82) I.N. Ross and E.M. Hodgson, J. Phys. E 18, 169 (1985).

(83) I.N. Ross, J. Boon, R. Corbett, A. Damerell, P. Gottfeldt, C. Hooker, M. Key, G. Kiehn, C. Lewis and O. Willi, Appl. Opt. 26, 1584 (1987).

(84) R.A. London and M. Rosen, Phys. Fluids 29, 3813 (1986).

(85) The G.O.I. was based on a design by Kentech Instruments Ltd., The Blackett Laboratory, Prince Consort Road, London, U.K..

(86) D.M. Benzel and M.D. Pocha, Rev. Sci. Instrum. 56, 1456 (1985).

(87) M.J. Ekart, R.L. Hanks, J.D. Kilkenny, R. Pasha, J.D. Wiedwald and J.D. Hares, Rev. Sci. Instrum. 57, 2046 (1986).

(88) T.P. Donaldson and I.S. Spalding, Phys. Rev. Lett. 36, 467 (1976).

(89) O. Willi and P.H.Y. Lee, Opt. Commun. 55, 120 (1985).

(90) O. Willi and P.T. Rumsby, Opt. Commun. 37, 45 (1981).

(91) P.E. Young, H.A. Baldis, R.P. Drake, E.M. Campbell and K.G. Estabrook, Phys. Rev. Lett. 61, 2336 (1988).

(92) N. Rizvi, Private Communication (1988).

(93) N.K. Moncur, Appl. Opt. 16, 1449 (1977).

(94) O. Willi, P.T. Rumsby, C. Hooker, A. Raven and Z.Q. Lin, Opt. Commun. 41, 110 (1982).

(95) V.V. Aleksandrov, M.V. Brenner, S.V. Loburev, N.G. Kovalskii and A.M. Rubenchik, Sov. J. Quantum Electron 16, 443 (1986).

(96) C.E. Max, W.C. Mead and J.J. Thomson, Appl. Phys. Lett. 29, 783 (1976).

(97) O. Willi, P.T. Rumsby and Z.Q. Lin, Laser interaction and related plasma phenomena, Vol. 6, Proc. 6th Workshop, eds. H. Hora and G.H. Miley (Plenum, New York, 1984) p.633.

(98) K. Estabrook, W.L. Kruer and D.S. Bailey, Phys. Fluids 28, 19 (1985).

(99) Y. Kato and K. Mima, Appl. Phys. B29, 186 (1982).

(100) S.P. Obenschain, J. Grun, M.J. Herbst, K.J. Kearney, C.K. Manka, E.A. Mclean, A.N. Mostovych, J.A. Stamper, R.R. Whitlock, S.E. Bodner, J.H. Gardner and R.H. Lehmberg, Phys. Rev. Lett. 56, 2807 (1986).

(101) A.N. Mostovych, S.P. Obenschain, J.H. Gardner, J. Grun, K.J. Kearney, C.K. Manka, E.A. Mclean and C.J. Pawley, Phys. Rev. Lett. 59, 1193 (1987).

(102) S.P. Obenschain, C.J. Pawley, A.N. Mostovych, J.A. stamper, J.H. Gardner, A.J. Schmitt and S.E. Bodner, Phys. Rev. Lett. 62, 768 (1989).

(103) M. Born and E. Wolf, *Principles of Optics*, 6th corrected ed. (Pergamon Press, New York, 1980) pp. 436–437.

(104) C.N. Danson, R. Bann, D. Pepler, N. Rizvi, I. Ross, P. Rumsby, R. Jackson, S.E. Coe, T. Afshar–rad, M. Desselberger and O. Willi, Annual Report to the Laser Facility Committee 1989, RAL–89–043.

(105) I.V. Aleksandrova, A.E. Danilov, V.V. Orlov, S.M. Savchenko, G.V. Sklizkov and S.I. Fedotov, Sov. J. Quantum Electron 13, 561 (1983).

(106) W.L. Kruer, Phys. Fluids 23, 1273 (1980).

(107) R.G. Evans, Plasma Physics 23, 99 (1981).

(108) J.J. Thomson, Nucl. Fusion 15, 237 (1975).

(109) K. Estabrook, J. Harte, E.M. Campbell, F. Ze, D.W. Phillion, M.D. Rosen and J.T. Larsen, Phys. Rev. Lett. 46, 724 (1981).

(110) C. Danson, Private Communication (1988).

(111) A.J. Schmitt and J.H. Gardner, J. Appl. Phys. 60, 6 (1986).

(112) Laboratory for Laser Energetics Review 36, pp. 158–172 (1988).

(113) Laboratory for Laser Energetics Review 37, pp. 40–55 (1988).

(114) O. Willi, D. Bassett, S. Coe, J. Edwards, M. Grande, P. Jaegle, G. Jamelot, M. Key, G. Kiehn, A. Klisnick, C. Lewis, D. O'Neill, G. Pert, S. Ramsden, C. Regan, S. Rose and R. Smith, 'XUV amplification in cylindrically expanding plasmas', Proc. of the A.P.S. 168, 115 (1988).

(115) O. Willi, V. Barrow, D. Bassett, S. Coe, J. Edwards, M. Grande, M. Key, G. Kiehn, C. Lewis, D. O'Neill, G. Pert, S. Ramsden, C. Regan, S. Rose, R. Smith and J. Wark, 'XUV amplification in cylindrically expanding plasmas', STS Press, Mclean, VA, 59 (1988).

(116) D. Bassett, O. Willi, G. Pert and R.G. Evans, Annual Report to the Laser Facility Committee 1987, RAL−87−041, pp. 57−58.

(117) G.J. Pert, J. Comput. Phys. 43, 111 (1981).

(118) R.G. Evans, A.J. Bennett and G.J. Pert, J. Phys. D 15, 1673 (1982).

(119) D. Bassett and O. Willi, Annual Report to the Laser Facility Committee 1987, RAL−87−041, pp 45−48.

(120) J.A. Stamper, E.A. Mclean and B.H. Ripin, Phys. Rev. Lett. 40, 1177 (1978).

(121) A. Raven and O. Willi, Phys. Rev. Lett. 43, 278 (1979).

(122) M.J. Colles, Opt. Commun. 1, 169 (1969).

(123) F.C. Jahoda and G. A. Sawyer, in 'Methods of Experimental Physics' Vol. 9B, ed. L. Marton, Academic Press New York 1971.

(124) R. Benattar, C. Popovics and R. Sigel, Rev. Sci. Instrum. 50, 1583 (1979).

(125) M. Born and E. Wolf, *Principles of Optics*, 6th corrected ed. (Pergamon Press, New York, 1980) pp. 51−55.